5-2015

Three Dimensional Simulations of Tornado Sheltering Effect of Man-made Structures

Piotr Gorecki

University of Arkansas, Fayetteville

Follow this and additional works at: http://scholarworks.uark.edu/etd

Part of the Civil Engineering Commons, and the Computer-Aided Engineering and Design Commons

www.manaraa.com

Three Dimensional Simulations of Tornado Sheltering Effect of Man-made Structures

Three Dimensional Simulations of Tornado Sheltering Effect of Man-made Structures

A dissertation submitted in partial fulfillment
of the requirements for the degree of
Doctor of Philosophy in Engineering

by

Piotr Gorecki
Opole University of Technology
Master of Science in Civil Engineering, 2010

May 2015
University of Arkansas

This dissertation is approved for recommendation to the Graduate Council.

_____
Dr. R. Panneer Selvam
Dissertation Director

_____   _____
Dr. Richard Coffman   Dr. Rick J. Couvillion
Committee Member   Committee Member

_____
Dr. Ernie Heymsfield
Committee Member

ABSTRACT

A three dimensional computational fluid dynamics (CFD) model was utilized to investigate tornado-like vortex interactions with wide man-made structures. The tornado-like wind profile was approximated using Rankine vortex model. By utilizing the CFD model, it was explained why tornadoes exhibit less damage on leeward side of large structures. During the preliminary stage of this study, a perpendicular vortex-prism interaction was analyzed. The prism height and the length were equal to the vortex core radius. The prism was also 12 times wider than the vortex core radius. During the vortex-prism interaction, the near-ground portion of the vortex was blocked by the leading face of the prism. To proceed with the travel, the primary vortex had to introduce a new low-level vortex behind the prism, which mitigated maximum flow speeds on the prism's leeward side. Various visualization techniques were employed to understand and quantitatively study the vortex sheltering effect. It was shown that the vortex flow speeds are reduced by more than 30% in a region of length equal to 6 times the prism height. The sheltering effect was also investigated for different prism sizes. It was demonstrated that the thinner the prism is, the more it disrupts the near-ground strength of the translating vortex. Following these findings, the tornado sheltering performance of a wide wall was studied. During the vortex-wall interaction a 20 m high wall was able to reduce the maximum tornado-like wind speeds by 30%, on a distance of 102 m behind the wall. The magnitude of the wind speed reduction was found to be dependent on the wall width and the wall height, relatively to the vortex core radius. The sheltering efficiency of the wall also changes depending on the tornado-like vortex impact angle on the wall. The new findings arising in this study can be applied for designing tornado-safe structures and areas.

ACKNOWLEDGEMENTS

TABLE OF CONTENTS

LIST OF FIGURES

LIST OF TABLES

NOMENCLATURE

x_i	non-dimensional Cartesian coordinates in streamwise (x_1), lateral (x_2) and vertical directions (x_3)
$\bar{f}$	grid filtered value of f
S_{ij}	strain-rate tensor
u_i	non-dimensional Cartesian velocity components in x_1, x_2 and x_3 directions
u, v, w	u_1, u_2, u_3
H	non-dimensional height of the rectangular prism
L	non-dimensional length of the rectangular prism
W	non-dimensional width of the rectangular prism
C_s, C_K	Smagorinsky model constants
ν_{SGS}	subgrid scale eddy viscosity
ν	non-dimensional kinematic viscosity
k_{SGS}	subgrid component of k (turbulent energy)
h_i	grid size in x_i direction
p	non-dimensional pressure
r_{max}	non-dimensional vortex core radius
r	non-dimensional distance from the vortex centre
u_{tran}	translational velocity of a vortex
u_θ	tangential velocity of a vortex

α vortex strength constant

β vortex angle of attack

ρ non-dimensional fluid density

Γ circulation

ω vorticity

u^* friction velocity

z_0 ground roughness length

t non-dimensional time

Re Reynolds number

Re_v vortex-based Reynolds number

LIST OF PUBLISHED PAPERS

- *Journal Papers:*

Gorecki P., Selvam R.P. (2015). *Tornado sheltering effect of a rigid wall – influence of the wall width.* Technical Transactions - Civil Engineering. Submitted for Publication.

Gorecki P., Selvam R.P. (2015). *Rankine Combined Vortex Interaction with a Rectangular Prism.* International Journal of Computational Fluid Dynamics 29(1), 120-132.

Gorecki P., Selvam R.P. (2014). *Visualization of tornado-like vortex interacting with wide tornado-break wall.* Journal of Visualization. Online publication date: 16-Nov-2014.

- *Conference Papers:*

Ragan Q. S., Selvam R.P., **Gorecki P.** (2013). *Tornado-induced wind-forces for cylindrical structures.* 12th Americas Conference on Wind Engineering 2013, ACWE 2013: Wind Effects on Structures, Communities, and Energy Generation 2, 927-935.

Gorecki P., Selvam R.P. (2013). *Three-dimensional simulation of tornado over complex terrain.* 12th Americas Conference on Wind Engineering 2013, ACWE 2013: Wind Effects on Structures, Communities, and Energy Generation 1, 543-560.

Selvam, R.P., **Gorecki P.** (2012). *Effect of tornado size on forces on thin 2D cylinder.* Proceedings of 3rd American Association for Wind Engineering Workshop. Hyannis, Massachusetts, USA.

Selvam, R.P., **Gorecki P.** (2012). *CFD for Infrastructure, Thermal Management and Energy.* Proceedings of International Conference on Application of Fluid Dynamic. Gaborone, Botswana.

- *Posters:*

Gorecki P. (2012). *Three-Dimensional Tornado Simulation over Complex Terrain*, High Performance Computing Center users' poster presentation, Fayetteville, AR, USA.

Gorecki P. (2012). *Three-Dimensional Simulation of Tornado-Hill Interaction*, Abstract-to-contract contest, Fayetteville, AR, USA.

1. INTRODUCTION AND DISSERTATION OBJECTIVES

1.1 Introduction

Every year tornadoes cause a loss of human life and significant damage to property. In 2011 alone in the United States of America the total cost of tornado damage was about 28 billion dollars. The total number of fatalities due to this atmospheric phenomenon was 551, which is the highest in the last 62-year period (NOAA, 2012). Tornadoes induce completely different set of wind forces than straight-line winds. Therefore, a properly designed structure for a straight-line wind might fail for a tornado-wind of the same speed (Selvam & Millett, 2003). Both numerical and laboratory studies led to the conclusion that the tornado-structure interaction and the tornado-induced forces depend on a number of factors, such as vortex angle of attack (Selvam & Millett, 2005; Sengupta, Haan, Sarkar, & Balaramudu, 2008), vortex translational speed (Sengupta, Haan, Sarkar, & Balaramudu, 2008), ratio of the vortex core radius to the building size (Haan, Balaramudu, & Sarkar, 2010; Selvam & Gorecki, 2012a; Alrasheedi & Selvam, 2011). In these tornado-structure interaction studies, a building was the main interest, whereas very little attention was paid on a traveling vortex path and strength. This was due to the fact that that the assumed tornado size was much larger than the building, and the building had minor influence on the vortex strength. Alrasheedi and Selvam (2011) showed that tornado-like wind forces are reduced when building size is comparable to the vortex core diameter. Selvam and Ahmed (2013) conducted post-damage investigations on the effect of hilly terrain on the tornado path and damage. They found from the detailed analysis of the Tuscaloosa, Alabama tornado (2011), that when the tornado went up the hill there was more damage than when the tornado went down the hill. They also documented a valley surrounded by hills, on the tornado path, with no visible damage. Thus, the tornado maximum wind speed varies, during the interaction with

large obstacles. These observations became the major motivation for this study. Based on the numerical simulations, this work discusses how large structures influence tornado-like vortex wind speeds and the tornado-like vortex path, close to the ground. It is also investigated whether the tornado sheltering effect exhibited by hills in nature can be obtained by wide made-man structures.

In this study a modified version of computational fluid dynamics (CFD) model, used by Selvam and Millett (2003), is applied. The particular case of a Rankine vortex impact on a prism, is proposed to be representative of flow aspects in a tornado interaction with large natural or man-made structures. The numerical investigations are begun with studies on grid spacing and computational domain size influence on a simulated Rankine vortex strength and shape. The next section analyzes a perpendicular interaction of a translating vortex with a wide rectangular prism. The vortex sheltering effect exhibited by the prism became the basis to study the tornado-like wind protection provided by a tornado-break wall. In the last section a variety of the wall and the tornado-like vortex dimensions are analyzed to reveal the performance of a tornado-break wall under different vortex impact circumstances.

1.2 Dissertation Objectives

The objectives for the current work are formed based on the study motivation and the current state of knowledge (literature review). The understanding of a tornado interaction with wide structures is developed based on vortex-prism interaction studies. CFD modeling was used to explain the influence of wide structures on the tornado near-ground velocities. The simulations of interactions between a travelling tornado-like vortex and a rectangular-shape prism revealed that the vortex strength and the path are substantially altered during the interaction. Based on these findings two major objectives of the dissertation are formulated:

Objective 1: Reveal the influence of wide structures on tornado-like vortex flow speeds close to the ground

Different visualization techniques are required to establish the understanding of tornado-like vortex interactions with wide structures. The shape of the structure is simplified to a wide rectangular-shape prism. The length (L) and height (H) of the prism are comparable to the tornado vortex core diameter. The width (W) of the prism is six times larger than the tornado-like vortex core (Figure 1.1). This assumption is made to understand how the near-ground portion of a translating tornado-vortex is affected when it passes wide structures. The tornado-like flow is modeled using the Rankine vortex. The task execution consists of the following steps:

- Resolve the grid spacing and the computational domain size influence on the parameters of the simulated Rankine vortex.
- Explain and visualize major features of an interaction between a Rankine vortex and a reference rectangular-shaped prism.

3

- Investigate the influence of the prism-to-vortex size ratio on the translating vortex path and the sheltering effect. For sheltering effect the wind speeds behind a prism are compared for different prism sizes. The sub-task includes varying the length and the height of the prism, with fixed prism width.
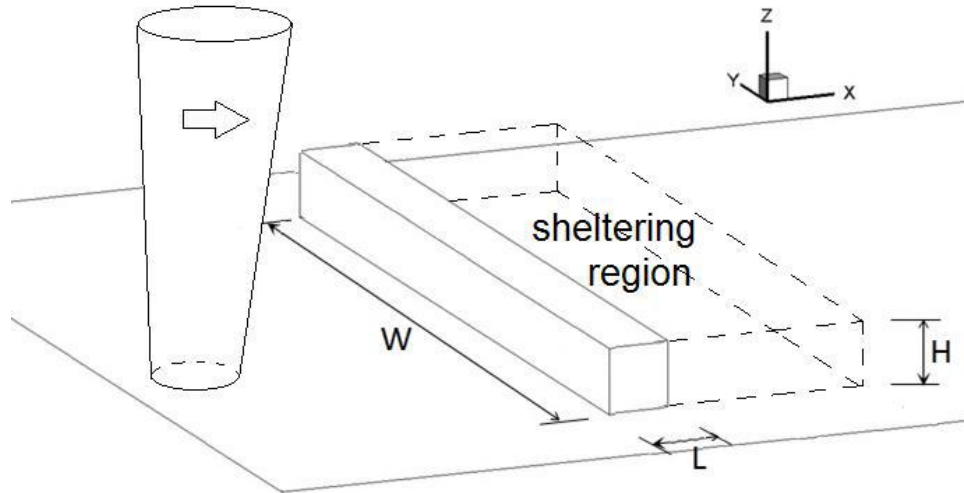
Figure 1.1 Overview of translating tornado interaction with the rectangular-shaped prism.

Objective 2: Determine the sheltering efficiency of a tornado-break wall under different vortex-wall impact circumstances

Through the analysis of the vortex-prism interaction it was revealed that a wide rectangular prism created a low-velocity region behind the leeward wall. Following this finding, the performance of a tornado-break wall is investigated (Figure 1.2). The wind speed reduction is measured in the sheltering region behind the wall. The flow velocity reduction is calculated as a relative difference between two simulations: without the wall in the computational domain and with the wall in the domain. The task execution consists of the following steps:

4

- Determine the influence of the length and the height of the wall on the tornado sheltering efficiency

- Determine the influence of the tornado angle of attack on the tornado sheltering efficiency

- Evaluate wind forces on a tornado-break wall under different vortex-wall interactions.
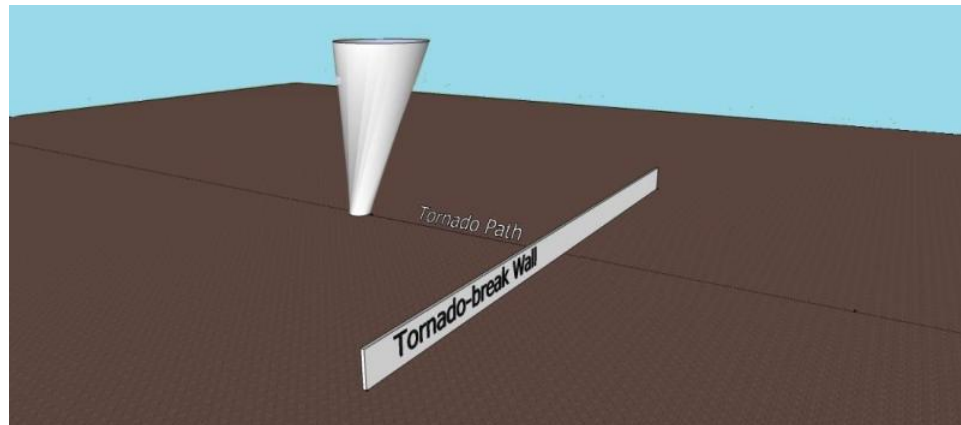
Figure 1.2 Overview of translating tornado interaction with tornado-break wall.

2. LITERATURE REVIEW

2.1 Objectives of Review

The main goal of this literature review is to conduct a comprehensive analysis of the current state of knowledge on the tornado-structure interaction. The major attention is paid on studies about tornado interaction with large natural or man-made structures. The review provides ideas for possible contribution in this area. Also, the literature survey is conducted to find similarities between the computational simulations, laboratory experiments and post-damage investigations of a tornado interaction with structures. The observations described in this section gives a confidence to the computational model work presented in this study.

The beginning of the literature survey briefly reviews basic information about tornadoes as an atmospheric phenomena. It includes a discussion on meteorological studies of wind velocity profiles of actual tornadoes. The actual profiles are compared to the Rankine vortex model, which is used in the current study for CFD simulations. Also, damage of tornadoes in hilly terrain is analyzed to find unique features of tornado interaction with large structures. Then, both advancements in laboratory and numerical modeling of the tornado-like vortex are presented. In the next section, the review of the vortex–structure interaction studies is presented. It includes the review on generic vortex-body interaction studies and blade-vortex interaction (BVI). In the last section the investigations on windbreak walls are reviewed in order to have a reference for tornado-break walls.

6

2.2 Tornado as Atmospheric Phenomenon

2.2.1 Basic information

Tornadoes are one of the most spectacular and devastating atmospheric phenomena. Huschke (1959) described them as violently rotating columns of air that take the shape of a funnel and spread between cumulonimbus clouds and the surface of the earth. The genesis of a tornado is not fully understood. Generally, it is considered that "warm moist Gulf air meets cold Canadian air and dry from the Rockies" (NOAA, 2012). This is, of course, a gross simplification of tornado genesis process. Most of the strong tornadoes are developed from supercells – thunderstorms with well-observed radar circulation (mesocyclone) (NOAA, 2012). It is believed that tornado genesis is mainly influenced by processes, which take place on the storm scale (Allaby, 1997)

- *Tornado structure*

Simple concepts of tornado vortex are illustrated in Figures 2.1 and 2.2.
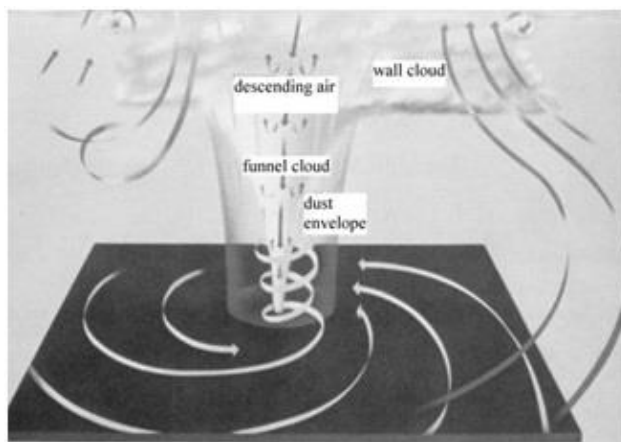
Figure 2.1 Structure of tornado vortex (Whipple, 1982).
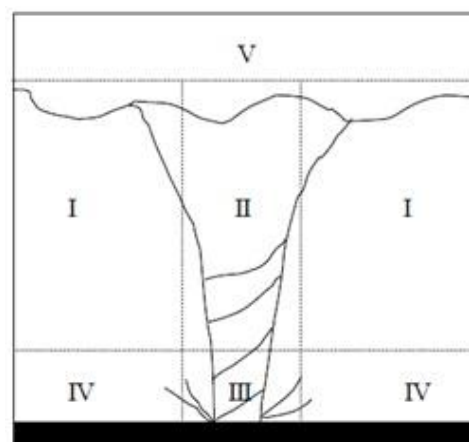
Figure 2.2 Tornado vortex with distinguished various flow regions (Wurman, Straka, & Rasmussen, Fine-scale Doppler radar observations of tornadoes, 1996).

7

Figure 2.1 describes the main features of the tornado vortex. A rotating funnel cloud is in contact with both the ground and the wall cloud. The rate of the circulation is decreasing away from the tornado vortex core. Inside the vortex a characteristic air suction is observed. The more precise tornado structure concept is provided by Wurman, Straka and Rassmussen (1996). They analyzed a real tornado using data retrieved from Doppler radar. As a result they distinguished five different flow regions (Figure 2.2). According to Wurman, Straka and Rassmussen (1996) Region I is a rising outer-flow region, where the tornado is embedded. Region II represents the core of the tornado. This region is associated with high wind velocities and a pressure drop. Region III can be described as a tip of Region II. There, the tornado flow is intensified and disturbed by frictional interaction with the surface. Around Region III there is the surface boundary layer region (Region IV). In Region V the angular momentum of the vortex is concentrated and transported downward.

- *Fujita Scale – tornado severity classification*

The wind speed of a tornado is the most important parameter to study. It is directly related with the intensity of tornado damage. Fujita (1971) introduced a scale for rating the tornado intensity. It provides maximum tornado wind velocity based on intensity of observed damage. At first, the Fujita Scale was enthusiastically adopted. However, after some time, it turned out that the velocities in Fujita Scale are greatly overestimated (Grazulis, 1993). In 2007 the United States accepted the Enhanced Fujita Scale, which provides a better correlation between the tornado damage and its maximum wind speed (NOAA, 2012). The comparison of the two scales is included in Table 2.1.

8

Table 2.1 Comparison of wind speeds between tornado EF-scale and F-scale (NOAA, 2012).

Fujita Scale (F)			Enhanced Fujita Scale (EF)		
Fujita Scale (F)	3-second Gust Speed		Enhanced Fujita Scale (EF)	3-second Gust Speed	
	[mph]	[km/h]		[mph]	[km/h]
F-0	45 – 78	73 – 127	EF-0	65 – 85	105 – 138
F-1	79 – 117	128 – 190	EF-1	86 – 109	139 – 177
F-2	118 – 161	191 – 261	EF-2	110 – 137	178 – 222
F-3	162 – 209	262 – 339	EF-3	138 – 167	223 – 271
F-4	210 – 261	340 – 424	EF-4	168 – 199	272 – 323
F-5	262 – 317	425 – 514	EF-5	200 – 234	324 – 380

- *Frequency of tornado occurrence*

The most common tornadoes are EF-0, EF-1 and EF-2. In 2011, 1704 tornadoes were reported in the United States (Table 2.2). From this number only 5% are EF-3, EF-4 and EF-5 tornadoes (NOAA, 2012).

Table 2.2 Reported tornadoes in the United States in 2011 (NOAA, 2012).

Total number of tornadoes	Tornado Intensity					
	EF0	EF1	EF2	EF3	EF4	EF5
1704	792	631	197	61	17	6

- *Tornado path and translational velocity*

The width and the length of a path of a tornado are commonly considered to be related with the magnitude of the damage intensity. This is true, but only to a certain extent. Brooks (2004) analyzed the relationship between a tornado path size and corresponding tornado intensity. He concluded that we cannot directly forecast tornado intensity based on its path size. In the United States tornado damage path, on average, has a width of 150 m and length about 8 km. However,

9

as was said earlier, tornadoes differ from one to another. There are both: tornadoes with a vortex diameter of a few meters and some with a diameter exceeding even 4 km (Allaby, 1997). The same applies to the tornado path length. The translational speed of a traveling tornado also varies. On average it is between 10 ms^{-1} and 70 ms^{-1} (Allaby, 1997). However, there are some reported tornadoes with translational velocities even equal to 3 ms^{-1}.

- *Direction of tornado travel*

The direction of a tornado travel is more stable than previously described parameters. In the United States tornadoes generally travel from the southwest to the northeast. In Figure 2.3 some deviations from this pattern are observed; however, the general rule is kept. The direction of tornadoes rotation is consistent – 90% of tornadoes rotate counterclockwise.
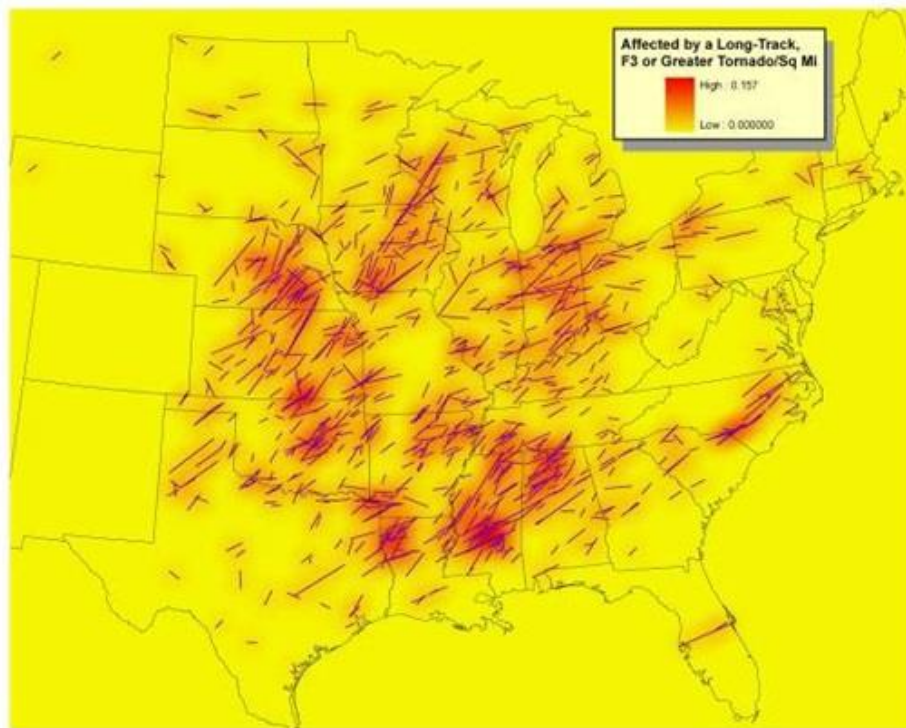
Figure 2.3 Path lengths and directions for tornadoes of intensity greater than F2.Tornadoes of years 1950 - 2004 (Passe-Smith, 2006).

- *Tornado Damage Characteristics*

Tornadoes cause a loss of human life and significant property damage. Most of the reported tornadoes occurred in the United States. Approximately, from 800 to 1400 tornadoes are reported each year in the U.S. (Ashley, 2007). Most of the tornadoes occurred in the so-called Tornado Alley, which is considered to be between the Rocky Mountains and the Appalachian Mountains. In Figure 2.3 the intensity of tornado occurrence in Tornado Alley is clearly observed. There are very few tornadoes in the western part of the U.S. In 2011, in the U.S., the total cost of tornado damage was about 28 billion dollars. The total number of fatalities due to this atmospheric phenomenon was 551, which is the most in a 62-year period (NOAA, 2012). The summary of casualties in a 5 year time span for different tornado intensities is provided in Figure 2.4. It is noticed that even very weak tornadoes can cause a loss in human lives. However, the most deadly tornadoes are F4 and F5. Even though F4 and F5 tornadoes are rare (Table 2.2) they result in the largest number of casualties. This shows of the importance to study strong tornadoes. Figure 2.5 illustrates a percentage of fatalities by locations where tornadoes occurred. It shows that the most fatalities occurred in the mobile home areas. Mobile homes have no foundations and are sensitive to lift up by a tornado.

11
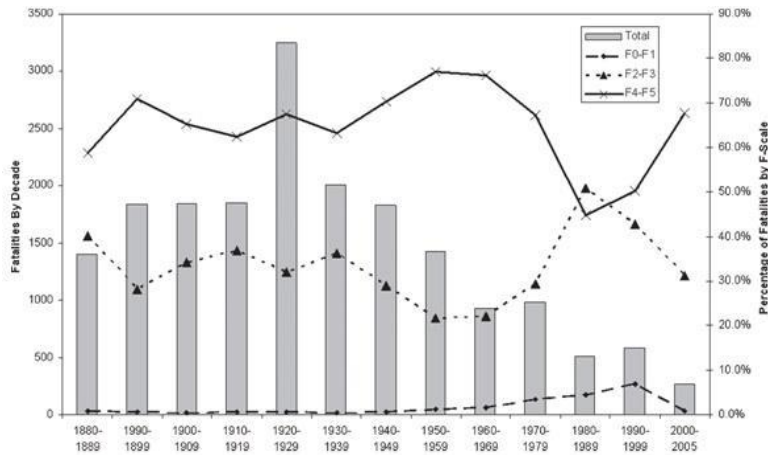
Figure 2.4 Number of fatalities for different tornado intensities. F0 - least intense tornado, F5- most intense (Ashley, 2007).
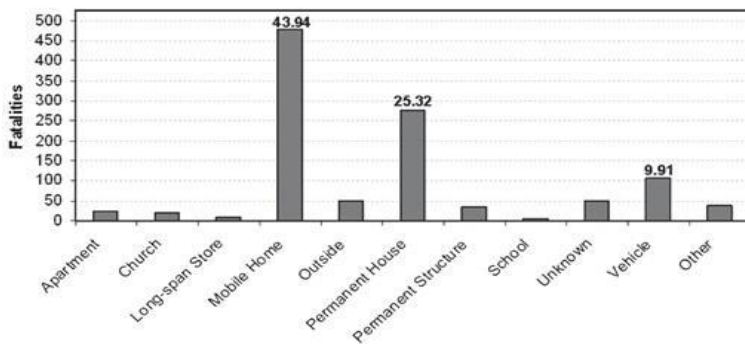
Figure 2.5 Tornado fatalities occurred in different locations (Ashley, 2007).

2.2.2 Tornado Wind Profile

The first measurements of tornado wind speeds were conducted by Wurman (2002). He applied a *Doppler on Wheels* mobile radar to study the tornado that occurred on 3 May 1999 in Oklahoma. The use of the mobile radar (Figure 2.6) enabled measuring size, strength, motion and structure of the tornado.

12

Figure 2.6 Doppler radar on Wheels (Wurman J. , 2002).
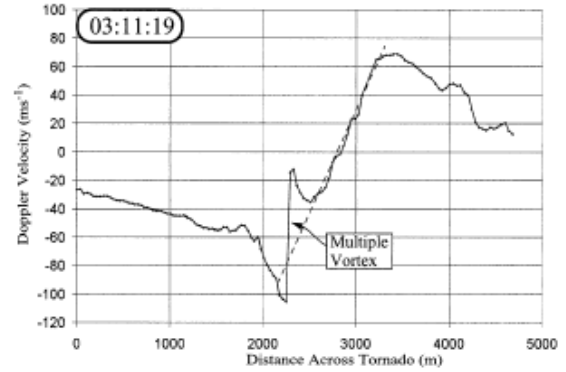
Figure 2.7 Doppler velocity across the tornado vortex (Wurman J. , 2002).

The tornado traveled in the north-northeasterly direction with the translational velocity ranging between 11–15 ms^{-1}. The wind profile of the large core flow region, retrieved from the Doppler radar measurements, is presented in Figure 2.7. The diameter of the core flow was about 1.2 km. The maximum wind speeds exceeded 100 ms^{-1} at the vortex core diameter. The estimated circulation values followed the $C = 2\pi VR$ equation (V-the maximum tangential velocity, R-the radius of the vortex core), which indicated the solid body rotation in the vortex core. Outside the solid body rotation, the velocities decayed with and the relation: $V \propto R^{-\alpha}$, where $\alpha= 0.5$ to 1.0. This profile corresponds with the analytical Rankine vortex (RV) model, where $\alpha=1$. Wurman and Alexander (2005) compared observed tornado damage with retrieved Doppler radar data. The studied tornado traveled at 15 ms^{-1} translational speed. The maximum wind speeds were exceeding 100 ms^{-1}. The tornado strength and core size were found to vary throughout the tornado path. The vortex wind profile measurements at two different stages of the tornado travel are presented in Figures 2.8 and 2.9.

13
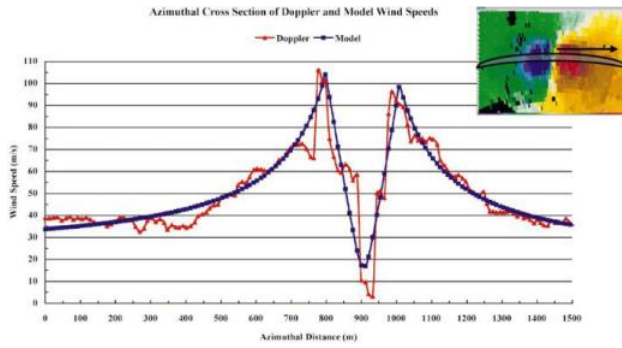
Figure 2.8 Tornado wind speed profile at initial stage of travel (Wurman & Alexander, 2005).
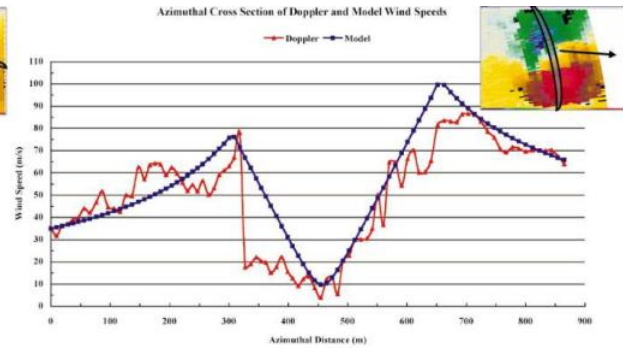
Figure 2.9 Tornado wind speed profile at later stage of travel (Wurman & Alexander, 2005).

By comparing the tornado damage and the actual wind speeds (Wurman & Alexander, 2005) found that the Fujita Scale (F-Scale) overestimates the tornado wind speed. Kosiba, Trappa and Wurman (2008) studied axisymmetric low-level wind field in Harper, KS (12 May 2004) tornado. The observed that the tangential velocity of the vortex is increasing with the height. They proposed logarithmic profile of the velocity-altitude relation. Kosiba, Trappa and Wurman (2008) also showed that the horizontal profile of tornado tangential velocity was changing at different stages of the tornado travel. Kosiba and Wurman (2010) studied axisymmetric wind field profiles of Spencer, SD, 1998 tornado. Figure 2.10 shows tornado tangential velocity at different instants.

14
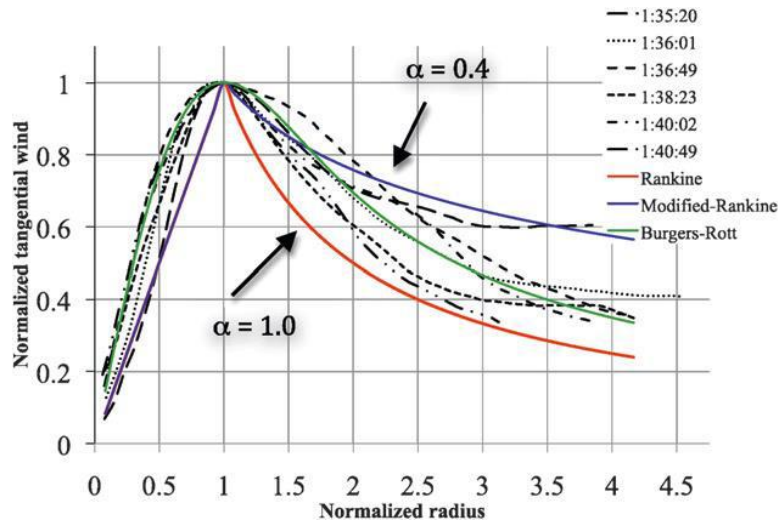
Figure 2.10 Tornado tangential velocity profiles ant different stages of travel (Kosiba & Wurman, 2010).

The velocities of the tornado were compared to different vortex analytical models. It was shown that especially in the free vortex region (outside the vortex core) the wind speeds are inconsistent. The best match of tangential velocity profile was observed for Burgers-Rott vortex (BRV). The Rankine vortex (RV) exhibited constantly lower velocities in the free vortex region. A decay coefficient of 0.45–0.65 was observed to be typical. Kosiba and Wurman (2010) also plotted the axisymmetric tangential winds in relation with height. They observed that the largest tangential velocity occurred at 40 meters above ground level. This was assumed to be the top of the boundary layer. Wurman, Kosiba and Robinson (2013) studied structure of Goshen County, Wyoming (5 June 2009) tornado. They were able to measure tornado velocity profile very near the ground and near the center of rotation. Measured tangential wind speeds between 3.5m and 30m above ground level were observed to be similar. Wurman et al. (2013) compared their data with actual damage caused by the tornado. They presented some limitations the Enhanced Fujita (EF) Scale for predicting the tornado maximum velocities. Kosiba, Robinson, Chan and Wurman (2014) investigated wind profile of the tornado, which crossed Hong Kong International Airport in 2004 (Figure 2.11). Similarly to the previously mentioned tornadoes, the Hong Kong tornado

15

was also changing its strength and size during the translating motion. The radius of the vortex core ranged from 30 m to 140 m. In contrast to the previous wind profiles, the free vortex region exhibited similar decay to Rankine vortex (Figure 2.12). The wind directions obtained from anemometer observations showed purely tangential flow of the tornado. The maximum tangential wind speeds were equal to 22 ms^{-1}.

Figure 2.11 Photographic image of Hong Kong Airport tornado (Kosiba, Robinson, Chan, & Wurman, 2014).
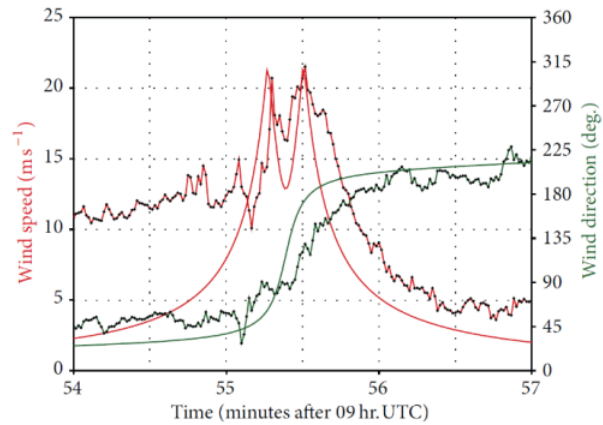
Figure 2.12 Rankine vortex distribution of Hong Kong Airport tornado (Kosiba, Robinson, Chan, & Wurman, 2014).

The summary of the Doppler radar measured tornadoes is given in Table 2.3.

Table 2.3 Characteristics of Doppler radar measured tornadoes.

Tornado	Date	Max. tangential velocity	Trans. velocity	Core radius	u_{trans}/r_{max}
Mulhall, OK	5/4/1999	100 ms^{-1}	13 ms^{-1}	700 m	0.019
Bridgecreek–Moore, OK	5/3/1999	126 ms^{-1}	9 ms^{-1}	175 m	0.051
Spencer, SD	5/30/1998	101 ms^{-1}	15 ms^{-1}	150 m	0.100
Hong Kong	9/6/2004	22 ms^{-1}	5 ms^{-1}	30 m	0.167

2.2.3 Post-damage Investigations of Tornadoes in Complex Terrain

▪ *Tornado's touchdown*

A few studies have been conducted showing that tornado genesis can be altered by specific topographic characteristics. It was presented that terrain can channel the flow creating favorable conditions to generate a tornado-vortex (Nuss, 1986; Hannesen, Dotzek, Gysi, & Beheng, 1998; Homar, Gaya, Romero, Ramis, & Alonso, 2003; Bosart, Seimon, LaPenta, & Dickinson, 2006). This does not mean that tornadoes occur more often in mountains, since the most of the reported tornadoes are generated in relatively flat terrain.

▪ *Tornado's path direction*

When a tornado occurs in a complex terrain it has to overcome frequent changes in the altitude. The influence of different terrain features was a subject of few studies. The most convenient way of investigating tornado path deviations due to the terrain is to apply post-damage observations. Observations are the most reliable for tornadoes traveling along forests, because the damage swath is accurately reflected by fallen trees (Bech, et al., 2009). Fujita (1989) analyzed the Tenton-Yellowstone tornado damage - F4 intensity. The tornado travelled 39.2 km with an average path width of 2.5 km (Figure 2.13). The translational velocity was about 25 m/s. The tornado's path was relatively straight, which indicates that there was no influence of the terrain on the tornado direction. Harrington and Newark (1986) investigated damage swaths of two tornadoes. First tornado had the F3 intensity with a damage length of 60 km and an average width of 135 m. In this case the tornado travel was independent of the terrain – straight. The second tornado analyzed by Harrington and Newark (1986) had F1 intensity. The damage length and the average width were respectively 11 km and 95 m. Here, the tornado exhibited a tendency

to avoid sudden changes in the terrain altitude. It chose the most convenient way and passed through lower ground rather than a high terrain. This may suggest that weaker tornadoes can locally change their direction; stronger tornadoes seem to keep their direction straight even in rough terrain. However, this conclusion has never been clearly stated in the literature and it needs to be investigated using more tornado travel data.
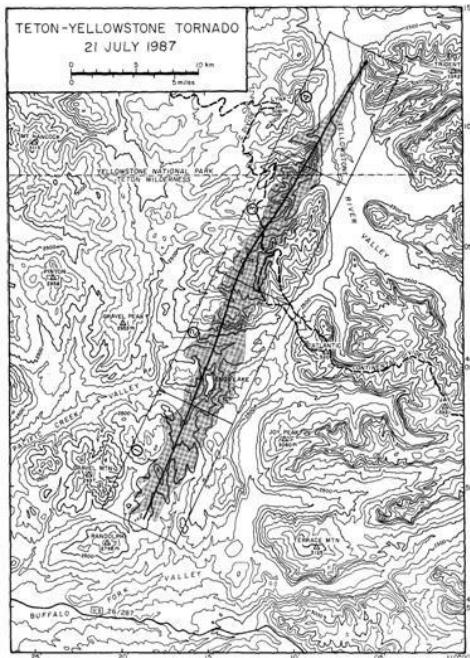
Figure 2.13 Tenton-Yellowstone tornado damage (Fujita, 1989).
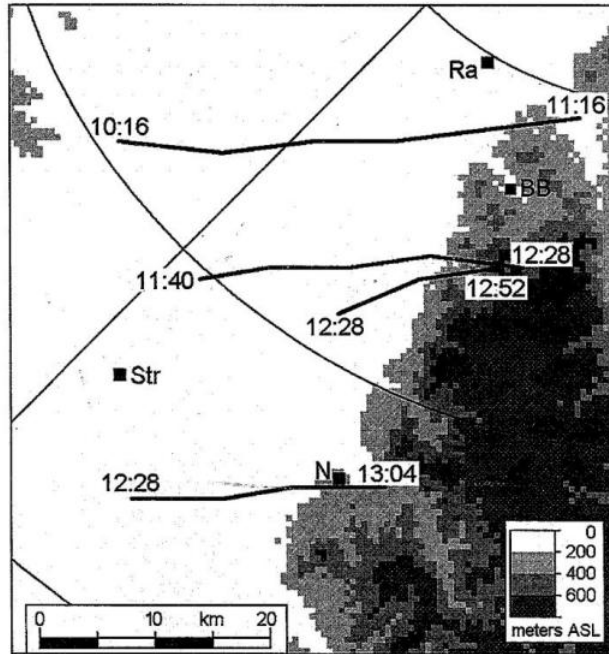
Figure 2.14 Paths of tornadoes disrupted in hilly terrain (Hannesen, Dotzek, Gysi, & Beheng, 1998).

Recently, the terrain topography influence is being studied using numerical simulations and laboratory experiments. Karstens (2012) utilized the laboratory tornado simulator to study the tornado-like vortex travel over 2D Gaussian hills. He noticed sinusoidal shape of the vortex path during the interaction with the hill (Figure 2.15). The ratio of the translational vortex velocity to the maximum rotational velocity was about 0.011, so less than all the tornadoes reported from Doppler radar studies. Ahmed and Selvam (2015) noticed that the shape of a tornado path

changes for different ratio of the translational vortex velocity to the maximum rotational velocity.
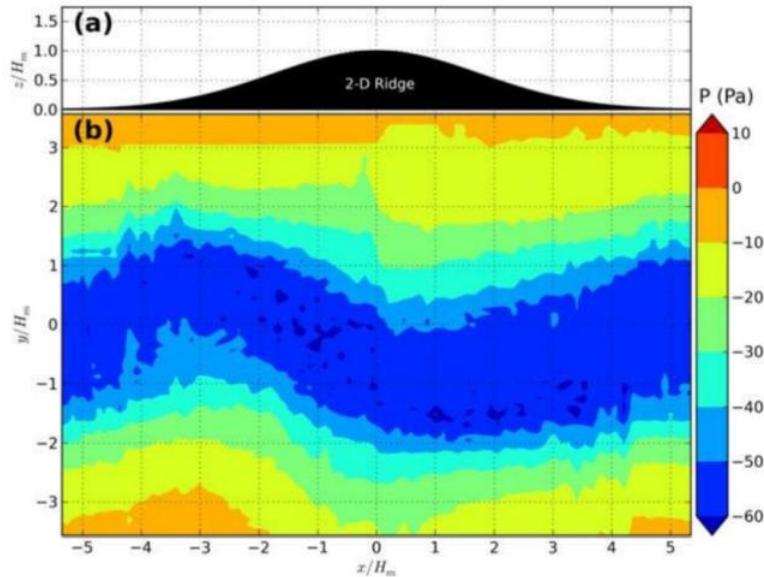
Figure 2.15 Pressure surface indicating laboratory simulated tornado path (Karstens, 2012).

Lewellen (2012) from his computer model presented very similar findings as Karstens (2012). He studied various combinations of vortex-terrain interactions and confirmed the dependence between the vortex path and terrain topography. Selvam and Ahmed (2013) utilized the Google Earth database to analyze damage of Tuscaloosa, AL (2011) and Joplin, MO (2011) tornadoes. The pictures were taken a day after the tornadoes occurred. They observed that a tornado locally changes its travelling direction to travel on a hill ridge.

- *Tornado's lift up*

Complex topography can also be responsible for tornado mitigation and dissipation. Hilly terrain causes shrinking and stretching of the vortex, which can lead to disruption of a tornado. Hannesen et al. (1998) provided a few examples of tornadoes that were created on flat terrain

19

and decayed immediately after hitting hilly terrain. Hannesen, Dotzek and Handwerker (2000) concluded that in these events a low-level tornado wind field was disrupted by the first hills, which caused the tornado dissipation. The other factor that can contribute to the tornado mitigation is the surface roughness. Elsom and Meaden (1982) found that urban areas cause damping of tornadoes vortex strength. These results have laboratory confirmation by Dessens (1972).

- *Topographic Influence on Magnitude of Tornado Damage*

Harrington and Newark (1986) conducted the first study to find a connection between topography and the size of damage swath. They found that tornadoes reach their greatest intensity in valleys and weaken when they pass hills or ridges (Figure 2.16).
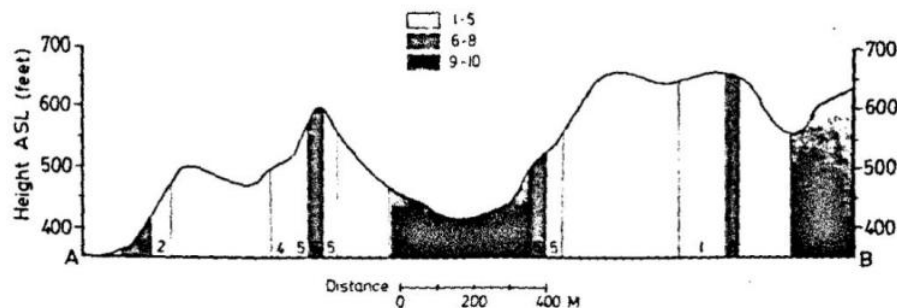
Figure 2.16 Tornado damage in hilly terrain (1 – no damage, 10 – severe damage). Tornado travels from point A to B (Harrington & Newark, 1986).

Harrington and Newark (1986) proposed the explanation of this phenomenon. According to them, this is caused by the conservative nature of the potential vorticity (the ratio of the absolute vorticity and the depth of the vortex). When a tornado goes downslope it stretches the vortex causing an increase in circulation, which means an increase in wind velocity. The opposite effect is observed when a tornado is climbing up the hill. Harrington and Newark (1986) did not notice

20

that behind the steep hill there is no damage. This is observed in Figure 2.16. The tornado left a large area without destruction and then intensified in the valley. Fujita (1989) drew the same conclusion as Harrington and Newark (1986). As is observed in Figure 2.17, the greatest damage intensity is on the lower ground level; at the high located plateau "tornado worked hard in maintaining its circulation, suggesting the importance of the balance in the supply and loss of angular momentum" (Fujita, 1989).
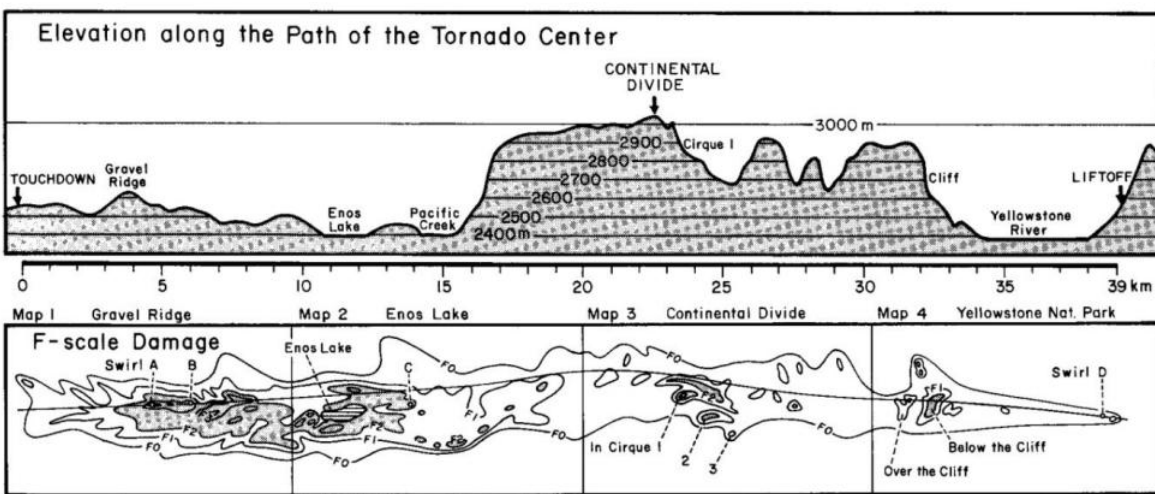
Figure 2.17 Tornado damage in hilly terrain. Tornado travels from left to right (Fujita, 1989).

Selvam and Ahmed (2013) investigated the effect of terrain on a tornado's path and damage. They noticed that when the tornado goes up the hill slope there is more damage than when a tornado goes down the hill slope (Figures 2.18 and 2.19).

21

Figure 2.18 Tornado damage, while traveling up the hill (Selvam & Ahmed, 2013).
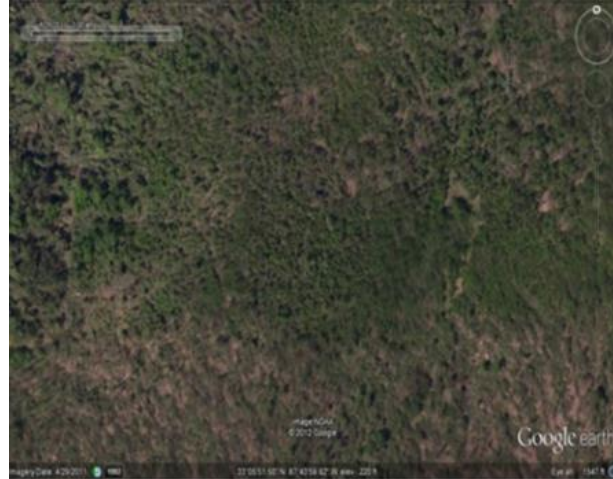
Figure 2.19 No tornado damage, while traveling down the hill (Selvam & Ahmed, 2013).

Selvam and Ahmed (2013) also showed that when a region is surrounded by hills, the damage inside this region is insignificant. Karstens (2012) used the tornado laboratory simulator and noticed the same Selvam and Ahmed (2013) about the damage up and down the hill slope. Another example of the theory of much damage at low located terrain and less damage at high located terrain was provided by Bech et al. (2009). However, they did not give any explanation for such phenomenon.

2.3   Vortex-Structure Interaction

2.3.1   Tornado-Wind Forces on Structures

- *Early attempts to calculate tornado-wind forces*

The tornado wind forces acting on a building were first calculated by Wen (1975). He first recognized the effect of both inertial forces and drag forces. He used semi-empirical equations based on the principles of the fluid dynamics. The tornado forces acting at the center of a building were calculated assuming that tornado wind is similar to the straight-line wind. The

22

major disadvantages of Wen's (1975) approach were calculating the inertial forces and the drag forces separately and not taking into account the tornado structure-interaction. The validity of Wen's procedure was questioned by McDonald and Selvam (1985) using computer simulation. They suggested modifications to the application of the inertia forces from Wen's procedure. However, McDonald and Selvam (1985) and Selvam (1985) assumed the inviscid wind flow in the CFD numerical model. This limits the value of the results, since the wind is viscous and turbulent. Dutta, Ghosh and Agarwal (2002) calculated tornado forces on multi-story building taking actual tornado wind velocity record. To calculate the forces on the building they assumed pressure coefficient form the design codes. This is a gross simplification and for sure does not match the actual tornado forces.

■ *2D viscous CFD model for tornado-structure interaction*

Selvam, Roy, Jung and Mehta (2002) conducted a two-dimensional simulation of the interaction between a traveling Rankine vortex and a circular cylinder. They found that the tornado forces are about 5 times less than those calculated by Wen (1975). Selvam et al. (2002) applied the direct simulation turbulence model in their CFD simulation. The validation of the model was accepted on the basis of drag and lift force coefficients when the tornado was far away from the circular cylinder. At this time only the straight-line wind was acting and the force coefficients were similar to those found in the literature. Recently, Selvam and Gorecki (2012a)studied an influence of the different ratios of tornado size to circular cylinder size on the tornado forces. They found that the tornado forces depend on the size of the building. When the building size is decreasing, comparing to the tornado size, the forces are increasing. The study was conducted up to the ratio of 8:1.

23

- *3D viscous CFD model for tornado-structure interaction*

Selvam and Millet (2002) conducted a first three-dimensional study of the tornado-structure interaction. The turbulence was applied using large eddy simulation (LES). The use of the 3D tornado simulation enabled Selvam and Millet (2002) to fully describe tornado wind forces on buildings. They found that when a vortex is completely surrounding a cubic building it causes strong updraft on the building's roof, as illustrated in Figure 2.20.
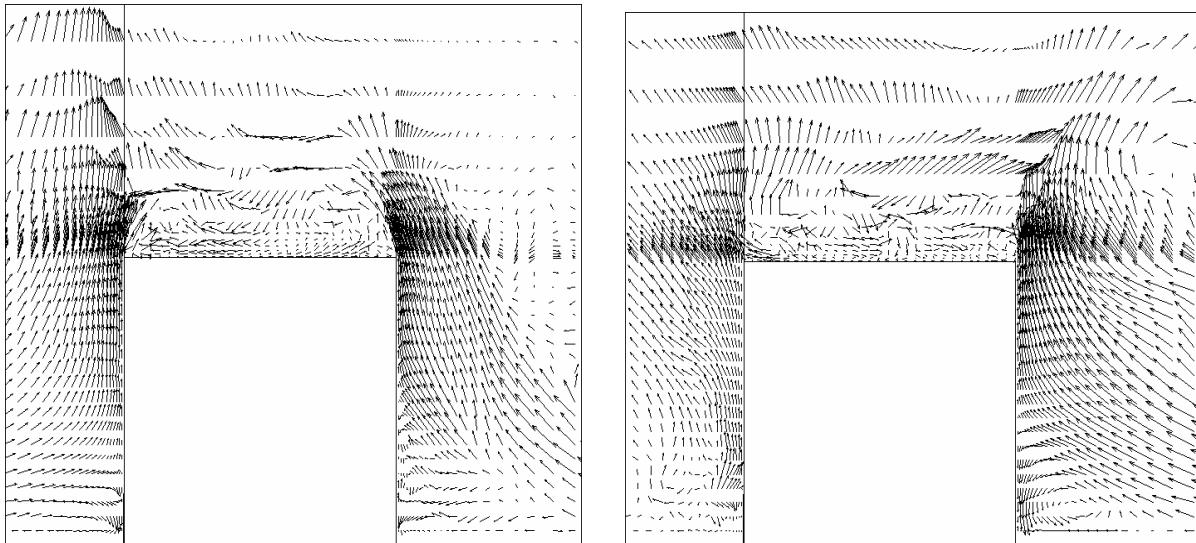
Figure 2.20 Views of vertical velocity with tornado surrounding building, left: *xz*-plane, right: *yz*-plane (Selvam & Millett, 2005).

The simulated tornado forces were compared with the simulated straight-line wind forces. They noticed that the vertical tornado force coefficients are twice as much as straight-line wind force coefficients. The horizontal tornado force coefficients were little less than straight-line wind force coefficients. This comparison was possible, since they assumed that the maximum horizontal velocity of the tornado is the reference velocity in the force coefficients calculations. Selvam and Millet (2002) also provided pressure distribution on the cubic building walls due to the tornado wind. The highest pressure was observed on the edges of flat roof. Selvam and Millet

(2003) conduced similar study as Selvam and Millet (2002), including more visualization of tornado-structure interaction. They suggested that the effect of tornado cannot be simulated using wind tunnels, because the wind direction changes very rapidly. Selvam and Millet (2005) studied the tornado forces and the straight-line wind forces on a cubic building for two different angles of attack. Selvam and Millet (2005) noticed that tornado horizontal and vertical force coefficients are respectively 45% and 100% greater than straight boundary layer force coefficients.

Sengupta et al. (2008) conducted both CFD simulations and laboratory experiments of different tornadoes interacting with a cubic building. Their tornado horizontal force coefficients were in good comparison with those obtained by Selvam and Millet (2005). The tornado vertical forces were found to be even greater than in (Selvam & Millett, 2005), which could be related with the use of different tornado updraft model. Sengupta et al. (2008) also noticed that the slower tornadoes produce greater forces on a building than the faster one. They compared their results with wind load standards (ASCE 7-05) and noticed that force coefficients provided in wind load provisions are more than 1.5 times less than tornado force coefficients resulted from their work.

Alrasheedi (2012) conducted computer studies of the tornado impact on buildings of different planar size. They reported that for buildings that are wider than the tornado vortex, the tornado force coefficients are similar to the straight-line wind force coefficients. This may suggest that the tornado wind impact significantly changes when interacting with larger rigid objects. Selvam and Ragan (2012) introduced the idea of the tornado interaction with a large rectangular shaped hill. Selvam and Gorecki (2012b) provided more insight in the interaction between tornado and a longitudinal rectangular-shaped prism by using different visualization techniques (Figure 2.21). They found that the hill creates a sheltering region on the leeward side. Selvam and Gorecki (2012b) also indicated in their tornado-hill simulation that the height of the computational

25

domain significantly influences the results. They concluded that the height of the domain should be at least 15 times greater than the height of the structure.
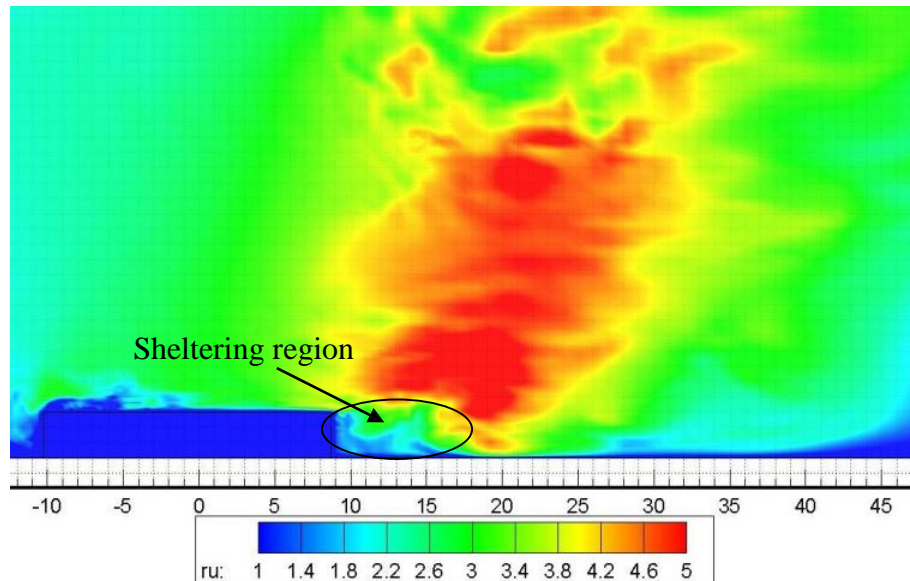
Figure 2.21 Close-up view of a creation of the low-velocity region behind the hill (Selvam & Gorecki, 2012b).

- *Laboratory Experiments*

Laboratory experiments concerning tornado forces on a structure are mostly conducted by placing a small cubic building in the vicinity of a stationary tornado vortex. Jischke and Light (1979) made the first attempt to study the tornado-structure interaction using a laboratory experiment. They mounted a cylindrical structure in a neighborhood of a tornado vortex. They found that by adding the tornado swirl to the flow caused significant changes in the wind forces on the structure. Jischke and Light (1983) measured tornado forces on a rectangular structure. They showed that the location and the orientation of a building relative to a tornado vortex alter the forces on the structure. Bienkiewicz and Dudhia (1993) simulated a stationary vortex interacting with a cubic building. They reported pressure coefficients on the walls and roof of the building. Sarkar, Haan, Balaramudu and Sengupta (2006) and Mishra et al. (2008) provided

26

force coefficients on a cubic structure for various positions of the model with respect to the

tornado center. The greatest vortex-induced vertical force was found when the vortex center

coincided with the center of the building. The greatest horizontal force was induced when the

building was located on the forced vortex radius of the tornado. It was demonstrated that the

tornado forces on a building change rapidly for different building locations. However, the results

from these studies are limited since a tornado is not a stationary phenomenon. It has translational

speed that influences the characteristics of the interaction. The first tornado simulator with

translation abilities (ISU simulator) was introduced by Haan, Sarkar, and Gallus (2008). The

simulator is illustrated in Figure 2.23. Using this simulator a few studies of tornado flow around

structures have been conducted. Sengupta et al. (2008) measured peak force coefficients on a

cubic building and found that they are more than 1.5 times greater than those suggested by

design standards. Haan et al. (2010) applied ISU simulator to calculate tornado-induced wind

loads on a low-rise building. They compared the measured force coefficients with ASCE 7-05

standard. The measured loads were 50% larger than the suggested by design code. The vertical

forces were more than twice greater than those from ASCE 7-05. Haan et al. (2010) also studied

the effect of tornado translational velocity on the induced wind forces. They noticed that the

interaction looks different for faster and slower tornadoes (Figure 2.22). This results in different

load magnitude and profile. The magnitude of load decreases for faster tornadoes.
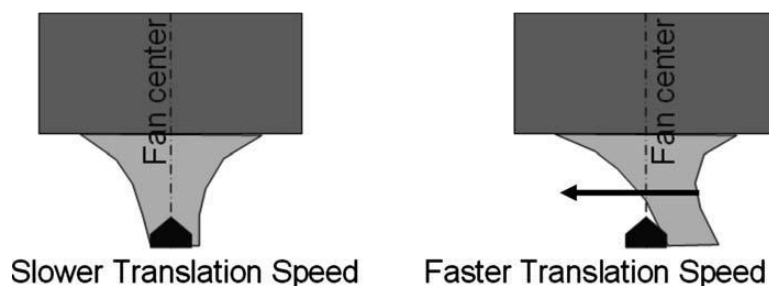
Figure 2.22 Tornado-building interaction for different translational speeds (Haan, Balaramudu, & Sarkar, 2010)

27

Hu et al. (2011) presented flow around a gable-roofed building and calculated tornado force coefficients. The forces were reported for different building orientation angles and distances from the tornado vortex. They compared the tornado forces with the straight line wind and found that the tornado produces at least 3 times greater forces on the roof than the straight line wind. Yang, Sarkar and Hu (2011) applied the ISU simulator to compare wind fields around a high-rise building caused by the tornado and the straight boundary layer. Kumar, Dayal and Sarkar (2012) took tornado pressures induced on a gable-roof building and applied them for the finite element analysis of the structure. They reported the most sensitive parts of the building.
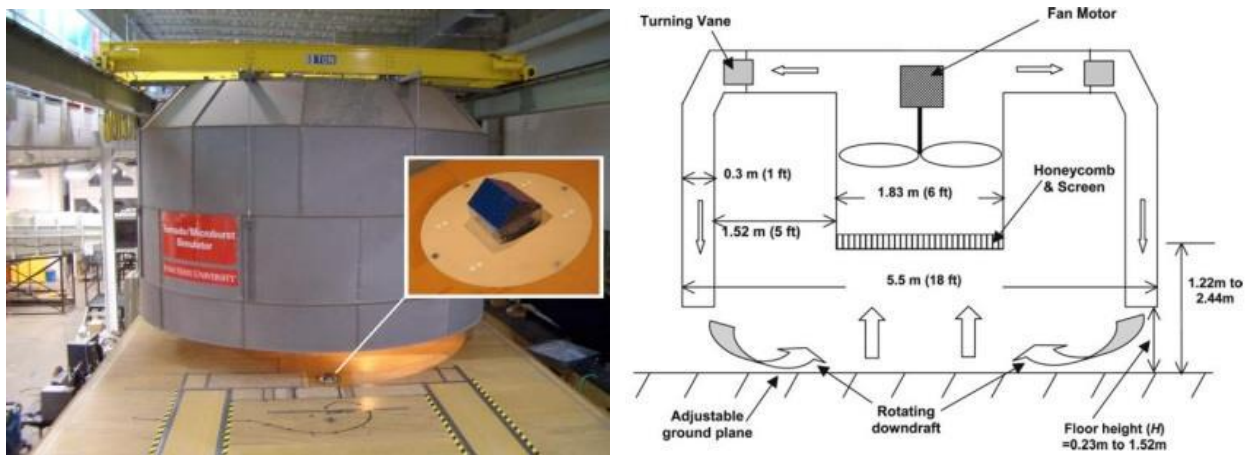
Figure 2.23 ISU tornado simulator (Haan, Sarkar, & Gallus, 2008).

- *Tornado forces on lattice structures*

In the literature there are also studies analyzing tornado forces on lattice structures such as transmission towers (Savory, Parke, Zeinoddini, Toy, & Disney, 2001; Hamada, Damatty, Hangan, & Shehata, 2010). In this case the authors assumed no tornado-structure interaction and

www.manaraa.com

assumed straight line wind force coefficients. However, this is true only to a very limited extend and there is no verification provided for such approach.

2.3.2 Blade-Vortex Interaction

The blade-vortex interaction (BVI) literature review is conducted to reveal the processes governing BVI and find analogies to the vortex-prism interaction. Generally, BVI occurs when an air vortex impacts a helicopter rotor blade. BVI are categorized into orthogonal, parallel and oblique, in terms of the direction of the vortex impact on a blade. The vortex interaction generates blade vibrations and radiated noise. This review is focused on the orthogonal type of interaction (Figure 2.24), which is the most relevant to the analyzed in the current work vortex-prism interaction.
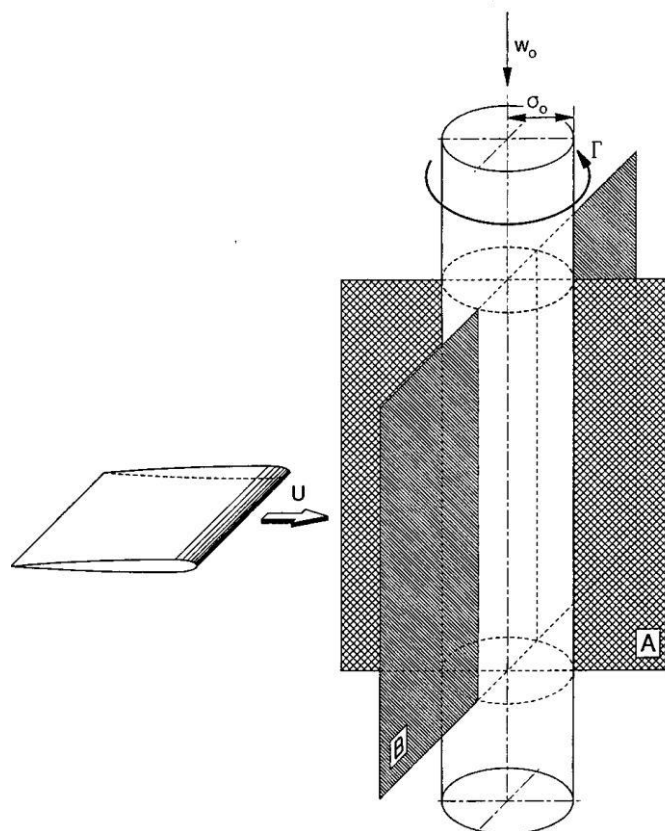
Figure 2.24 Problem geometry for orthogonal blade-vortex interaction (Krishnamoorthy & Marshall, Three-dimensional blade–vortex interaction in the strong vortex regime, 1998).

Both experimental and numerical studies have been conducted on the orthogonal blade-vortex interaction (OBVI). In general, it was revealed that the pressure distribution on blade surfaces varies substantially depending on the relative location of the vortex core to the blade leading edge. The response pressure was also noticed to be different on the top and the side surfaces of the blade. During OBVI the traveling vortex behavior is highly influenced by the blade thickness. For blades much thicker than the vortex core: the path, strength and the structure of the swirl are altered during the interaction. When the blade thickness is much smaller than the vortex core, the deformation of the travelling vortex is insignificant (Krishnamoorthy & Marshall, Three-dimensional blade–vortex interaction in the strong vortex regime, 1998).

- *Basic features of OBVI*

During OBVI the leading edge of the blade is subjected to the impulsive and convective force. When the travelling vortex is initially cut by the blade leading edge, the axial velocity of the vortex is stopped impulsively. The blade creates a physical barrier for the vortex axial flow. In Figure 2.25 the axial flow is pointing towards the upper surface of the rotor blade. The instantaneous cut of the vortex causes impulsive compression and thickening of the vortex on the upper surface. On the lower surface there is an impulsive suction with thinning of the vortex (Coton, Marshall, Galbraith, & Green, 2004). The thickening of the vortex reduces the swirl strength, while the vortex thinning intensifies the suction. Figure 2.26 shows the pressure distribution on the blade upper surface.

30
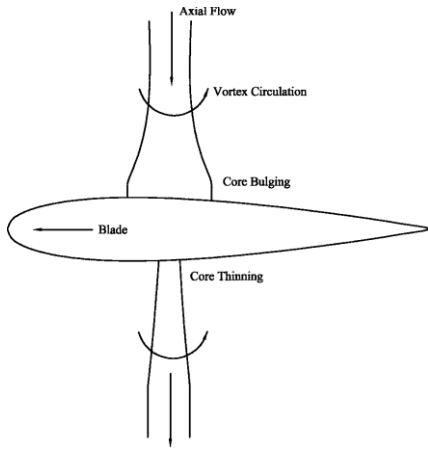
Figure 2.25 Vortex thickening and thinning during orthogonal BVI (Coton, Marshall, Galbraith, & Green, 2004).
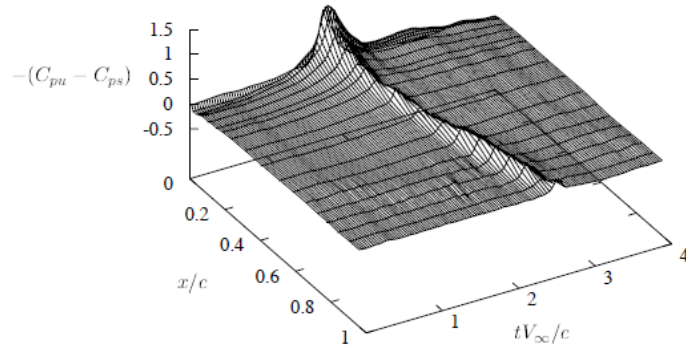
Figure 2.26 Pressure coefficient across the blade chord during BVI (Coton, Marshall, Galbraith, & Green, 2004).

- *Parameters governing orthogonal blade-vortex interaction*

According to Coton et al. (2004) there are three dimensionless parameters governing the OBVI:

- Impact Parameter ($I = 2\pi aU / \Gamma$)

- Blade thickness parameter ($T = D / a$)

- Axial flow parameter ($A = 2\pi aw_o / \Gamma$)

Where: a – vortex core radius, U – vortex translation velocity, w_0 – maximum vortex axial velocity, Γ – vortex circulation, D – blade thickness,

- *Impact parameter*

Krishnamoorthy, Gossler and Marshall (1999) conducted experimental studies by varying the impact parameter ($I = 0.02 – 0.4$). The experiments revealed that there are two types of the OBVI depending on the impact parameter. If the impact parameter is low (strong-vortex regime – high circulation) the vorticity from the blade boundary layer is ejected and pulled towards the vortex by the rotational velocity. This effect occurs before the vortex core impacts the blade leading

edge. The vortex-induced velocity is much higher than the free stream flow causing reversed flow in the vicinity of the blade leading edge (Figures 2.27 and 2.28). The fluid velocity is orientated away from the blade and pulls the boundary-layer ejected vorticity towards the vortex. The ejected vorticity is eventually wrapped around the vortex core. This causes thinning of the vortex core and disruption of the vortex structure even before the impact event. Marshall (2002) demonstrated that the critical distance between the blade and the columnar vortex when the vorticity ejection occurs (S_{crit}) is governed by a simple formula ($S_{crit}U/\Gamma$=0.055).
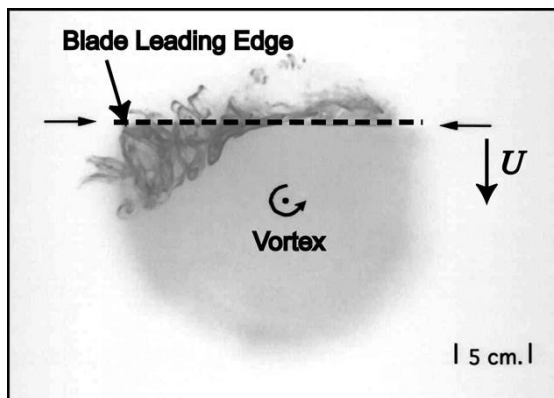
Figure 2.27 Vorticity ejection from blade (Krishnamoorthy & Marshall, 1998).
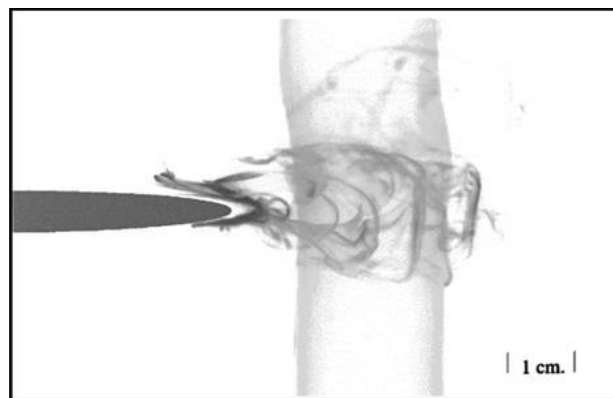
Figure 2.28 BVI in strong vortex regime (Krishnamoorthy & Marshall, 1998).

If the impact factor is high (weak-vortex regime – low circulation) the vortex induced velocity is not sufficient to eject the boundary layer vorticity. The boundary layer vorticity has different sign than the swirl vorticity. This causes cross diffusion between the boundary-layer vorticity and the primary swirl vorticity, which enhances the cutting process (Figures 2.29 and 2.30).

32
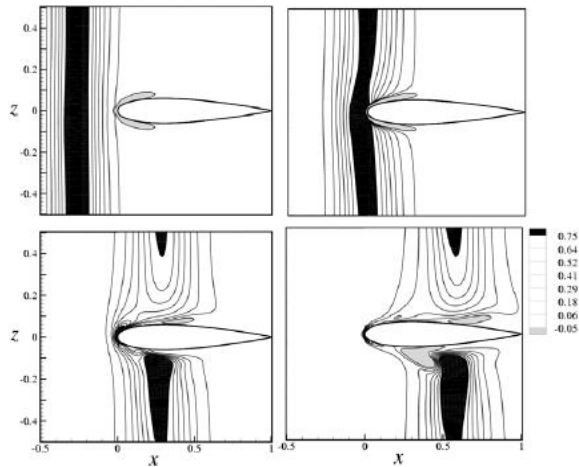
Figure 2.29 BVI in weak vortex regime (Liu & Marshall, 2004).
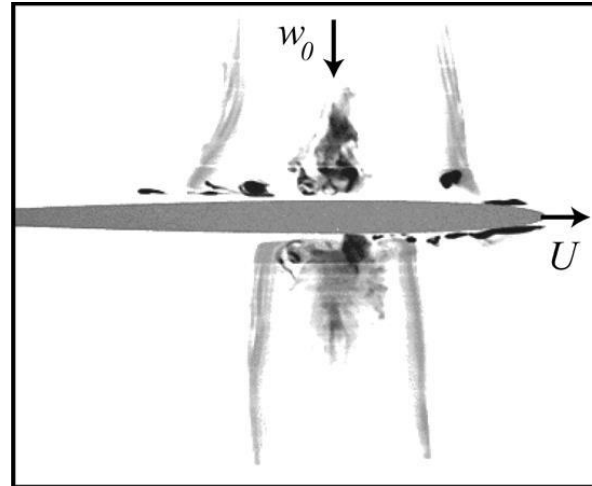
Figure 2.30 Instantaneous cutting of a columnar vortex (Marshall & Krishnamoorthy, 1997)

Here, the characteristic feature of the vortex thinning and thickening is observed. The vortex core diameter is different on both sides of the blade.

- *Blade thickness parameter*

The blade thickness parameter influences the behavior of the travelling columnar vortex before the impact. When the thickness of the blade is larger than the vortex core size, the columnar vortex is subjected to substantial displacement before the interaction. The vortex streamwise bending during orthogonal cylinder-vortex interaction in presented in Figure 2.31.
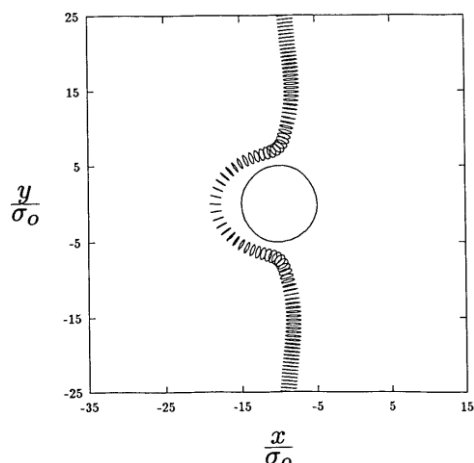
Figure 2.31 Vortex streamwise bending during BVI (Marshall & Yalamanchili, 1994).
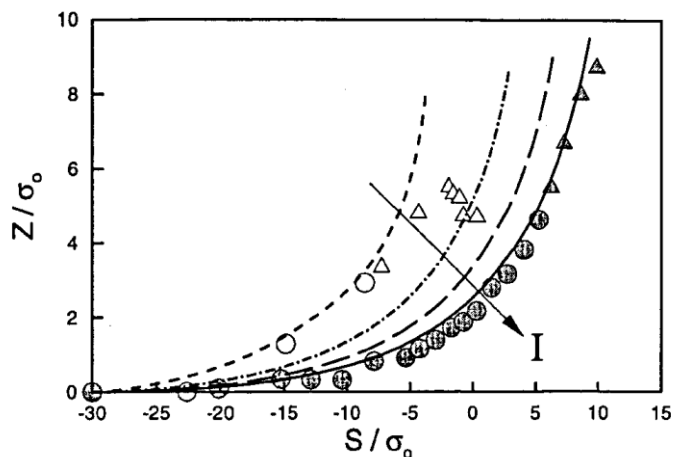
Figure 2.32 Vortex spanwise displacement as a function of impact parameter (Krishnamoorthy, Gossler, & Marshall, 1999).

The bending increases with the increase of the thickness of the structure. In the stretched section of the core, the vortex diameter is thinner than in the upper portions of the vortex. Another characteristic aspect of the vortex-cylinder interaction is the lateral displacement of the vortex, in front of the cylinder. Affes and Conlisk (1993) explained this effect based on an invicid theory, which was later confirmed by laboratory experiments (Krishnamoorthy, Gossler, & Marshall, 1999). The path of the vortex is dependent on the circulation direction of the vortex and on the impact parameter (Figure 2.32). When the blade or cylinder is relatively thin to the vortex the streamwise and the lateral displacement of the vortex is not observed.

   ▪ *Axial flow parameter*

The axial flow parameter is used to distinct the vortex flow structure. For axial flow parameter larger than 0.71 the vortex is *supercritical*. It is characterized by narrow core and intense suction. For axial flow parameter lower than 0.71 the vortex is *subcritical* and the vortex circulation dominates the rotational flow. Krishnamoorthy and Marshall extensively studied OBVI for *subcritical* regime. The subcritical vortex exhibits a development on the vortex breakdown

34

during blade cutting. The bubble-type type breakdown is followed by a double-helix breakdown (Figure 2.33). The flow field of the *subcritical* vortex is presented in Figure 2.34.
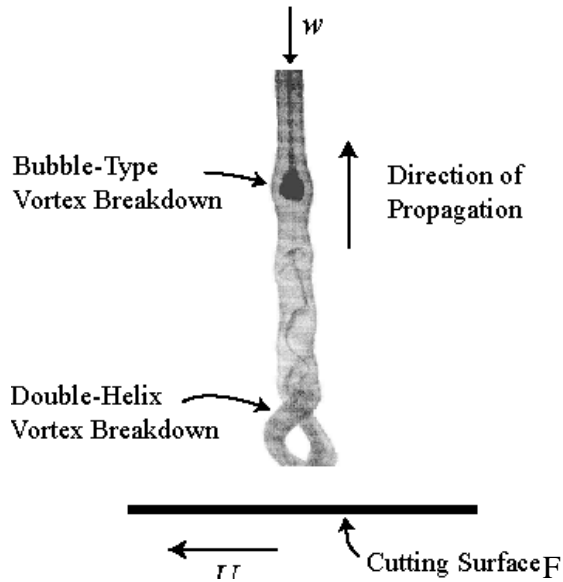
Figure 2.33 Double-helix vortex breakdown during BVI (Krishnamoorthy & Marshall, 1994)
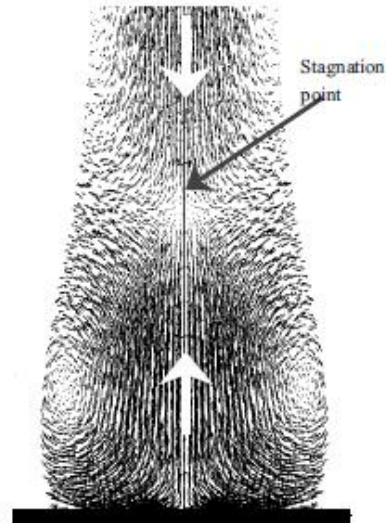
Figure 2.34 Vortex spanwise displacement as a function of impact parameter (Marshall & Krishnamoorthy, 1997).

2.4   Windbreak Walls

Wind barriers are widely used for purposes, such as reduction of wind erosion of stockpiles, wind protection on bridges or on railways. A rigid wall immersed in the flow creates a low velocity region on the leeward. The sheltering efficiency of the wall is mainly related to the wall height. Initialy, windbreak walls were designed to be solid, however the recent research have shown that porous walls exhibit better sheltering effects.

The reasearch concernig wind barriers was started by Kaiser (1959). He first introduced a distinction in terminology between *mean wind speed reduction* of windbreak wall and *wind*

protection. Kaiser (1959) noticed that solid walls give greater *mean wind speed reduction* than porous walls. However, solid walls produce greater turbulence in the recirculation region behind the wall. This effect may reduce overall effectiveness of the wind barrier. The impact of turbulence can be reduced by the application of porous barriers.

■ *Solid vs. Porous Wall*

Raine and Stevenson (1977) explained the difference between flow over a solid wall and porous wall. For solid walls, the flow separation is started from the top (Figure 2.35). The separation streamline divides the low-velocity flow close to the ground and the high velocity flow aloft. In the separation zone the flow is turbulent. The flow returns to be translational behind the reattachment point. For permeable (porous) windbreak walls some of the fluid flow through the wall, which is called *bleed flow* (Figure 2.36). This prevents the formation of the turbulent zone behind the wall. Castro (1971) conducted two-dimensional simulation of the flow over solid plates and porous plates. He concluded that the recirculation zone behind the wind barrier disappears when the porosity of the plate reaches 30%.
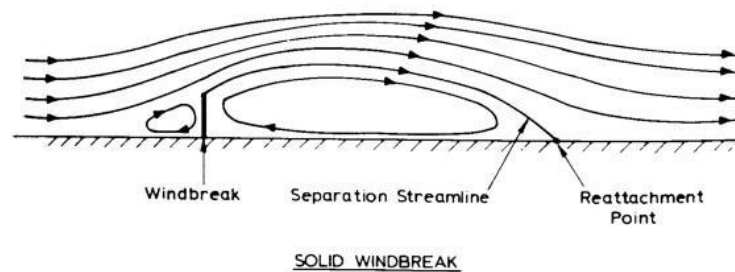
Figure 2.35 Streamlines of the flow over a solid windbreak wall (Raine & Stevenson, 1977).
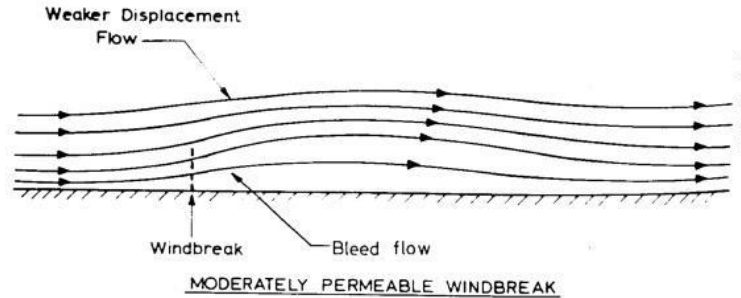
Figure 2.36 Streamlines of the flow over a porous windbreak wall (Raine & Stevenson, 1977).

- *Mean wind speed reduction*

The wind speed reduction on the leeward side of a windbreak is the highest close to the wall, and it is decreasing away from the wall. The mean wind speed field behind the solid wind barrier is presented in Figure 2.37. The wind speeds are reduced for more than 20% at a distance of 20H away from the wall, where H is the wall height.
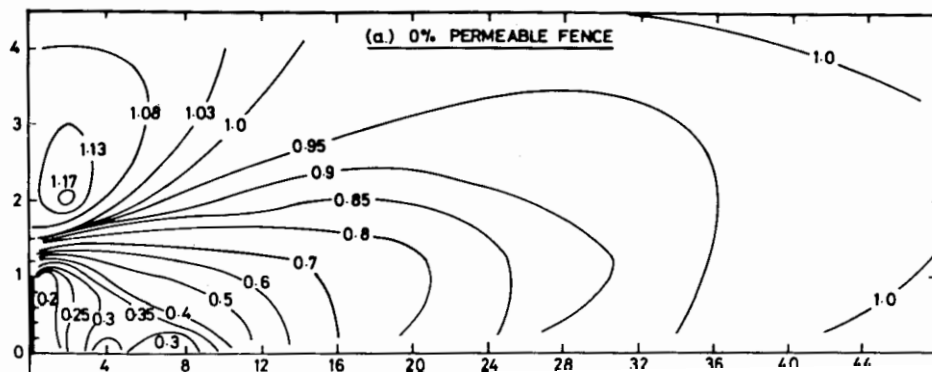
Figure 2.37 Contour of mean wind speed behind the solid wall (Raine & Stevenson, 1977).

Permeable walls are characterized by porosity percentage. Porosity of a wind barrier is a fraction of open area over the entire barrier area. Cornelis and Gabriels (2005) observed that a porous wall exhibits better sheltering effect than a solid wall. They conducted wind tunnel experiments and concluded that porosity from 20% to 35% gives the optimal wind speed reduction of the windbreak wall. Dong, Luo, Qian and Wang (2007) demonstrated that the maximum wind speed

37

reduction is provided by walls with porosity between 20% and 30%. He noticed that for porosities greater than 30% the wind flowing through the holes dominates and protection abilities of these walls are limited. On the other hand, for porosity lower than 20% the reverse flow in the wake region becomes significant. Cornelis and Gabriels (2005) found that the largest safe area, behind a wall, is provided by wind barrier with evenly distributed porosity. Kozmar, Procino, Borsani and Bartoli (2012) investigated the effect of different angle of attack of the free stream wind on the efficiency of a wind barrier. They noticed that as the horizontal wind incidence angle increases the sheltering efficiency of the barrier is reduced. Wang and Zheng (2003) conducted CFD simulation of porous windbreak wall and concluded that the flow behind the wind barrier is influenced by both the hole size and wall porosity. Dierickx, Cornelis and Gabriels (2003) observed that porous windbreaks are more effective for smooth turbulent flows rather than rough turbulent ones. Table 2.4 provides a summary of general remarks of wall with different porosity percentage.

Table 2.4 Summary of flow characteristics on the leeward of windbreak walls.

Wall porosity	*Wind field on the lee region*
0% (solid wall)	Reverse flow in the wake region is significant. The circulation causes pressure decrease behind the wall.
0-20%	Wind flowing through the holes reduces downstream wake region. The sheltering effect is better comparing to the solid wall.
20-35%	Optimal wind speed reduction. The wake region is disturbed by the ventilated air
Above 35%	Wind flowing through the holes dominates and protection abilities of these walls are limited

38

- *Pressure fluctuations behind the wall caused by wake region*

Perera (1981) studied the difference in flow between porous and solid wind fences. He noticed better sheltering effect of porous fences. Flow over the solid wall was characterized by downstream wake region. The circulation region behind the prism causes decrease in pressure. According to Perera (1981) this region disappeared when the wall porosity was 30%. Yaragal, Govinda Ram and Murthy (1997) demonstrated experimentally that porous fences reduce the pressure fluctuation in the downstream region of the fence. They concluded that fence with porosity 30% reduces pressure fluctuations by 50%.

- *Wind barriers protecting structures*

Wind walls are extensively used close to traffic to prevent overturning of trains or sideslip of cars due to strong winds. Li, Wang and Bell (2007) simulated the performance of the porous windbreak wall with a rigid building behind the wall (Figure 2.38). They measured mean wind speeds behind the wind barrier.
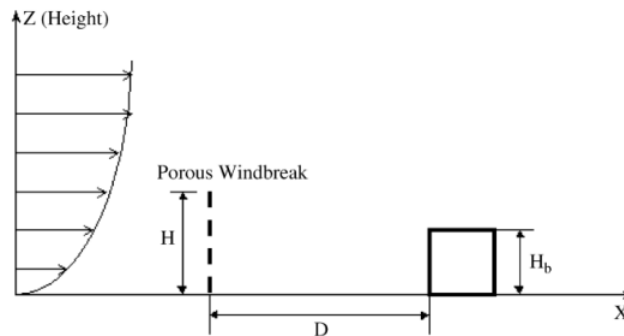
Figure 2.38 Description of the problem analyzed by Li et al. (2007).

The wind speeds on the leeward were found to be affected by the presence of a building. They noticed that when a building is within a distance of 5 times the height of the wall, the downstream flow structure is mostly influenced by the building rather than by the wall. The

39

influence of the building location on wind speeds is presenter in Figure 2.39. The influence of

building height in the wind speeds is shown in Figure 2.40. It is noticed that when the building is

higher than the windbreak, the building is exposed to higher wind velocities.
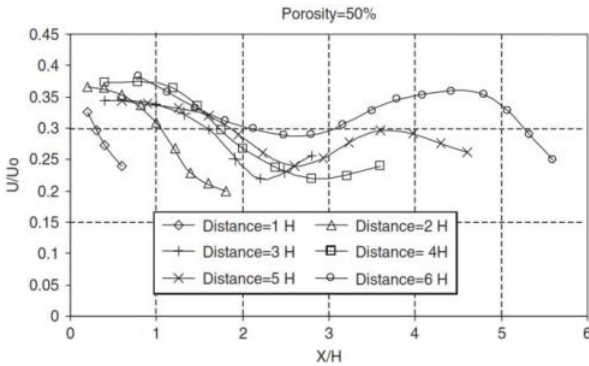
Figure 2.39 Effect of the building location on the mean wind speeds behind a windbreak wall of height 15 m (Li, Wang, & Bell, 2007).
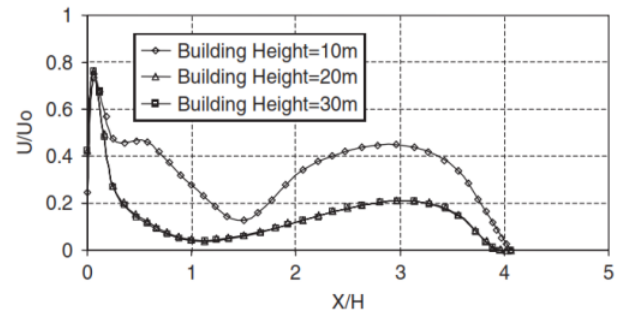
Figure 2.40 Effect of the building height on the mean wind speeds behind a windbreak wall of height 15m (Li, Wang, & Bell, 2007).

Li, Feng, Yang and Hou (2011) demonstrated that application of wind barrier to railway can

significantly reduce wind forces on the train. Lingling, Xifeng, Mingzhi and Sha (2012) analyzed

wind-wall protection for trains. They considered three cases: no windbreak wall, a solid wall and

30% porosity wall. They studied the influence of the wind barrier on the overturning moment

induced on the train. Lingling et al. (2012) demonstrated that porous wall generate better

efficiency than solid wall. In the case of the porous wall, the overturning moment was reduced

even by 75% comparing to no-wall-protection case. For the solid wall the reduction was about

50%. Kun and Renxian (2012) optimized the sheltering wall dimensions for high-speed railway.

They analyzed side forces and rolling moments acting on the train located behind the solid wall.

They found that different wind forces are induced in the case of straight railway than for curved

railway. The optimal height of the wall is different for these two cases. It was also demonstrated

that the wind forces are independent on the train speed. Kwon, Kim, Lee and Song (2011)

conduct wind tunnel experiments of wind barriers with porosity of 50%. They concluded that the

40

barrier height should be equal to 12.5% of road width to provide minimum 50% of wind speeds reduction across the road. They also found that the pressure coefficient of the wind barrier is equal to 0.8.

- *Wind barriers preventing erosion of stockpiles*

The wind erosion of stockpiles in an open storage yard is an important concern in the wind engineering domain. Lee and Park (1998) and Lee & Kim (1999) investigated the influence of porous wind fences on the coal pile surface-pressure distributions. They found from wind tunnel tests that the wind fence of porosity equal to 40% most effectively reduces pressure fluctuations on the surface of 2D prismatic stockpile. Park and Lee (2003) add back fence behind the stockpile, which reduced pressure fluctuations on the leeward surface of the pile, compared with no back fence case. Santiago, Martin, Cuerva, Bezdenejnykh and Sanz-Andrés (2007) conducted wind tunnel experiments with different turbulence models to investigate the most efficient wind barriers to protect stockpiles. They observed that the fence with porosity 30-40% provides the optimal reduction of pressures acting on the prismatic stockpile. Lee and Lim (2001) numerically studied pressures on stockpiles as a function of fence porosity, its height and position relatively to the pile. The optimal porosity was found to be between 30 and 50%. Yeh, Tsai and Yang (2010) studied an application of porous fence around stockpiles under wind of different directions (Figure 2.41). They showed that a rectangular fence provides better sheltering effect than octagonal fence for wind acting in the normal direction. However, for the wind incident with an angle of 45^0, the octagonal wind barrier works better.
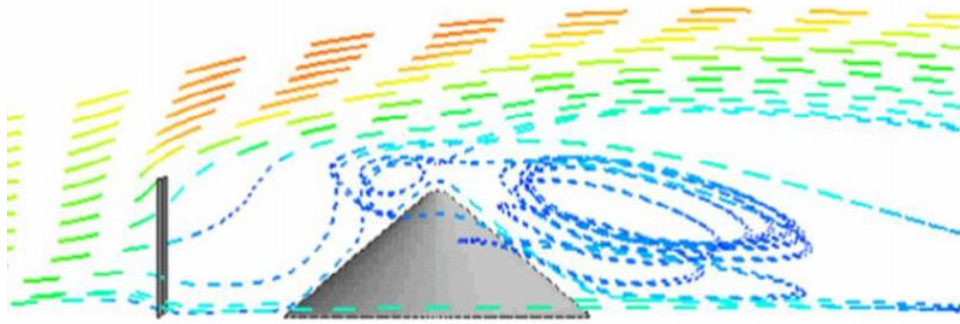
Figure 2.41 Streamlines of the flow over stockpile, protected by a porous wall (Yeh, Tsai, & Yang, 2010).

- *Conclusions from the review on wind barriers*

The following conclusions can be drawn from the presented literature review on windbreak walls:

- For a solid wall the wind speeds are reduced for more than 20% at a distance of 20H away from the windbreak wall, where H is the wall height.

- The downstream wake region, characteristic for a solid wall, disappears when the wall is porous. The optimal porosity is 30%. Such porous wall exhibits better sheltering effect than a solid wall

- Porous walls reduce pressure fluctuations in the sheltering region.

- Wind direction different than normal to a wall reduces the sheltering effect

- When a building is within a distance of 5H away from a windbreak wall, the downstream flow structure is mostly influenced by the building rather than by the wall porosity

- No research has been done measuring wind forces on a building located behind the wall. Only the wind field was studied.

- Most of research assumes the infinite wall break wall, so that the influence of wall width is neglected.

42

3. COMPUTER MODELING

3.1 Vortex Modelling

In the CFD simulations of the vortex-structure interaction, the most challenging part is to impose a translating vortex with predefined parameters into the flow. There are three common ways of creating the vortical flow:

- *Initial and time-dependent boundary conditions derived from analytical vortex model*

Selvam and Millett (2003; 2005) utilized the large eddy simulation (LES) turbulence model. Their velocity boundary conditions were derived from the Rankine vortex model (RVM). The moving tornado-like vortex was simulated of initial and time-dependent boundary conditions. In blade-vortex interaction (BVI), Liu and Marshall (2004) initiated the vortex in the computational domain by applying boundary conditions, similar as Selvam and Millett (2003) did. The only difference was: for the tornado-building interaction on the ground surface, the velocities are set to be 0. In BVI the blade is immersed in the flow and the velocities are as well specified on the bottom boundary. Filippone and Afgan (2008) simulated a travelling vortex by applying similar boundary conditions as Liu and Marshall (2004). They utilized the Menter shear-stress transport model for the turbulent shear stresses. Thom and Duraisamy (2010) approximated the compressible Euler equations to simulate the BVI. They pointed out the importance to preserve the vortex structure and parameters over the numerical simulation. This was easier since they did not use full Navier-Stokes equations. They reported their CFD results to be in good acceptance with the laboratory experiments. Rizzetta and Visbal (2011) built the LES model to simulate the Taylor-like vortex. The vortex flow was created as a result of the time-dependent boundary conditions.

43

- *Sliding Mesh Algorithm*

Here, the CFD computational domain is divided into two or more meshed zones. The zones are connected to each other by grid interfaces. In a particular zone the rotating flow is created from the boundary conditions. This zone is transported through the domain, and in the each time step the appropriate interface values are calculated to transfer the flow conditions to all other meshed zones (Sengupta, Haan, Sarkar, & Balaramudu, 2008; Lewellen, Gong, & Lewellen, 2008; Lewellen, 2012).

- *Modelling Laboratory Simulator*

The third method of introducing vortex flow consists in creating a CFD model that geometrically and conceptually corresponds with a tornado laboratory simulator (Kuai, Haan Jr, Gallus Jr, & Sarkar, 2008). Hangan and Kim (2008) simulated a stationary vortex in a cylindrical computational domain. They specified the side wall as an inflow and the upper boundary as an outflow. The wind profile of the simulated vortex was in good comparison with the field data. Natarajan and Hangan (2012) developed the translating vortex simulation by moving the floor boundary. They studied the influence of the surface roughness on the simulated vortex.

3.2   Development of Selvam Vortex-Structure Interaction Model

Advancement in numerical modeling resulted in the increase of applications of computer simulations for various CFD problems. The vortex-structure interaction problems are very complex from the analytical side, and formulating a reliable model is still very challenging. There are few research groups that successfully utilizes CFD to study vortex flows. The main advantages of the use of computer simulations are:

44

- Numerical modeling is much cheaper than laboratory experiments. Having a computer program allows conducting vortex interaction experiments almost anywhere by a quite experienced engineer.

- Using a computer simulation one can easily modify all vortex and structure dimensions and parameters to obtain results in fairly short time.

- The output data contains of a lot of information available anywhere in the computational domain during the entire simulation time.

For about 30 years the CFD research has being conducted in the Computational Mechanics Lab at the University of Arkansas. Selvam (1985) and McDonald and Selvam (1985) simulated tornado forces on a building using the boundary element method. They assumed the inviscid flow equations. This limited their results, since the wind is viscous and turbulent. The improvement to the model was made by Selvam (1990). He conducted a two-dimensional simulation of wind loads on a cubic house. The (k-ε) turbulence model was considered. The Navier-Stokes equations were approximated using the finite difference procedure. Selvam (1993) conducted similar CFD simulation, including a tornado-like vortex in the flow. However, the turbulence model (k-ε) and the boundary conditions applied in these works were not satisfactory to the author. Selvam (1996b) and Selvam (1997a) used control volume scheme and different turbulence models looking for these giving most accurate results with less computational time. He found that large eddy simulation (LES) is most viable turbulence model for use in practical problems, which works very well for transient problems. Selvam (1996a) compared the finite element and the finite difference procedures to approximate the Navier-Stokes equations. The finite element method (FEM) was found to be more accurate for the given grid. Selvam (1997b) used LES and FEM to model flow around a circular cylinder. Soon later he applied LES and

45

FEM for two-dimensional simulation of wind flow around bridges (Selvam, 1998). The FEM procedure was improved by application of adaptive p-finite elements (Selvam & Qu, 2002). Selvam et al. (2002) proposed 2D model of tornado-structure interaction. The Navier-Stokes equations for incompressible flow were approximated by control volume method, which was found to be more computationally efficient than FEM. The turbulence was considered by LES. The Reynolds number of the flow was set to be $R_e=1000$ in order to have some confidence of the work. For $R_e=1000$ the results of straight line wind forces were available from the literature. Two-dimensional model was useful because it gave an understanding of developing the boundary layer close to the structural boundaries. The 3D model introduced by Selvam and Millet (2002; 2003) was numerically analogous to 2D. However, in a 3D case the appropriate grid resolution in the boundary layer was at this time unreachable, due to the large number of grid points (limited computing capabilities). Later, Selvam and Millet (2005) applied more refined grid near the building boundaries. They used 1.6 million nodes and the results were still not converging. The lack of computer and storage system delayed further investigations of the proper grid refinement (2010b). Recently, Alrasheedi and Selvam (2011) applied 6.5 million nodes for a tornado-building interaction. For further details concerning development of tornado-structure interaction model one should refer to (Selvam, 2008) and (Selvam, 2010a).

3.3   Characteristics of Rankine Vortex Model

- *Velocity Profile*

The tornado-like flow is modelled using the Rankine Vortex Model (RVM). According to Doppler radar data of actual tornadoes (Wurman, Robinson, Alexander, & Richardson, 2007; Kosiba, Robinson, Chan, & Wurman, 2014), the horizontal and the vertical wind velocity distribution varies among tornado outbreaks. Also, a particular tornado constantly changes its structure over the travel. This resulted in many different tornado mathematical models. In the current study the choice of the tornado vortex model is dictated by the numerical modeling requirements. Among the retrieved tornado velocity models, the RVM satisfies the NS equations and at the same time exhibits a tornado-like velocity distribution (Kosiba, Robinson, Chan, & Wurman, 2014). The RVM only specifies horizontal velocities, while there is no control on the vertical velocities in the simulated tornado-vortex. The vortex axial flow is created by self-induced conditions – low pressure in the vortex center. This effect was also observed by Filippone and Afgan (2008). The RVM equation is specified as follows:

$$u_\theta = \begin{cases} \alpha\, r & for \quad r < r_{max} \\ \alpha\, r_{max}^2\, \dfrac{1}{r} & for \quad r \geq r_{max} \end{cases} \tag{3.1}$$

According to the RVM the tangential velocity of a tornado, u_θ, increases linearly, $u_\theta = \alpha r$, up to the vortex radius r_{max}, where r is the distance from the vortex centre and α is a vortex core strength constant, as shown in Figures 3.1 and 3.2. For r larger than r_{max}, the tangential velocity is hyperbolically decreasing. The RVM is divided into the forced vortex region, or the vortex

47

core ($r<r_{max}$), and the free vortex region ($r>r_{max}$). The RVM was first introduced for the tornado-structure interaction problems by Selvam (1985).
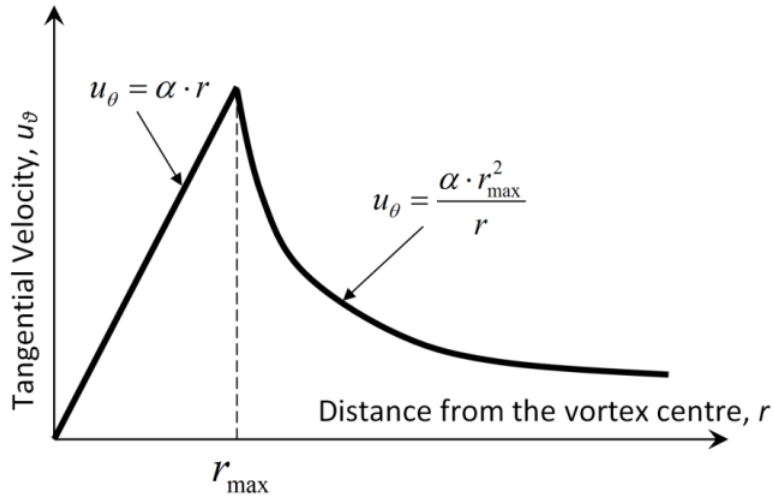
Figure 3.1 Tangential velocity of RCV model.
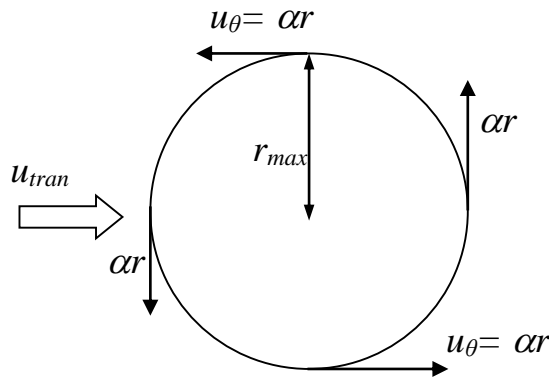
Figure 3.2 Plan view of RCV model with translational velocity.

The RCVM model satisfies the conservation equations and the vortex superposition on the free stream flow does not create any anomalies.

- *RVM Vorticity and Circulation for Inviscid Flow*

The vorticity of the flow is calculated as a curl operator of the velocity vector function. In the case of RV model, the vorticity has to be calculated separately for both free and forced vortex regions. Since the vortex model is described in the cylindrical coordinates, the vorticity is:

$$\vec{\omega} = \nabla \times \vec{u} = \left(\frac{1}{r} \frac{\partial u_z}{\partial \theta} - \frac{\partial u_\theta}{\partial z} \right) \vec{r} + \left(\frac{\partial u_r}{\partial z} - \frac{\partial u_z}{\partial r} \right) \vec{\theta} + \frac{1}{r} \left(\frac{\partial (r u_\theta)}{\partial r} - \frac{\partial u_r}{\partial \theta} \right) \vec{z} \qquad (3.2)$$

RV model assumes only tangential velocity ($v_\theta \neq 0, \ v_r = v_z = 0$), thus:

$$\vec{\omega} = \frac{1}{r} \left(\frac{\partial (r u_\theta)}{\partial r} - \frac{\partial u_r}{\partial \theta} \right) \vec{z} = \left(\frac{u_\theta}{r} + \frac{\partial v_\theta}{\partial r} - \frac{1}{r} \frac{\partial u_r}{\partial \theta} \right) \vec{z} \qquad (3.3)$$

Substituting: $u_r = 0, \quad u_\theta = \begin{cases} \alpha r & for \ r \leq r_{max} \\ \dfrac{\alpha r_{max}^2}{r} & for \ r > r_{max} \end{cases}$, the vorticity magnitude is:

$$|\omega| = \begin{cases} \alpha + \alpha - 0 = 2\alpha & for \ r \leq r_{mzx} \\ \dfrac{\alpha r_{max}^2}{r^2} - \dfrac{\alpha r_{max}^2}{r^2} - 0 = 0 & for \ r > r_{mzx} \end{cases} \qquad (3.4)$$

This means that in the free vortex region ($r > r_{mzx}$) there is no vorticity and flow is irrotational. In the free vortex region the fluid rotates by the action of the forced vortex. When the flow is forced to rotate, the vorticity is non-zero ($r \leq r_{mzx}$). Fluid particles in the same radial distance from the vortex center, in the forced vortex region, have the same angular velocity. Therefore, this flow is often termed as a solid body rotation.

49

The vorticity is related to the circulation, which is often used to describe the strength of a particular vortex. Circulation is calculated as an integral of the vorticity in the certain region *S*. Since in the Rankine Vortex model the vorticity is held only in the vortex core, the total vortex circulation is calculated as:

$$\Gamma = \iint_S \omega \cdot dS = 2\alpha\pi \, r_{max}^2 \tag{3.5}$$

- *Pressure distribution inside RVM for Inviscid Flow*

For the calculation of pressure distribution inside the tornado vortex Euler equations for incompressible flow are applied. The Euler equations correspond to the Navier-Stokes equations, so that the viscosity and the heat conduction terms are not considered. According to the Bernoulli equation, pressure depends on the fluid velocity. In the case of vortex flow, pressure varies with velocity in the radial direction. Pressure at any point of the vortex, can be found from the equation of motion in the *r* direction (assuming: $u_\theta \neq 0$, $u_r = u_z = 0$):

$$\frac{1}{\rho}\frac{\partial p}{\partial r} = \frac{u_\theta^2}{r} - g\frac{dz}{dr} \tag{3.6}$$

Where: *p* – pressure, *ρ* – fluid density, u_θ – tangential velocity, *r* – radial coordinate, *z* – elevation, *g* – standard gravity.

The pressure distribution is obtained by integrating equation (3.5):

$$\frac{p}{\rho} = \int \frac{v_\theta^2}{r}dr - gz \tag{3.7}$$

50

In the simulation pressure is assumed not to vary in the *z*-direction, thus:

$$p = \rho \int \frac{v_\theta^2}{r} dr \qquad (3.8)$$

First, the pressure distribution is calculated for the free vortex region. It is known that far away from the vortex there is only atmospheric pressure, because the vortex influence is very small (Figure 3.1). The tangential velocity for the free vortex region is $u_\theta = \alpha r_{max}^2 / r$, thus a difference in pressure between two points is:

$$p_2 - p_1 = \rho \int_{r_1}^{r_2} \frac{u_\theta^2}{r} dr = -\frac{1}{2} \rho \alpha^2 r_{max}^4 \left(\frac{1}{r_2^2 - r_1^2} \right) \qquad (3.9)$$

Assuming that r_1 corresponds to a fluid particle far away from the vortex ($r_1 \to \infty$), the pressure is equal to the atmospheric pressure p_a. In the numerical simulation, atmospheric pressure is assumed to be 0, so pressure in any point of the free vortex ($r > r_{mzx}$) is:

$$p = -\frac{1}{2} \rho \alpha^2 r_{max}^4 \frac{1}{r^2} \qquad (3.10)$$

In the case of the forced vortex region ($r \le r_{mzx}$), the tangential velocity is linear ($u_\theta = \alpha r$) and a difference in pressure between any two points is:

$$p_2 - p_1 = \rho \int_{r_1}^{r_2} \frac{u_\theta^2}{r} dr = \frac{1}{2} \rho \alpha^2 \left(r_2^2 - r_1^2 \right) \qquad (3.11)$$

51

Knowing that pressure distribution has to be continuous along *r* direction, the pressure value at the end of forced vortex (*r=r_max*) has to be equal to pressure at the beginning of the free vortex:

$$p_1 = -\frac{1}{2}\rho\alpha^2 r_{max}^2 \tag{3.12}$$

Substituting (3.12) to (3.11), the pressure distribution inside the forced vortex is obtained:

$$p = \frac{1}{2}\rho\alpha^2 r^2 - \rho\alpha^2 r_{max}^2 \tag{3.13}$$

Thus, in the center of the vortex, the minimum pressure is equal to:

$$p_{min} = -\rho\alpha^2 r_{max}^2 \tag{3.14}$$

The final equation for pressure distribution in RCV model is described by equation (3.15) and plotted in Figure 3.3.

$$p(r) = \begin{cases} \dfrac{1}{2}\rho\alpha^2 r_{max}^4 \dfrac{1}{r^2} & \text{for } r > r_{mzx} \\[4mm] \dfrac{1}{2}\rho\alpha^2 r^2 - \rho\alpha^2 r_{max}^2 & \text{for } r \le r_{mzx} \end{cases} \tag{3.15}$$
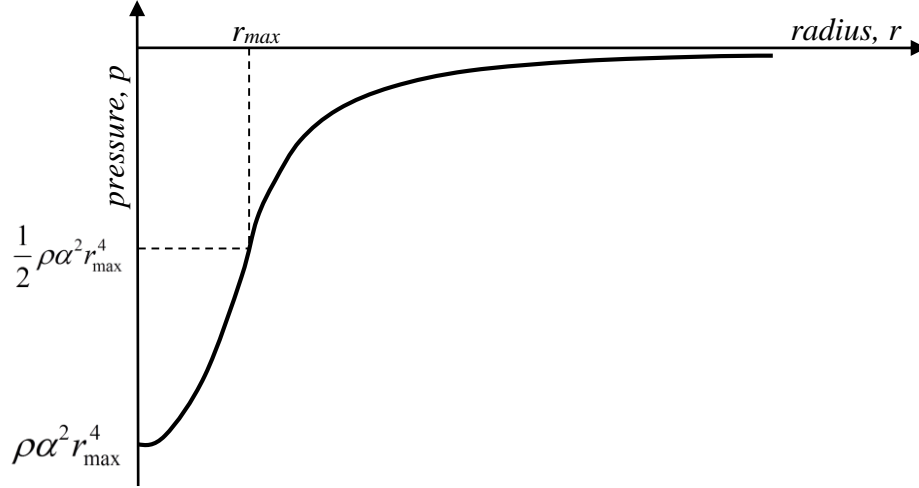
Figure 3.3 Axisymmetric pressure distribution of RCV model.

The profile resembles near-ground pressure of actual tornadoes, measured by Karstens, Samaras, Lee, Gallus and Finley (2010).

3.4   Navier-Stokes Equations

The vortex flow is simulated using the Navier-Stokes (NS) equations for the incompressible flow:

$$\frac{\partial \overline{u}_i}{\partial x_i} = 0 \tag{3.16}$$

$$\frac{\partial \overline{u}_i}{\partial t} - \frac{\partial}{\partial x_j}\left(\overline{u}_i \overline{u}_j\right) = -\frac{1}{\rho}\frac{\partial \overline{p}}{\partial x_i} + \nu \frac{\partial^2 \overline{u}_i}{\partial x_i \partial x_j} - \frac{\partial \tau_{ij}}{\partial x_j} \tag{3.17}$$

The sub-grid scale (SGS) tensor is given as:

$$\tau_{ij} = \overline{u_i u_j} - \overline{u}_i \overline{u}_j \tag{3.18}$$

53

The SGS tensor is modelled by applying the standard Smagorinsky type subgrid scale model. This method is one of the simplest ways to simulate the turbulent scales that cannot be resolved by grid:

$$\tau_{ij} - \frac{\delta_{ij}}{3}\tau_{kk} = -2\nu_{SGS}\bar{S}_{ij} \tag{3.19}$$

$$\bar{S}_{ij} = \frac{1}{2}\left(\frac{\partial \bar{u}_i}{\partial x_j} + \frac{\partial \bar{u}_j}{\partial x_i}\right) \tag{3.20}$$

$$\nu_{SGS} = (C_s h)^2 \left[2(\bar{S}_{ij})^2\right]^{\frac{1}{2}} \tag{3.21}$$

$$h = (h_1 h_2 h_3)^{\frac{1}{3}} \tag{3.22}$$

$$k_{SGS} = \frac{\nu_{SGS}^2}{(C_K h)^2} \tag{3.23}$$

The C_s and C_K constants are taken to be respectively 0.1 and 0.094, as suggested by Murakami and Mochida (1995). Selvam (1997a) demonstrated that for those values there is a good agreement between flow field data around a structure and the LES simulation. The final form of the momentum equation (3.17) for the standard Smagorinsky model, which was employed for the numerical approximations, is:

$$\frac{\partial \bar{u}_i}{\partial t} - \frac{\partial}{\partial x_j}(\bar{u}_i \bar{u}_j) = -\frac{\partial}{\partial x_i}\left(\frac{\bar{p}}{\rho} + \frac{2}{3}k_{SGS}\right) + \frac{\partial}{\partial x_j}(\nu + \nu_{SGS})\bar{S}_{ij} \tag{3.24}$$

3.5   Boundary Conditions

The geometry of the problem with applied boundary conditions is illustrated in Figure 3.4. The counter clockwise rotating vortex is convected along x-axis with a constant translational velocity, u_{tran}. The vortex is smoothly introduced into the computational domain. Additionally to

54

the vortex flow, a free stream flow of a constant velocity is imposed in the entire domain. The

free stream velocity magnitude and its direction are equal to the translational velocity of the

vortex.
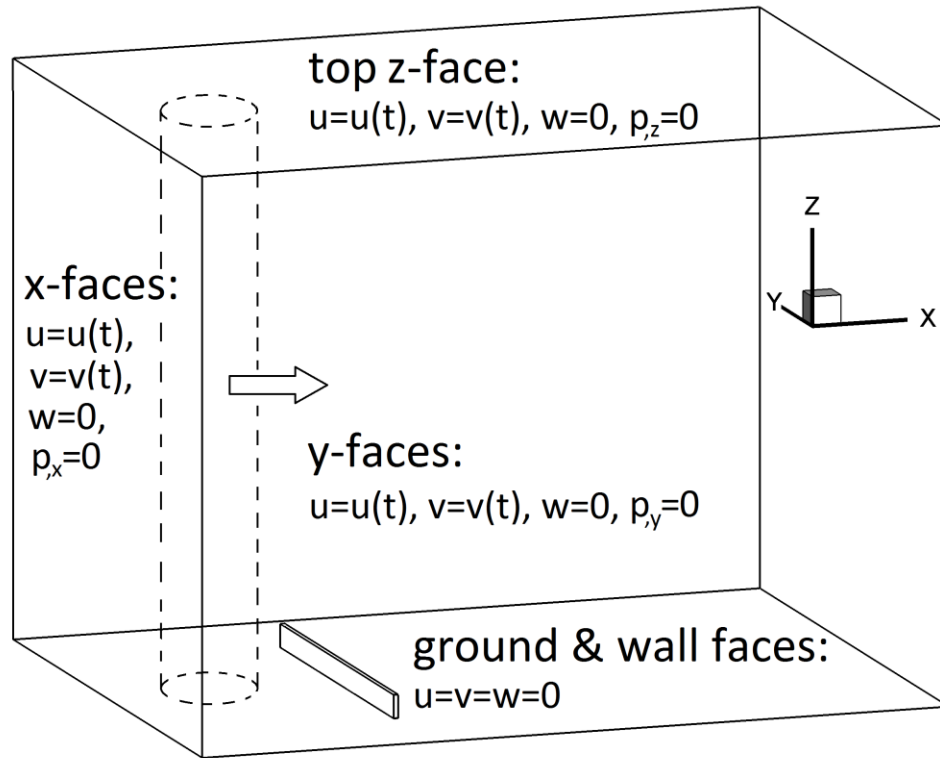
Figure 3.4 Geometry of the problem with applied boundary conditions.

The simulated flow is a result of initial conditions and time-dependent boundary conditions

employed over the simulation time on the domain boundaries, as illustrated in Figure 3.4. At the

side computational domain boundaries and the top boundary the undisturbed Rankine-combined

vortex model velocity is specified at all times. Only on the bottom surface and the prism walls

the no-slip boundary condition is applied. The boundary layer of prism walls is resolved by the

grid. The ground surface is modelled using a logarithmic law wall function. To obtain the

boundary condition values the sum of RVM and the free stream velocities is mapped on the

55

computational domain boundaries. Assuming that the time, t, is zero when the centre of the vortex coincides with the centre of the structure, the velocity horizontal components at the boundaries are:

$$u(x, y, z, t) = \begin{cases} \left(u_{tran} - y \cdot \alpha\right)Z_f & for \ r \leq r_{max} \\ \left(u_{tran} - y \dfrac{\alpha \, r_{max}^2}{r^2}\right)Z_f & for \ r > r_{max} \end{cases}$$ (3.25)

$$v(x, y, z, t) = \begin{cases} \left[(x - u_{tran} \, t) \, \alpha\right] Z_f & for \ r \leq r_{max} \\ \left[(x - u_{tran} \, t) \dfrac{\alpha \, r_{max}^2}{r^2}\right] Z_f & for \ r > r_{max} \end{cases}$$ (3.26)

$$w(x, y, z, t) = 0$$ (3.27)

Since the RVM does not include any condition for the vertical velocity component, $w=0$. In equations (3.25-3.26) Z_f creates the domain surface boundary layer along the height, z, according to the logarithmic law:

$$Z_f = \frac{u^*}{\kappa} \ln\left(\frac{z + z_0}{z_0}\right)$$ (3.28)

Z_f reaches 1.0 at the top of the prism and 0 on the ground level. The surface roughness length, z_0, is equal to 0.04 m.

The computation is conducted on the orthogonal grid and the RCV model is transferred to the Cartesian coordinates as:

$$r = \left[(x - u_{tran} \, t)^2 + y^2\right]^{\frac{1}{2}}$$ (3.29)

56

On boundary faces the normal derivative of pressure is considered to be zero:

$$\frac{\partial p}{\partial n} = 0 \qquad (3.30)$$

The numerical calculations are conducted based on the dimensionless values to simplify and facilitate the computation. The dimensionless length, velocity and time (respectively: L^*, U^*, t^*) are calculated as follows:

$$L^* = L/L_{ref} \qquad (3.31)$$
$$U^* = U/V \qquad (3.32)$$
$$t^* = t \cdot V/L_{ref} \qquad (3.33)$$

Where: L, U and t are length, velocity and time; L_{ref} – referenced length equal to one third of the height of the structure; V – referenced velocity, equal to the translational velocity. Based on dimensional pressures and velocities other flow properties, such as velocity magnitude, vorticity vectors or q-criterion can be calculated (see Appendix 1).

The details of the model derivation are also available in Selvam (1985).

3.6 Solution of NS Equations and Convergence Criterion

The NS equations are approximated using the control volume procedure. The equations are solved in time using a semi-implicit method, as suggested by Selvam (1997b). For an approximation of continuity and momentum equations the four step advancement scheme is utilized:

(1)   Solve for u_i from equation (3.17). The diffusion and convection terms are considered implicitly. The pressure is considered in the right hand side of the equation. For simplicity here p/ρ is considered as p.

(2)   Get new velocities as $u'_i = u_i + \Delta t \cdot p_{,i}$ where u_i' is not specified.

(3)   Solve for pressure from $p_{,ii} = u'_{i,i}/\Delta t$.

(4)   Correct the velocities for the incompressibility: $u_i = u'_i - \Delta t \cdot p_{,i}$

Step 2 eliminates the checkerboard pressure field when using equal order interpolation for velocity and pressure in the case of a finite difference method. The time step is calculated according to the Courant-Frederick-Lewis (CFL) number. The CFL number is kept to be less than one; this gives time step around 0.01 units for most of the computation.

The discretized velocity equations are solved by the line iterations in the x-, y- and z- directions until convergence is achieved. The pressure equations are approximated using preconditioned conjugate gradient procedure (PCG). To solve the velocities an under-relaxation factor of 0.7 was applied. Since the flow has high vortex strength in the inner core, for suitable convergence, sub-iterations are needed at each time step. The variables are solved sequentially in an implicit manner at each time step. The absolute sum of the residue error for each variable is reduced to

58

reach certain convergence value, which is IM·JM·KM·10^{-5}, where IM, JM and KM are number of grid points in the x-, y- and z- direction respectively. At the same time the iteration is repeated until the beginning residue of all of the variables reduces to the converged value. The sub-iterations make sure that a converged solution is obtained. At the beginning of the computation the velocities are assumed as undisturbed values and hence the sub-iteration number is very high to reduce the error.

3.7   CFD Simulation Process

- *Pre-processing*

The first step of CFD simulation is creating model geometry. This step consist of defining the size and location of a structure, and the size of a computational domain. Then, the computational domain volume has to be discretized into a computational mesh. Both the CFD model geometry and the mesh quality are crucial to obtain converged and reliable results. In the current work the size of the domain and mesh spacing are defined based on conclusions drawn from *Grid Refinement and Computational Domain Size* section. A typical computation mesh for the vortex-structure interaction study consists of several million grid points. The coordinates of each node have to be written in the input file for the CFD solver. If this is done by hand, it would be very tedious and time consuming. To reduce the time in grid and geometry preparation, a FORTRAN code was developed especially for the current work. The pre-processing code automatically creates an input text file for the solver. With such a code it is possible to prepare the input file for a single simulation in less than 10 minutes. The computational mesh is created based on: size of domain, size of a building, location of a building, grid spacing on vortex path, grid spacing on

building faces and first grid spacing next to building face. Other input parameters for the simulation are: Rankine vortex radius, strength constant and translational velocity, fluid viscosity, time step, total time and logarithmic near-ground flow velocity profile.

■ *Solver*

The solution of the Navier-Stoke equations is conducted using the University of Arkansas Computational Mechanics Lab CFD code. The solver runs are performed in UNIX environment. The numerical calculations are conducted based on the input text file prepared during the pre-processing stage. An actual wall time of a simulation depends mainly on the number of grid points and the smallest grid spacing. In a typical vortex-structure simulation there is about 6 million grid points, and the first grid spacing next to a building face is 0.001 units. Such a simulation takes about 20 days for a wall time. An output file from a single time step is 1.4 GB. There is about ten thousand time steps in a single simulation. Therefore, it is not possible to store all output data from generated by the solver. It is also important to monitor CFD solution while the solver is running, in case of any mistake in setting up the simulation.

■ *Post-processing*

One of the major challenges of the post-processing stage, in the current work, is data handling. The solver generates an output file every specific number of time steps. This is done to limit the total number of written files. The post-processing is performed in *Tecplot* software, which works under Windows. Therefore, output files from UNIX have to be transferred to Windows. This is done using *SSH Secure Shell* software. Then, the output files are converted from ASCII to binary code using *preplot.exe* program, provided in *Tecplot* package. The binary conversion reduced the file size by about 85%. This is substantial advantage in terms of memory storage. Also, *Tecplot*

60

software better handles binary files. For this work a batch file was developed, which automatically launches *preplot.exe* program and converts one by one ASCII files into binary code. The batch file can be found in Appendix 3. For one vortex-structure simulation it is recommended to have at least 100 output files. For this number of files the entire process of downloading ASCII output files and converting them into binary takes about eight hours. To quickly visualize the simulation, a video from output data can be created through *Tecplot*. For the purposes of current work a *Tecplot* macro was created to enhance creating videos. The source code of the macro is included in Appendix 3. The important advantage of the macro is, it does not require to load all the output data in RAM memory, at one time. The files are loaded one by one, after a *Tecplot* layout for a video is specified. The visualization of a simulation was the most time consuming part of a CFD process. Depending on visualization needs this stage takes from one to even several weeks. In the next subsection some visualization techniques are discussed that enhanced the CFD simulation post-processing.

3.8 Visualization of CFD simulation

3.8.1 Identification of Simulated Vortex

The proper vortex identification is very important in analyzing CFD simulations of vortex-structure interaction. There are many methods to identify a vortex in a simulated flow. Most of the methods are based on post-processing calculations on velocity vector field of the simulated flow. The review of the vortex identification methods is provided by Holmen (2012). In the current work the simulated vortex is identified by two different variables:

- *Pressure minimum*

61

In a steady two-dimensional flow, the minimum pressure indicates the center of the rotating motion. In Section 3.3 the pressure distribution of the inviscid, two-dimensional Rankine vortex (RV) model was calculated. In the center of the vortex the pressure is minimum and it is increasing radially away from the vortex center. The pressure of an idealized two-dimensional vortex is only depended on the radial distance from the center of rotation. Thus, it is possible to visualize the simulated vortex by pressure iso-surface, as shown in Figure 7.1.
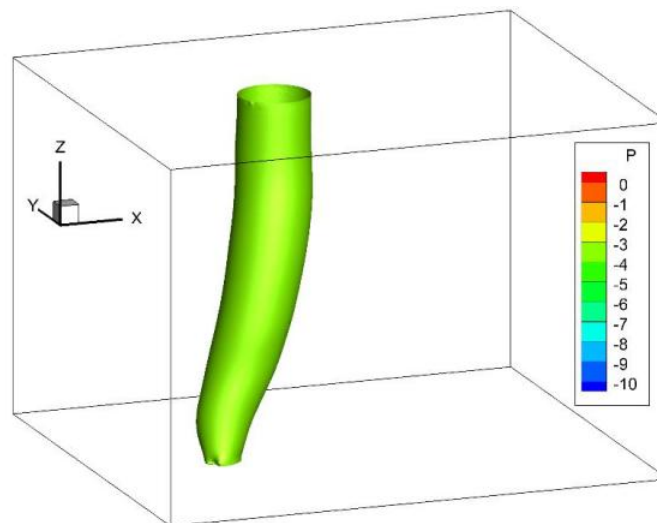
Figure 3.5 Pressure iso-surface (P=-3.0) of the simulated Rankine vortex.

The iso-surface is created from nodes with equal flow values. In Figure 3.5 only nodes with pressure values equal to -3.0 are shown. The remaining nodal values are masked.

The pressure distribution on a horizontal plane can be achieved by the use of a slice, as shown in Figures 3.6 and 3.7.
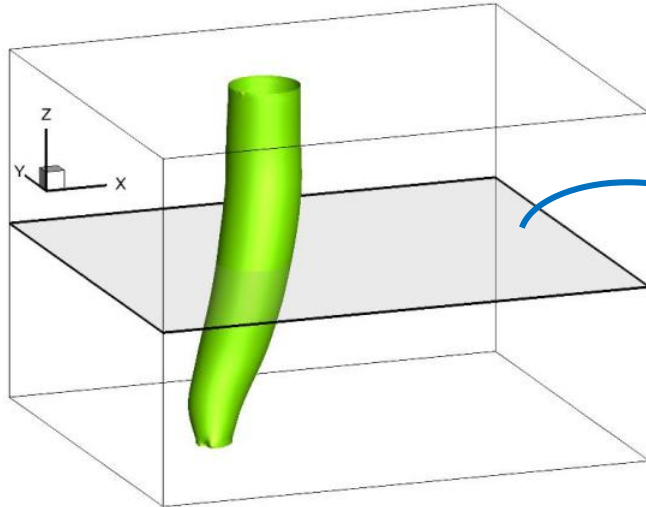
Figure 3.6 Horizontal slice in z-plane across the simulated vortex
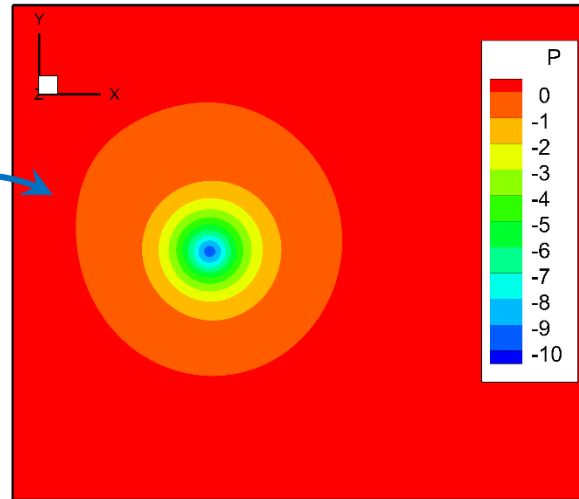
Figure 3.7 Pressure distribution in z-plane in the mid-height of the simulated vortex.

In Figure 3.7 the pressure minimum indicates the vortex center. Away from the vortex, pressures are increasing and reach zero. As it is observed in Figure 3.7 it is impossible to clearly distinguish the transition between the forced vortex flow and the free vortex flow. This is a disadvantage of identifying the Rankine vortex by pressure.

Vortex identification by pressure can be also misleading when the flow unsteady, turbulent, three-dimensional and interacts with a structure. In these cases minimum pressure in the domain can be found in different locations rather than the vortex center.

- *Z-vorticity*

Vorticity is calculated as a curl operator of the flow velocity. It indicates the local spinning motion of the flow. In RV model the non-zero vorticity is held only in the vortex core (forced vortex region), as showed in Section 3.3. The vortex core rotates in a rigid body motion and the vorticity is equal to twice the vortex strength parameter (2α). Outside the vortex core (free vortex region) the z-vorticity is zero, which means that the flow is irrotational. Figure 3.8 presents the z-vorticity contour at the mid-height of the simulated vortex.

63
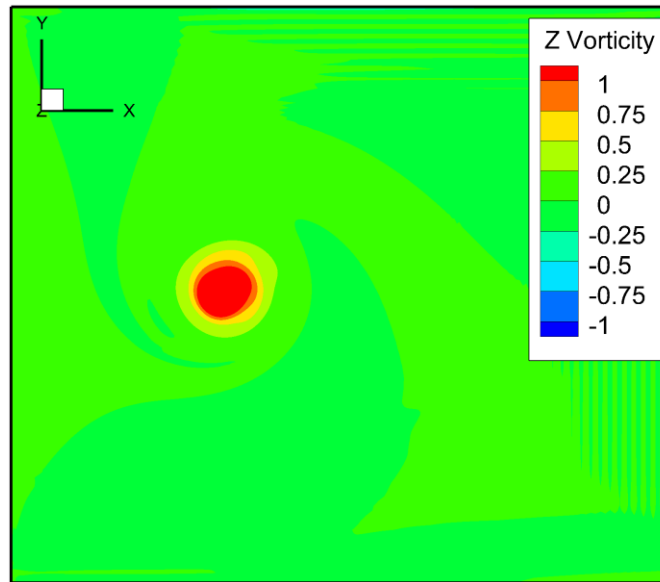
Figure 3.8 Z-vorticity distribution in z-plane on the mid-height of the simulated vortex.

Although, in the free vortex region the flow particles travel along the curved trajectories, their mean angular velocity about the center of mass is zero. Thus, the vorticity can be used to identify the vortex core region. This is an advantage over visualizing flow pressure. In Figure 3.8 the vortex core is indicated by the high z-vorticity values. Outside the vortex core the vorticity is equal to zero. The property of the RV model to hold vorticity in the core was utilized in this work to visualize the vortex path. The vorticity vectors were numerically calculated in the post-processing stage based on flow velocities. The vorticity calculation is included in Appendix 5.

The non-zero vorticity can also occur for flow particles travelling straight, which is misleading in identifying the simulated vortex. This happens when there is sheer in the flow (flow speeds vary across streamlines). Therefore, close to the boundary layer of wall surfaces, the vortex identification by vorticity is impeded.

64

3.8.2   Visualization of Transient Simulation

In the vortex-prism interaction presented in the current work, the simulated flow (i.e. pressure, velocity, vorticity) changes instantaneously over the time. To capture the most important flow features, during the simulation, different visualization techniques are utilized. The transient simulation is preferably illustrated by videos that contain a number of time steps. Appendix 4 includes two procedures how to create videos of the simulated flow using *Tecplot* software. Videos can visualize iso-surfaces and contour slices of scalar variables, and streamlines and vectors for vector variables. These visualizations can be presented either separately or simultaneously.

However, videos have limited application since it is impossible to include them in a written document. Also, videos are unable to qualitatively describe transient effects, because they include a number of frames, which can be analyzed separately. Therefore, in this work new visualization techniques were introduced to summarize the entire interaction on single contours:

- ▪ *Visualization of Sheltering Effect*

During a vortex-structure interaction, flow speeds in sheltering regions are constantly changing with regard to time and position. The objective was to create a visualization, which would qualitatively describe flow speed reductions on the leeward side of a structure. It was proposed to find only maximum flow speeds during the entire simulation. The algorithm to create a single contour for flow speed reductions behind an obstacle is presented in the flow chart in Figure 3.9. The algorithm is introduced in the post-processing stage, so it does not interfere with the solver.

65
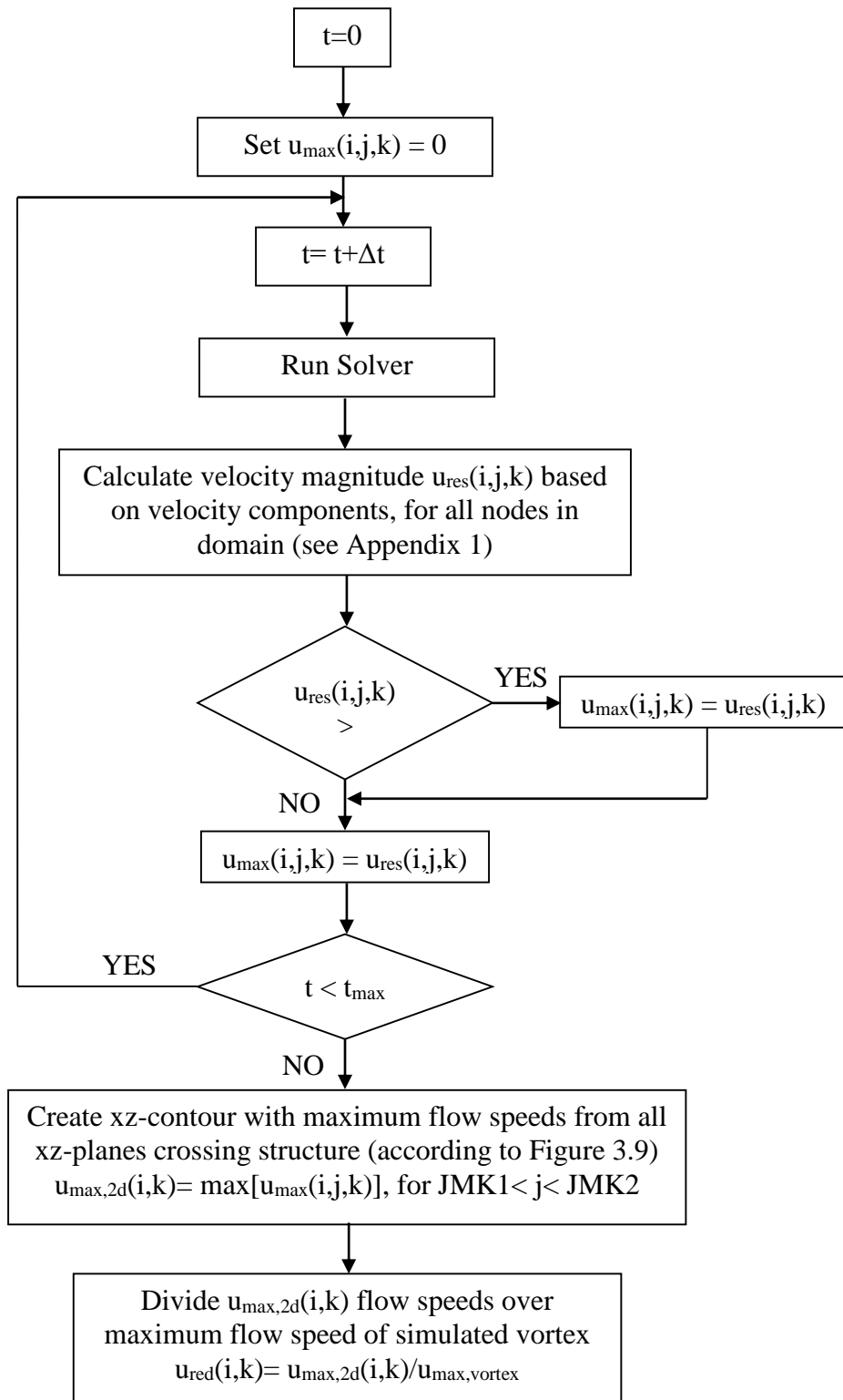
Figure 3.9 Algorithm to find flow speed reductions around an obstacle.

First, maximum flow speeds in each grid point are found for the entire simulation. From such a domain, a two dimensional contour is extracted from all xz-planes crossing structure (according to Figure 3.10). The maximum flow speeds are divided over the maximum flow speed of a simulated vortex during no-prism interaction.
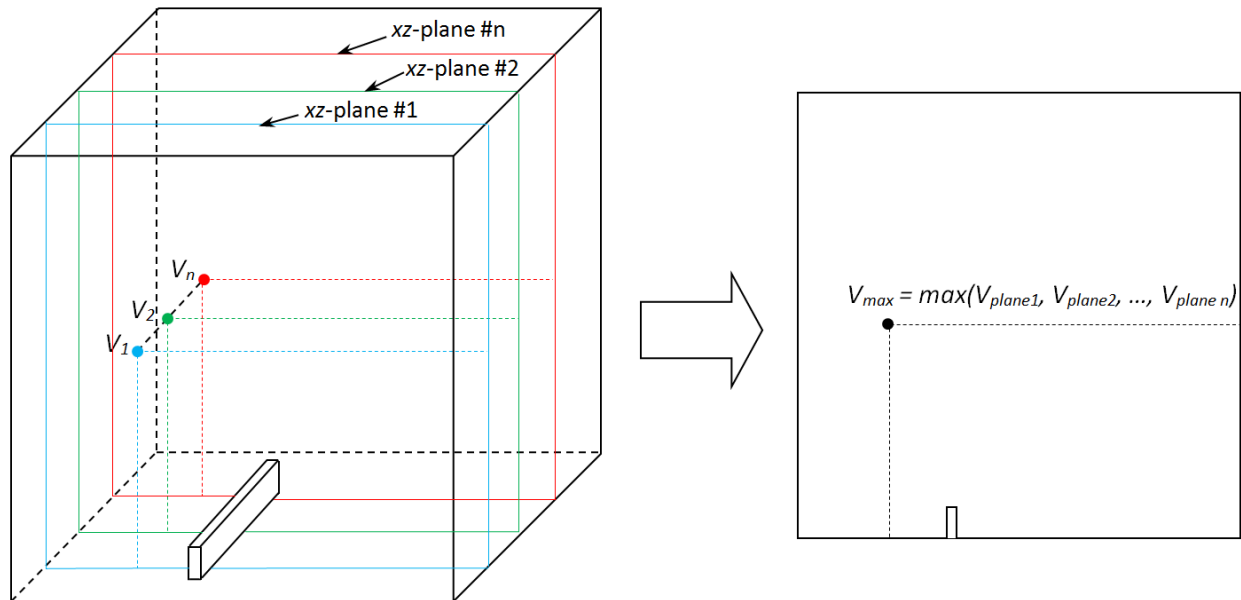
Figure 3.10 Construction of maximum resultant velocity contour for transient simulation.

A single contour with maximum flow speed reductions helps to visualize and immediately evaluate vortex sheltering effect of a given obstacle.

- *Visualization of Vortex Path Deviation*

The path deviations are illustrated using very similar concept as a visualization of the sheltering effect. An example of vortex path deviation is illustrated in Figure 5.12. It was proposed to find only minimum pressures on the ground slice (z=0) during the entire simulation. It is assumed

67

that the minimum pressure indicated the translating vortex center. Thus, the trance of minimum pressure indicates the translating vortex path.

- *Visualization of Vortex Strength*

The vortex strength throughout the entire simulation is presented on a single xy-contour. An example of such a contour is demonstrated in Figure 5.11. Since the non-zero z-vorticity occurs in the vortex core, it is proposed to find maximum z-vorticity values during entire simulation time in xy-plane. The z-vorticity distribution on a vortex path indicates vortex strength changes during vortex translation.

4.   GRID REFINEMENT AND COMPUTATIONAL DOMAIN SIZE

4.1   Introduction

In the CFD vortex-structure simulations it is often assumed that the simulated vortex has similar parameters as those applied in the boundary conditions (Selvam & Millett, 2005; Liu & Marshall, 2004). It is convenient to use those values for the calculation of force and pressure coefficients. However, the dissipative effects are altering the vortex structure and its strength over the simulation. Those effects are strongly dependent on the computational grid quality and the computational domain dimensions. In this section several simulations are conducted to verify the influences of the domain and the mesh on the simulated vortex. In the simulations presented in this section there is no prism on the vortex path. The simulated vortex parameters are investigated.

In order to get reliable results using CFD simulation one needs to calibrate the model at first. Selvam and Millet (2005) showed that the grid resolution close to the structure influences the aerodynamic forces. The size of the computational domain also alters the simulated vortex (Liu & Marshall, 2004). This section investigates the influence of both the grid size and the domain size on the simulation of the travelling and interacting tornado. The grid and the domain size are also important, while paying attention on the computational time. Larger domains require more grid points, which extends the simulation time. Another issue is the memory storage. Simulations with a lot of grid points produce huge data files. For each grid point the CFD code outputs 11 variables (3 Cartesian coordinate components, 3 velocity components, pressure, resultant velocity, 3 vorticity components). The additional variables can be calculated during the post-processing (Appendix 1). For instance, if a numerical simulation consists of 4 million grid

69

points, a single output data file in a certain time step would be the size of about 1.1GB. The studied vortex-structure interaction is transient and at least few output files, at different time instants are needed. To create a video of the simulation, about 50 time steps are required. This makes the memory storage a considerable issue. The goal of the current chapter is to create grid and domain dimensions that provide converged results and optimize the computational time and the memory.

4.2   Computational Domain Size

The influence of each domain dimension on the simulated should be investigated separately. This enables one to obtain the most optimized domain size, with a reduced number of grid points. The nomenclature for the boundary walls of the computational domain is provided in Figure 4.1. For all of the simulations provided in this chapter the vortex parameters are the same as in Table 4.1. The simulation is carried out based on dimensionless values. During the post-processing stage these values can be converted into SI units using appropriate reference values.

70
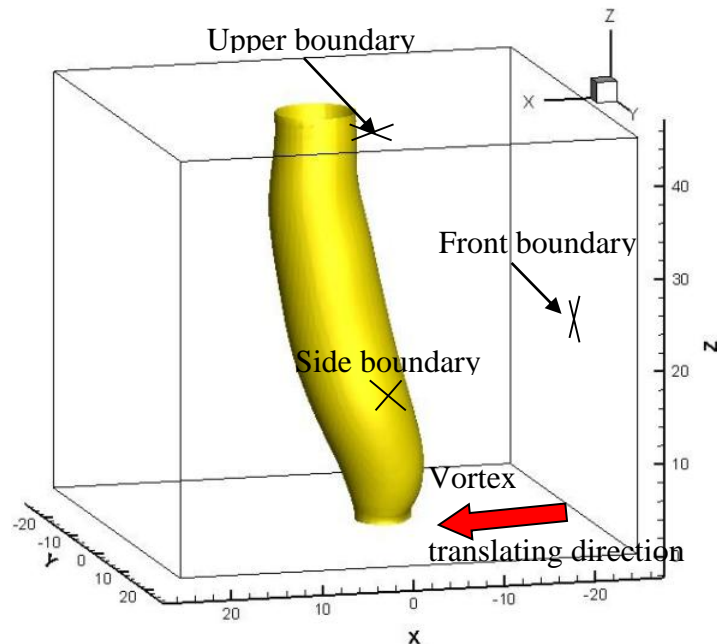
Figure 4.1 Nomenclature for the computational domain boundaries.

Table 4.1 Rankine vortex parameters and the ground roughness.

Units	α	r_{max}	u_{tran}	$u_{\theta,max}$	u_{max}	z_0
Dimensionless	1.0	3.0	1.0	3.0	4.0	0.00375
SI	1.0 (s^{-1})	36 m	12 ms^{-1}	36 ms^{-1}	48 ms^{-1}	0.045 m

▪ *Influence of side boundaries on vortex*

Three numerical simulations are conducted to check whether the lateral size of the computational domain affects the traveling Rankine vortex. All the remaining domain dimensions are kept constant. The domain parameters and grid size are included in Table 4.2. In each simulation the grid spacing is the same. In Table 4.2 the grid size is normalized to the radius of the vortex core.

Table 4.2 Computational domain dimensions for side boundaries sensitivity study.

GRID	Domain dimensions	Grid spacing (Δ/r_{max})	Total # of points
A	50.0 x 50.0 x 25.0		540,653
B	50.0 x 75.0 x 25.0	0.167	808,303
C	50.0 x 100.0 x 25.0		1,075,953

The vortex minimum pressure and the maximum resultant velocity over the simulation time are plotted in Figures 4.2 and 4.3, respectively. It is noticed that the simulated vortex exhibits similar characteristics in three domains. Thus, the assumed domain width of 50 units ($16.7 \cdot r_{max}$) is enough to prevent influencing the vortex characteristics. The difference in the minimum pressure drop between the simulations is at most 3%. The same is true with the maximum velocities. This means that the side boundary can be kept about $8 \cdot r_{max}$ away from the Rankine vortex center.

71
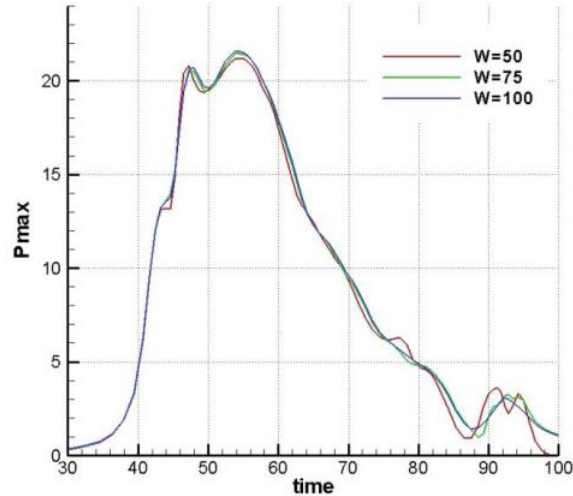
Figure 4.2 Maximum absolute value of the pressure drop for different widths of the domain.
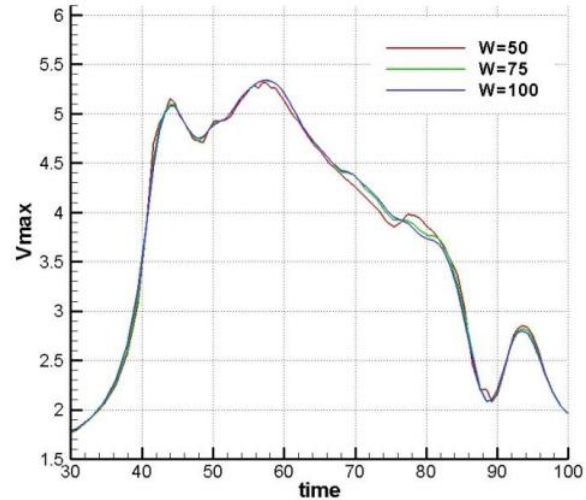
Figure 4.3 Maximum velocity of the vortex for different widths of the domain.

- *Influence of upper boundary on vortex*

The importance of the computational domain height on the CFD vortex simulation was noticed by Liu and Marshall (2004), in the blade-vortex interaction (BVI) study. They concluded that the height should be at least 2 times the blade chord. This was based on the force coefficients calculated on the blade. The Liu and Marshall's (2004) rule relates the size of the domain with the size of the structure (blade). The author of the current work claims that the size of the domain should be rather related with the size of the simulated vortex. The influence of the computational domain height on the vortex is verified by three simulations: Grid A, D and E (Table 4.3).

Table 4.3 Computational domain dimensions for domain height sensitivity study.

GRID	Domain dimensions	Grid spacing Δ/r_{max}	h/r_{max}	Total # of nodes
A	50.0 x 50.0 x 25.0		9.33	540,653
D	50.0 x 50.0 x 45.0	0.167	15.0	948,693
E	50.0 x 50.0 x 70.0		23.3	1,458,743

72

In each simulation grid spacing is equal to 0.5 units ($\Delta/r_{max} = 0.167$) over the entire domain. Only the height dimension of the domain is changed in each simulation. In Figure 4.4 the maximum resultant velocity of the vortex flow against the simulation time is plotted for the three grids.
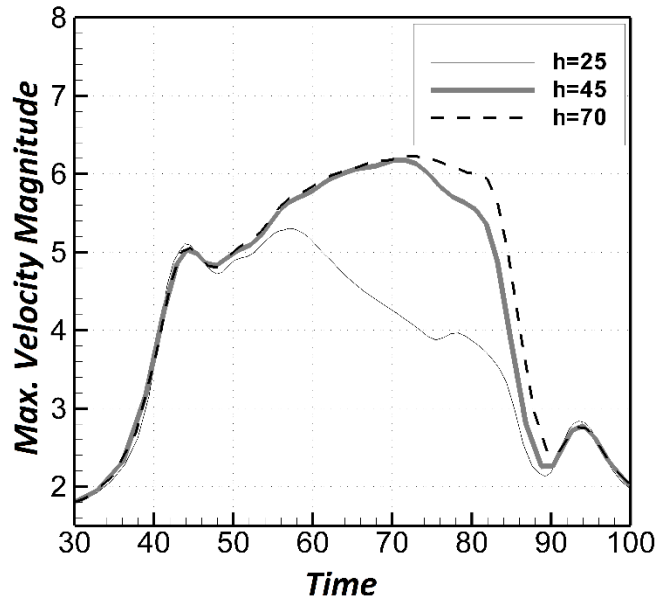
Figure 4.4 Maximum resultant velocity against simulation time for different computational domain heights.

The vortex enters the domain at about t=40 units and leaves at t=90 units. It is noticed that until t=55 units the maximum fluid velocity is similar for all three domains. From this instant, the vortex in the smallest domain (h=25 units) starts to weaken. The maximum fluid velocity is not preserved over the travel, which excludes this grid from the further considerations. For Grid D (h=45 units) and E (h=70 units) the maximum flow velocity is very similar over the entire simulation time. The maximum velocity magnitude reaches about 6.2 units, at t=72 units. This is greater than the initially defined maximum horizontal fluid velocity, u_{max}=4.0 units (Table 4.1). The difference is mainly caused by the vertical velocity component. In the RCV model the vertical velocity component is equal to 0; however, the axial flow is created by the self-induced

73

conditions. The similar effect was also observed by Filiponne and Afgan (2008). The comparison between the defined vortex parameters and the retrieved from the CFD simulations are included in Table 4.4. For each grid the maximum tangential velocity and the radius of the maximum fluid velocity are reported when the vortex is located at about the origin of the domain. The location of the simulated vortex is determined from the simulation time. The tangential velocities are captured along x-axis to clear out the free stream components. The tangential velocity profile of Grid D the most closely resembles the specified Rankine vortex parameters (Table 4.4). The radius of the vortex core is 9% thinner than the defined in the boundary conditions. The vortex maximum tangential velocity is greater by 6% than the defined one. The highest domain generated (Grid E) generated the vortex that is 12% thinner than the assumed RCVM.

Table 4.4. Summary of the computational domain height dependence simulations.

Grid	h/r_{max}	# nodes	r_{sim}/r_{max}	$u_{\theta,max}$
A	9.3	540,653	1.15	2.41
D	15	948,693	0.91	3.19
E	23.3	1,458,743	0.88	3.42

4.3 Grid Refinement

- *Grid refinement close to the structure*

Selvam and Millett (2005) studied grid refinements near cubic building wall faces. They found that it has significant influence on the tornado forces on a building. The more they refined the grid the greater tornado forces they obtained. They suggested that the finest grid spacing, close to the structure, should be at least 0.005H, where H is a dimension of a cubic building. Selvam and Millett (2002; 2003) refined their grid mostly around the building (Figure 4.5). The grid spacing increases exponentially away from the cubic building walls. Near the building the grid is very

fine. Due to the fluid flow around the building faces, the boundary layer is created close to the structural walls. In this layer the flow is highly turbulent, which results in the generation of eddies of various sizes. To capture that effect using the large eddy simulation turbulence model (LES), very fine grid is required. In the current study Selvam and Millett (2005) findings are applied for vortex-structure interaction problems.
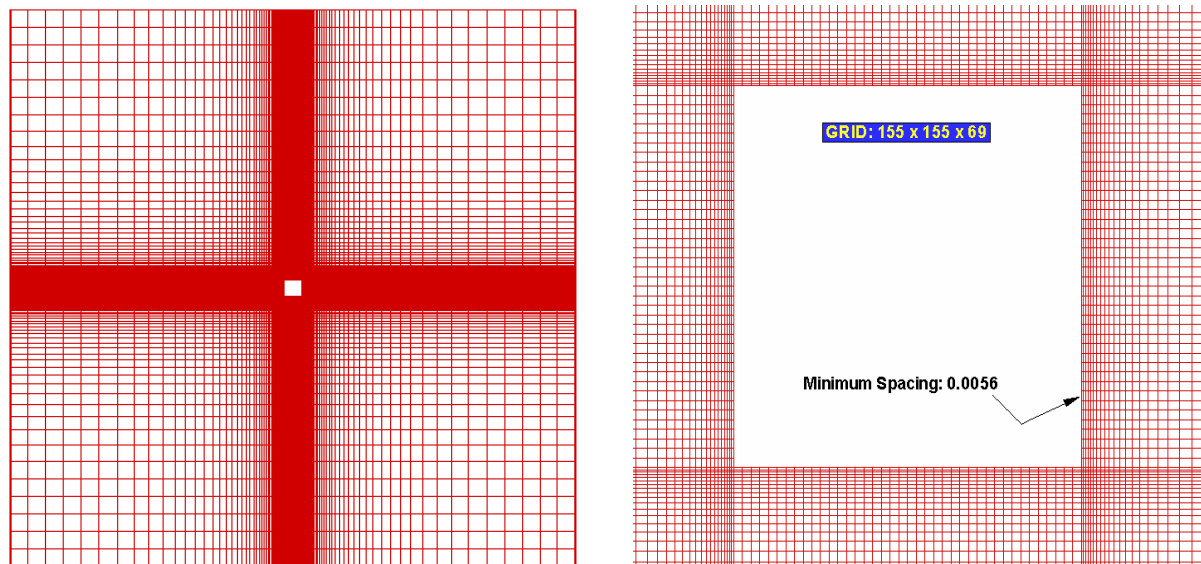
Figure 4.5 Grid refinement in domain and around a cubic building (left – plan view, right – close-up view), (Selvam & Millett, 2003).

- *Grid refinement in the computational domain*

In the literature there is no investigation as to how the grid in the domain influences the strength of the simulated vortex. In the previous studies (Selvam & Millett, 2003; Alrasheedi & Selvam, 2011) the grid in the whole domain was generally coarse and fine only close to the building (Figure 4.5). However, no attention was paid to what happens to the vortex while it approaches the structure. The problem – whether the applied grid is able to maintain the consistent parameters of the vortex – has never been analyzed. The grid size dependence on the simulated vortex is verified by simulations D, F and G (Table 4.5). Each mesh is equally spaced in the

entire domain. The grid size and the vortex core size are related by the ratio Δ/r_{max}. The finest

grid includes 24 points across the vortex core. Further refinement of the grid was limited by the

computational resources.

Table 4.5 Mesh properties and results for grid size influence study.

GRID	Domain size	Grid spacing Δ/r_{max}	Grid points	r_{sim}/r_{max}	$u_{\theta,max}$
F	50.0 x 50.0 x 45.0	0.333	127,449	1.23	2.74
D	50.0 x 50.0 x 45.0	0.167	948,693	0.91	3.19
G	50.0 x 50.0 x 45.0	0.083	6,019,749	0.97	3.04

The finest grid (Grid G) produces the most accurate vortex parameters. The maximum tangential

velocity is about 1% greater than the assumed. The simulated vortex core is 3% thinner than the

assumed RCV model.

Figure 4.6 illustrates the tangential velocity distribution of the simulated vortex when the swirl is

at about the origin of the domain. While the forced vortex core region looks fine for all the

simulations, all the grids failed to properly represent the free vortex region decay. The velocities

outside the vortex core are greater than the in the RCVM. The decay coefficients are less than

1.0 which is similar to the observations made on actual tornadoes (Figure 2.10).
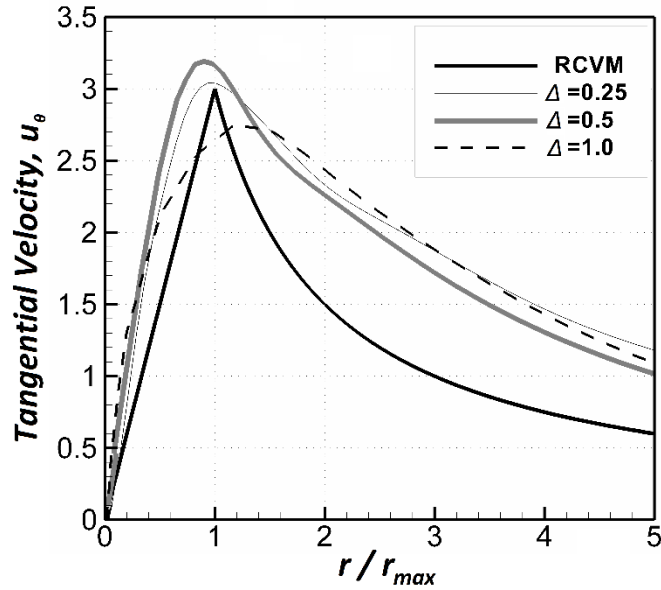
Figure 4.6 Tangential velocity distribution for different grid sizes.

Figure 4.7 presents the vertical velocity distribution across the vortex, for the three grids.

Although, the vertical velocity is not modelled by the Rankine vortex model, the self-induced

conditions created the vortex axial flow. This effect is not controlled and requires a separate

study. For Grid G the vertical velocity reaches almost 2 units on the vortex core radius. In the

vortex centre the axial velocity is negative, which means there is a fluid downdraft.

77
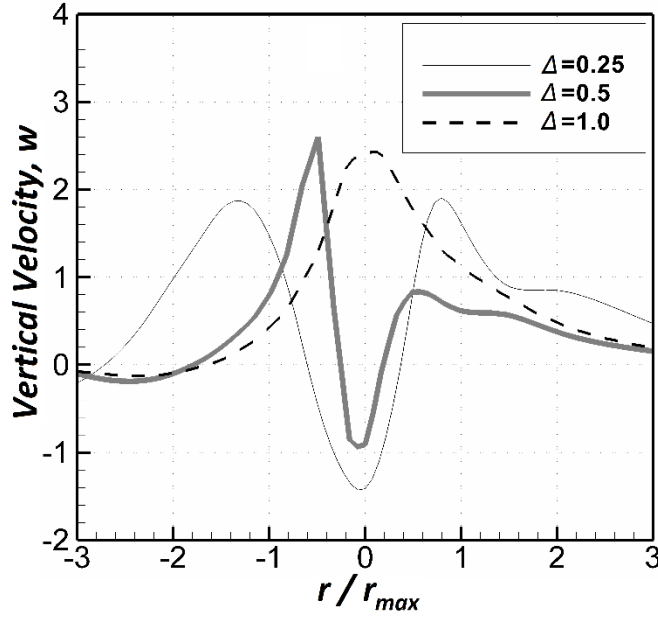
Figure 4.7 Vertical velocity distribution for different grid sizes.

In Figure 4.8 the maximum horizontal velocity in the computational domain against the time is

presented for three grids. The velocity is normalized to the assumed maximum tangential

velocity (4.0 units).
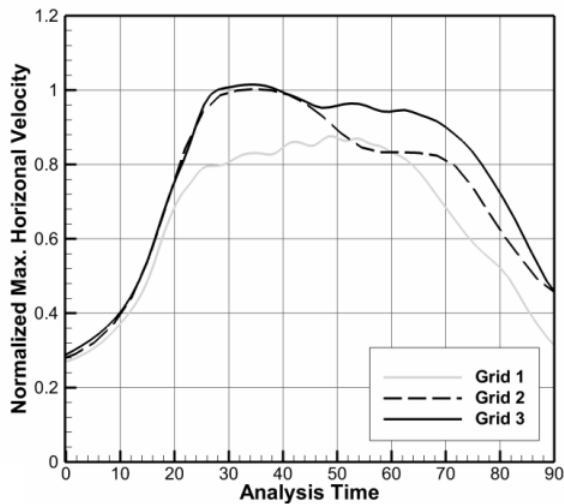
Figure 4.8 Normalized maximum horizontal
velocity over simulation time.
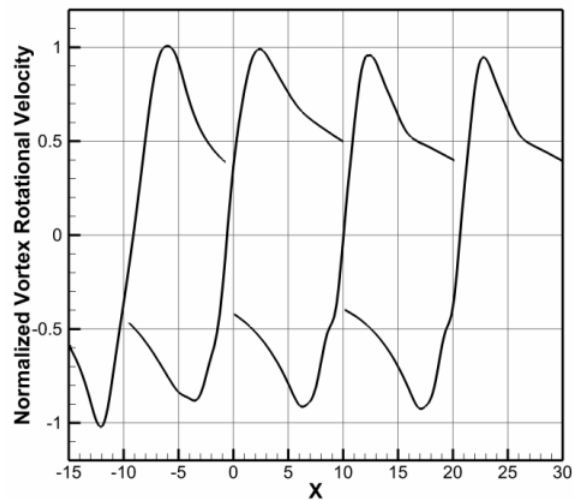
Figure 4.9 Normalized tangential velocity
distribution at four time instants for Grid G.

Initially, the Rankine vortex is out of the computational domain. The entrance of the vortex to the domain is indicated by the sudden increase in the flow velocity. The vortex leaves the domain, when the velocities are suddenly decreasing. Figure 4.8 shows that Grid G provides the most stable maximum wind velocity during the simulation time. The maximum velocities are within about 10% of the assumed value during the vortex travel. In the case of coarse Grid G the fluid velocity reaches lower maximum values than assumed on the boundary. Grid D exhibits substantial decrease in the maximum velocities during the vortex travel. Figure 4.9 presents the vortex tangential velocity at four different time instants for Grid G. The vortex velocity was measured in the perpendicular to the free stream flow direction. The velocities are normalized to the assumed vortex rotational velocity (3.0 units, Table 4.1). Here, it is shown that the vortex maintains the RCVM structure over the travel. The difference is that the simulated vortex has smoother transition from the forced vortex region to the free vortex region. The vortex core diameter is decreased by about 7% at the end of the simulation.

- *Grid refinement on the vortex path*

In the Rankine vortex model the highest gradient of the tangential velocity is located in the vicinity of the vortex core diameter. Away from the vortex core the flow velocity is smoothly decreasing and the velocity gradient is relatively low. Grids H and I (Figures 4.10 and 4.11) are studied to verify whether the fine grid is required in the entire domain or just on the vortex path. The results (Table 4.6) show that the differences in the vortex parameters for Grids G, H and I are within about 5%. This means that the fine grid is required only on the $6 \cdot r_{max}$ wide lane on the vortex path (Figure 4.11). The application of Grid I reduced the total number of grid points by about 32% compared to the Grid G.

79

Table 4.6 Grid parameters and results for different Rankine vortex path refinement

GRID	Range of fine grid (0.25) in y-direction	Grid points	r_{sim}/r_{max}	$u_{\theta,max}$
G	All domain	6,019,749	0.97	3.04
H	$10 \cdot r_{max}$	4,821,789	0.96	3.11
I	$6 \cdot r_{max}$	4,103,013	1.02	2.90
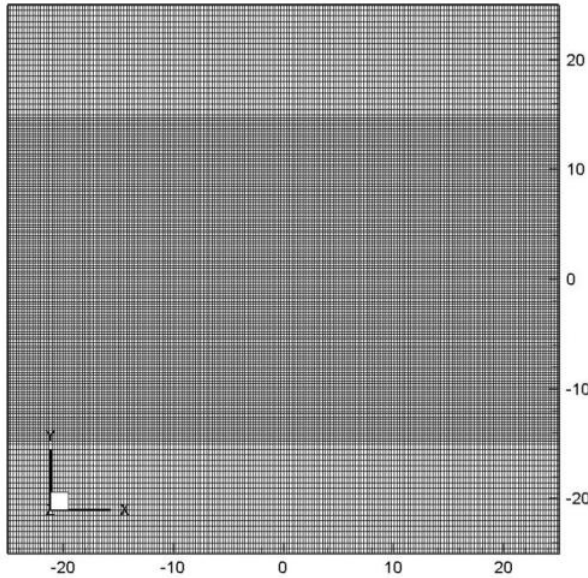
Figure 4.10 Grid H refinement in any *xy*-plane.
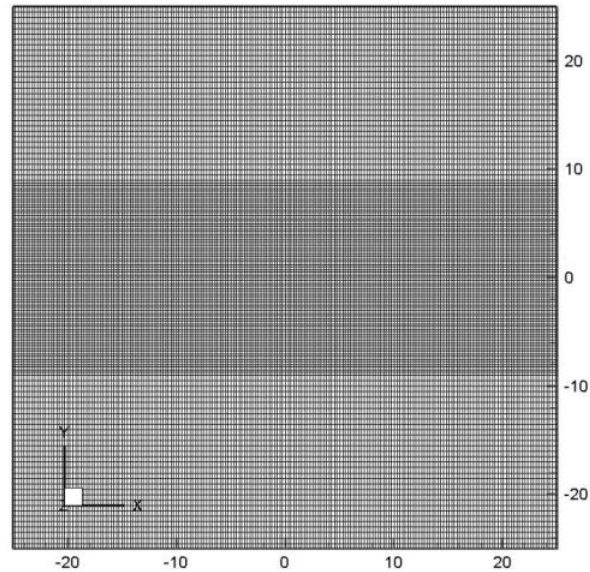
Figure 4.11 Grid I refinement in any *xy*-plane.

4.4   Conclusion

The CFD simulation of a translating Rankine vortex was found to be dependent on the grid resolution and the computer domain size. The size of the computational domain was investigated for the optimal dimensions of the side boundaries and the upper boundary. The side boundaries can be kept about $8 \cdot r_{max}$ away from the Rankine vortex travelling path. The proper definition of the height of upper boundary is required to maintain the vortex strength and shape during its travel. It was found that the height of the domain has to be at least 15 times greater that the vortex core radius (r_{max}) to maintain the vortex maximum velocities.

The computational mesh sensitivity investigations were conducted to assure numerical convergence of the computed results. Grid resolution study showed that the grid spacing influences the velocity distribution in the simulated vortex. Too coarse mesh around the vortex core produces a weaker vortex. Fine grid is desired around the Rankine vortex core region, which is determined by radius r_{max}. In this region there are high gradients of pressures and velocities. It was demonstrated that there should be at least 24 nodes across the vortex core diameter. The total number of grid points in the domain can be reduced by applying fine mesh only on the $6 \cdot r_{max}$ path of the vortex travel, where the high velocity gradients exist. This reduces the total number of the nodes by more than 30%.

5.   VORTEX-PRISM INTERACTION

5.1   Introduction

The idea of the tornado-like vortex interaction with large rigid structures was first introduced by Alrasheedi and Selvam (2011). They studied forces on large low-rise buildings. Through the analysis of the aerodynamic force coefficients they concluded that a travelling vortex causes lower overall force coefficients on larger buildings. However, they did not provide any explanation for this effect. Selvam and Ragan (2012) studied the interaction of a Rankine vortex and a wide rectangular prism. They noticed differences between the vortex-prism interaction and the vortex-building interaction, simulated by Selvam and Millett (2005) . The prism was wide enough, so that the tornado-like vortex was unable to surround it during the travel. Because of that the rectangular prism exhibited sheltering abilities behind the prism. Selvam and Gorecki (2012b) showed that on the leeward region of the prism the wind speeds were significantly reduced, creating a tornado-protected area. The current chapter follows these findings and extends the current knowledge of tornado-like wind interaction with large man-mad structures.

The prism is modeled as a rectangular-shaped rigid block. At first an interaction of a Rankine vortex with a reference prism is carefully investigated. This is conducted to reveal all the features of the vortex-prism interaction. Various visualization techniques are applied and the major attention is paid on the flow speeds around the prism. The vortex sheltering abilities of the reference prism are calculated based on the resultant velocities of the flow. Following these findings, the prism dimensions and vortex dimensions are varied to study their influence on the sheltering performance of prisms. Also, the Rankine vortex strength and path during the interaction are investigated under different vortex-prism interactions.

5.2 Problem Geometry and Computational Model

5.2.1 Rankine Vortex Parameters

The vortex velocity field is modelled according to the Rankine vortex model. The vortex is characterized by three parameters: α – the vortex strength, r_{max}- the radius of the forced vortex region and u_{tran} – the translational velocity of the vortex. The vortex is advected, along x-axis, with the free stream flow. The translational velocity of the vortex is equal to the free stream velocity. The non-dimensional vortex parameters, and converted dimensional values, are reported in Table 5.1. The table also includes the ground roughness used in the simulations, which corresponds to the roughness of short grass.

Table 5.1 Rankine vortex parameters and the ground roughness.

Units	α	r_{max}	u_{tran}	$u_{\theta,max}$	u_{max}	z_0
Dimensionless	1.0	3.0	1.0	3.0	4.0	0.00375
SI	1.0 (s^{-1})	36 m	12 ms^{-1}	36 ms^{-1}	48 ms^{-1}	0.045 m
U.S.	1.0 (s^{-1})	118 ft.	26.8 mph	80.5 mph	107.4 mph	1.77 in.

The dimensions and the strength of the simulated vortex resemble the actual tornado studied by Kosiba et al. (2014). The simulated vortex is assumed to travel along x-axis with a translational velocity, u_{tran}, of 1.0 unit (12 m s^{-1}). This means that the centre of the vortex moves 1.0 x-distance unit (12 m) per 1.0 time unit (1 sec). The maximum tangential velocity, found on the vortex core radius, is equal to 3.0 units (36 m s^{-1}). The sum of the translational velocity and the maximum tangential velocity gives the maximum assumed horizontal flow speed.

At the beginning of the simulation the vortex is located out of the boundary to start and then the vortex slowly enters into the computational time. When the Rankine vortex is far away from the

83

prism, only the free stream flow is present in the computational domain. The total computational time of the simulation is 180 time units. According to the applied boundary conditions, the simulated vortex is supposed to be at the location of the leading face of the prism at time 90 units. This means that at t=0 the vortex-induced velocities around the prism are about 0.1 units, which is only about 3% of the vortex maximum tangential velocity. The vortex-based Reynolds number is:

$$\text{Re}_v = \frac{\Gamma}{v} = 5.7 \cdot 10^6 \tag{5.1}$$

Where the vortex circulation, Γ, is calculated according to Equation (3.5).

5.2.2   Computational Domain and Reference Prism Dimensions

The computational domain dimensions and the reference prism size are included in Table 5.2. The domain and the prism parameters are provided in dimensionless units, SI units and U.S. units. Figure 5.1 shows the computational domain. It also includes the reference prism.

Table 5.2. Reference prism size and computational domain size.

Units	Reference Prism			Computational Domain		
	$L\ (x)$	$W\ (y)$	$H\ (z)$	$l_D\ (x)$	$w_D\ (y)$	$h_D\ (z)$
Non-dimensional	3.0	36.0	3.0	69.0	60.0	48.0
SI	36 m	432 m	36 m	828 m	720 m	576 m
U. S.	118 ft.	1417 ft.	118 ft.	2716 ft.	2362 ft.	1890 ft.
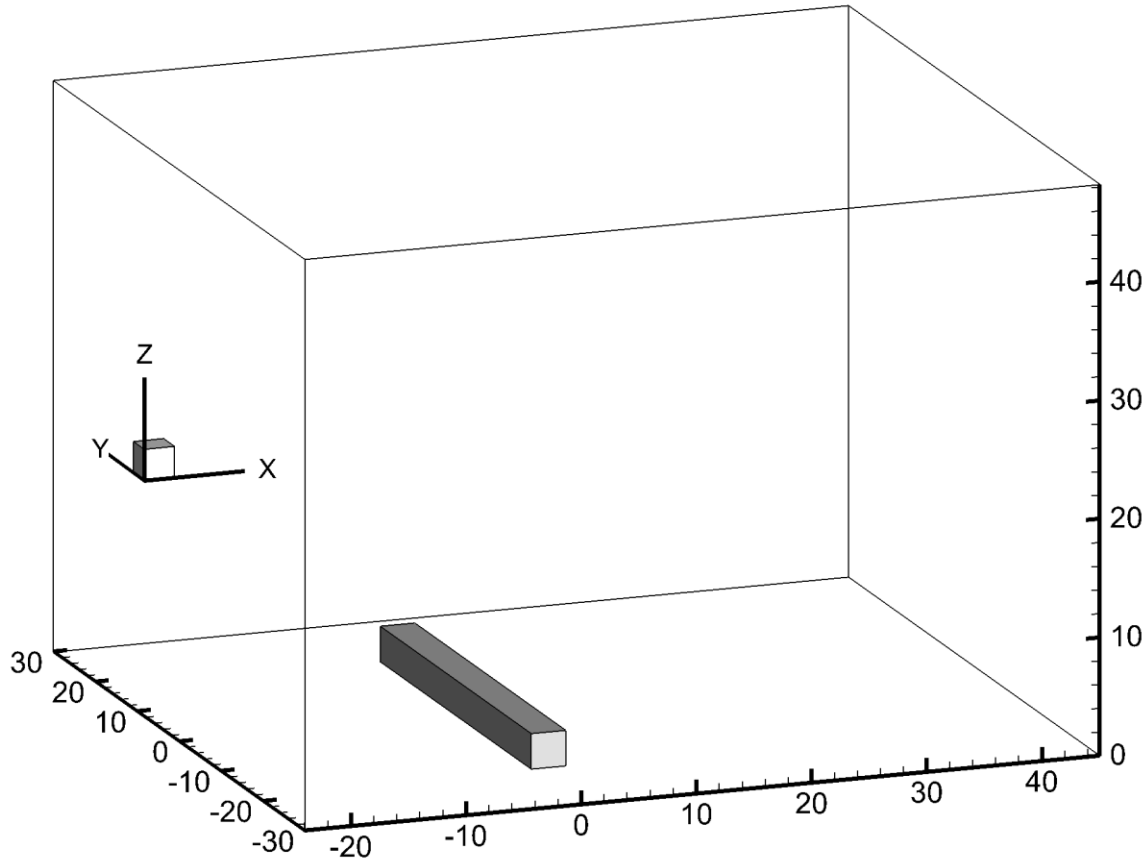
Figure 5.1 Isometric view of computational domain with reference prism.

The size of the computational domain is determined based on conclusions drawn in the *Computational Domain Size* section. All the domain dimensions are referred to the Rankine vortex core radius (r_{max}). The width of the domain (*y*-direction) is equal to 60 units ($20 \cdot r_{max}$), which is the same as assumed in the *Computational Domain Size* section. The height of the domain is 48 units ($16 \cdot r_{max}$). It is greater than $15 \cdot r_{max}$, which was demonstrated as a minimum domain height. The length of the domain depends on the simulation needs. In the vortex-prism simulation the distances before and behind the prism should be appropriately defined. It was shown that the vortex reaches its greatest intensity after traveling about $5 \cdot r_{max}$ distance units in the computational domain. Here it is assumed that the prism windward face is 24 units away from the inlet boundary ($8 \cdot r_{max}$). Behind the prism, there must be sufficient distance to analyze

the sheltering effect of the prism. It means that the domain size should allow the vortex to recover its strength and shape after the interaction with the prism. The domain length behind the prism is assumed to be about 45 units ($15 \cdot r_{max}$), which is based on trial simulations.

The dimensions of the reference prism are provided in Table 5.2. The pictorial description for the dimensions can be found in Figure 5.2.
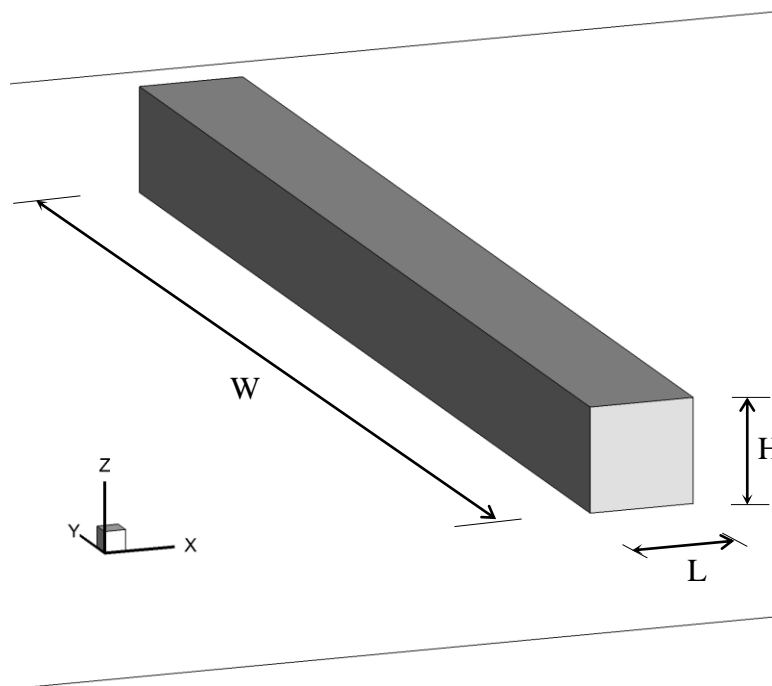
Figure 5.2 The nomenclature for the prism dimensions - close-up view.

The length (*L*) and the height (*H*) of the prism are assumed to be equal to the radius of the forced vortex region (r_{max}) – 3.0 units, or 36 meters. The choice of these dimensions was made on the basis of the conclusions from Alrasheedi and Selvam (2011). They noticed that when the size of the vortex is comparable with the size of the structure, the structure significantly influences the strength of a translating vortex. In this study the prism spreads almost across the entire domain. The width of the prism (W) is equal to 36 units ($12 \cdot r_{max}$), or 432 meters. Such a wide prism makes the interaction dependent only on two dimensions – the length and the height of the prism.

86

The Reynolds number based on the height of the prism and the maximum horizontal velocity is:

$Re=1.2 \cdot 10^6$.

5.2.3 Grid Refinement

The computational mesh is constructed following the conclusions from the *Grid Resolution*

section. The algorithm to prepare the grid is included in Appendix 3.Table 5.3 contains the grid

parameters. Figures 5.3 through 5.8 illustrate different views of the discretized domain.

Table 5.3 Grid resolution for the vortex-prism interaction.

Grid spacing on vortex path	Grid spacing outside vortex path	First grid spacing next to prism faces	Grid points (x, y, z-axis)	Total # of points
0.25	0.50	0.005	243x203x144	7,103,376
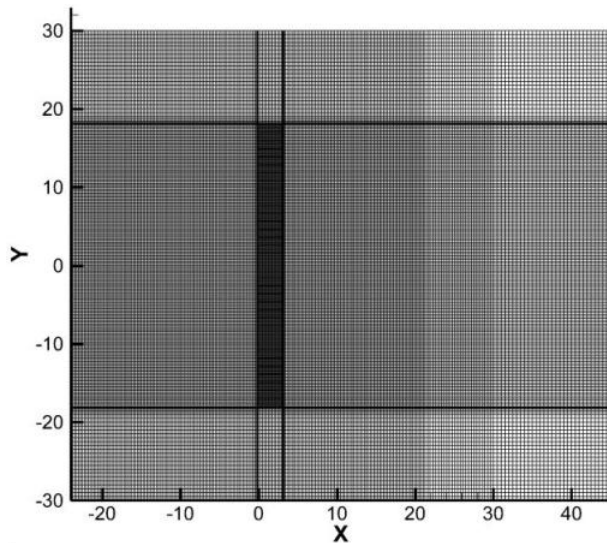
Figure 5.3 Grid resolution on the prism level: z=3.0, *xy*-plane.
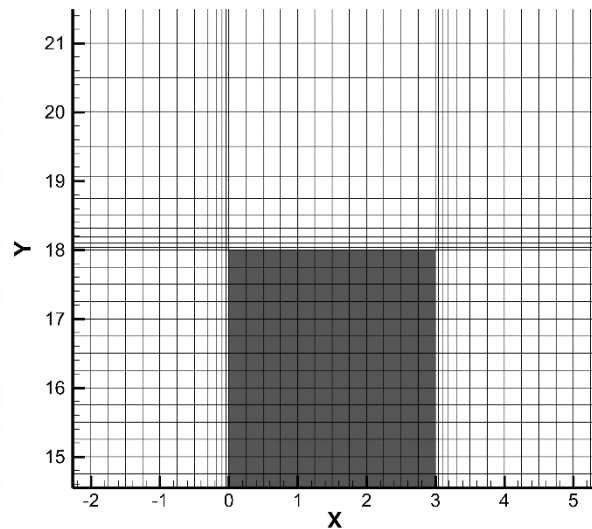
Figure 5.4 Grid resolution on the prism level: z=3.0, *xy*-plane. Close-up view.

87
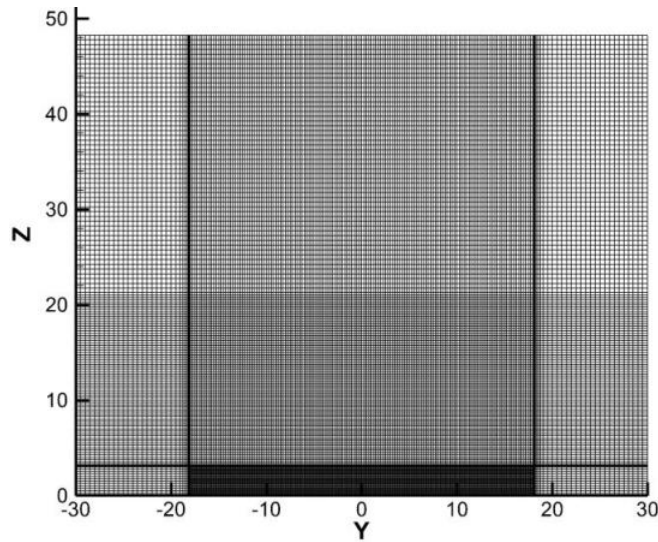
Figure 5.5 Grid resolution across the prism, x=0.0, yz-plane.
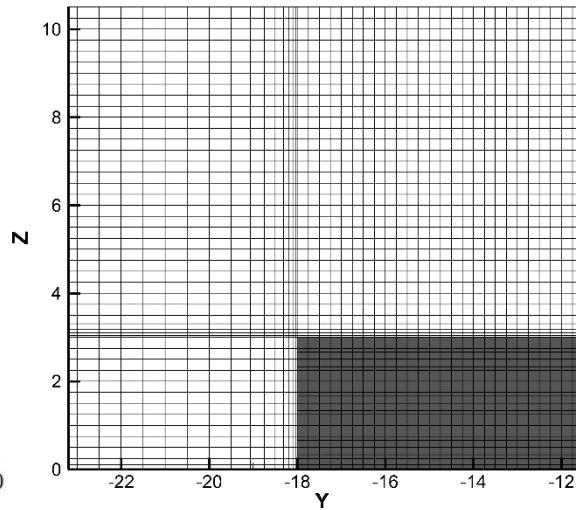
Figure 5.6 Grid resolution across the prism, x=0.0, yz-plane. Close-up view.
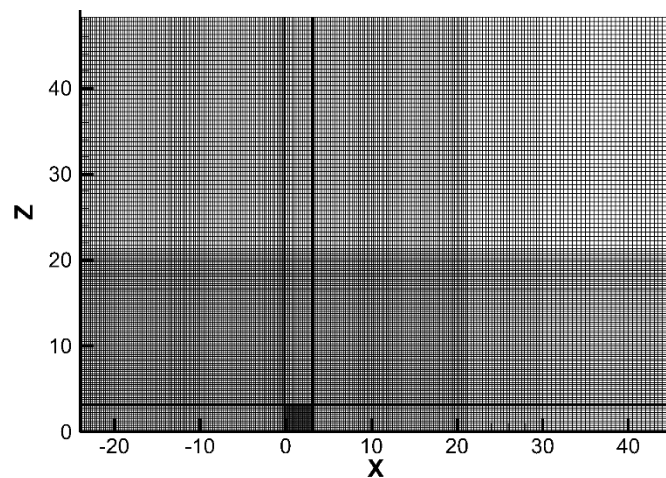
Figure 5.7 Grid resolution across the prism, y=0.0, xz-plane
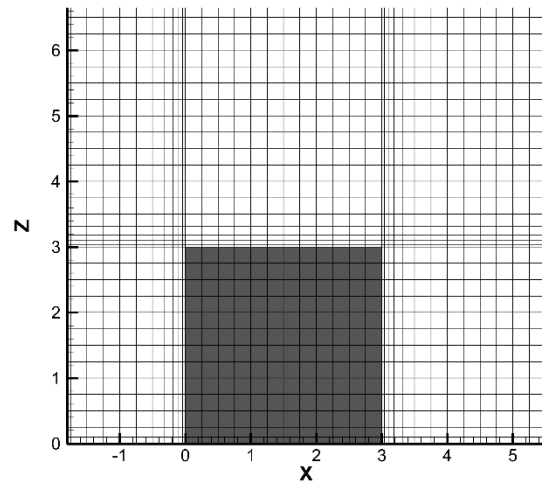
Figure 5.8 Grid resolution on the prism level, y=0.0, xz-plane. Close-up view.

In the xy-plane the grid is more refined on the Rankine vortex's path as is illustrated in Figures 5.3 and 5.4. The grid spacing there is equal to 0.25 units, which is 1/12 of r_{max}. The lane of refined mesh spread 36 units wide, which is 12·r_{max}. This width, as suggested in the *Grid Refinement* section, is sufficient to properly maintain the Rankine vortex structure. Outside the vortex path, the grid spacing in y-direction is equal to 0.5 units. Figure 5.4 shows the transition between the coarse and fine spacing. The grid is also coarse at the end of the domain, for x

88

greater than 28.0 units. In this region very fine grid is not necessary, since the vortex is leaving the domain there. It is assumed that before entering the coarse-grid region the vortex has recovered its structure. The computational grid in the *yz*-plane is presented in Figures 5.5 and 5.6 illustrates. The grid refinement in the *xz*-plane is illustrated in Figures 5.7 and 5.8. The grid in the *z*-direction has a spacing of 0.25 until the altitude of 21 units. Above 21 units the grid spacing starts to increase and attains 0.5 units in the upper portion of the domain. The boundary layer on the prism faces is resolved by the application of fine grid. For the applied computational model the influence of the grid resolution on the vortex-induced forces, was studied by Selvam and Millett (2005). They showed that tornado-wind forces converge when the first grid spacing next to the building is at least 0.005D, where D is a dimension of the building. In the current study the first grid spacing next to the prism walls is equal to 0.005 units. On the ground boundary layer the logarithmic law is applied and such a fine grid is not required.

5.3   Interaction of Rankine Vortex with Reference Prism

The vortex is advected in the free stream direction (along x-axis) with a constant impact speed, u_{trans}, perpendicularly toward the prism. At the beginning of the simulation the center of the vortex circulation is assumed to be 90 units, in the streamwise direction, away of the prism leading face. This means that the vortex core starts the travel outside the domain and it is smoothly introduced inside of the domain using the prescribed boundary conditions and the initial conditions. The simulation begins with the free stream flow that slowly changes into the rotational flow, as the time goes. This reduces any anomalies created by the superposition of the vortex flow over the free stream flow. According to the assumed boundary conditions, the vertical axis of the vortex is supposed to meet the leading face of the prism at t=90 units.

The head-on interaction of the translating vortex with the rectangular-shaped prism is presented in Figures 5.9 (a-f). The figures include visualization, at four different time instants, of the isometric view and the yz-plane view of the computational domain. The vortex is visualized by the iso-surface of the negative pressure. The pressure drop is a result of the rotating flow, as described by the inviscid theory in *Section 3.3*.

90
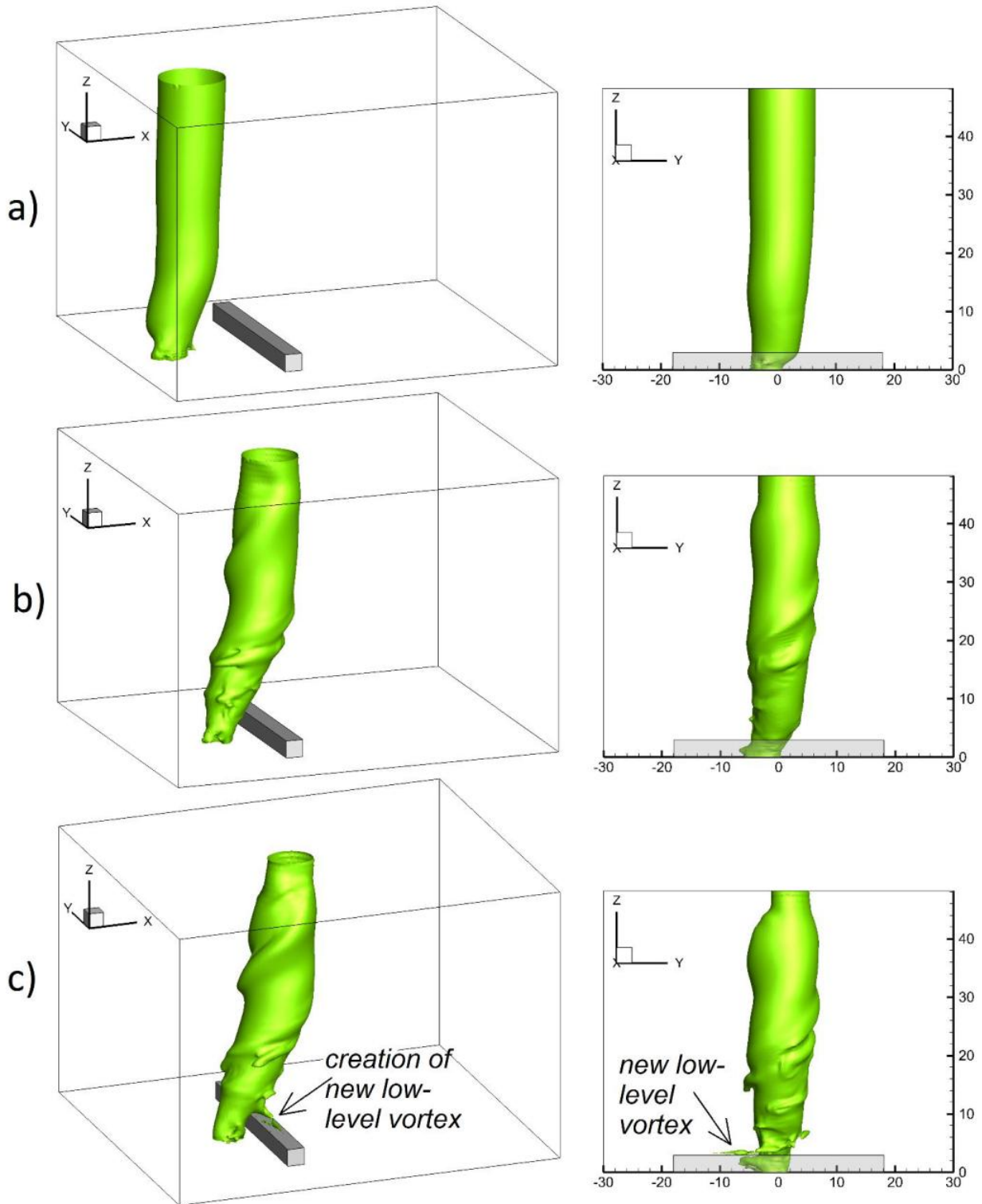
Figure 5.9 (a-c) Pressure iso-surface of Rankine vortex interaction with reference prism (P=-3.0): a) t= 75.2, b) t= 85.0, c) t= 87.3.
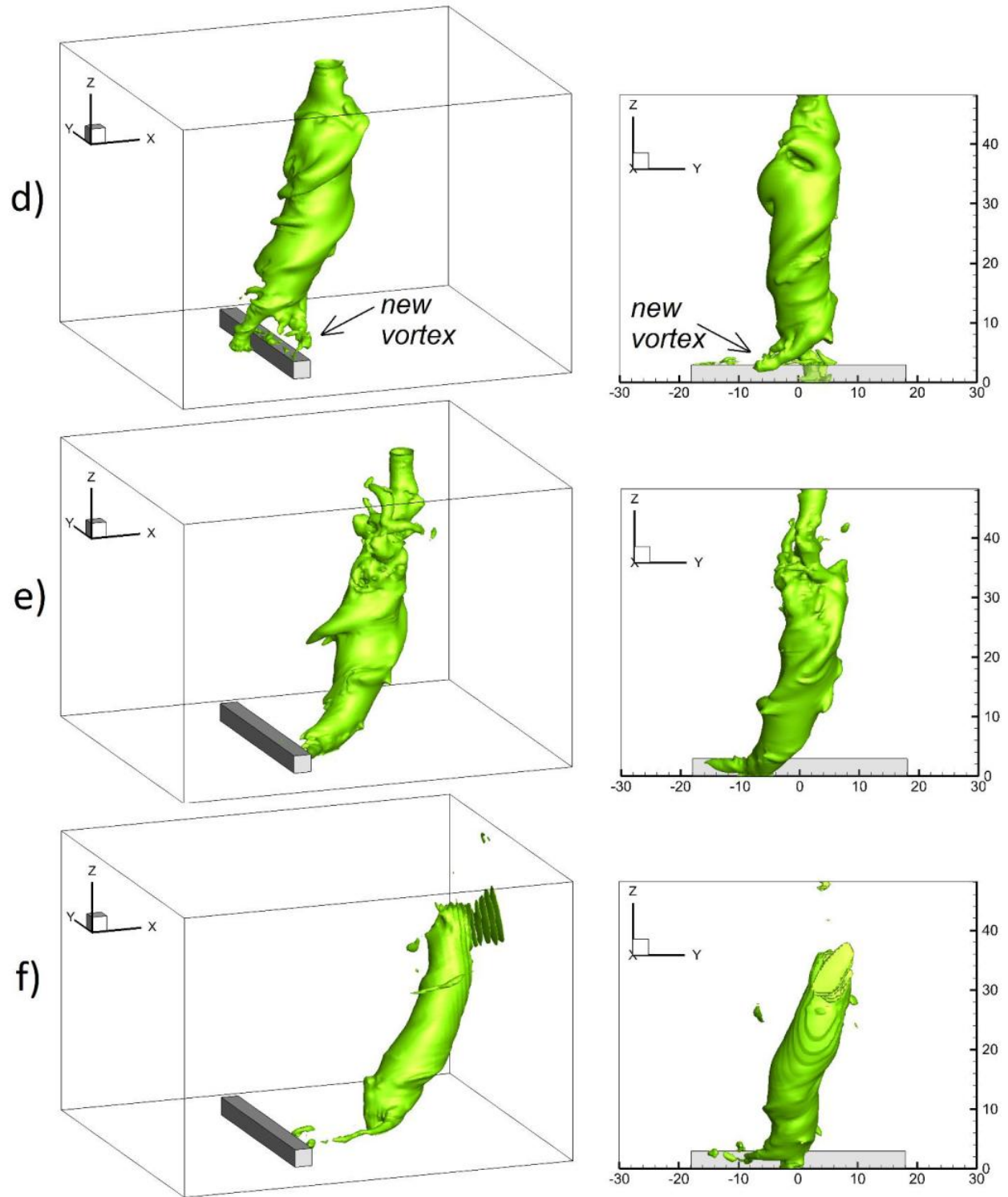
Figure 5.9 (d-f) Pressure iso-surface of Rankine vortex interaction with reference prism
(P=-3.0): d) t= 91.9, e) t= 101.2, f) t= 109.8.

In front of the prism (t= 75.2) the vortex exhibits a regular cylindrical shape (Figure 5.9a). The vortex is inclined in the streamwise direction. The streamwise vortex bending occurs because of both the surface roughness and presence of the prism, which blocks the rotating flow. The prism spreads wide across the domain and provides a rigid barrier for the low-level portion of the flow. As the vortex moves forward the pressure iso-surface is disturbed (t= 85.0), which means that the velocity field of the vortex is no longer axisymmetric. The prism is wide and high enough, so that the vortex cannot smoothly flow over it. The low-level portion of the columnar vortex is blocked by the leading face of the prism. The low-level part of the swirl starts to separate in order to transport the rotation behind the prism, as illustrated in Figure 5.9c. The yz-plane in Figure 5.9c shows that the blocked low-level vortex is displaced in the lateral direction. The displacement is governed by the inviscid effects, as explained by Affes and Conlisk (1993). The vortex is advected along the leading face of the prism in the cross-stream direction by the ambient velocity. The major vortex circulation is transported behind the prism by creating new vortices, formed from the main vortex (Figure 5.9d). At t= 101.2 the original low-level vortex dissipated since there was no circulation energy diffused into it. The vertical flow is now observed only on the leeward side of the prism (Figure 5.9e). The new low-level portion of the swirl circulates around horizontal direction, behind the prism. This rotation is originated from both the vortex shedding and the recirculation on the leeward, created due to the streamwise vortex-induced flow. As the vortex moves away from the prism, it straightens up and starts to recover its initial cylindrical shape (Figure 5.9f).

93

5.3.1 Vortex Bending and Lateral Displacement during Interaction

- *Vortex Bending*

During the interaction it is observed that the near-ground portion of the travelling vortex undergoes streamwise bending and lateral displacement. Similar observations were made by Krishnamoorthy et al. (1999) in the perpendicular vortex-cylinder interaction. They studied the vortex path deviations up to the face of the cylinder. They did not describe what happens when the vortex passes the wide structure. In Krishnamoorthy et al. (1999) simulation the vortex was fully immersed in the flow (no bottom wall boundary – as it is in the current study). They found that the path deviations are governed by the impact parameter ($I= 2\pi r_{max}u_{tran}/\Gamma$). The impact parameter describes the ratio of the vortex translational velocity to the maximum tangential velocity. In the case of the Rankine vortex the impact factor is: $I=u_{tran}/u_{\theta,max}$. Krishnamoorthy et al. (1999) found that the chordwise displacement (streamwise bending) is consistent and almost not influenced by the impact parameter. Only for very small impact parameters (0.027) the streamwise bending is not observed. For the reference prism simulation the impact parameter is equal to 0.33.

Figure 5.10 shows the xz-plane of the vortex at four different time instants. The vortex bending is observed to increase as the vortex is closer to the prism.
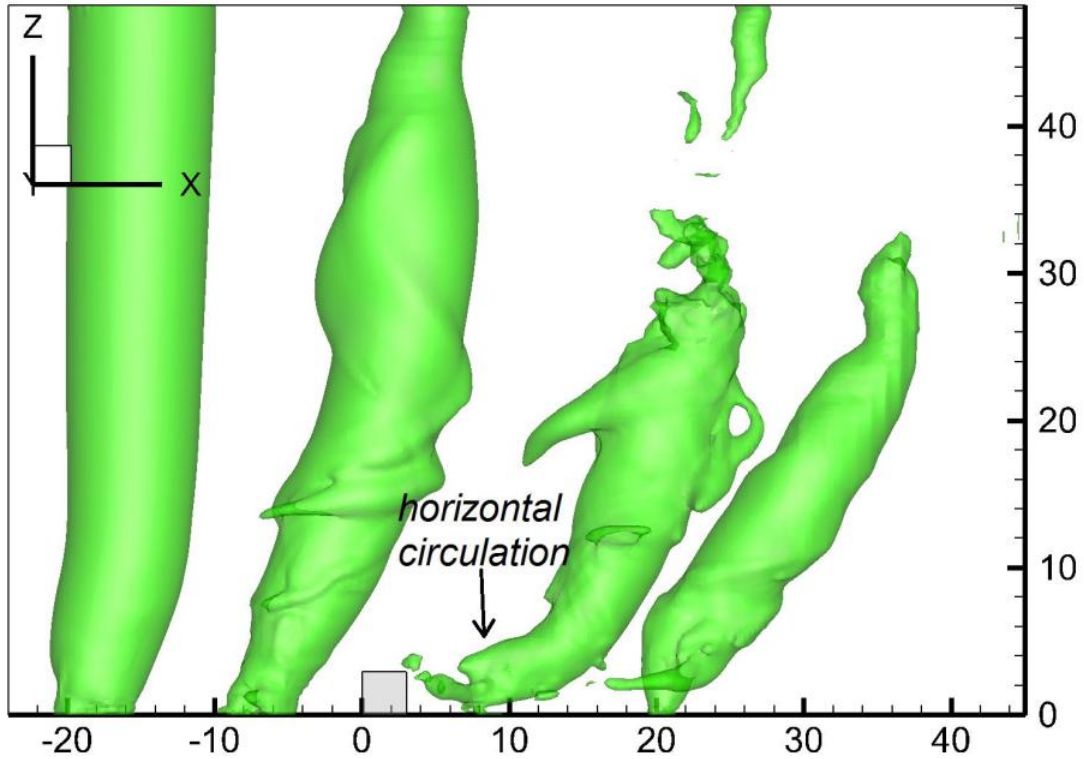
Figure 5.10 Pressure iso-surface of streamwise bending of Rankine vortex (P=-4.0): a) t= 71.7, b) t= 85.0, c) t= 101.2, d) t= 109.8.

When the vortex enters the computational domain it exhibits a columnar shape, at t=71.7. Only very close to the ground surface, the streamwise roughness drag is observed. As the vortex moves towards the prism the entire vortex column begins to tilt in the streamwise direction. The prism is high enough, so that the vortex is blocked by the leading wall. Also, the vortex cannot bypass the wide prism. Right before the vortex-prism interaction (t= 85.0) the upper portion of the vortex is about 10 units ahead from the near-ground portion of the vortex. During the interaction the stuck low-level vortex is detached from the main vortex and left in front of the prism. The main vortex creates, on the leeward side, a new low-level circulation. The new low-level vortex circulates in a horizontal plane (Figure 5.10). The vertical circulation in the lower-level portion of the vortex is retrieved after some distance away from the prism.

95

The streamwise vortex bending in vortex-prism interaction is different than the one observed in blade-vortex interaction. In BVI, the blade is much thinner and it is fully immersed in the flow. This helps in so-called vortex cutting effect, frequently observed in BVI.

- *Vortex Lateral Displacement*

Krishnamoorthy et al. (1999) also showed that a columnar vortex exhibits spanwise (lateral) displacement in front of a circular cylinder. The displacement occurred for a wide range of impact parameter. The magnitude of the lateral displacement of the vortex was strongly dependent of the impact parameter. Particularly, the lower the impact factor is, the greater the vortex displacement in the lateral direction, in front of the prism.

In order to visualize the Rankine vortex displacement in the current study, a new technique was utilized. The vortex core is indicated by the positive z-vorticity values. From all the time steps, in the xy-plane at the prism height level, maximum vorticity magnitudes were found in each grid point of the plane. Since the vortex has positive vorticity inside the core and zero vorticity outside the core (free vortex region), the created contour should present the vortex path during the entire interaction. The utilized method could be misleading very close to boundary walls since the shear rotation also holds high vorticity values. The consolidated z-vorticity contour is presented in Figure 5.11. For the visualization purposes the lowest z-vorticity values are cleaned out from the contour.
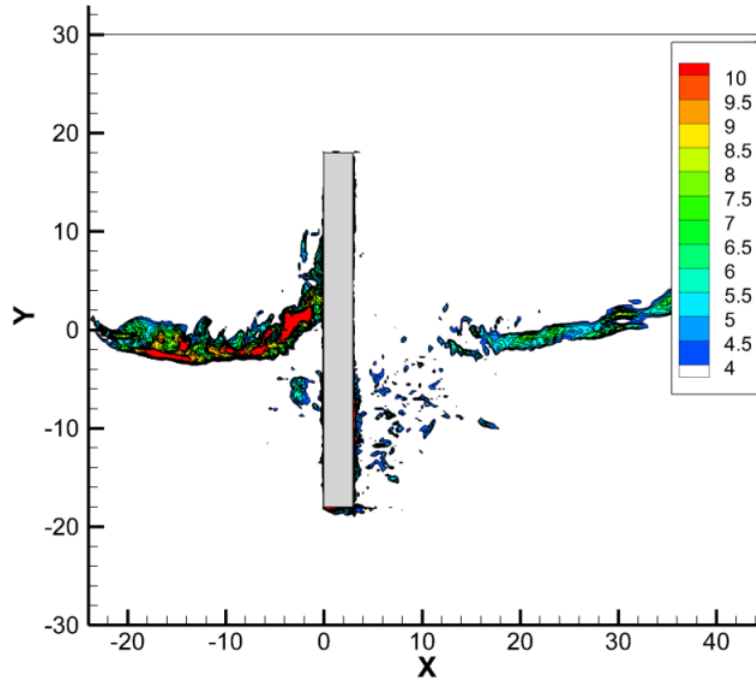
Figure 5.11 Consolidated z-vorticity xy-contour at z=3.0 units.

The simulated vortex clearly deviates from the assumed straight path. In front of the prism the vortex undergoes the lateral displacement in the positive y-direction. The displacement reached about 6 units ($2 \cdot r_{max}$). Right behind the prism, a region without vertical circulation is observed. The region length is about 9 units along x-direction. Further away from the prism, the vertical circulation is recovered and the vortex travels along a straight path. The recovered vorticity behind the prism has lower vorticity magnitudes than in front of the structure, which means that the vortex strength was mitigated by the interaction.

The path of the translating vortex can be also presented using pressure contour. In Figure 5.12 pressure at the ground surface of the domain and at the top of the prism are plotted. This idea was also utilized by Karstens (2012) to study the vortex path deviation in the tornado-like vortex-hill interaction.

97
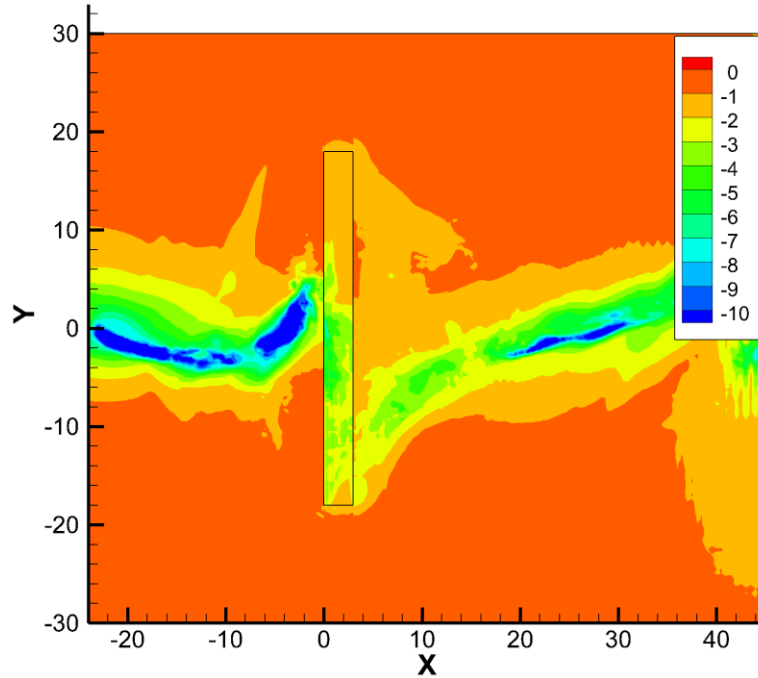
Figure 5.12 Consolidated pressure contour at the ground surface and at the top of the prism.

The pressure contour shows that behind the prism, where z-vorticity is low, some rotation exists. As was explained in previous section, right behind the prism the vortex has horizontal rotation. The horizontal rotation behind the prism is less in the strength, as illustrated in Figure 5.12.

5.3.2   Secondary Vorticity Ejection

To evaluate how the vortex strength and shape is altered during the interaction the vorticity around z-axis contours are analysed. Figures 5.13 (a-f) illustrate the xy-contours of the z-vorticity at six different time instants. The z-vorticity contours are retrieved right above the prism top wall to capture the prism boundary layer. In each contour the dotted line indicates the predefined path of the vortex.
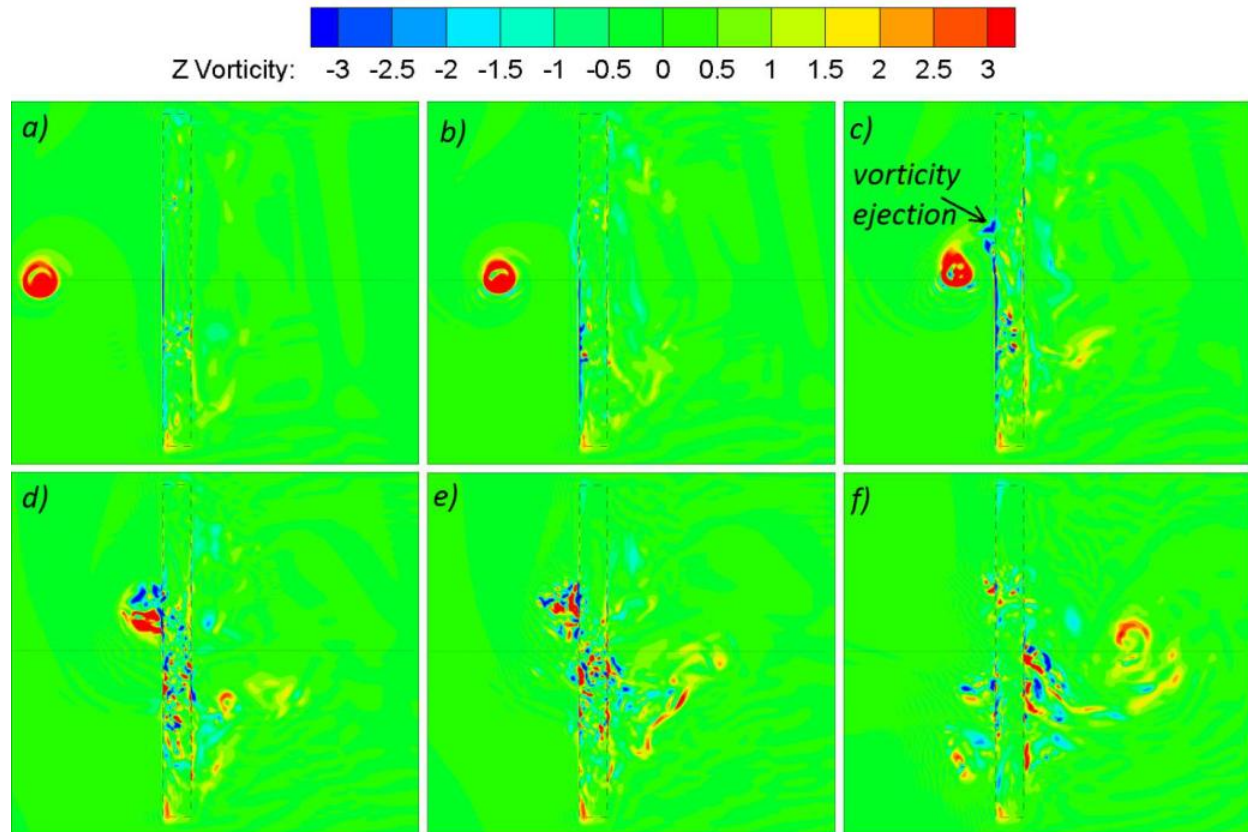
Figure 5.13 Z-vorticity contours right above the top of the prism for vortex-prism interaction: a) t= 75.2, b) t= 85.0, c) t= 87.3, d) t= 91.9, e) t= 101.2, f) t= 109.8.

The vortex approaches the prism on the straight path as illustrated in Figures 5.13a and 5.13b. When it is at about r_{max} distance from the prism the swirl starts to displace in the lateral direction (Figure 5.13c). At this time instant it is also observed that the main vortex is surrounded by the negative vorticity. This negative vorticity is ejected from the prism boundary layer and interacts with the swirl core, when the vortex is very close to the prism. The boundary-layer vorticity ejection occurs when the streamwise velocity around the prism reaches negative values. It means that the vorticity is ejected when the reversed rotational flow of the vortex exceeds the free stream velocity. The ejected negative vorticity mitigates the vortex strength and reduces its diameter. This effect was experimentally investigated by Krishnamoorthy et al. (1999). As the time goes the blocked vortex is subjected to more and more ejected vorticity. In Figures 5.13d

99

and 5.13e it is observed that the circular structure of the swirl is completely disrupted. The vortex core starts to recover its circular shape at $3 \cdot r_{max}$ distance behind the prism (Figure 5.13f). The flow around the prism is very turbulent during the interaction, which also impedes the vortex from immediate reestablishment of the circulation behind the prism.

5.3.3   Aerodynamic Forces on Prism

At the beginning of the simulation the vortex is out of the computational domain. The centre of the vortex is 90 distance units ($30 \cdot r_{max}$) away from the leading wall of the prism. According to the Rankine vortex model, the vortex-induced velocity 90 units away from the centre of rotation is equal to 0.1 units. This means that the initial flow field conditions consist of 1.0 unit free stream velocity perpendicular to the prism and 0.1 unit vortex-induced velocities parallel to the prism. As the vortex approaches the prism the vortex-induced velocity is increasing.

To calculate the overall forces on the prism at each time step pressures on the walls are integrated and mapped on each Cartesian direction. The aerodynamic force coefficient on the prism in x-direction, for the entire simulation, is plotted in Figure 5.14. For the calculation of force coefficient reference flow velocity is assumed to be 4.0. According to the boundary conditions the centre of the vortex core coincides with the prism at about 90 time units.

100
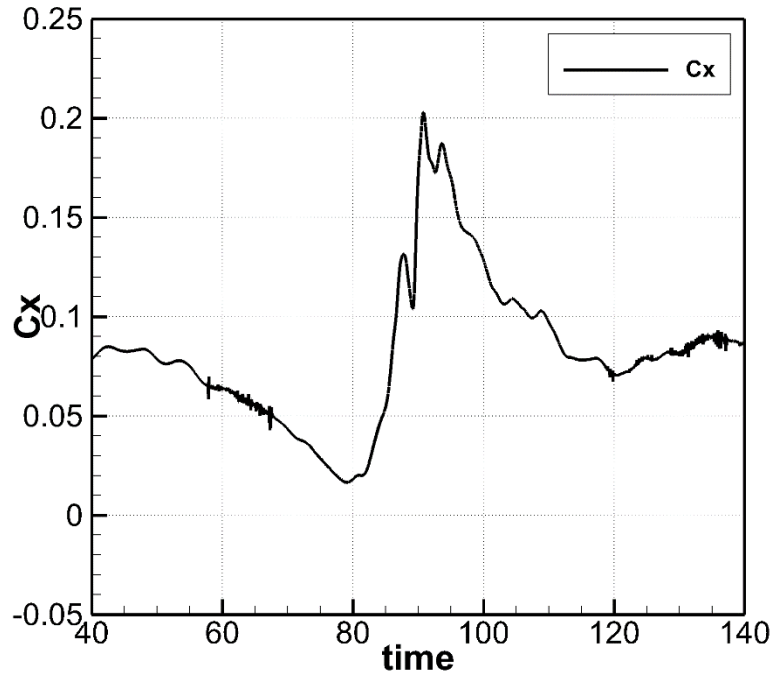
Figure 5.14 Force coefficient in x-direction against the simulation time.

The maximum force occurs at t= 90 units, at the assumed time lag. At the beginning of the simulation the force coefficient is equal to about 0.07 units, for the reference velocity equal to 4.0 units. However, the force coefficient should be calculated using the reference velocity equal to 1.0 unit, since when the vortex is far away from the prism only free stream flow occurs. In this case the force coefficient is equal to 1.12. This is very similar to the drag coefficient of a two-dimensional wall normal to the flow, reported by Holmes (2007). As the Rankine vortex approaches the prism the force is decreasing. The vortex induces lateral velocity components, parallel to the prism span. This changes the flow angle of attack and reduces the overall force coefficients. At about t=80 units the forces start to rapidly increase. At this instant, the vortex core is very close to the leading face of the prism and it induces high velocities directing perpendicular on the prism's windward face. The time instant of the maximum force is captured in Figures 5.15 and 5.16. Figure 5.15 presents pressures on the windward wall. Figure 5.16 presents pressures on the leeward wall of the prism.

101
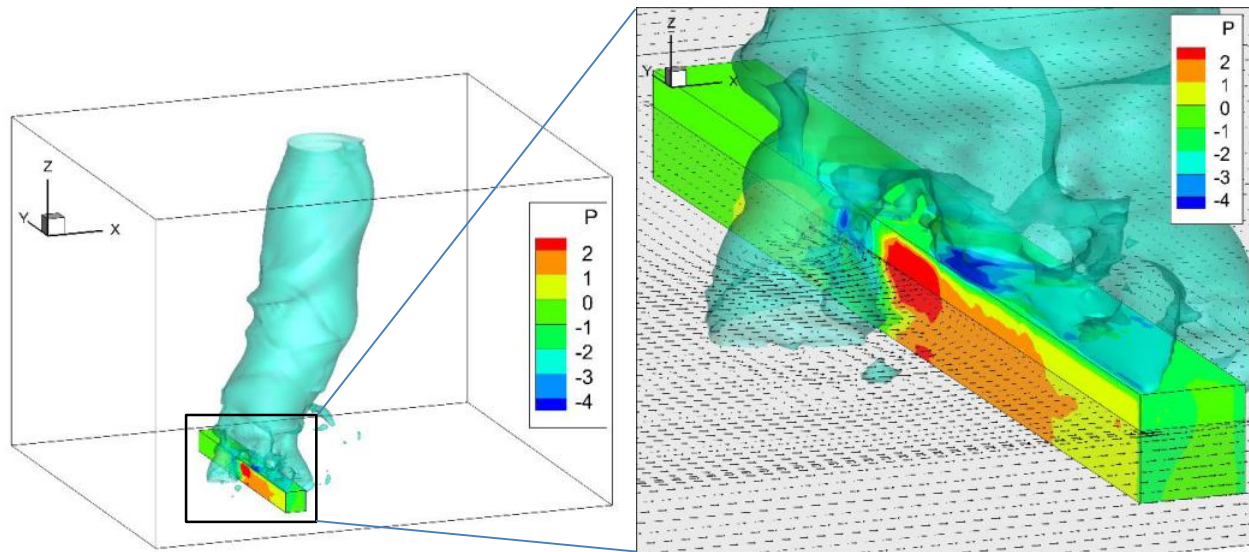
Figure 5.15 Zoom out and close-up views of pressures on windward prism (t= 90.6).
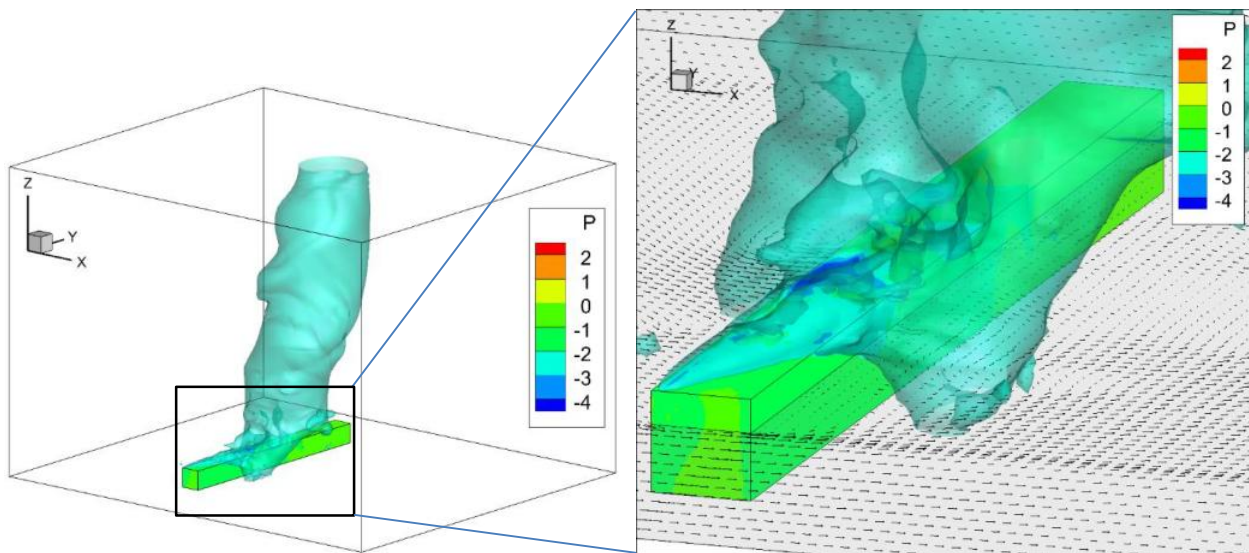
Figure 5.16 Zoom out and close-up views of pressures on leeward prism (t= 90.6).

On the windward wall (Figure 5.15) the vortex induces very high and localized aerodynamic force on the prism's wall. It is caused by the action of vortex core. The velocity vector field shows that the high vortex velocities, localized within the vortex core diameter, are directed perpendicularly to the windward wall. The wall is not evenly loaded, since the vortex rates in the counter clockwise direction, and the maximum flow speeds are acting only on one side of the prism. On the roof of the prism negative pressure is observed, which caused by the suction of the

102

vortex. The leeward wall is not subjected to the substantial aerodynamic loads (Figure 5.16). Right behind the prism, the vortex is unable to develop the circulation, since the prism blocks vortex inflow. Also, to create pressures on the leeward wall the vortex has to develop velocities in the reverse direction, against the free stream. According to the Rankine vortex model and the vortex parameters from Table 5.1 the maximum resultant velocity acting in the reverse direction is 2.0 units. It is twice as lower as the maximum velocity in the free stream direction. The high pressure magnitudes on the windward wall and on the ridge of the prism agree with the observations of the actual tornadoes impacting in complex terrain. Selvam and Ahmed (2013) noticed that there is not much tree damage on the leeward slope of a hill (Figure 2.19). Also, in Harrington and Newark (1986) it was observed that the tornado damage is only on the windward side and on the ridge of a hill (Figure 2.16).

The maximum force coefficients in the free stream direction and the vertical direction are presented in Table 5.4. The force coefficients are calculated using both free stream velocity and the maximum tangential flow velocity. For the horizontal force coefficient the windward wall is used as a projected area. For the vertical force coefficients the roof surface of the prism is assumed as the projected area. Table 5.4 also includes the overall maximum forces acting on the prism and maximum pressure coefficients, calculated according to Equations (A1.3-A1.6).

Table 5.4 Maximum absolute instantaneous forces during vortex-prism interaction.

Reference Velocity	C_x	F_x	C_z	F_z
Free stream (1.0)	3.25	21.12 kN	3.63	23.61 kN
Maximum tangential (4.0)	0.203		0.227	

103

5.3.4   Sheltering Effect

The presence of the prism on the vortex path greatly affects the near-ground velocity field. The low-level portion of the vortex is disrupted behind the prism and it recovers the full circulation only at some distance away from the prism (Figure 5.11). This creates a region, right behind the prism, where the flow speeds are reduced. To quantitatively measure the sheltering efficiency of the prism, the resultant velocities of the fluid are analysed. Studying the flow speeds is important, since flow velocities are responsible for creating aerodynamic forces on structures. The sheltering effect of rigid structures has been widely investigated to protect buildings (Li, Wang, & Bell, 2007), vehicles (Kozmar, Procino, Borsani, & Bartoli, 2012) or stockpiles (Lee & Park, 1998) from the straight-line winds. However, the sheltering effect has never been considered in terms of the vortical flows.

The sheltering efficiency of the prism is evaluated as a ratio between the maximum flow speeds behind the prism to the maximum vortex resultant velocities of no-prism simulation. To find the maximum flow speeds behind the prism a new visualization technique is utilized. The two-dimensional contour is built during the post-processing of the output data. In each grid point of the *xz*-contour the maximum resultant velocity is found from all *xz*-planes crossing the prism and from all of the time steps. Figure 5.17 presents a construction process of *xz*-contour with the maximum resultant velocities.
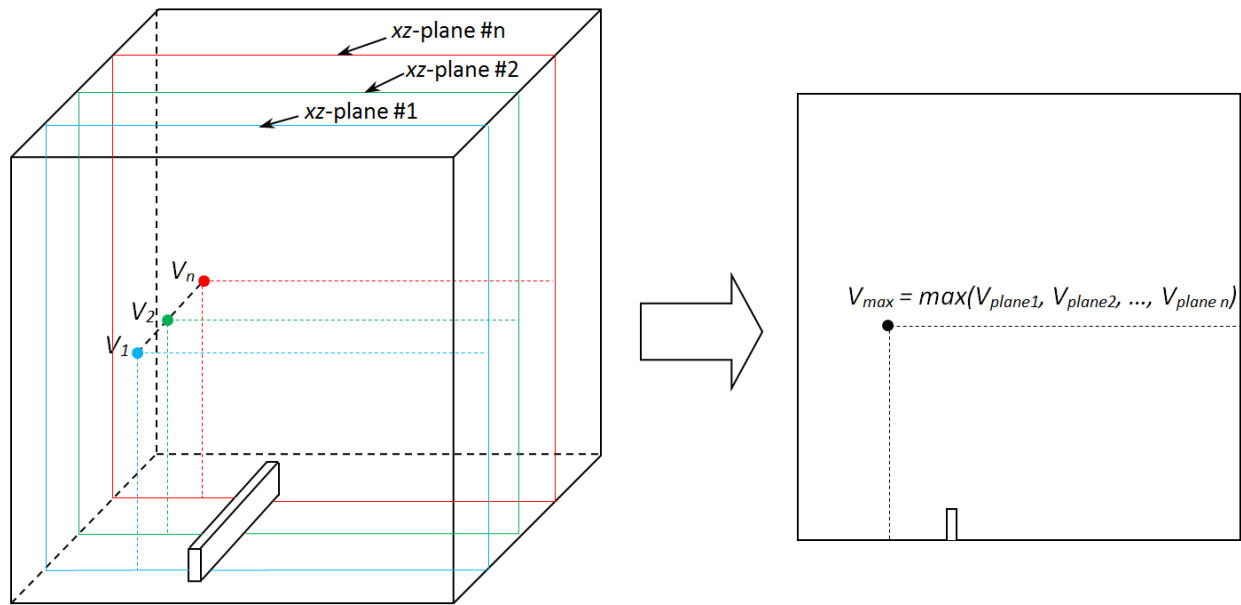
Figure 5.17 Construction of the maximum flow speed contour for prism sheltering effect.

Having such a contour it is possible to describe the distribution of the maximum flow speeds behind the prism regardless of time and the prism width. Figure 5.18 illustrates the dimensionless maximum flow velocities around the reference prism during the vortex-prism interaction. The velocities are normalized to the maximum flow speed in the no-prism case: 6.92 units (or 83.3 ms^{-1}). Figure 5.19 shows analogous maximum resultant velocity contour, but for xy-plane.
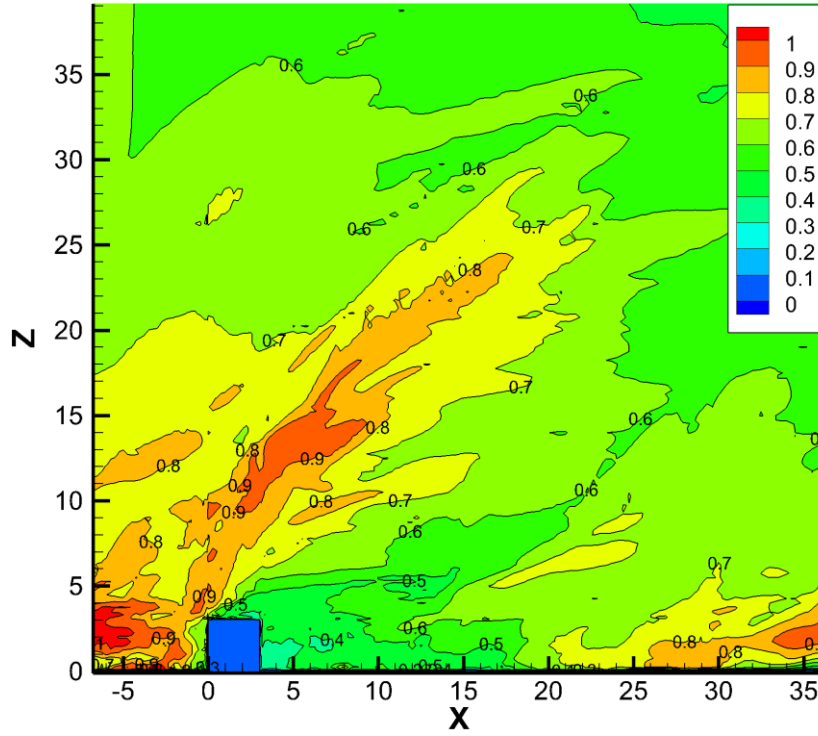
Figure 5.18 Normalized maximum resultant velocities around the reference prism in xz-plane.
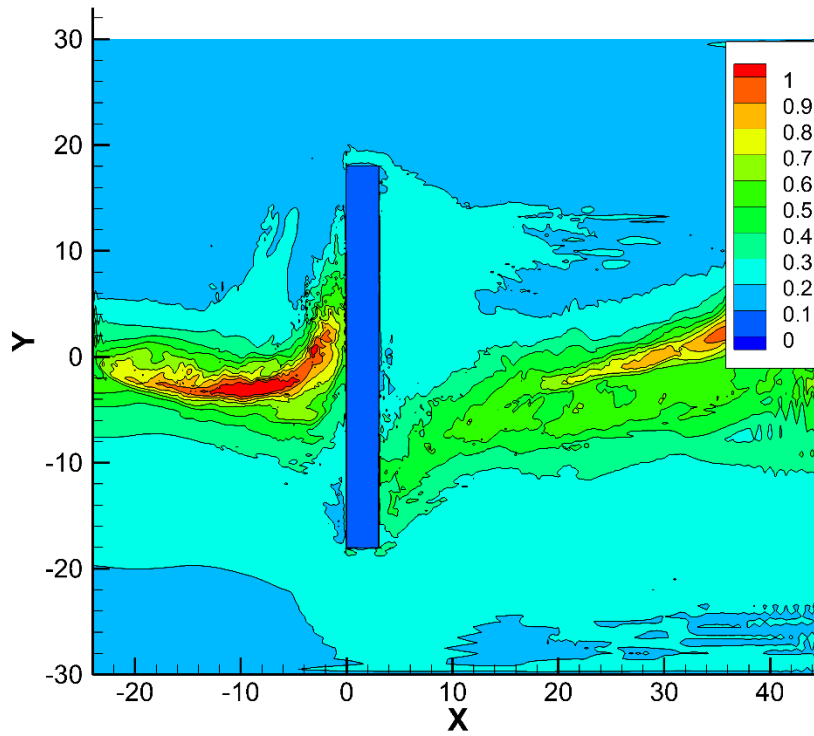
Figure 5.19 Normalized maximum resultant velocities around the reference prism in xy-plane.

In front of the prism the fluid velocities reach maximum values, while near the leeward wall of the prism the velocities are around two times less. The prism increases the maximum flow speeds near the leading face of the prism. This is correlated with blocking the vortex core by the windward wall. The vortex core is stuck in front of the prism and due to the bending and stretching of the cylindrical vortex (Figure 5.10) the vortex core is decreased. Because of the conservation of angular momentum the velocities of the shrunk vortex are increased. Behind the prism a sheltering region of relatively low velocities is left. Higher flow speeds are observed about 18 units ($6 \cdot r_{max}$) away from the leeward wall of the prism.

To more precisely investigate the flow speeds in the low-velocity zones, it is proposed to divide the area behind the prism into three sheltering regions (Figure 5.20). The dimensions of the regions are preliminary defined based on the resultant velocity contours in Figures 5.18 and 5.19. The length and the height of the sheltering regions are related to the height of the prism. The width of the sheltering regions is equal to the width of the prism. In the first sheltering region it is expected to have the lowest flow velocities, since it lies right behind the prism. The highest flow speeds are expected to in Region 3.
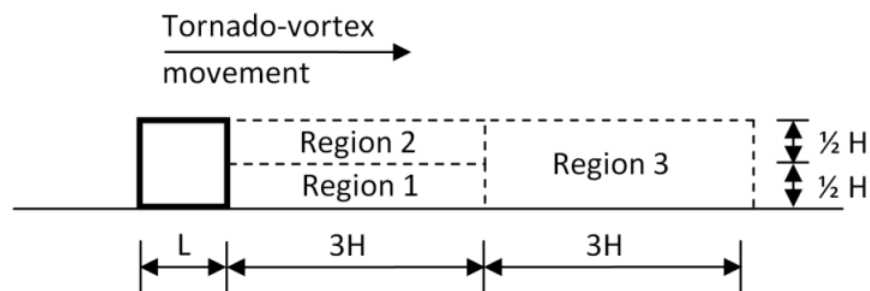
Figure 5.20 Division of the sheltering zone into three sheltering regions

In Table 5.5 the flow speed reduction in each of the sheltering regions are reported for the vortex interaction with the reference prism. The flow speed reduction is calculated as a ratio between

www.manaraa.com

the maximum resultant velocities found in a sheltering region to the maximum flow speeds for no-prism case (6.92 units or 83.3 ms^{-1}). The normalized maximum velocities found in the sheltering regions against the simulation time, for the reference prism-vortex interaction are presented in Figure 5.21. The maximum velocities found in the sheltering regions for no-prism simulation are presented in Figures 5.22. Here, in each time step the flow velocity is found from all nodes located in the particular sheltering region.
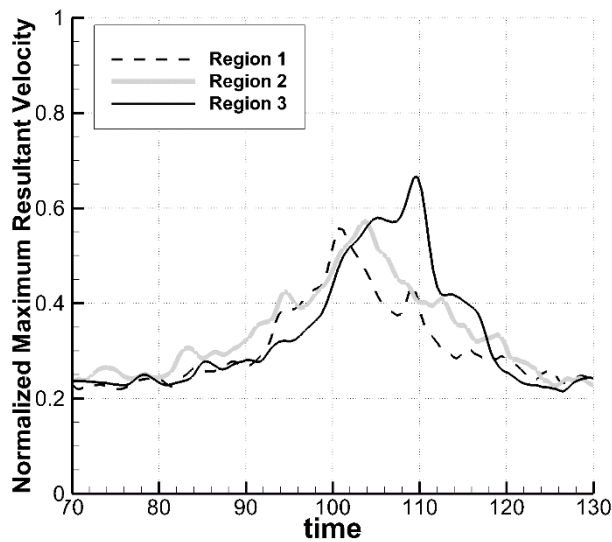
Figure 5.21 Maximum normalized flow speeds for vortex-prism interaction.
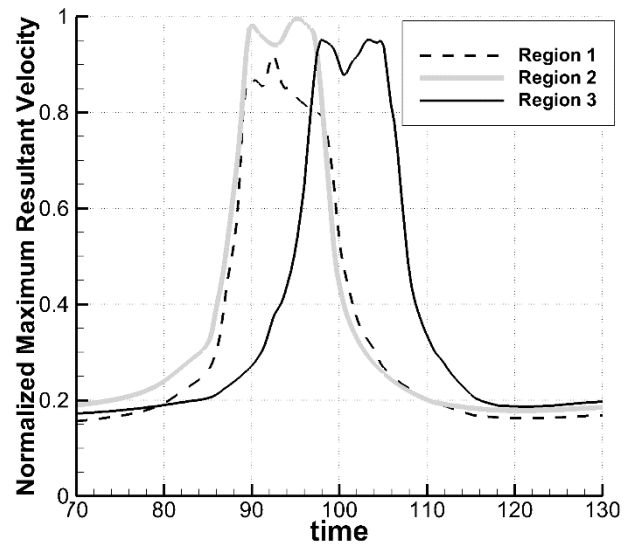
Figure 5.22 Maximum normalized flow speeds for no-prism simulation.

The most favourable sheltering effect is observed in Region 1 and Region 2. These regions are located right behind the prism. The fluid velocities there are reduced by at least 43.5%. Region 3 exhibits less sheltering efficiency. The flow speed reductions there are more than 28.5%. The maximum resultant velocities in the no-prism simulation (Figure 5.22) show that the extreme velocities occur in each region for about 8 time units. In the vortex-prism interaction the highest flow speeds are rather instantaneous. Table 5.5 includes the maximum velocities, in SI units, found in the three sheltering regions, during the entire simulations. Table 5.5 also provides the corresponding flow speed reductions.

108

Table 5.5 Flow speeds in the sheltering regions for vortex-prism interaction.

Sheltering region	Dimensions	Maximum resultant velocity	Flow speed reduction
1	9 x 1.5 (108m x 18m)	45.7 ms^{-1}	45.0 %
2	9 x 1.5 (108m x 18m)	46.9 ms^{-1}	43.5 %
3	9 x 3.0 (108m x 36m)	56.0 ms^{-1}	28.5 %

Figure 5.23 presents the dimensionless space averaged flow speeds for the vortex-prism interaction. In each time step an average value of all nodal flow speeds in calculated. Figure 5.24 shows the dimensionless space averaged flow speeds for the no-prism simulation. The comparison of those two figures represents the overall flow speed reduction in the sheltering zones. The greatest overall velocity magnitude reduction of about 25% is observed in Region 2. It is also noticed that the peak values of average flow speeds occurs earlier in time for the simulation with the prism. For the vortex-prism interaction in Region 1 and Region 2, the maximum overall velocity occurs at about t= 102 units. This corresponds to the time instant when the low-level portion of the primary vortex rotates around the horizontal direction (Figure 5.9e).
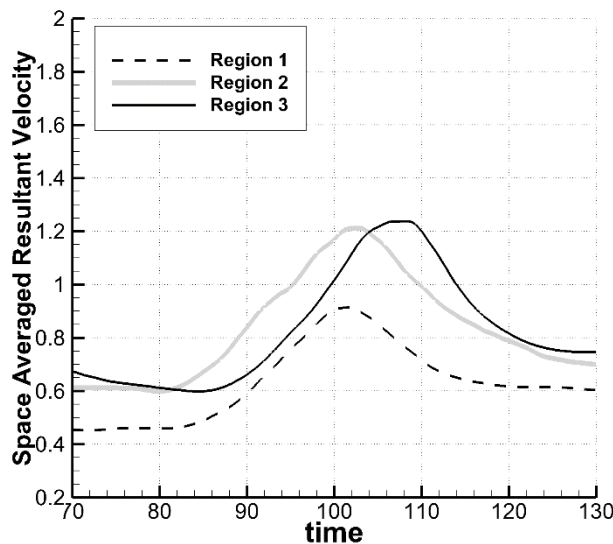
Figure 5.23 Dimensionless space averaged flow speeds for vortex-prism interaction.
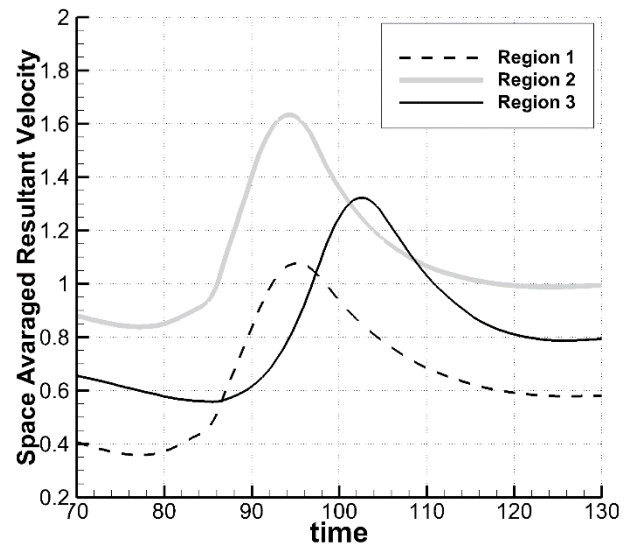
Figure 5.24 Dimensionless space averaged flow speeds for no-prism simulation.

109

5.4   Prism Length Parameter

To check how the length dimension of the prism influences the vortex-prism interaction, two additional simulations are conducted with different prism lengths and the same prism heights and widths. The prism length parameter is introduced here. The size of the analyzed prisms in dimensionless (ND) and SI units are provided in Table 5.6.

Table 5.6 Dimensions of prisms for prism length sensitivity study.

Prism	Prism height		Prism length		Prism width		Prism length parameter
	ND	SI	ND	SI	ND	SI	L/r_{max}
2	3.0	36 m	9.0	108 m	36.0	432 m	3.0
1	3.0	36 m	3.0	36 m	36.0	432 m	1.0
3	3.0	36 m	1.0	12 m	36.0	432 m	0.33

The prism lengths are chosen so that they are less, equal and greater than the vortex core radius (r_{max}). Prism 2 is three times longer in the streamwise direction than the vortex core radius. Prism 1 is the reference prism and its length is equal to the vortex core radius. Prism 3 is a wall-type structure, in which the streamwise dimension is three times less than the vortex core radius.

▪ *Vortex-Prism Interaction*

The vortex-prism interactions for Prisms 2 and 3 are illustrated by pressure iso-surfaces in Figures 5.22 and 5.23. The both simulations resemble the previously presented vortex interaction with reference prism. First, the columnar vortex is blocked by the leading face of the prism. Then, to proceed with the travel, the vortex induces the new low-level circulation behind the leading face of the prism. The circulation is then gradually transferred to the new low-level vortex, while the original low-level vortex blocked by the wall and it is losing its strength over the time.

110

In the case of the long prism (Figure 5.25) the interaction is smoother, since the vortex can renew its low-level circulation at the roof surface of the prism. The prism is long enough ($3 \cdot r_{max}$), so that the vortex core can circulate on the roof. Behind the prism, the new low-level vortex is rotating along y-axis, since it is originated from the vortex shedding on the prism walls. The horizontal vortex is quickly merged to the primary columnar vortex.

For the wall-type prism (Figure 5.26) the columnar vortex cannot circulate on the top surface of the prism. Prism 3 forces the vortex to abruptly create new low-level rotation behind the prism. Figure 5.26b shows two low-level vortices, the original one (in front of the prism) and new one (behind the prism). In all vortex-prism interactions the new low-level vortex, behind the prism, is originated from the vortex shedding.
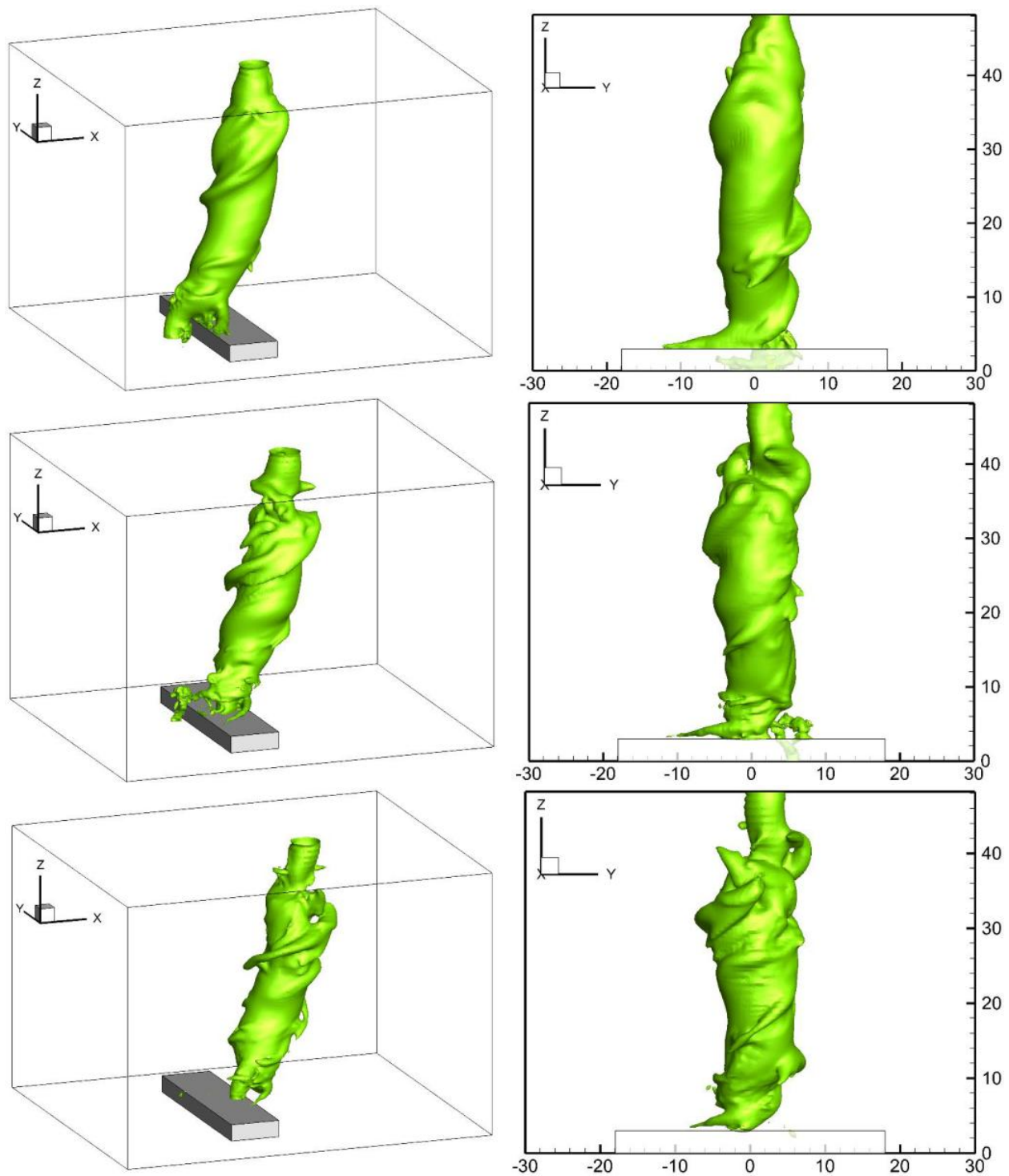
Figure 5.25 Pressure iso-surface (P= -3.0) of vortex interaction with Prism 2; a) t=90.6,
b) t=94.6, b) t=97.2.

112
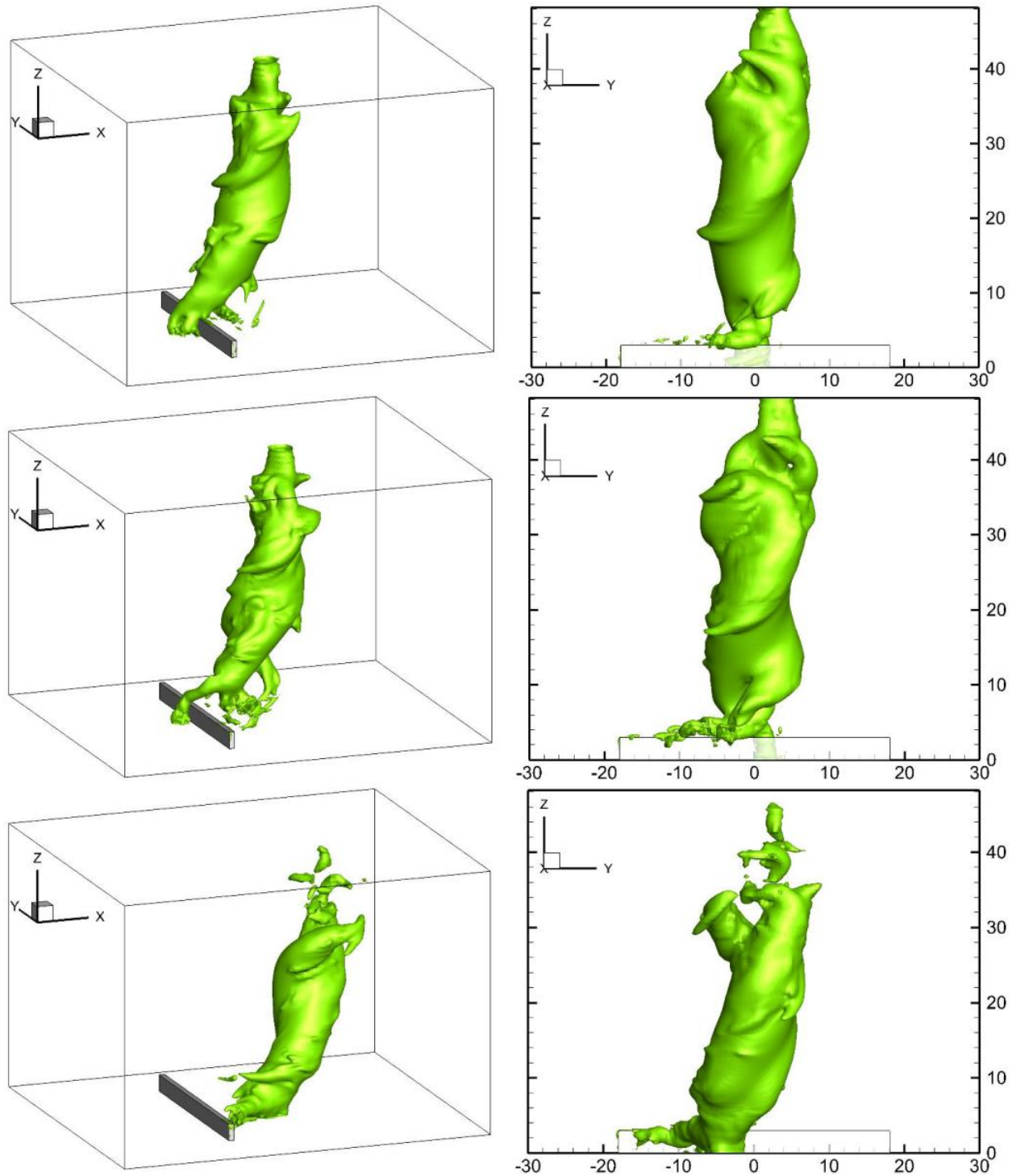
Figure 5.26 Pressure iso-surface (P= -3.0) of vortex interaction with Prism 3; a) t=90.2, b) t=94.6, c) t=101.3.

The vortex strength is more mitigated, while interacting with thinner prisms. For Prism 2 the

cylindrical shape of the lower portion of the vortex is maintained during the entire interaction

- *Vortex Strength Mitigation*

The vortex strength during the interaction is described by the z-vorticity contours. Figures 5.27 and 5.28 include consolidated contours representing the entire vortex-prism simulation. In the figures small vorticity values are masked to better visualize the vortex strength and path.
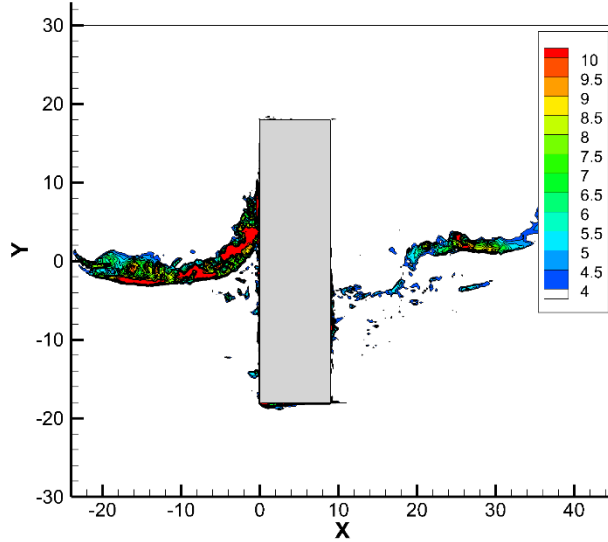
Figure 5.27 Consolidated z-vorticity xy-contour at z=3.0 units for Prism 2.
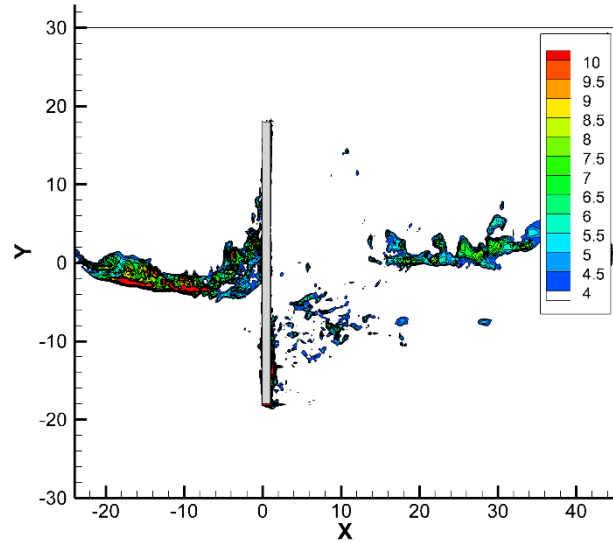
Figure 5.28 Consolidated z-vorticity xy-contour at z=3.0 units for Prism 3.

For all the prism lengths it is observed that the vortex is stronger in front of the prism than behind the prism. Behind the rectangular structure there is a region where z-vorticity values are relatively small. Only after some distance the stronger vortex circulation is recovered. The distance of the vertical circulation recovery, behind the leeward wall, is different for the three prisms. This distance is responsible for the length of the sheltering region. In general, the longer the prism is the shorter vortex sheltering region it creates. This indicates that the thinner prism is able to more effectively mitigate the strength of the travelling vortex and be better tornado shield.

- *Vortex Lateral Displacement*

In Figures 5.29 and 5.30 the lateral displacement for Prism 2 and Prism 3 are presented by consolidated contours of pressure on the ground surface and on the top surface of the prism. The similar contour for Prism 1 is included in Figure 5.12.
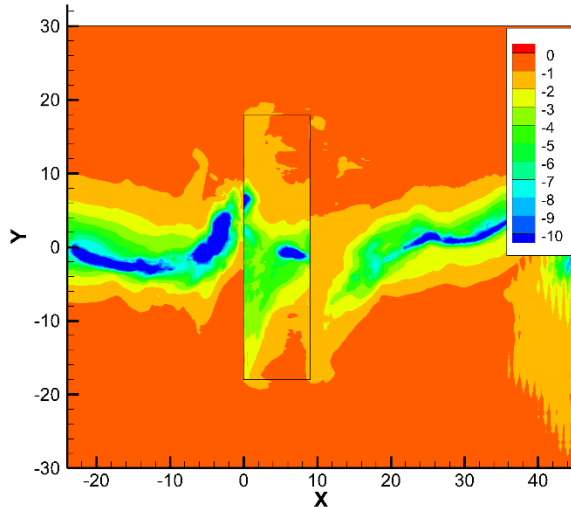
Figure 5.29 Consolidated pressure xy-contour at ground level and prism's roof for Prism 2.
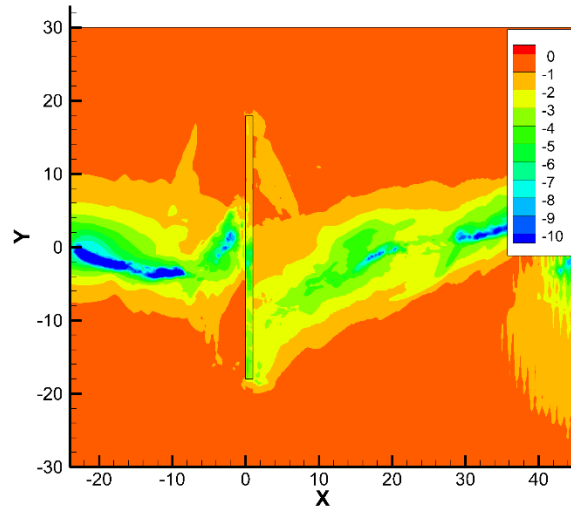
Figure 5.30 Consolidated pressure xy-contour at ground level and prism's roof for Prism 3.

Each prism causes substantial vortex path deviations in the near-ground level. In front of the windward wall the vortex is displaced in positive y-direction. This is due to the ambient velocity, which carries vortex near-ground portion of the vortex along the leading face of the prism. Behind the prism the vortex appears on the negative y-axis side. This is consistent for all prism lengths. For the longer prism the vortex induces substantial suction pressure on the roof. Also, the magnitude of the pressure on the ground surface is higher for the simulation of Prism 2.

Figure 5.31 summarized the influence of the prism length on the vortex lateral displacements. The vortex paths are retrieved from the ground pressure contours. The lines are drawn along minimum pressure values. It is observed that the vortex displacement in front of the prism is

115

smaller for thinner prims. Behind the prism no structure length dependence on the vortex path is observed.
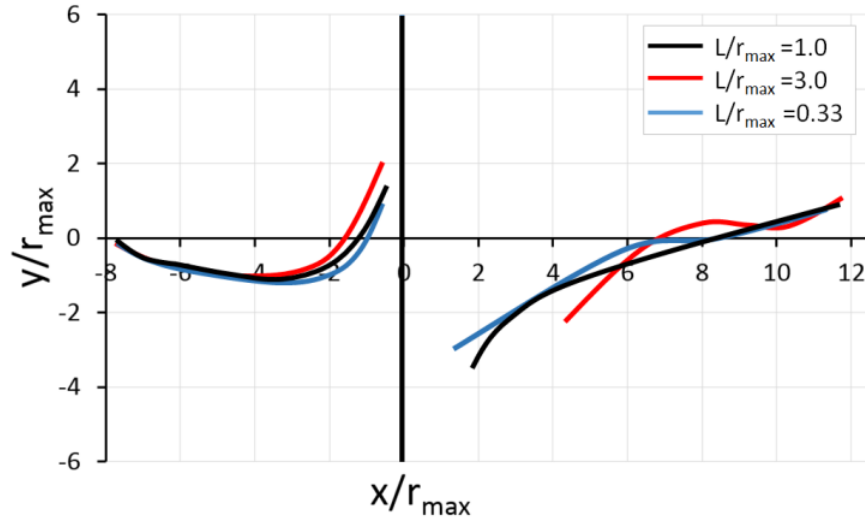
Figure 5.31 Near-ground lateral displacements of vortex for prisms of different lengths.

Figure 5.32 shows the line of the vortex centre at t=90 units for the three simulations. Each vortex line is created from the points of the minimum pressure in horizontal planes.
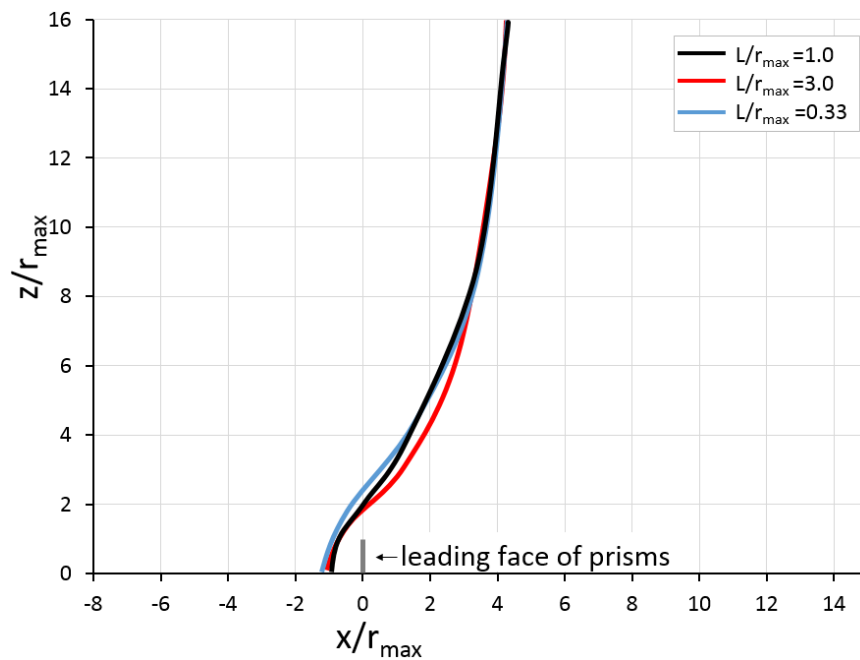
Figure 5.32 Streamwise vortex bending for prisms of different lengths.

116

The magnitude of vortex bending is very similar for different prism lengths. The near-ground portion of the vortex is dragged about $5 \cdot r_{max}$ behind the upper portion of the vortex.

- *Forces on Prisms*

Figure 5.33 presents the comparison of force coefficients in x-direction for the three analyzed prisms. The force coefficients were calculated with the reference velocity equal to 4.0. The projected area was assumed as the area of the leading face of the prism. Thus, for the three simulations the projected area is similar.
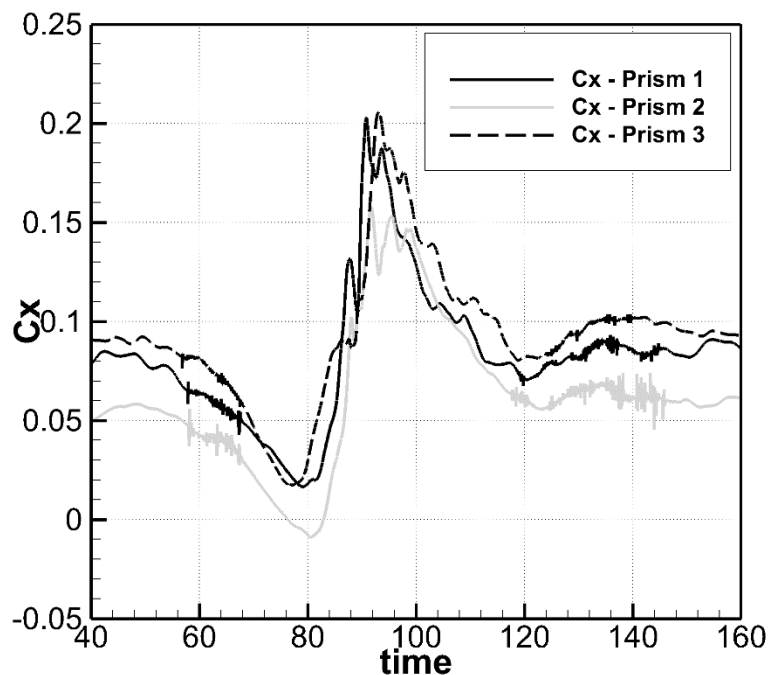
Figure 5.33 Force coefficients in x-direction against the simulation time for three prisms.

The forces on Prism 1 and 3 have very similar magnitudes. However, the peaks occur at different time instants. Forces on the longest prism are found to be lower. The maximum aerodynamic force is created when the vortex is blocked by the leading wall (Figure 5.15). The vortex remain blocked until the new low-level circulation, behind the prism, is created. When the length of the

prism is greater than the vortex core diameter (Prism 2), the vortex is able to circulate on the roof the prism. This causes the smoother type interaction and lowers the aerodynamic forces. The comparison of the forces for three prism is included in Table 5.7. For the calculation of vertical force coefficient the roof is assumed to be the projected area. It is observed that both the vertical force coefficients and x-direction force coefficients are increasing for thinner prisms.

Table 5.7 Maximum absolute instantaneous forces during vortex-prism interaction.

Prism	Prism length parameter, L/r_{max}	C_x	C_z
2	3.0	0.158	0.178
1	1.0	0.203	0.227
3	0.33	0.206	0.224

- *Sheltering Effect*

The maximum flow speeds behind Prism 2 and Prism 3 are presented in Figures 5.34 and 5.35. The two-dimensional contour includes maximum resultant velocities over the entire simulation time. Also, in each grid point, the maximum flow velocity is chosen from all *xz*-planes, according to Figure 5.17. The velocities are normalized to the maximum vortex velocity from the no-prism simulation. For the longer prism less sheltering effect is noticed. The Rankine vortex recovers high flow speeds at a distance about 13 units behind the leeward face of the prism (Figure 5.34). For the thinner prism, higher flow speeds are observed about 26 distance units behind the leeward wall.
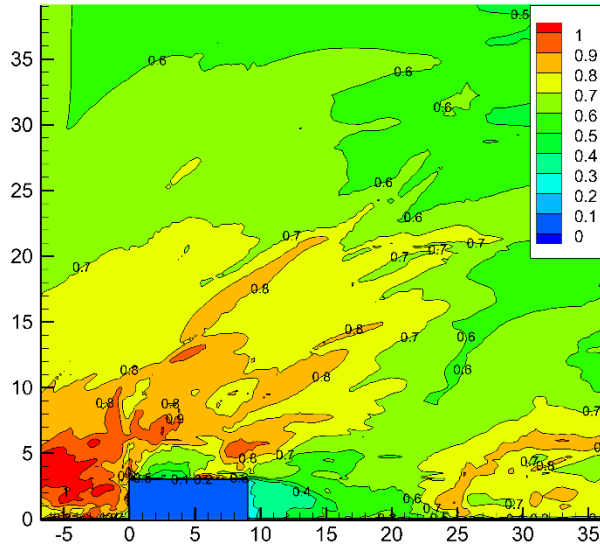
Figure 5.34 Consolidated maximum velocity magnitude xz-contour for Prism 2.
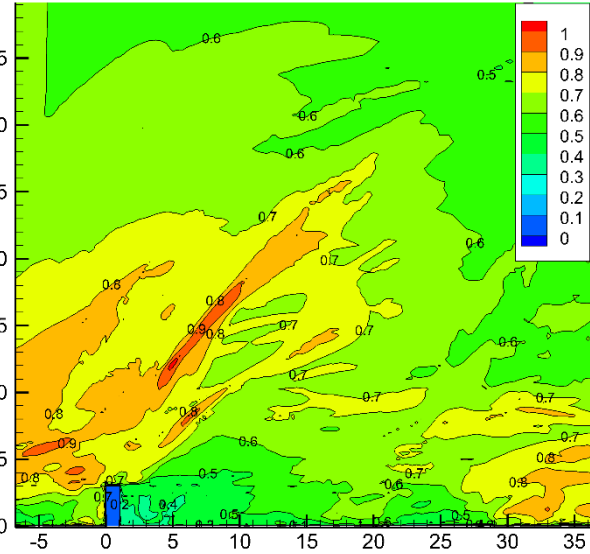
Figure 5.35 Consolidated maximum velocity magnitude xz-contour for Prism 3.

Figures 5.35 and 5.36 illustrate xy-plane consolidated maximum resultant velocity contours for Prism 2 and Prism 3. In front of Prism 2 the flow velocity is much greater than for Prism 3. The thin prism is observed to gradually decrease the vortex maximum velocity as it approaches the leading face.
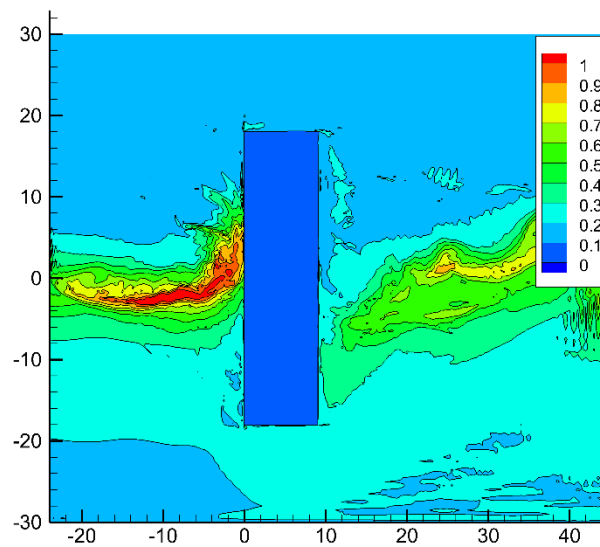
Figure 5.36 Consolidated maximum velocity magnitude xy-contour for Prism 2.
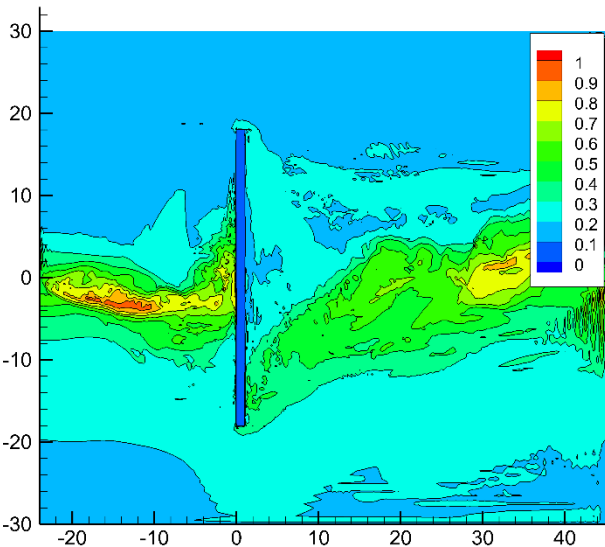
Figure 5.37 Consolidated maximum velocity magnitude xy-contour for Prism 3.

119

The maximum flow speeds found in the three sheltering regions for the three prisms are provided in Table 5.8. The sheltering regions are defined the same as in Figure 5.20. The maximum flow speeds in the zones are non-dimesionalized to the maximum reference flow speed of the Rankine vortex (6.92 units).

Table 5.8 Flow speed reduction in the sheltering regions depending on prism length.

Prism #	Prism length parameter L/r_{max}	Region 1	Region 2	Region 3	Shelter length ($u_{red} > 30\%$)
2	3.0	42.3 %	39.4 %	11.6 %	4.32H (156m)
1	1.0	45.0 %	43.5 %	28.5 %	5.67H (204m)
3	0.33	50.7 %	54.2 %	32.6 %	8.43H (304m)

The thinner the prism is, the better the sheltering performance it exhibits. For all three sheltering regions the flow speed reduction increases with the decrease in prism length .The highest velocities are observed in Region 3, which is the furthest away from the leeward wall of the prism. In Region 1 and Region 2 the maximum resultant velocities are reduced by more than 39% for all the prisms. This means that the aerodynamic forces on structures or people located in these regions would be decreased by at least 63%. The prism length affects especially Region 3, which was observed in Figures 5.34 and 5.35. When the length of the prism is larger than the vortex core radius, the vortex-prism interaction is smother since the vortex can rotate on the prism ridge. Because of that vortex strength is better preserved during the interaction and higher flow speeds are observed in the sheltering regions.

120

5.5   Prism Height Parameter

To check how the height dimension of the prism influences the vortex-prism interaction, two new simulations are conducted with different prism heights and the same prism lengths and widths. The nomenclature of the prism dimensions is presented in Figure 5.2. For this study the prism height parameter is introduced. The sizes of the analyzed prisms in dimensionless (ND) and SI units are provided in Table 5.9.

Table 5.9 Dimensions of prisms for prism height parameter sensitivity study.

Prism	Prism height		Prism length		Prism width		Prism height parameter
	ND	SI	ND	SI	ND	SI	H/r_{max}
1	3.0	36 m	3.0	36 m	36.0	432 m	1.0
4	2.0	24 m	3.0	36 m	36.0	432 m	0.67
5	1.0	12 m	3.0	36 m	36.0	432 m	0.33

The reference prism height is equal to the vortex core radius. The two remaining prisms are smaller than the reference prism. Prims 5 is six times smaller than the diameter of the vortex core.

- *Vortex-Prism Interaction*

The vortex-prism interactions for Prisms 4 and 5 are illustrated by pressure iso-surfaces in Figures 5.38 and 5.39. Intuitively, the height dimension of the prism should have the greatest influence on the vortex-prism interaction. Figures 5.9, 5.38 and 5.39 resenting the interactions from three prisms confirm this hypothesis. Prism 1, with the height equal to the radius of the vortex core, mitigates the most the strength and the shape of the translating vortex. When the prism is as high as the vortex radius, the vortex bends in the travelling (streamwise) direction. The prism blocks the near-ground portion of the vortex. This alters splitting the near-ground

vortex, since the new circulation is established behind the prism. Situation is different for small prism. When the height of the prism is three times smaller than the vortex core radius (Prism 5), the vortex travels smoothly over the prism (Figures 5.39a-c). Smaller prisms are unable to block the travelling vortex. The vortex is able to travel over the prism, preserving the straight path and its vertical shape. Figure 5.39b shows the instant when the vortex circulation is on the prism's ridge. This effect is not seen for the highest prism (Prism 1). The vortex interaction with medium size prism (Prism 4) exhibits less magnitude of the vortex strength mitigation than Prism 1. Prism 4 is high enough, so that it can block the near-ground portion of the vortex (Figure 5.38a-c). The vortex quickly reestablishes its circulation on the ridge of the prism, by introducing new low-lever vortex (Figure 5.38b). This feature resembles the vortex interaction with reference prism. Nevertheless, for all three prism heights it is observed that the travelling vortex is unable to circulate right behind the prism. The wide leeward wall is a barrier for vortex circulation at the near-ground-level.
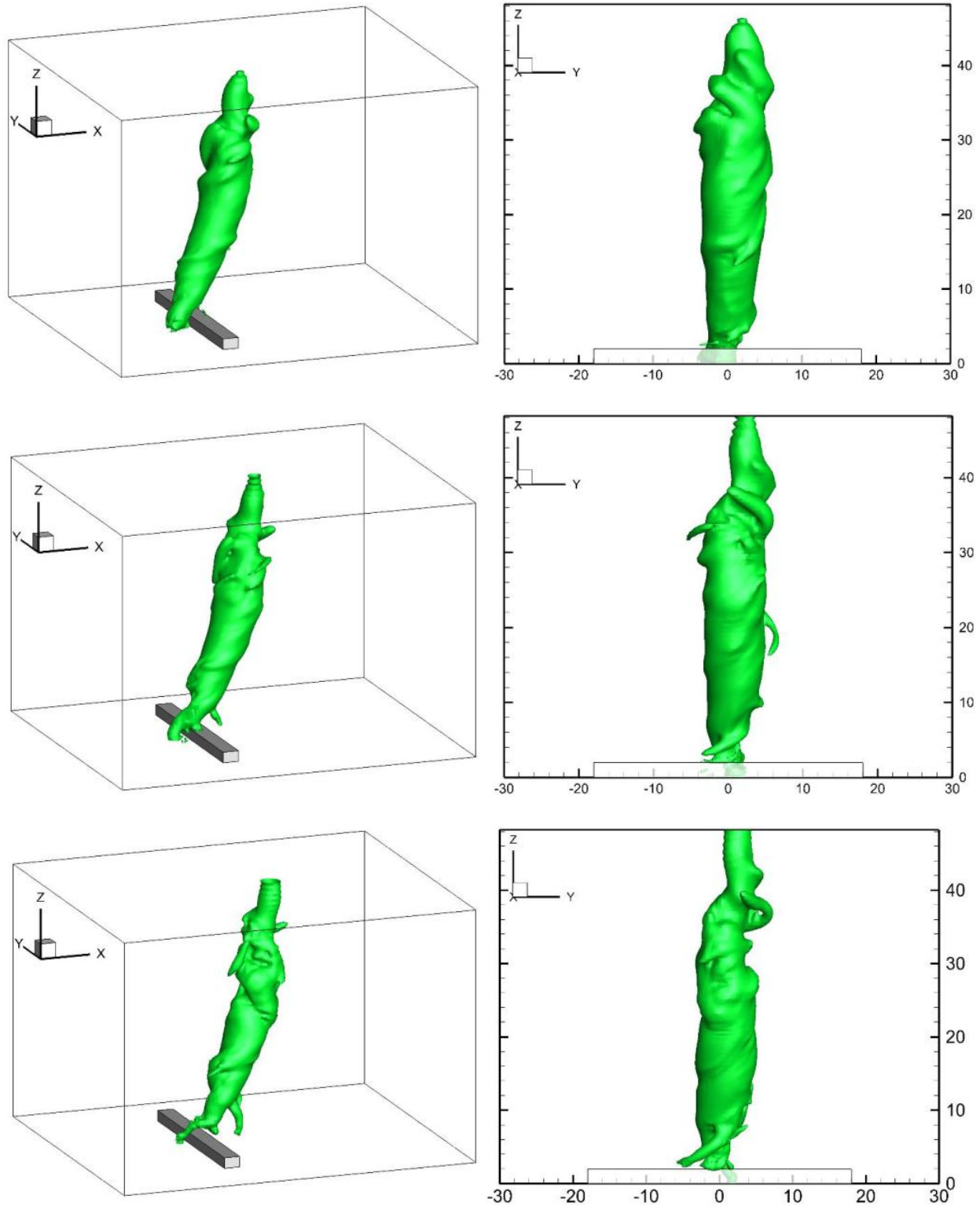
Figure 5.38 Pressure iso-surface (P= -5.0) of vortex interaction with Prism 4; a) t=88.1, b) t=90.0, b) t=92.1.
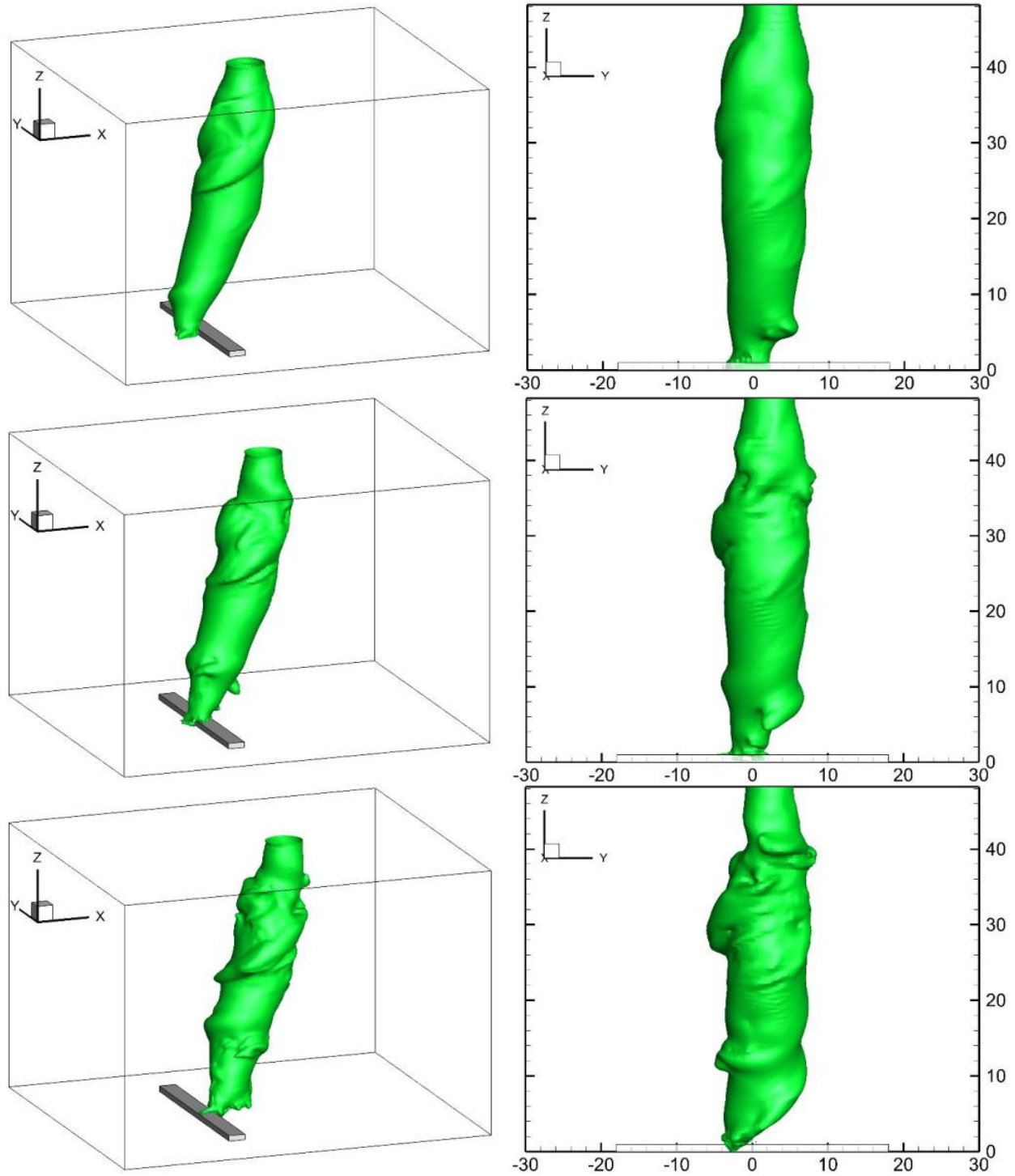
Figure 5.39 Pressure iso-surface (P= -5.0) of vortex interaction with Prism 5; a) t=85.8, b) t=87.9, c) t=90.0.

- *Vortex Strength Mitigation*

The strength of the lower portion of the vortex for Prism 4 and Prism 5 are presented by consolidated z-vorticity contours in Figures 5.40 and 5.41. The strength of the vortex in the reference simulation is provided in Figure 5.11. The vorticity values are extracted the xy-plane at the prism height level.
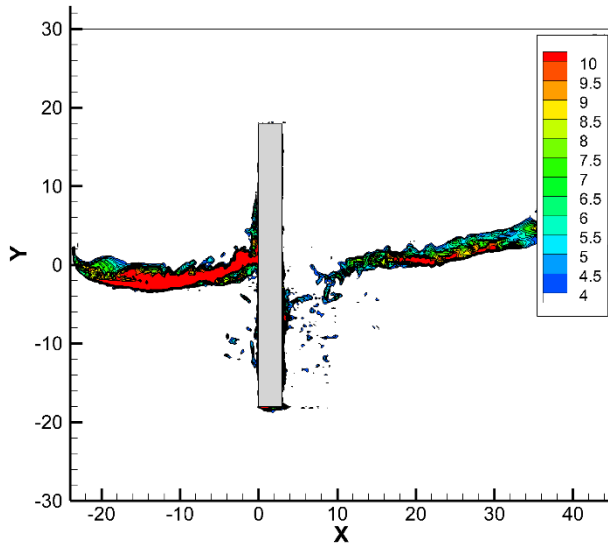
Figure 5.40 Consolidated z-vorticity xy-contour at z=2.0 units for Prism 4.
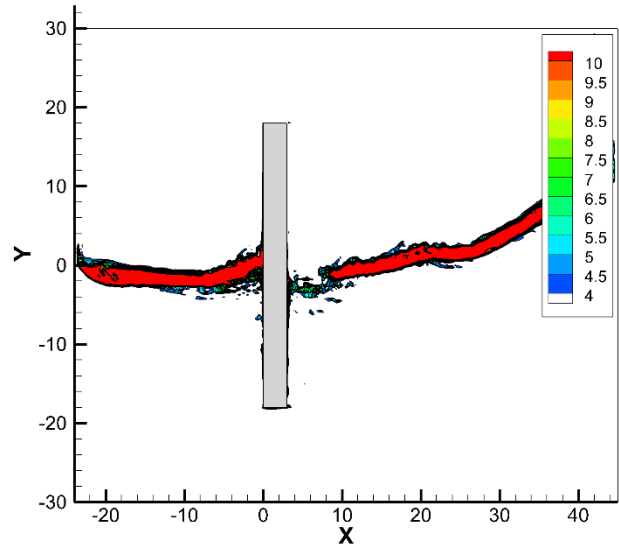
Figure 5.41 Consolidated z-vorticity xy-contour at z=1.0 units for Prism 5.

From Figures 5.11, 5.40 and 5.41 it is noticed that the strength of the vortex circulation, measured by the vorticity magnitude, is altered by the height of the prism. The higher the prism is the greater the vortex strength is reduced during the interaction. The travelling vortex disruption occurs both in front of the prism and behind the prism. Only for the smallest prism (Prism 5) the vortex keeps its strength in front and behind the structure. In Figure 5.41 it is observed that the vortex recovers its full strength about 5 units behind the leeward face. This means that there is a sheltering region with lower velocities. When the prism height is more than 1/3 of the vortex core radius, the prism causes mitigation of the vortex strength behind the prism.

In Figure 5.11 and 5.40 it is noticed that the vorticity values behind the prism are lower than in front of the prism.

- *Vortex Lateral Displacement*

Figures 5.42 and 5.43 present consolidated contours of pressure on the ground surface and on the top surface of Prism 4 and Prism 5. The pressure on the surface for Prism 1 is illustrated in Figure 5.12.
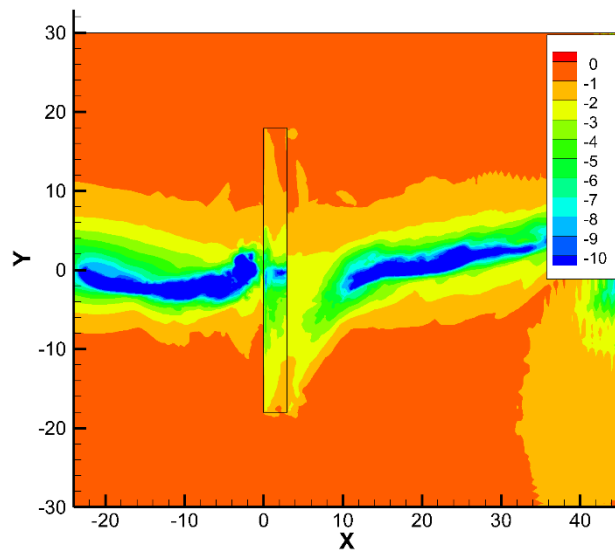
Figure 5.42 Consolidated pressure xy-contour at ground level and prism's ridge for Prism 4.
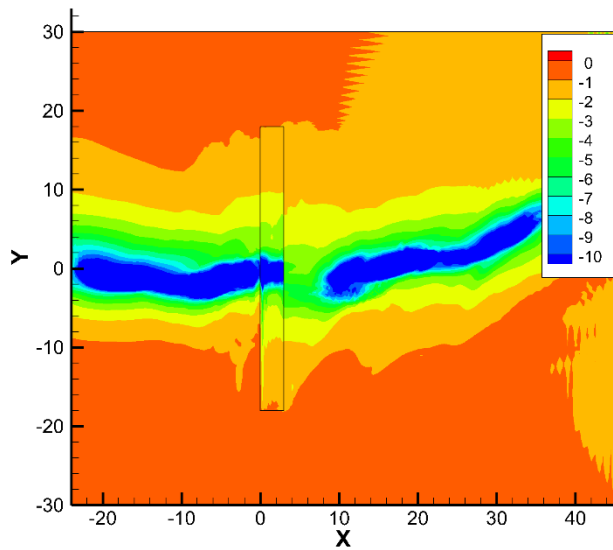
Figure 5.43 Consolidated pressure xy-contour at ground level and prism's ridge for Prism 5.

The pressure contours show that the smaller the prism is, the less it influences the traveling vortex strength and the path. The reference prism, which height is equal to the vortex core radius, induces vortex lateral displacement in front of the prism (Figure 5.12). This effect is not observed when the prism height is three times less than the vortex core radius (Figure 5.43). For Prism 5 the vortex preserves almost straight path in front of the prism. The travelling vortex is also able to circulate on the top surface of the smallest prism, which is indicated by the suction pressure. When the prism height is three times less than the vortex core radius, the vortex is able

126

to maintain its vertical shape during the interaction. Nonetheless, for all three prism heights the sheltering effect is observed. Right behind the prism, the suction pressure is mitigated. The wide prism prevents flow rotation, right behind the prism. Also, the translating velocity causes the lower portion of the vortex to pass over sheltering region.

Figure 5.44 summarizes the influence of the prism height on the vortex lateral displacements. The vortex paths are retrieved from the minimum ground pressure contours. It is observed that the vortex displacement in front of the prism depends of the prism height. The vortex undergoes more displacing when it interacts with Prism 1, which is the highest. When the prism height to the vortex core radius ratio is smaller than one, the vortex tends to have straighter path.
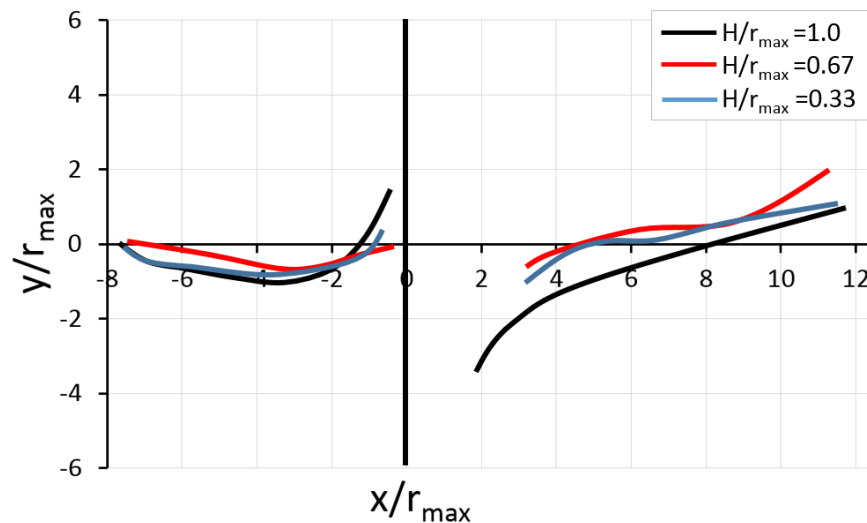
Figure 5.44 Near-ground lateral displacements of vortex for prisms of different heights.

Figure 5.45 presents the vortex bending during the interaction. When the prism height is three times smaller than the vortex core radius the prism is unable to block the travelling vortex. From the figure it is observed that the near-ground vortex is located on the top of the prism.
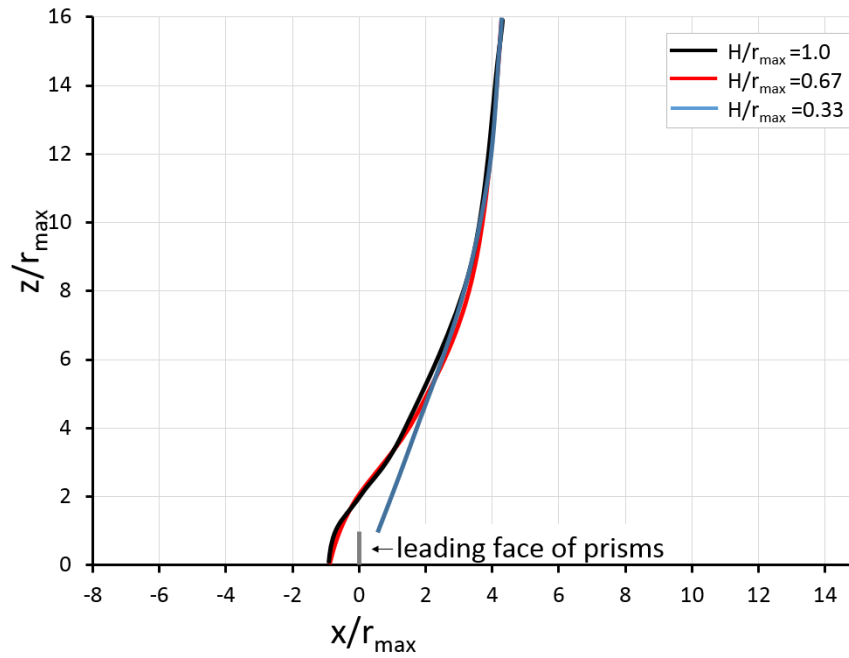
Figure 5.45 Streamwise vortex bending for prisms of different heights.

▪ *Forces on Prisms*

Table 5.10 presents the comparison of force coefficients in x-direction and in z-direction for

three analyzed prisms. The force coefficients were calculated with the reference velocity equal to

1.0. The x-axis projected area was assumed as an area of the leading face of the prism. For the

calculation of vertical force coefficient the roof is assumed to be the projected area.

Table 5.10 Maximum absolute instantaneous forces during vortex-prism interaction.

Prism	Prism height parameter, H/r_{max}	C_x	C_z
1	1.0	0.203	0.227
4	0.67	0.215	0.244
5	0.33	0.188	0.334

The forces in x-direction on the prism have similar magnitudes. There is no clear relation

between the prism height and force coefficient in x-direction. It is different for the vertical

coefficients. Here, the vertical forces are increasing along with the decrease of prism height. This

128

was expected from the pressure on the surface contours (Figure 5.12, 5.42 and 5.43). For the lowest prism the vortex can develop the circulation on the top surface of the prism.

- *Sheltering Effect*

The maximum flow speeds behind Prism 4 and Prism 5 are presented in Figures 5.46 and 5.47. The two-dimensional contour includes maximum resultant velocities over the entire simulation time. Also, in each grid point, the maximum flow velocity is chosen from all *xz*-planes, according to Figure 5.17.
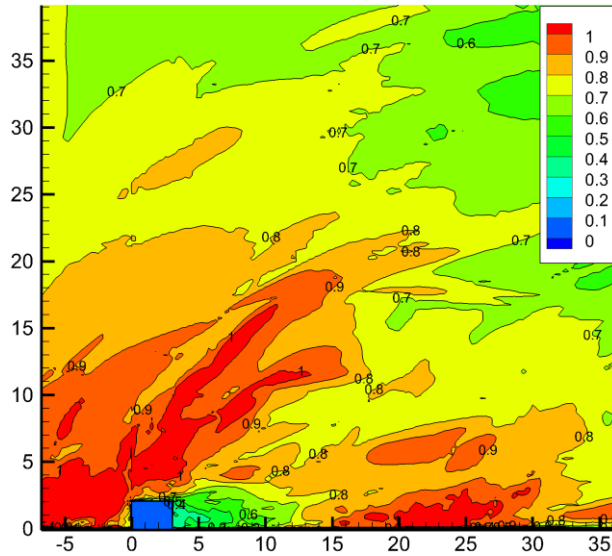
Figure 5.46 Consolidated maximum velocity magnitude xz-contour for Prism 4.
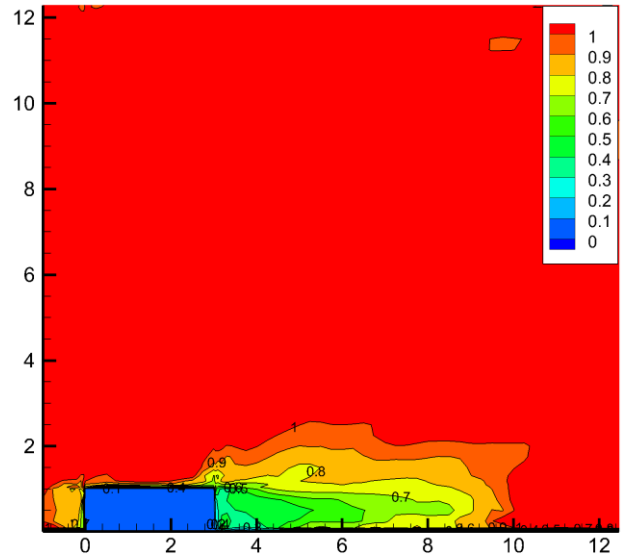
Figure 5.47 Consolidated maximum velocity magnitude xz-contour for Prism 5.

From Figures 5.18, 5.46 and 5.47 it is noticed that the sheltering effect is highly dependent on the height of the prism. The higher the prism, the better vortex sheltering effect it exhibits. This results was intuitively expected. Therefore, the sheltering regions dimensions were related to the height of the prism (Figure 5.20). Prism 5, which height is three times less than the vortex core radius, exhibits flow speeds reduction only in very fine leeward region (Figure 5.47). The flow velocity magnitudes outside the sheltering region are not reduced.

129

Figures 5.48 and 5.49 illustrate horizontal consolidated maximum resultant velocity contours for Prism 4 and Prism 5. The maximum resultant velocities are found up to the prism height level.
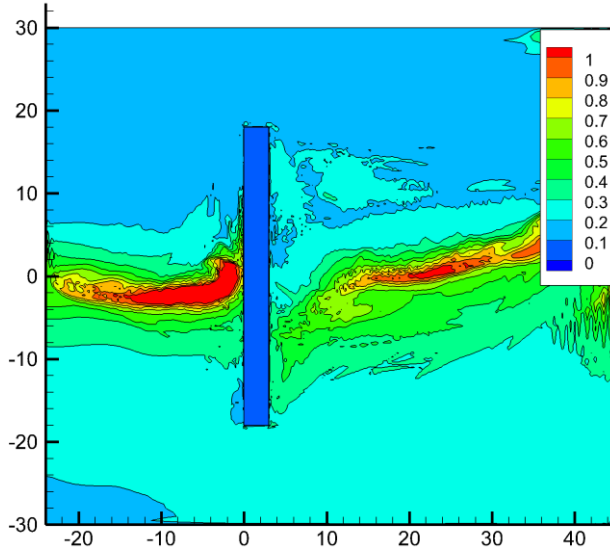
Figure 5.48 Consolidated maximum velocity magnitude xy-contour for Prism 4.
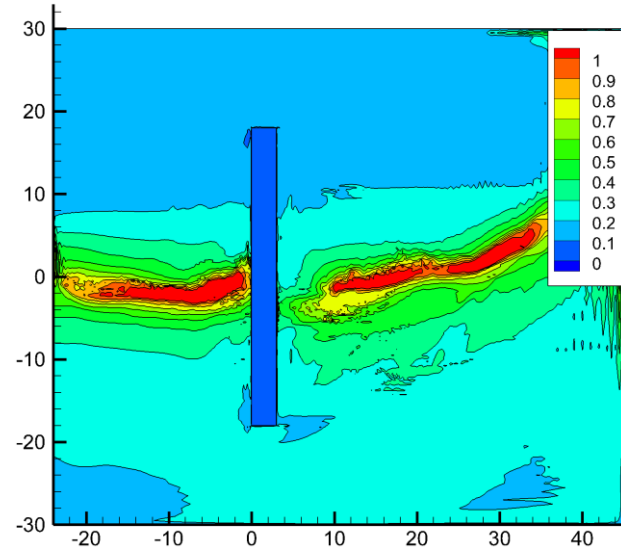
Figure 5.49 Consolidated maximum velocity magnitude xy-contour for Prism 5.

From the x-y contours it is noticed that even the small prism exhibits sheltering region, on the leeward side. Also, the vortex interaction with the small prism (Figure 5.49) preserves its strength after the interaction. For higher prism the velocity magnitudes after the interaction are distinctly reduced.

The maximum flow speeds found in the three sheltering regions for the three prism heights are provided in Table 5.8. The sheltering regions are defined the same as in Figure 5.20. The size of the sheltering zones is assumed to be dependent on the height of the prism. The maximum flow speeds in the zones are non-dimesionalized to the maximum reference flow speed of the Rankine vortex (6.92 units) when there is no prism.

Table 5.11 Flow speed reduction in the sheltering regions depending on prism height.

Prism #	Prism height parameter, H/r_{max}	Region 1	Region 2	Region 3	Shelter length ($u_{red} > 30\%$)
1	1.0	45.0 %	43.5 %	28.5 %	5.67H (204m)

4	0.67	33.4 %	36.4 %	6.8 %	3.35H (80m)
5	0.33	34.1 %	41.4 %	17.7 %	3.30H (40m)

For all prism height the sheltering effect occurs. There is not a clear relation between the sheltering effect and the ratio of the vortex radius to the prism height. However, all the prisms exhibit sheltering abilities in Region 1 and Region 2. For the region that is three times longer than the prism height the flow speeds are reduced at least by 33% up to the prism height. Such a flow speed reduction would contribute to the reduction of the aerodynamic forces by at least 55%, so more than twice. Right behind the prism the vortex cannot develop its circulation, and it flies over the leeward zone, leaving low-speed region (Figure 5.39c). In Region 3 the sheltering effect is diminished for lower prisms. When the prism height is comparable to the Rankine vortex radius the prism affects the vortex strength and structure during the interaction. This effect reflects in the flow speeds behind the prism. When the prism height is 1/3 of the vortex core radius the vortex flows almost undisturbed over the prism. It preserves its strength behind the prism. Hence the, velocities are higher in Region 3 for Prism 4 and Prism 5.

5.6   Impact Parameter

Krishnamoorthy, Gossler and Marshall (1999) showed that the translational velocity of a vortex has substantial influence on the way of the vortex-cylinder interaction. They defined an impact parameter as a crucial factor for the vortex-cylinder interaction. For the Rankine vortex the impact parameter is a ratio of the translational velocity to the maximum rotational velocity. In this section two additional simulations are analyzed, with different vortex translational velocities. The reference prism dimensions are assumed for all simulations. The prism and the vortex parameters for the current study are included in Table 5.12.

Table 5.12 Input parameters for prism and vortex for impact parameter sensitivity study.

Vortex #	Vortex transitional velocity		Impact parameter u_{trans}/u_θ	Prism Dimensions	
	ND	SI [ms^{-1}]		ND	SI [m]
2	0.5	6	0.167	3.0 x 36.0 x 3.0	36 x 432 x 36
1	1.0	12	0.333	3.0 x 36.0 x 3.0	36 x 432 x 36
3	2.0	24	0.667	3.0 x 36.0 x 3.0	36 x 432 x 36

Since the translational velocity is different for the three simulations, the maximum horizontal velocity also varies among the simulations. For Vortex 2 the predefined maximum horizontal velocity is 3.5 units (42 ms^{-1}). For Vortex 3 the maximum horizontal velocity is 5.0 units (60 ms^{-1}). The impact parameter varies from 0.167 to 0.667. Higher impact parameters were difficult to simulate since the free stream velocity was so high that it dominated the flow in the computational domain.

The vortex-prism interactions for Vortex 2 and Vortex 3 are illustrated by pressure iso-surfaces in Figures 5.50 and 5.51. Both simulations exhibit similar features to the vortex interaction with the reference prism. The slower vortex is observed to be substantially mitigated in the lower-level portion. The pressure iso-surface of the vortex is visibly thinner than for the reference interaction. In Figure 5.50b the two near-ground vortices, in front of the prism and behind the prism, circulate around prism spanwise direction, which indicate that they are formed from the wake and the vortex shedding of the prism. The vortices are clearly separated and they merge in the upper portion of the main columnar vortex. This resembles double-helix vortex breakdown, observed in the blade-vortex interaction studies (Figure 2.33). The two vortices rotate around each other. In Figure 5.50c it is observed that the double-helix wave propagates upwards. For Vortex 3 the interaction is less destructive for the travelling vortex (Figures 5.51a-c). The vortex is illustrated by the lower value of pressure iso-surface (P= -5.0) to better visualize the interaction. In front of the prism the vortex exhibits significant axial bending (Figures 5.51a). The vortex is stretched in the axial direction until it is instantaneously cut on the prism level (Figures 5.51a). Looking at time instants at different vortex stages it is observed that the higher translational velocity resulted in much faster interaction between Vortex 2 and Vortex 3. Also the faster vortex does not exhibit the double helix shape behind the prism, as it was noticed for the slower vortex.

133
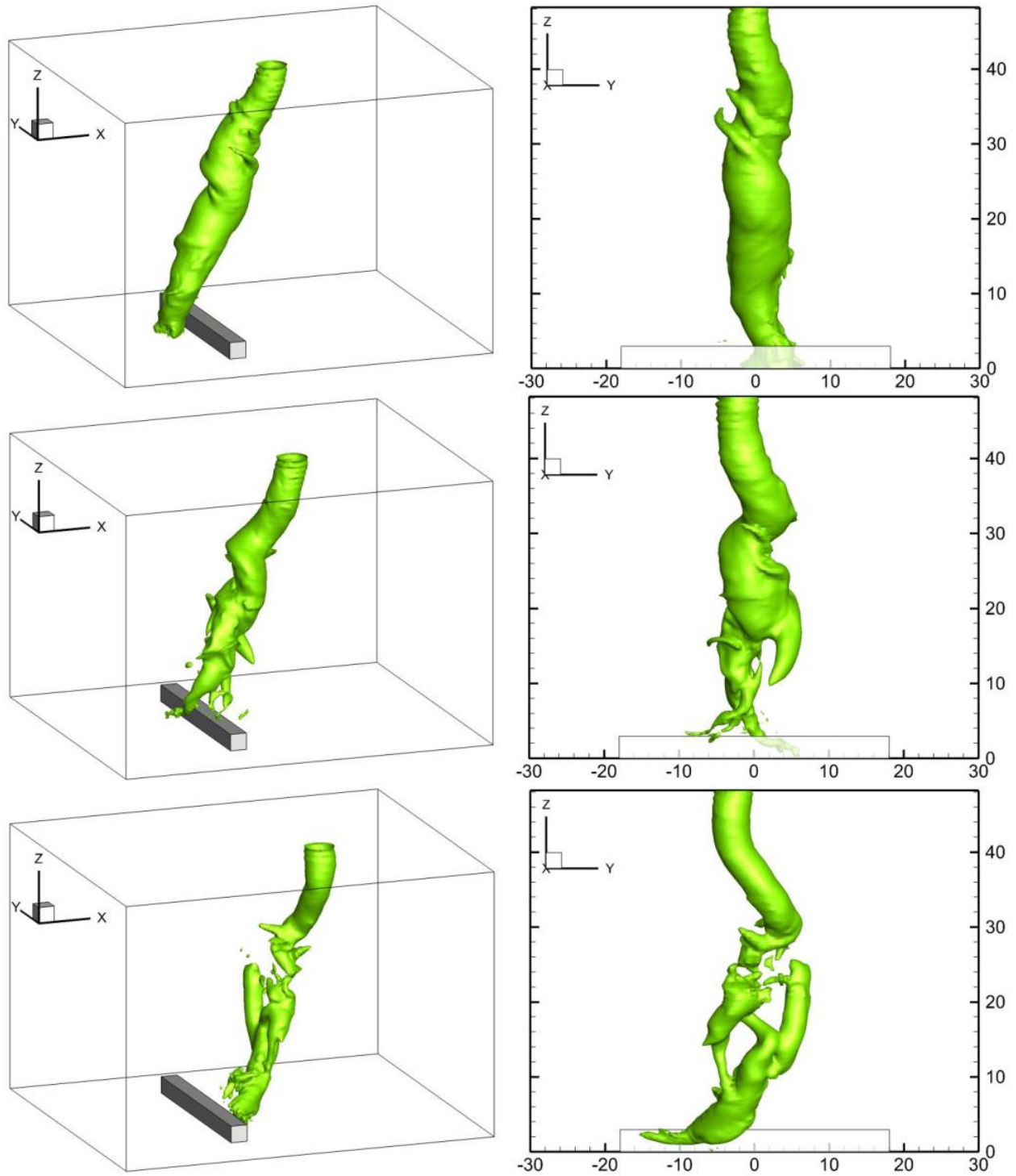
Figure 5.50 Pressure iso-surface (P= -3.0) of slower vortex ($u_{trans}=0.5$) interaction with Prism 1; a) t=90.3, b) t=96.1, c) t=103.7.
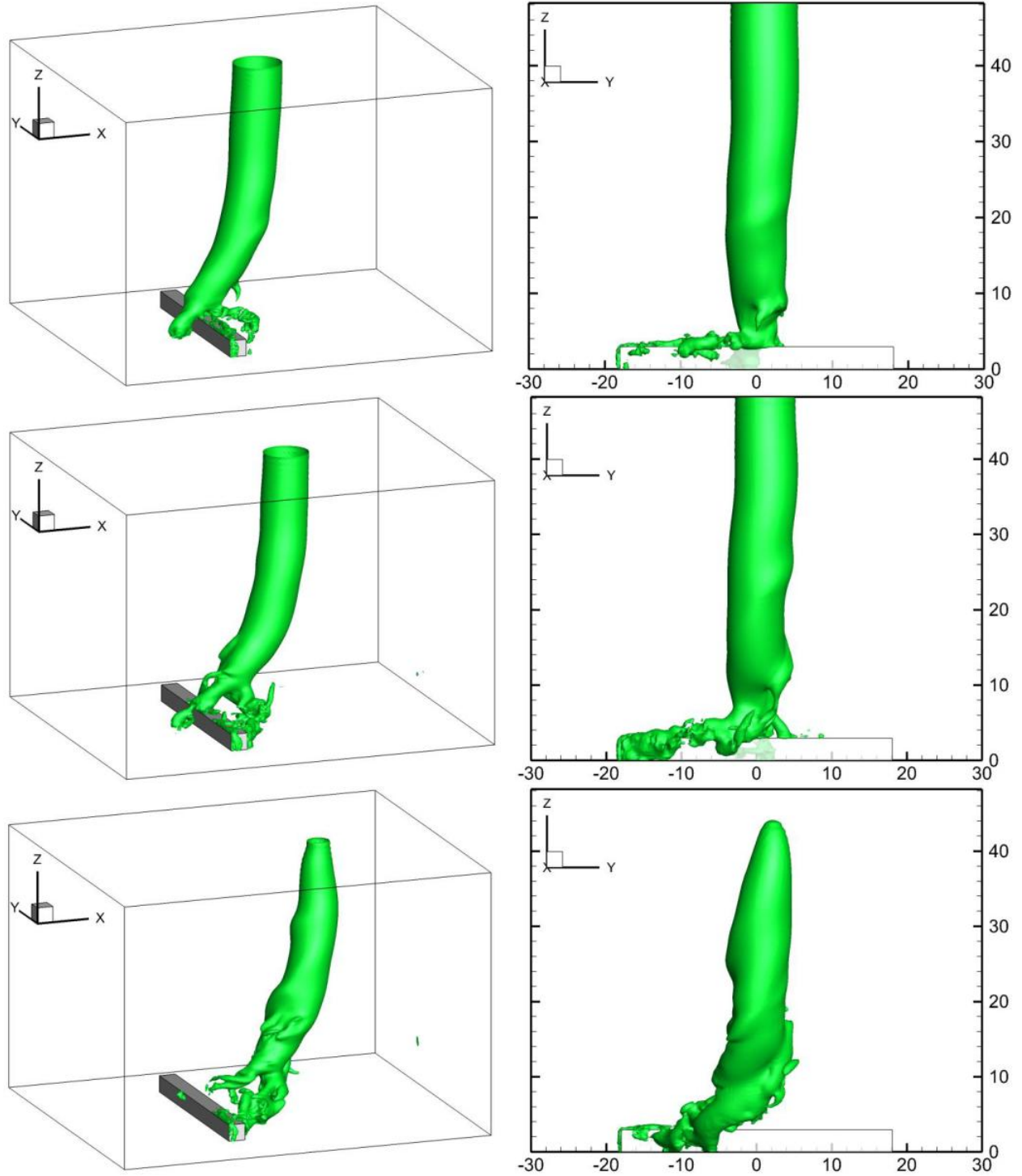
Figure 5.51 Pressure iso-surface (P= -5.0) of faster vortex ($u_{trans}=2.0$) interaction with Prism 1; a) t=90.0, b) t=91.9, c) t=95.9.

- *Vortex Strength Mitigation*

As is observed in Figures 5.50 and 5.51 the strength of the vortex in the near-ground level depends on the impact parameter. The higher the translational velocity the weaker the vortex is near the prism. The mitigation of the vortex s related with the vortices ejection effect (Figure 2.28). As the vortex approaches the leading face of the prism, it induces higher velocities around the structure. On the leading wall of the prism the negative vorticity is generated since the flow is directed along the wall in the positive y-direction, due to the counter clockwise vortex rotation. When the vortex is very close to the wall boundary layer, the vortex-induced velocities are very strong which causes ejection of vorticity patches from the boundary layer (Figure 5.52a). The negative vortices patches wrap around the positive vorticity of the Rankine vortex. This causes thinning and weakening of the vortex as explained by Krishnamoorthy and Marshall (1998). For the vorticity to be ejected from the boundary layer, there must be a condition when the vortex-induced velocity close to the wall overcomes the free stream velocity. Only then the vorticity can be ejected in the reverse direction to the free stream flow.
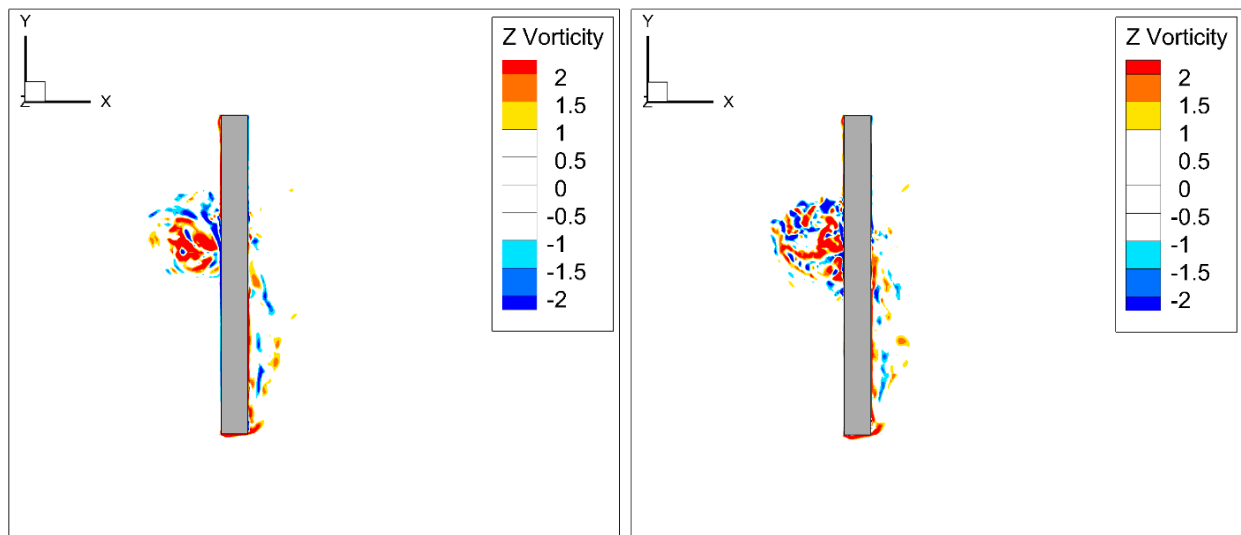
Figure 5.52 Vorticity ejection in the vortex-prism interaction ($u_{trans}=0.5$); left: t=90.0, right: t=91.9.

Thus, the incident of the vorticity ejection is dependent to the ratio of the free stream flow to the maximum tangential velocity – impact parameter. The less the impact parameter is the faster the vorticity ejection occurs. Figures 5.53a and 5.53b show that for higher translational velocity the vortex preserves its strength in front of the leading face.
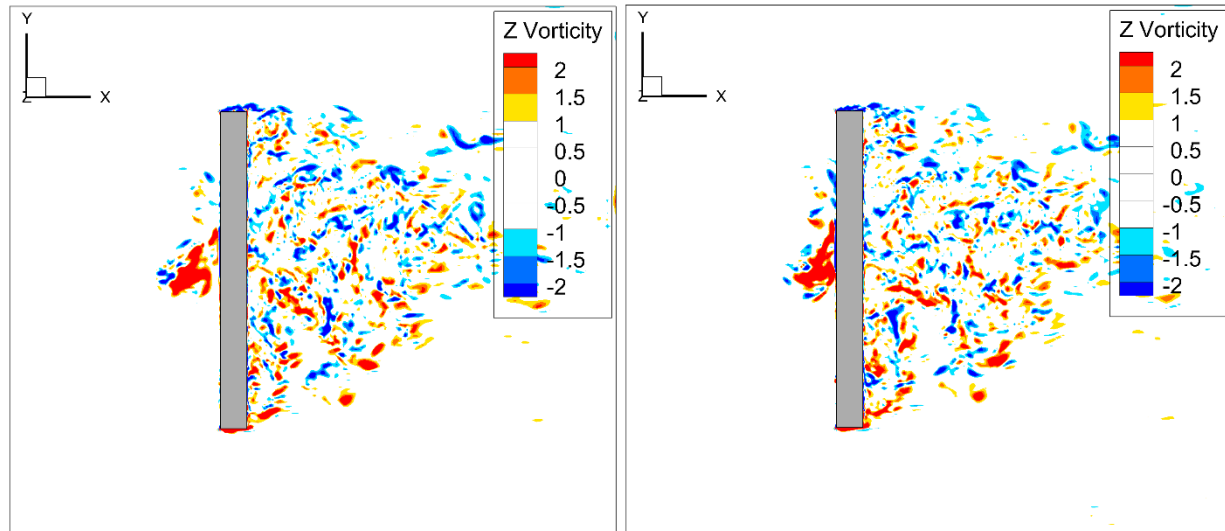
Figure 5.53 Vorticity contour in the vortex-prism interaction (u_{trans}=2.0) left: t=90.0, right: t=91.9.

The strength of the lower portion of the vortex for Vortex 2 and Vortex 3 throughout the travel are presented by consolidated z-vorticity contours in Figures 5.54 and 5.55. The vortex strength in the reference simulation is provided in Figure 5.11. The vorticity values are extracted the xy-plane at the prism height level.
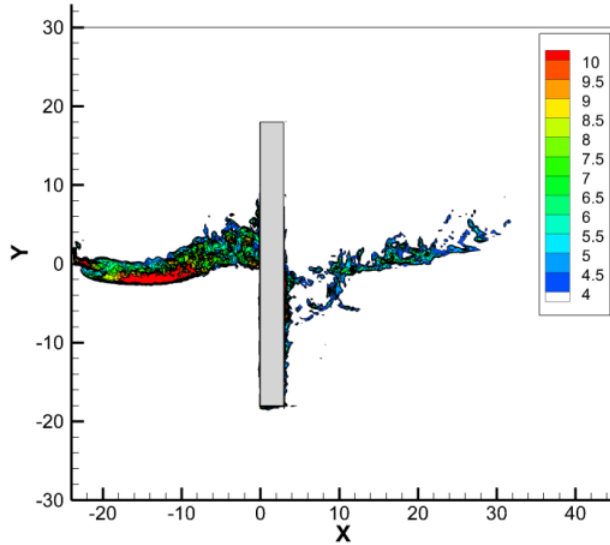
Figure 5.54 Consolidated z-vorticity xy-contour at z=3.0 units for Vortex 2.
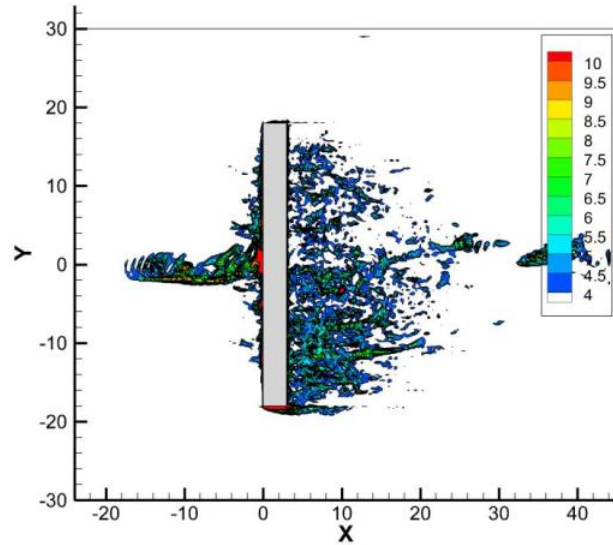
Figure 5.55 Consolidated z-vorticity xy-contour at z=3.0 units for Vortex 3.

The strength of the slow vortex (Figure 5.54) is significantly mitigated behind the prism. The vorticity magnitude around z-axis starts to decrease as the vortex approaches the leading face of the prism. After the interaction the vertical rotation is observed, but is much weaker. For the faster vortex simulation, the free stream velocity is 2/3 of the maximum tangential velocity of the travelling vortex. Therefore, the very turbulent flow behind the prism is observed. The vortex might also flow around both sides of the prism and hence the vortex strength is distributed all around the leeward side. However, further study is needed for clear understanding.

- *Vortex Lateral Displacement*

Figures 5.56 and 5.57 present consolidated contours of pressure on the ground surface and on the top surface of the prism for different vortex translational speeds. The pressure on the surface for reference simulation is illustrated in Figure 5.12.
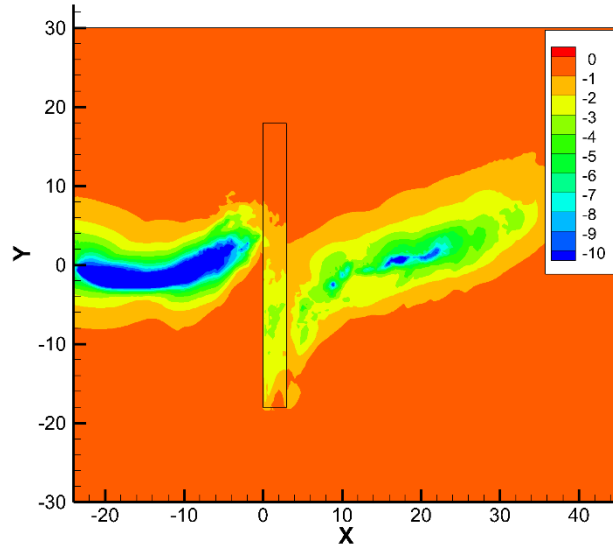
Figure 5.56 Consolidated pressure xy-contour at ground level and prism's roof for Vortex 2.
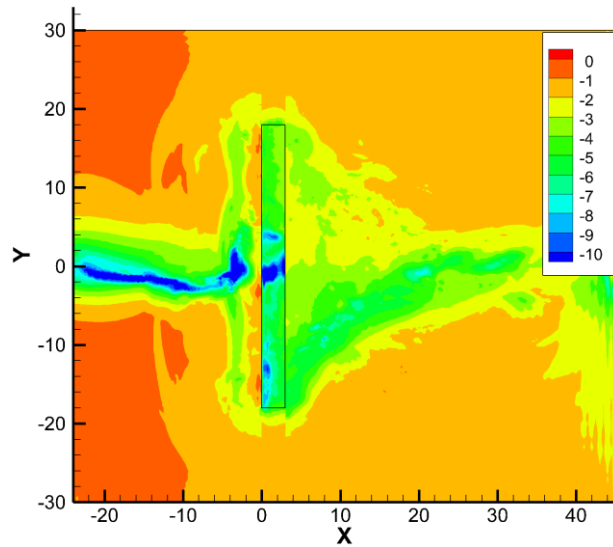
Figure 5.57 Consolidated pressure xy-contour at ground level and prism's roof for Vortex 3.

The path of the Rankine vortex is observed to be dependent on the impact parameter. The slowest vortex experiences lateral path deviation in front of the prism, whereas path of the fastest vortex is straighter. Also, the pressure suction magnitude induced on the ground surface is different for three translational velocities. In front of the prism the slowest vortex exhibits curved path (Figure 5.56). The travelling vortex induces very high suction pressure on the ground surface as it approaches the prism. The suction is substantially mitigated at about r_{max} distance front of the windward wall. The vortex lateral displacement, at this distance, is about $1.5 \cdot r_{max}$ from the x-axis. At the top of the prism the vortex recovers on the other side of x-axis, with lateral displacement about $2 \cdot r_{max}$. Behind the prim the path undertakes a diagonal curvature. The vortex suction strength, behind the prism, is noticed to be reduced. When the vortex translational speed is high the path of the vortex is straight until the vortex meets the encounters windward wall (Figure 5.57). Then, the vortex experiences sudden displacement in positive y-direction. On the top of the prism the suction pressure is observed, which indicates that the vortex was cut by

139

the prism and it maintained its vertical circulation. Behind the prism the path direction is observed to be similar for the three simulations.

Figure 5.58 illustrates the comparison of the vortex path directions for three different impact parameters. The paths are retrieved from pressure on the ground contours.
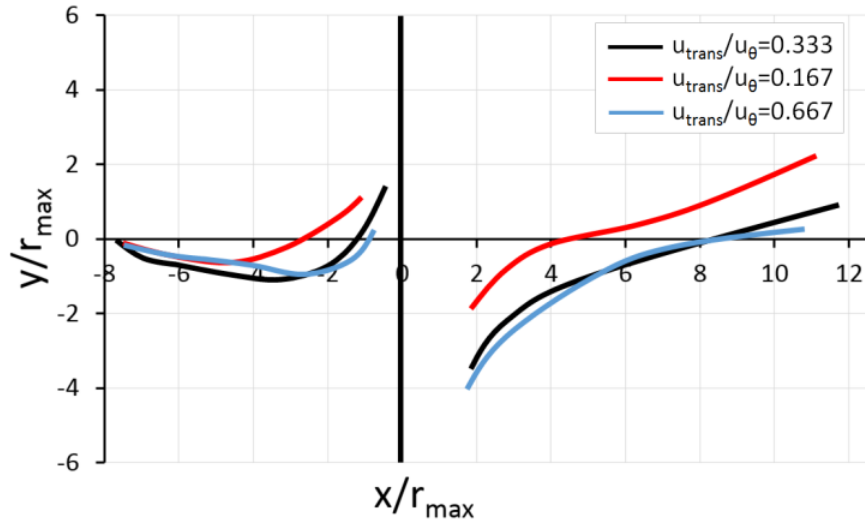
Figure 5.58 Near-ground lateral displacements of vortex for prisms of translational velocity.

As soon as the three vortices enter the computational domain, they exhibit lateral displacement in the negative y-direction. At about $4 \cdot r_{max}$ distance from the windward wall the slowest vortex changes its travelling direction towards the positive y-direction. The reference vortex and the fastest vortex exhibit similar path characteristics, but the change in the path direction happens at different distance away from the windward wall. The lower the impact parameter is the faster the vortex starts to deflect in the positive y-direction. For the low free stream velocity the vortex induced velocities dominate the flow field and the vortex the ambient velocity. Behind the prism the path of Vortex 2 (low impact parameter) differs from others. Vortex 2 recovers its circulation closer to the x-axis, and the vortex lateral displacement right behind the prism is about $2 \cdot r_{max}$. For larger impact parameters, the vortex lateral displacement right behind the prism is about $4 \cdot r_{max}$.

140

For all three cases of the translational velocity the curvature of the path behind the prism is similar.

- *Forces on Prisms*

The influence of the translational velocity on the forces induced on the prism is included in Table 5.13. The force coefficients caused by Vortex 1, Vortex 2 and Vortex 3 were calculated with the reference velocity equal to respectively 4.0, 3.5 and 5.0 units. The difference in the reference velocity is caused by the different maximum horizontal velocity (the sum of the rotational velocity and the translational velocity) for each vortex. The projected area for forces in x-direction was assumed as an area of the leading face of the prism. For z-direction forces, the roof area was taken as a projected area.

Table 5.13 Maximum instantaneous forces on prism during vortex-prism interaction.

Vortex	Impact Parameter, u_{trans}/u_θ	C_x	C_z
2	0.167	0.218	0.265
1	0.333	0.203	0.225
3	0.667	0.188	0.198

The increase in the impact parameter results is lower aerodynamic forces on the prism walls. Both in streamwise and in the vertical direction the total force on the prism is dependent on the impact parameter.

- *Sheltering Effect*

The maximum flow speeds behind the reference prism caused by Vortex 2 and Vortex 3 are presented in Figures 5.59 and 5.60.In each grid point, the maximum flow velocity is chosen from all *xz*-planes, according to Figure 5.17. The same kind of contour for Vortex 1 is presented in Figure 5.32. The difference in the translational speed affects the maximum flow speeds around

141

the prism. It is observed that for the slow vortex the flow field around the wall is significantly

mitigated (Figure 5.59). This means that the main vortex strength was affected, while

approaching the prism. However, the vortex exhibits high velocities, right behind the prism, in

the sheltering regions, which is not desired. For the slowest translational speeds the vortex

spends more time in the sheltering regions. Due to that it can recover its circulation behind the

prism faster and induce higher velocities. For the faster translational speed (Figure 5.60) the

consolidated velocity magnitude contour is different. The vortex keeps the high flow velocities

during the interaction. It is observed from the contour (Figure 5.60) that the vortex is cut by the

prism and flies behind the prism, leaving the low-velocity region. Outside the sheltering region

the velocities are higher. The vortex recovery occurs about 22 units away from the leeward face

of the prism.
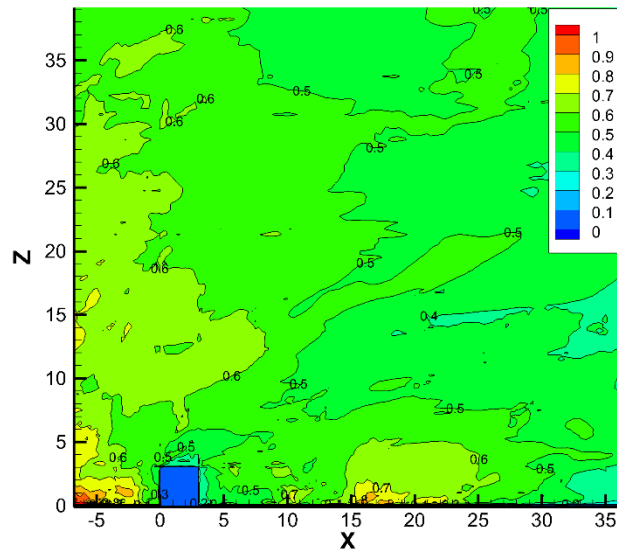
Figure 5.59 Normalized maximum velocity
magnitude xz-contour for Vortex 2.
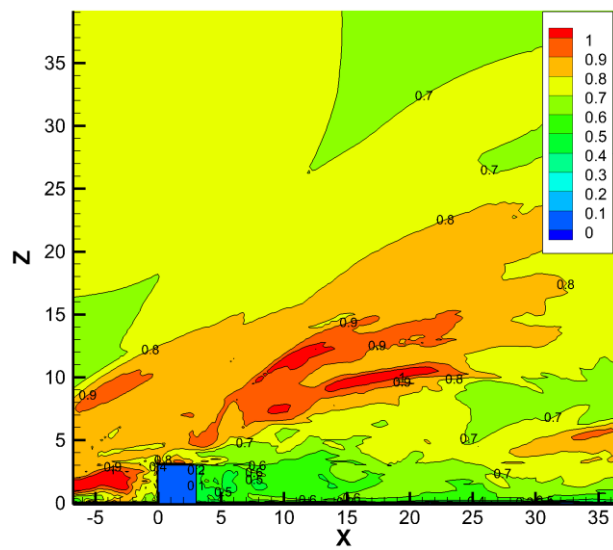
Figure 5.60 Normalized maximum velocity
magnitude xz-contour for Vortex 3.

Figures 5.61 and 5.62 illustrate the maximum flow speed reduction in xy-plane. The slower

vortex exhibits higher strength before the prism. However, the maximum velocity is significantly

142

reduced right in front of the prism. The same effect was observed in the consolidated pressure contour (Figure 5.56). On the other hand, the fast vortex is gaining the strength as it is closer to the prism. Also a sudden displacement in the lateral direction, near the windward wall, is observed. Behind the prism the velocity magnitude of both vortices is substantially reduced.
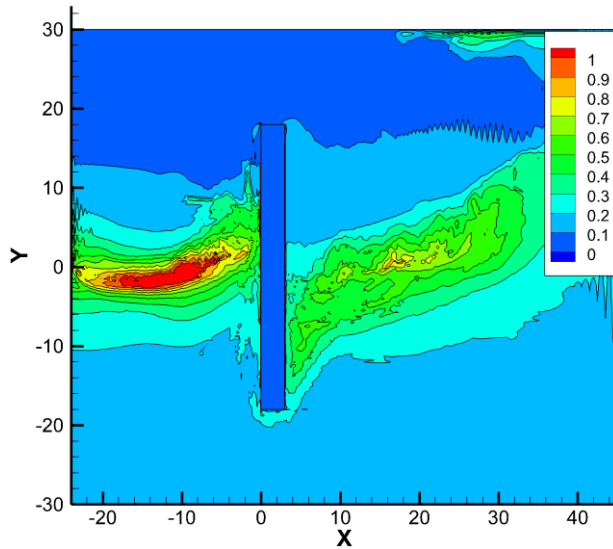
Figure 5.61 Normalized maximum velocity magnitude xy-contour for Vortex 2.
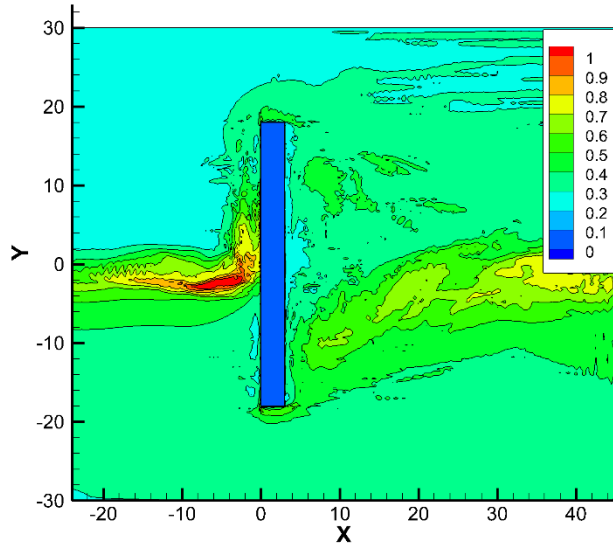
Figure 5.62 Normalized maximum velocity magnitude xy-contour for Vortex 3.

The influence of the vortex translational velocity on the sheltering abilities of the prism is estimated based on the flow speed reduction. The flow speed reduction is calculated as a percentage difference between the maximum flow speed found in the sheltering zone and the maximum flow speed of the no-prism simulation. For each translational speed the vortex induces different maximum flow speed, since the maximum flow speed is a sum of the maximum tangential velocity and the vortex translational velocity. Thus, the flow speeds in each simulation are normalized to a different number. Table 5.14 includes the flow speed reduction in the sheltering regions for the three vortices.

143

Table 5.14 Vortex transitional velocity influence on flow speed reduction in sheltering regions.

Vortex #	Impact parameter, u_{trans}/u_θ	Region 1	Region 2	Region 3	Shelter length ($u_{red} > 30\%$)
2	0.167	29.4 %	38.9 %	16.0 %	2.38H (86m)
1	0.333	45.0 %	43.5 %	28.5 %	5.67H (204m)
3	0.667	36.0 %	39.2 %	28.9 %	3.68H (133m)

The impact parameter is observed to affect the flow velocities in the sheltering regions. When the translational speed is equal to 1/3 the maximum tangential velocity, the prism exhibits the best sheltering abilities. When the vortex translational velocity is small relatively to the maximum tangential velocity, the sheltering abilities are decreased. The prism's sheltering abilities are also decreased when the vortex translational velocity is almost equal to the maximum vortex rotational velocity. Thus, there is no proportional relation between the impact parameter and the sheltering effect of the prism. For Vortex 2 and Vortex 3, the best sheltering effect is observed in Region 2, while for the reference vortex, the best sheltering abilities are in Region 1. In Region 1 the maximum flow velocities are between 29-45% reduced for the different vortex translational speeds. This would reduce aerodynamic forces on possible structures located in Region 1 by at least twice, irrespective of the vortex translational speed.

5.7 Conclusion

Large eddy simulation was employed to numerically simulate the Rankine vortex interaction with a wide rectangular prism. First, the perpendicular vortex interaction with the reference prism was investigated in detail. The particular case of the Rankine vortex impact on the prism could be representative of a tornado-like wind interaction with a large natural or man-made structure. The height and the length of the reference prism were equal to the vortex core radius.

The reference prism was also 6 times wider than the vortex core. In such a case the vortex was unable to travel smooth and undisturbed over the prism. During the travel the near-ground portion of the vortex undergoes streamwise bending and lateral displacements, deviating from the assumed path. The translating vortex is also blocked by the leading face of the prism. To continue with a travel the simulated vortex had to introduce a new near-ground circulation behind the prism. This resulted in a creation of a low-velocity zone behind the prism. The quantitative analyses of the sheltering efficiency of the prism were conducted by plotting maximum resultant velocities on a single resultant velocity contour. Based on such a contour the area behind the prism was divided into 3 sheltering regions. It was demonstrated that the most favourable sheltering conditions are right behind the prism. The prism of the height and the length equal to the radius of the vortex core can reduce flow speeds by more than 28.5% on a distance of six times the prism height, away from the leeward wall.

The parametric study was conducted to reveal the influence of the prism size and vortex translational velocity on vortex path deviations and the sheltering effect. In the parametric investigations, the following parameters were studied:

- *Prism Length Parameter.* It was defined as a ratio of the prism length to the Rankine vortex core radius. When the prism length was greater than the vortex core radius, the vortex established flow rotation on the prism ridge. The low-level circulation was transferred from the ground to the roof of the prism and then from the prism roof on the ground, behind the prism. For thin, wall-type prisms, the low-level vortex was unable to circulate on the top of the prism. The Rankine vortex had to create a new near-ground vortex behind the prism. This led to abrupt split of the low-level portion of the vortex and mitigation of the vortex flow speeds. The investigations of flow speed reductions in the

145

sheltering regions showed that the lower the prism length is, the better sheltering abilities it exhibits. The wall-type prism exhibited the best sheltering effect. It reduced flow speeds more than 30% on a distance of about eight times the prims height

- *Prism Height Parameter.* It was defined as a ratio of the prism height to the Rankine vortex core radius. The height parameter was demonstrated to be crucial in the vortex-prism interaction. When the prism height was greater or comparable to the radius of the forced vortex region, the prism caused mitigation of the vortex flow speeds and the vortex path deviation. For the prism three time smaller than the vortex core radius the vortex kept its strength and the straight path during the entire travel. Since the vortex was not disrupted, the sheltering abilities of small and flat prisms were limited to a fine sheltering zone. Assuming that the sheltering region size is proportional to the prism height, the sheltering effect was observed for all of the analyzed prism height parameters. At least 33% of the flow speed reduction, in Sheltering Region 1, right behind the prism, was provided regardless of the prism height parameter.

- *Impact Parameter.* It was defined as a ratio of the Rankine vortex translational velocity to the vortex core radius. The impact factor between 0.167 and 0.667 was studied. The impact parameter was found to affect the strength and the path of the travelling vortex. For the impact parameter equal to 0.667, the travelling vortex kept its straight path and deviated just before the windward wall. When the free stream flow that carries the vortex is relatively small comparing to the maximum vortex tangential velocity, the vortex starts to deviate sooner before the windward wall. Also, when the free stream flow was much less than the vortex rotational speed, the secondary vorticity ejection from the boundary layer of the prism leading face was enhanced. As a result, the flow speeds of the

146

translating vortex were greatly reduced even in front of the prism. In the case of the sheltering effect, no clear relation to the impact parameter was observed. Regardless of the impact parameter, the flow speeds on the prism leeward side were reduced by more than 29%, on a length equal to three times the prism height.

6. TORNADO-BREAK WALL

6.1. Introduction

In this section a new idea of a tornado-break wall is introduced. Based on the vortex-prism interaction studies it was found a wall-type prism exhibits sheltering performance from tornado-like flow. Thin and wide prisms mitigate the travelling vortex structure and strength more effectively than long and wide prisms. The vortex strength mitigation results in the lower vortex-induced flow velocities in the leeward side of a prism. Quantitative measurements of the sheltering effect of the vortex-wall interaction are the main objective of this section. The idea of the tornado-break wall was originated from three sources:

- Post-damage observations of different tornado outbreaks in complex terrain (Selvam & Ahmed, 2013): uneven damage on the windward and leeward side hills.
- CFD simulations of the Rankine vortex interaction with two-dimensional rectangular-shaped prisms: *Chapter 5.*
- Literature review on windbreak walls, protecting various structures from the straight-line winds.

The sheltering performance of tornado-break walls is measured as wind speed reduction in the sheltering regions. The sheltering region dimensions are consistent with those used in Chapter 5 (Figure 5.20). The wind speed reduction is reported for different wall sizes and different angles of tornado-like vortex impacts to observe performance of a tornado-break wall. In this chapter the wind forces on the sheltering walls are also analyzed.

6.2. Problem Geometry and Computational Model

6.2.1. Tornado-like Vortex Modelling

A modified version of the three-dimensional CFD model, reported in *Chapter 3*, is used to simulate the tornado-like flow over a wide wall. The tornado-like flow is modelled using the Rankine Vortex Model (RVM). According to Doppler radar data of actual tornadoes (Wurman, Robinson, Alexander, & Richardson, 2007; Kosiba, Robinson, Chan, & Wurman, 2014), the horizontal and the vertical wind velocity distribution varies among tornado outbreaks. Also, a particular tornado constantly changes its structure over the travel. This resulted in many different tornado mathematical models. In the current study the choice of the tornado vortex model is dictated by the numerical modeling requirements. Among the retrieved tornado velocity models, the RCM satisfies the Navier-Stokes equations and at the same time exhibits a tornado-like wind velocity distribution (Kosiba, Robinson, Chan, & Wurman, 2014).

The Rankine vortex is characterized by three parameters: α – the vortex strength, r_{max}- the radius of the forced vortex region and u_{tran} – the translational velocity of the vortex. The vortex is transported with the straight-line wind equal to the vortex translational velocity. The non-dimensional Rankine vortex parameters, and converted dimensional values, are reported in Table 6.1.

Table 6.1 Tornado-like vortex parameters and ground roughness for tornado-wall interaction.

Units	α	r_{max}	u_{tran}	$u_{\theta,max}$	u_{max}	z_0
Dimensionless	1.0	3.0	1.0	3.0	4.0	0.00375
SI	1.0 (s^{-1})	30 m	10 ms^{-1}	30 ms^{-1}	40 ms^{-1}	0.0375 m
U.S.	1.0 (s^{-1})	98 ft.	22.4 mph	67.1 mph	89.5 mph	1.48 in.

Table 6.1 also includes the ground roughness, which is assumed to be a height of grass. The vortex is assumed to travel along *x*-axis with a translational velocity, u_{tran}, of 1.0 unit (10 m s^{-1}).

149

This means that the centre of the vortex moves 1.0 x-distance unit (10 m) per 1.0 time unit (1 sec). The maximum tangential velocity, on the vortex core radius, is equal to 3.0 units (30 m s^{-1}). The sum of the translational velocity and the maximum tangential velocity gives the maximum assumed horizontal wind speed.

6.2.2. Computational Domain and Wall Dimensions

The computational domain dimensions and the reference wall size are included in Table 6.2.

Table 6.2. Reference prism size and computational domain size.

Units	Tornado-break wall			Computational Domain		
	$L\ (x)$	$W\ (y)$	$H\ (z)$	$l_D\ (x)$	$w_D\ (y)$	$h_D\ (z)$
Non-dimensional	0.25	36.0	2.0	69.0	60.0	48.0
SI	2.5 m	360 m	20 m	690 m	600 m	480 m
U. S.	8 ft.	1181 ft.	66 ft.	2264 ft.	1969 ft.	1575 ft.

The domain and the wall parameters are provided in dimensionless units, SI units and U.S. units. Figure 6.1 presents the computational domain with the reference wall. The description for the wall dimensions is found in Figure 6.2.
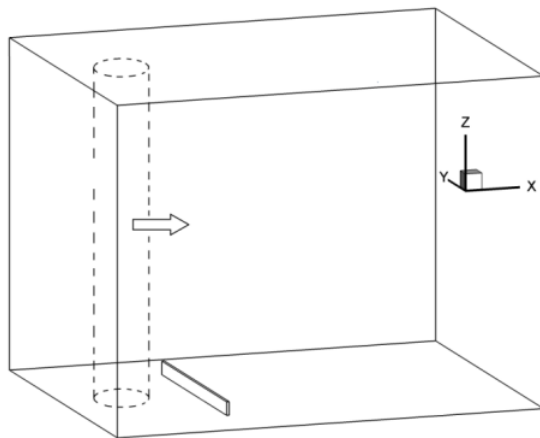
Figure 6.1 Isometric view of the computational domain with reference wall.
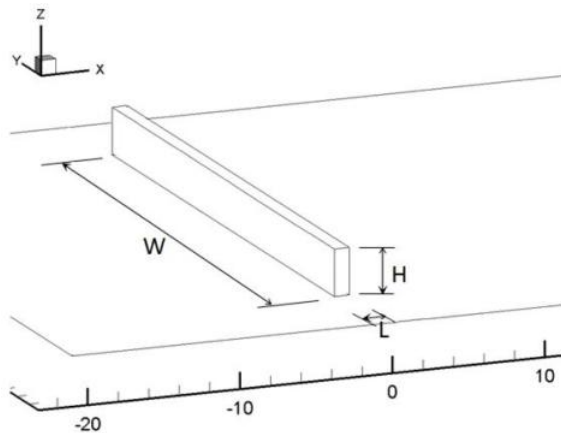
Figure 6.2 The nomenclature for wall dimensions.

150

The reference wall has height of 2.0 units (20 m), which is one third of the vortex core diameter. The wall is also six times wider than the vortex core diameter. The tornado-break wall is assumed to be located closer to the inlet boundary, since the region behind the wall is of main interest for the sheltering effect study. At the bottom surface and on the tornado break-wall faces the no-slip boundary conditions are used. The ground boundary layer is modelled using the logarithmic law. The fluid velocity increases until the top level of the on the tornado break-wall. The boundary layer on the tornado-break wall faces is resolved by fine grid. The computational domain is a rectangular block with dimensions 69.0 x 60.0 x 48.0 units.

6.2.3. Grid Refinement

The computational mesh for the vortex-wall interaction is constructed following the conclusions from the *Grid Resolution* section. Table 6.3 includes the grid parameters.

Table 6.3 Grid resolution for the vortex-wall interaction.

GRID	Grid spacing on vortex path	Grid spacing outside vortex path	First grid spacing next to wall faces	Grid points (x, y, z-axis)	Total # of grid points
A1	0.25	0.50	0.001	246x205x145	7,312,350

The numerical model consists of about 7.3 million grid points. The grid spacing of 0.25 units is applied in the most of the domain. The boundary layer on the tornado-break wall faces is resolved by the application of fine grid of 0.001 units. For the applied computational model the influence of the grid resolution on the vortex-induced forces, was studied by Selvam and Millett (2005). They showed that tornado-wind forces converge when the first grid spacing next to the building is at least 0.005D, where D is a dimension of the building. On the ground boundary

layer the logarithmic law is applied and the refined grid is not required. Figure 6.3 illustrates different planes of the discretized domain.
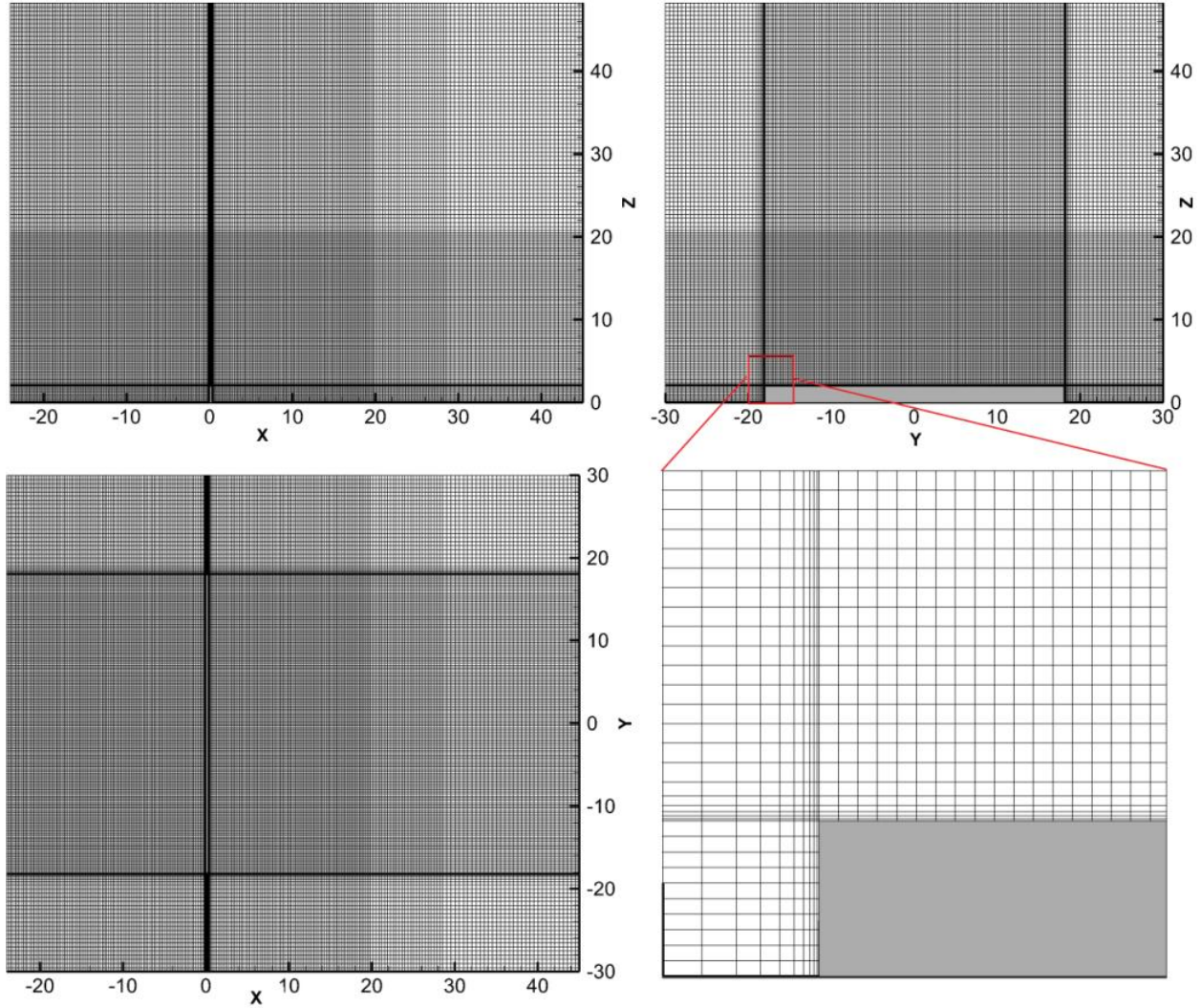
Figure 6.3 Grid refinement in different views for the vortex-wall interaction simulations.

In the *xz*-plane the grid is more refined on the tornado's path. The grid spacing there is equal to 0.25 units, which is $1/12 \cdot r_{max}$. The lane of refined mesh spreads over the entire wall span. Outside the wall span, the grid spacing in *y*-direction is equal to 0.5 units. In the vertical direction the grid spacing is 0.1 units on the wall level and it gradually increases until 0.5 units at the top of the domain.

6.3. Interaction of Tornado-like Vortex with Reference Wall

The tornado-like vortex is translated in the free stream direction (along x-axis) with a constant impact speed, u_{trans}, towards the wall. At the beginning of the simulation the center of the vortex circulation is assumed to be 90 units before the wall in the streamwise direction. This means that the vortex core starts the travel outside the domain and it is smoothly introduced inside of the domain using the appropriate boundary and initial conditions. The simulation begins with the free stream flow that slowly changes into the rotational. This reduces any anomalies created by the superposition of the vortex flow over a free stream flow. According to the prescribed boundary conditions the center of the vortex is supposed to coincide with the center of the wall at t=90 units. Figures 6.4a-d illustrate the pressure field during the vortex-wall interaction. The tornado-like vortex is indicated by the low pressure created by the vortical flow. In Figures 6.4a-d each row describes different time instant. Each time instant is visualized by three different images. In the first and the second image, the tornado-like vortex is illustrated by the pressure iso-surface (isometric view and the yz-view). The third image presents the xy-plane through the middle of the wall with the pressure contour.
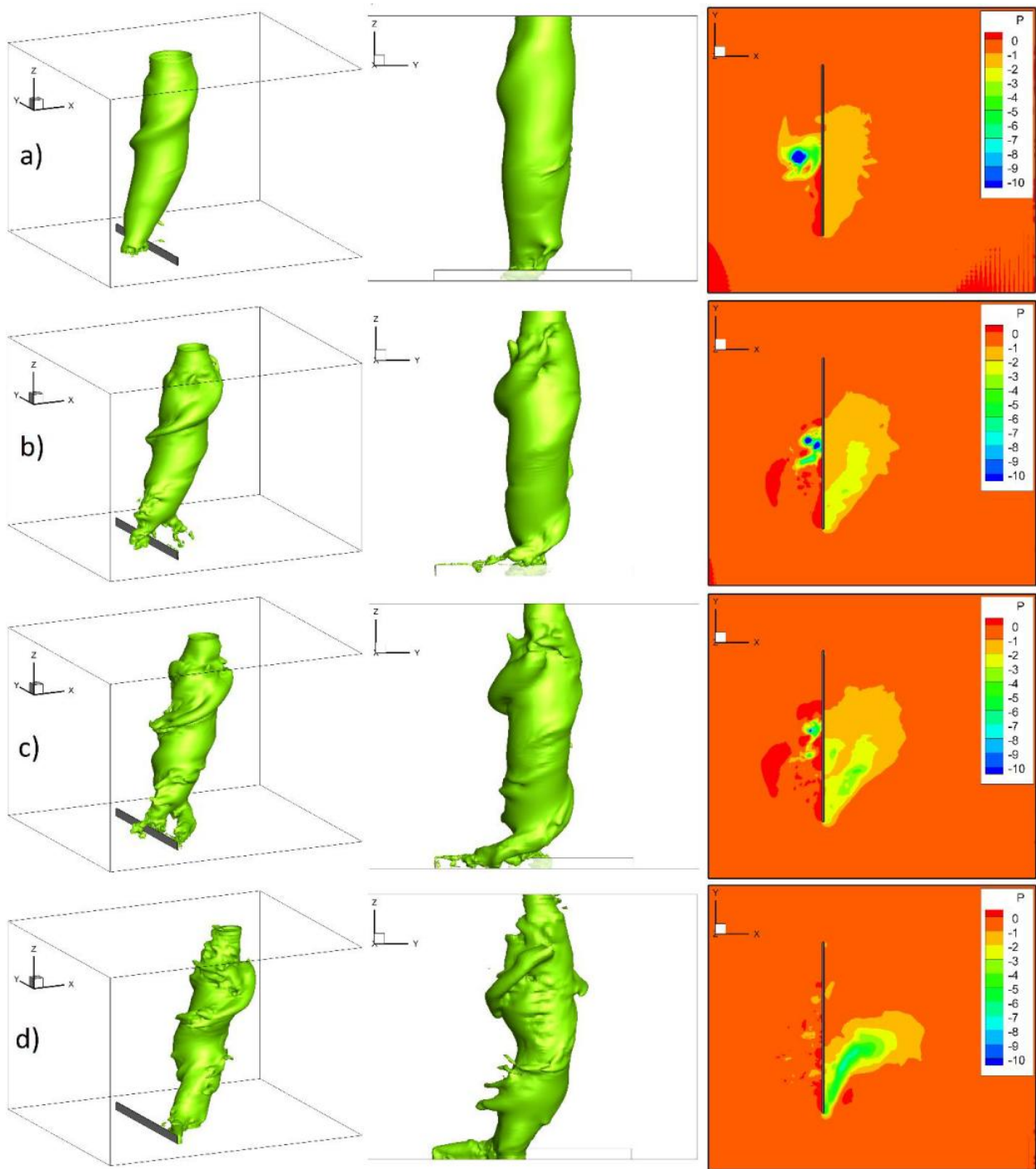
Figure 6.4 Tornado-like vortex structure during the interaction, described by pressure iso-surfaces and contours (P=-3.0): a) t=84.1, b) t=88.1, c) t=90.1, d) t=94.0.

At t=84.1 (Figure 6.4a) the vortex is located in front of the wall leading face. Although the upper

portion of the tornado vortex already crossed the wall, the lower portion of the vortex remains on

154

the windward side of the wall. The blockage of the low-level rotation by the solid wall results in inclination of the tornado-like vortex in the streamwise direction. The vortex is also axially stretched in the vicinity of the wall, which makes the vortex diameter thinner close to the wall and wider above the wall. As the tornado is advected downstream the low-level vortex breaks up and a new near-ground circulation, behind the wall, is established (Figure 6.4b). During this process a lateral displacements of both the original and the new low-level vortices are observed (Figure 6.4c). The vortex in front of the wall is displaced by about core radius distance in the wall spanwise direction. The newly established vortex, behind the wall, is created on the opposite spanwise side of the wall The close-up view of the velocity vector field right above the wall, during the vortex break-up, is illustrated in Fig. 6.5.
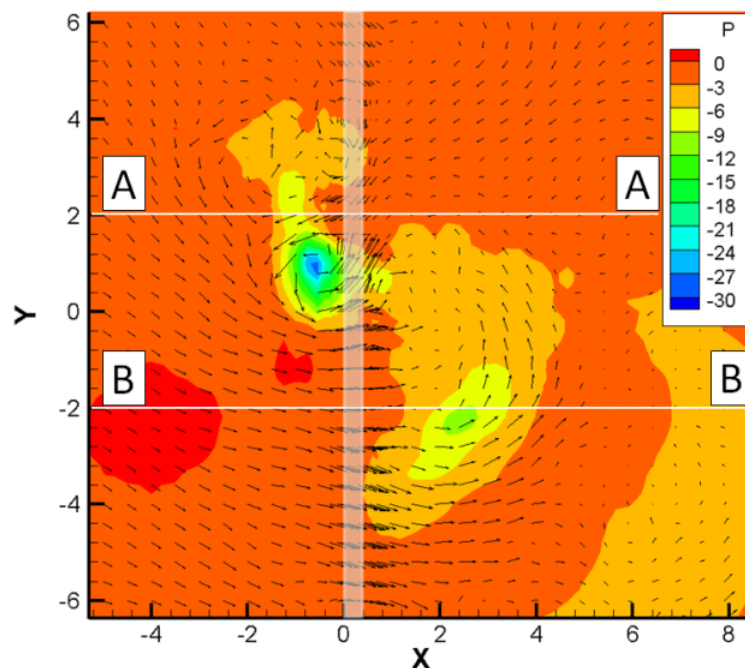
Figure 6.5 Separation of the low-level portion of the tornado into two vortices located on the both sides of the wall (Gorecki & Selvam, 2014).

155

The flow exhibits reversed directions, normal to the wall, which is indicated by lines A and B. The flow in opposite directions results in two recirculation wakes on the opposite sides of the wall. Figures 6.6 and 6.7 show xz-planes formed from the cross sections A and B (Figure 6.5).
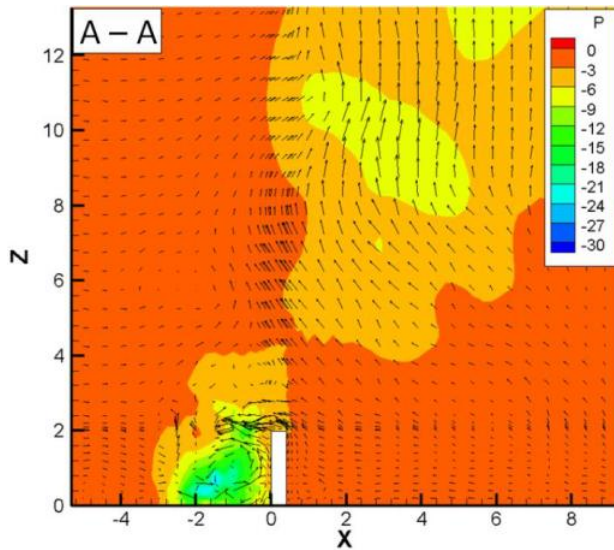
Figure 6.6 Horizontal wake created by the rotational wind near the front side of the tornado-break wall (Gorecki & Selvam, 2014).
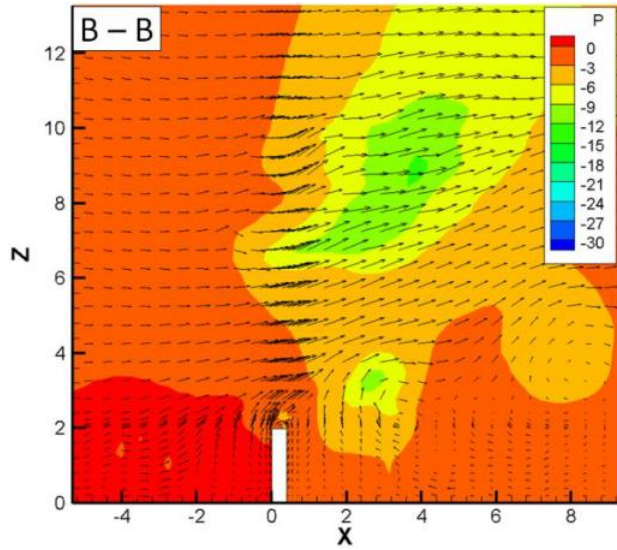
Figure 6.7 Horizontal wake created on the leeward side of the wall (Gorecki & Selvam, 2014).

The two vortices circulate around the wall spanwise direction. During the interaction they form two vortex ends observed in Figure 6.4b. The flow wake behind the prism forms a horizontal vortex along the wall (Figure 6.7). This vortex is then merged to the primary tornado-like vortex.

As the tornado-like vortex travels ahead, the blocked vortex by the wall leading face loses connection with the upper portion of the tornado-like vortex and dissipates (Figure 6.4c). At t=94.0 the tornado circulation is fully transferred behind the wall. The newly formed low-level vortex spreads out spanwise along the wall width. Since the wall is much wider than the tornado, the vortex core cannot surround the wall as it did with a building (Selvam & Millett, 2003). The low-level tornado circulation is significantly influenced by the wall and the tornado-like vortex

reestablishes its original near-ground circulation, only after some distance behind a wall (Figure 6.4d).
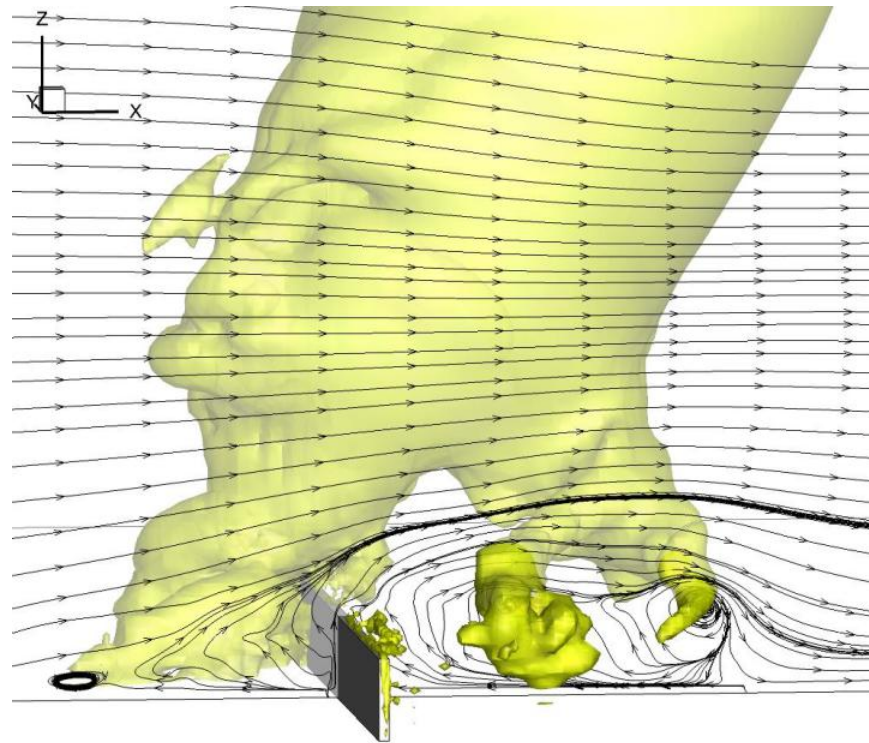
Figure 6.7 Horizontal near-ground vortices originated from the flow wake behind the prism: t=88.1.

The tornado-vortex behavior during the interaction with a wall reveals very similar features as a normal vortex interaction with a thick cylinder (Krishnamoorthy, Gossler, & Marshall, 1999), in which laboratory experiments showed substantial streamwise bending and spanwise displacement of a vortex during the impact. In the orthogonal blade-vortex interaction and the cylinder-vortex interaction it was commonly observed that the translating vortex was influenced by the wall at some distance before the impact (Krishnamoorthy & Marshall, 1998; Krishnamoorthy, Gossler, & Marshall, 1999). The cause was the boundary layer separation and ejection of secondary vortices from the leading surface. The ejection occurred prior the interaction, when the primary vortex was sufficiently close to the body, so that the streamwise

157

velocity component near the body had a negative sign (Krishnamoorthy & Marshall, 1998). The ejected vorticity wrapped around the primary vortex core and caused its degradation over the impact. The similar effect of a secondary vorticity ejection was observed in the current study. In Figure 6.8 the z-vorticity contours, at 0.1H distance above the wall, are illustrated.
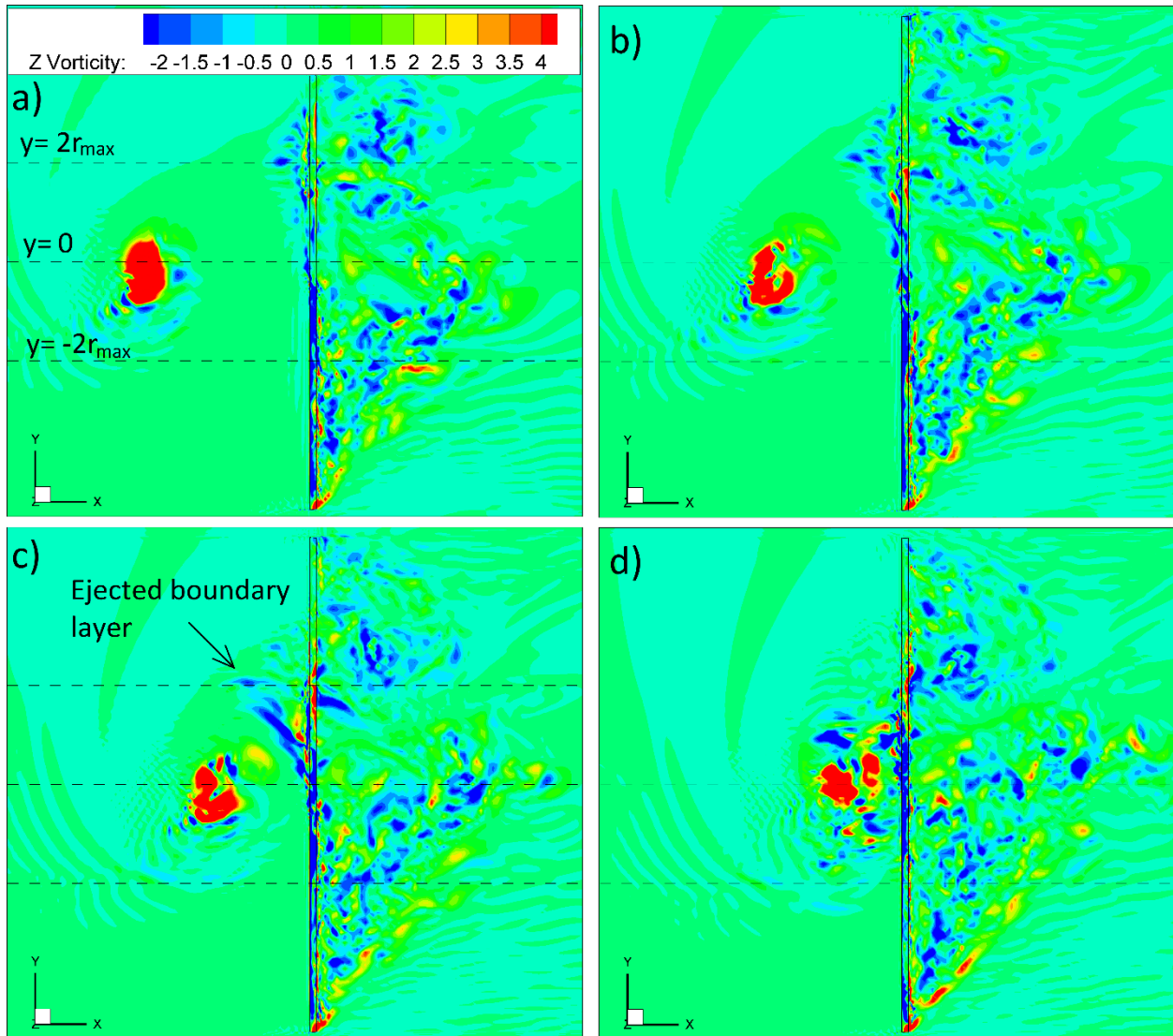
Figure 6.8 Z-vorticity contours right above the wall presenting the ejection of the wall boundary layer (Gorecki & Selvam, 2014).

When the tornado-vortex is far away from the wall the vortex induced velocity around the wall is relatively small and the streamwise component of the fluid velocity is positive along the entire

wall. As the vortex is advected toward the wall the velocities around the wall are more

dominated by the vortex flow. The rotating fluid induces negative streamwise velocity at some

parts along the wall (Figure 6.8a). The boundary layer is separated both from the leading face

and the top face of the tornado-break wall. Figure 6.8a shows that the boundary layer starts to be

ejected at about a vortex core diameter distance from the center of the wall. The closer the vortex

is to the wall, the larger region of the negative vorticity is ejected from the wall (Figure 6.8b). In

Figure 6.8c a clear azimuthal streak of the secondary vorticity separated from the wall boundary

layer is observed. The ejected vortices are found to quickly wrap around the tornado vortex.

Figure 6.9 illustrates that effect using two iso-surfaces with opposite vorticity signs.
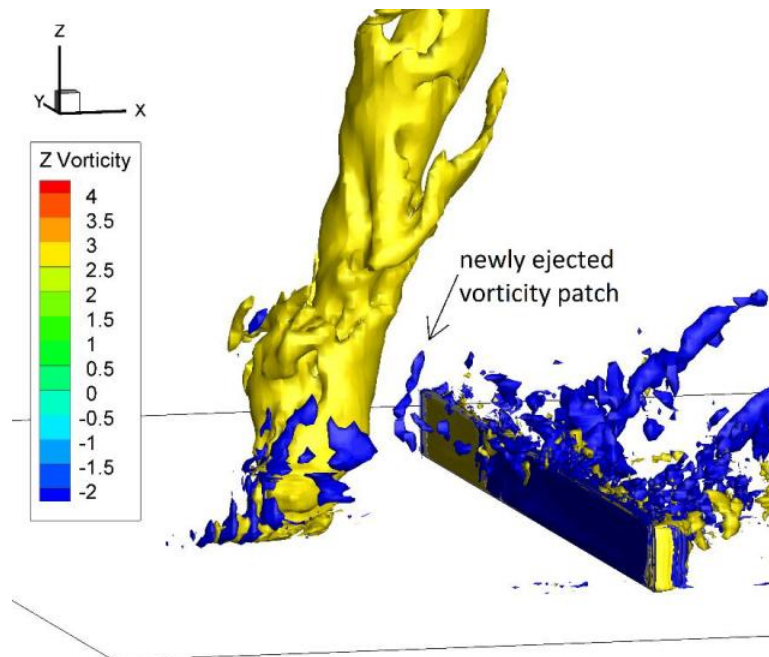
Figure 6.9 Ejected, negative vorticity surrounding the tornado-like vortex (Gorecki & Selvam, 2014).

The near-ground portion of the tornado vortex (yellow) is surrounded by negative vorticity

patches (blue). Above the wall level the tornado vortex core is free from the negative vorticities.

Opposite signs of the vorticity causes diffusion between positive and negative vorticity, which

results in the mitigation of the tornado vortex, similarly as it was described in the blade-vortex interaction (Krishnamoorthy & Marshall, 1998) or wall-vortex interaction (Orlandi & Verzicco, 1993). In Figures 6.8b-d the primary tornado vortex core is observed to gradually change its shape, break up and eventually degenerate (Figure 6.4d).

The disturbance of the tornado vortex strength progresses when the vortex passes the wall. It is noticed in Figure 6.8 that behind the wall the flow is very chaotic. When the tornado vortex passes the wall it encounters greatly turbulent region behind the wall. Such conditions cause further decay of the tornado vortex structure and strength. The damaging influence of turbulence on a columnar vortex was studied by Marshall and Beninati (2005).

6.3.1. Sheltering Effect of Tornado-break Wall

In the engineering point of view the magnitude of the tornado disruption by the tornado-break wall should be quantitatively measured. The tornado-break wall is designed to serve as a tornado barrier and reduce wind forces on structures located on the leeward side. Wind pressure load is a squared function of the corresponding wind velocity. Therefore, the velocity magnitude is the most relevant quantity to analyze in evaluating the performance of the tornado-break wall. The wind speeds behind the wall are constantly changing with regard to time and position. It is very tedious to analyze the entire computational domain, in each time step, to find the highest wind velocities behind the wall. Thus, it is proposed to find only maximum wind speeds behind the wall that occurred during the entire tornado-like vortex translation. Such a result can be plotted on a single velocity contour. In each grid point of the contour a maximum wind speed is found from all xz-planes crossing the wall and over the entire simulation time. The maximum wind speeds, in the contour, are updated after calculation of a successive time step. The xz-planes are

160

chosen since they are perpendicular to the wall spanwise direction and provide the length of the possible sheltering region. The process of finding the maximum wind speeds, V_{max}, from all xz-planes is illustrated in Figure 5.17. A single velocity contour reduces the problem of the sheltering effect into two dimensions and makes it easier to quickly evaluate the performance of the analyzed tornado-break wall.

In Figure 6.10 the xz-contour of the maximum resultant velocities is presented. The maximum velocity magnitudes are normalized to the maximum tornado-induced wind speed for the no-wall simulation (6.92 units or 69.2 ms^{-1}). The sheltering region behind the wall is clearly observed. The wind velocities are reduced up to 8H distance units away from the wall. The wind speed reduction in the most of the sheltering region is greater than 50%. In such a case the wind forces on structures possibly located behind the wall would be decreased by 4 times.
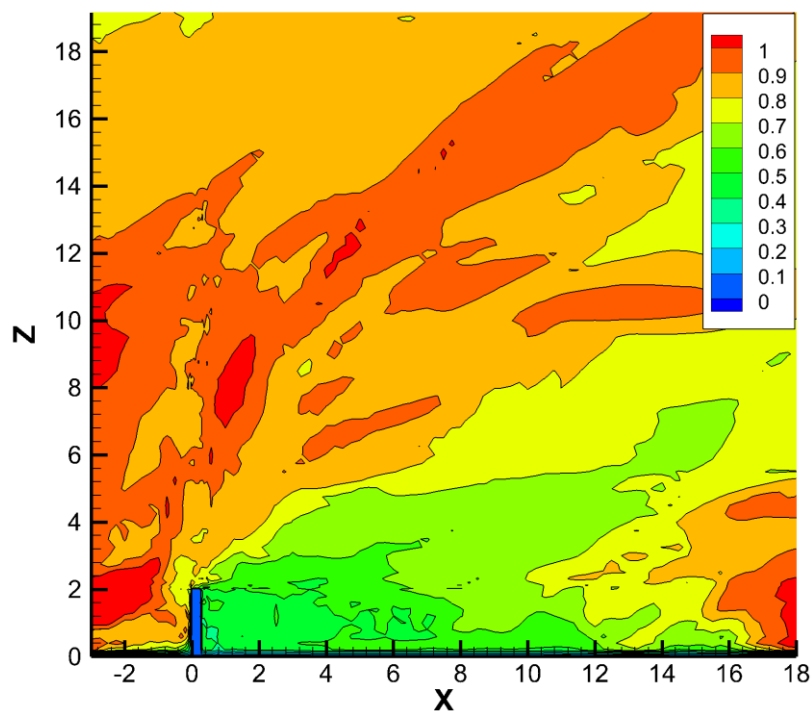
Figure 6.10 Normalized maximum winds speeds around the tornado-break wall for the entire simulation.

In Figure 6.11 the same operation of finding maximum wind speeds, as described in Figure 6.10, is conducted for xy-planes. Only xy-planes up to the wall height are analyzed, since up to this level the sheltering effect is of interest. The highest wind speeds contour reflects the path of the tornado-vortex during the impact. The characteristic lateral displacement in front of the wall and behind the wall, explained in previous sections, is clearly observed. Figure 6.11 shows that the tornado-like vortex path during the interaction with large rigid structures is deviated from the straight direction.
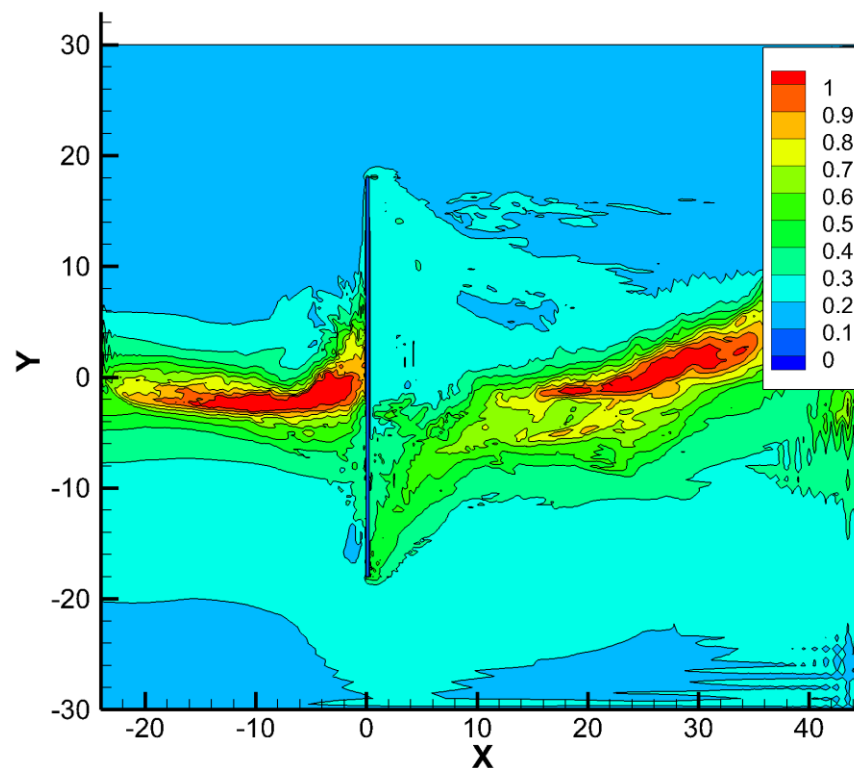
Figure 6.11 Normalized maximum winds speeds captured up to the height of the wall for the entire simulation.

Table 6.4 includes the minimum wind speed reduction in the sheltering regions compared to the tornado-like vortex wind speeds. The dimensions of the sheltering regions are specified in Figure 5.20. Figure 6.12 shows the maximum wind speeds in the sheltering region against the simulation time.

162

Table 6.4 Wind speeds in the sheltering regions for vortex-wall interaction.

Sheltering region	Dimensions	Maximum wins speeds	Wind speed reduction
1	6 x 1.0 (60m x 10m)	37.6 ms^{-1}	45.7 %
2	6 x 1.0 (60m x 10m)	38.8 ms^{-1}	44.0 %
3	6 x 2.0 (60m x 20m)	51.6 ms^{-1}	25.5 %
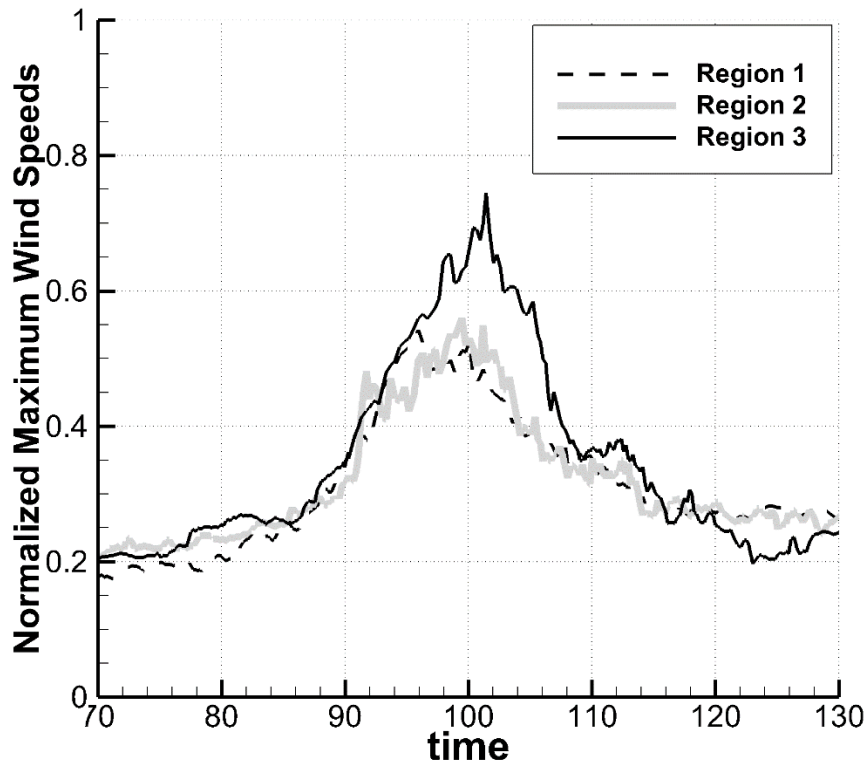
Figure 6.12 Normalized maximum winds speeds in sheltering regions.

The best sheltering effect is observed for Region 1 and Region 2. The 20 m high solid wall provides more than 41 % of the tornado-wind speed reduction in a zone that is 60 m long and 6 m high. The maximum wind speeds are reduced from 69.2 ms^{-1} to 40.8 ms^{-1}. The wind speed reduction in Region 3 is about twice less than in Region 1 and 2. Outside the sheltering regions the wind speeds are much higher (Figure 6.10). The tornado-break wall is more efficient tornado barrier than the prism of the same height, as observed in Table 5.8.

6.3.2. Forces on Tornado-break Wall

On the tornado-break wall only wind pressures in the x-direction are analyzed, since in the other directions the wall is thin and stiff. The x-axis overall force coefficient against the simulation time is presented in Figure 6.13. The projected area is assumed to be equal to 72 units, which is the area of the lading face of the wall. The reference velocity is 40 ms^{-1}.
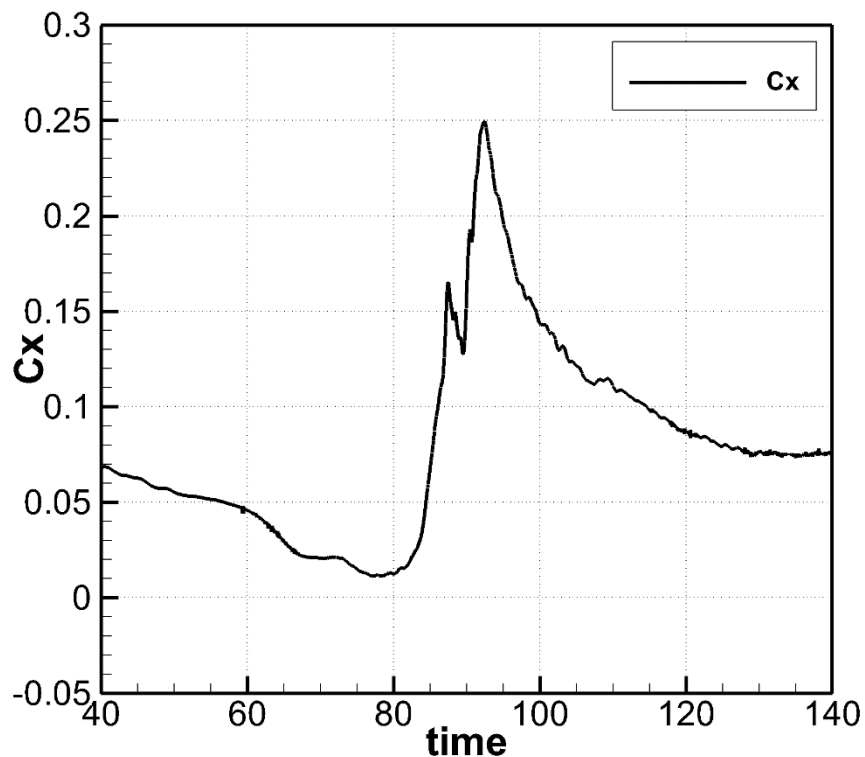
Figure 6.13 Overall force coefficient in x-direction over the simulation time.

The maximum force coefficient of the wall is similar to those observed in the vortex-prism interaction. The maximum force coefficient is equal to 0.250 and it is induced at t=92.4. The pressures on the windward face at this time are presented in Figure 6.14. The pressures on the leeward face are included in Figure 6.15. In both figures the translucent iso-surface of the tornado-like vortex is provided. The maximum pressure coefficient induced on the wall is 5.46.

164
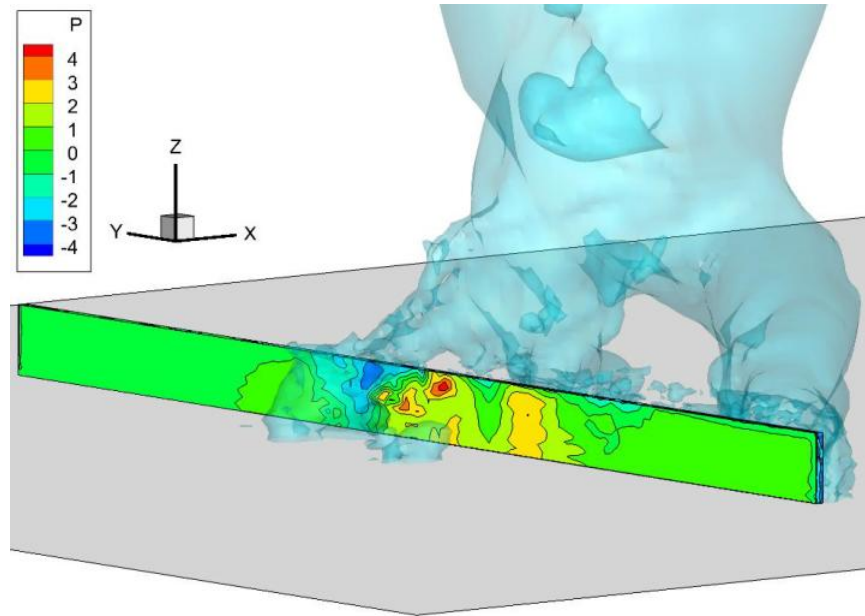
Figure 6.14 Pressures on the windward face of the tornado-break wall, t=92.4.
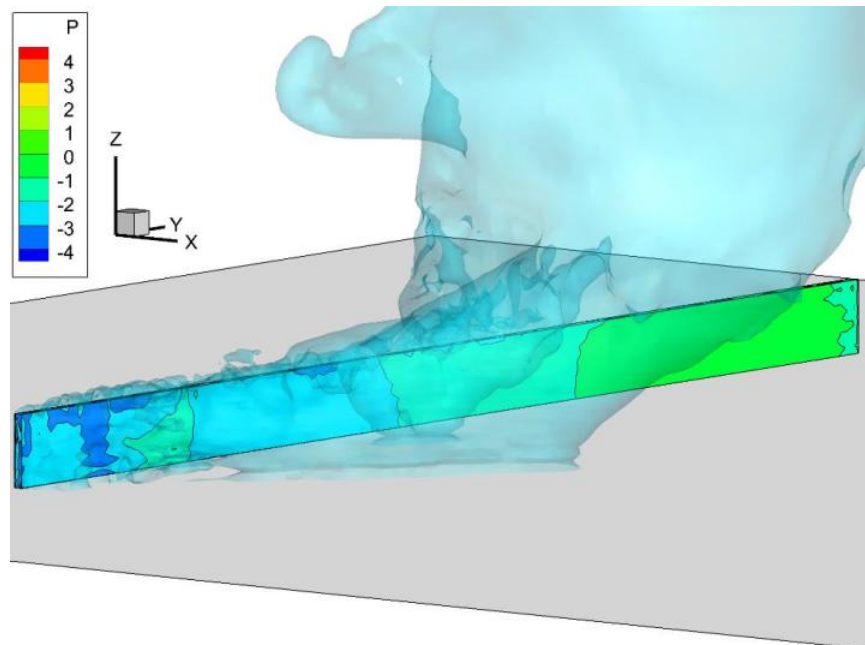
Figure 6.15 Pressures on the leeward face of the tornado-break wall, t=92.4.

The maximum overall force on the wall is induced when the primary vortex already passed the wall. At t=92.4 the blocked thin near-ground vortex induces high pushing force on the windward wall. On the other side of the wall the vortex causes suction on the leeward face.

6.4. Wall Width Parameter

Two additional simulations of the tornado-like vortex – wall interaction are conducted to study the influence of the wall width on the sheltering efficiency. For all simulations the height of the wall is equal to 20 m and the thickness is 2.5 m. The spanwise dimension of the wall is different for each simulation. The dimensions of the walls are summarized in Table 6.5.

Table 6.5 Dimensions of tornado-break walls for width parameter influence study.

Wall	Wall height		Wall thickness		Wall width		Wall width parameter
	ND	SI	ND	SI	ND	SI	W/r_{max}
1	2.0	20 m	0.25	2.5 m	36.0	360 m	12
2	2.0	20 m	0.25	2.5 m	24.0	240 m	8
3	2.0	20 m	0.25	2.5 m	12.0	120 m	4

The two additional prisms are narrower than the reference prism. Intuitively, the sheltering abilities of such walls should be lower. The wall width dimension is related with the vortex core radius by the wall width parameter.

- *Sheltering Effect*

The sheltering efficiency of the walls is measured in the regions defined in Figure 5.20. To calculate the wind speed reduction in the sheltering regions the maximum computed wind speeds are normalized to the maximum tornado-induced wind speed for the no-wall simulation (6.92 units or 69.2 ms^{-1}). Figures 6.16 and 6.17 presents the xz-contours of the maximum normalized wind speeds over the entire simulation time for Wall 2 and Wall 3. It is noticed that the existence of the wall on the vortex path induces higher tornado-like vortex velocities than in the no-wall simulation.

166

Figure 6.16 Consolidated maximum velocity magnitude xz-contour for Wall 2.

Figure 6.17 Consolidated maximum velocity magnitude xz-contour for Wall 3.

The magnitude of the tornado-break wall sheltering efficiency is altered by the wall width dimensions. When the wall is six times wider than the vortex core diameter (Wall 1) the length of the sheltering region is equal to about 8H. In this region the wind speeds are reduced by more than 20%. For Wall 2, which width is four times wider than the vortex core diameter, the length of the sheltering region is reduced by about twice – into about 4H. When the wall width is reduced to twice the vortex core diameter, the length of the sheltering zone is reduced to about 2H. The relation of the sheltering region length to the wall width is illustrated in Figure 6.18.
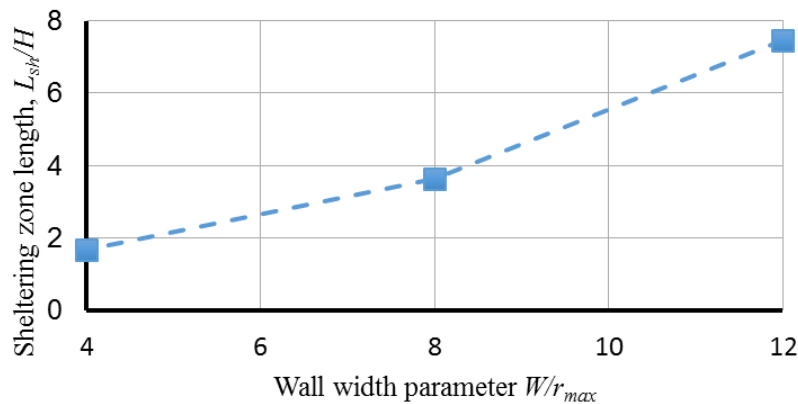
Figure 6.18 Sheltering zone length with wind speeds reduced by at least 20%.

167

Figures 6.19 and 6.20 present the sheltering effect of respectively Wall 2 and Wall 3. The maximum velocity magnitudes are found over the entire simulation time and in all horizontal planes up to the wall height.
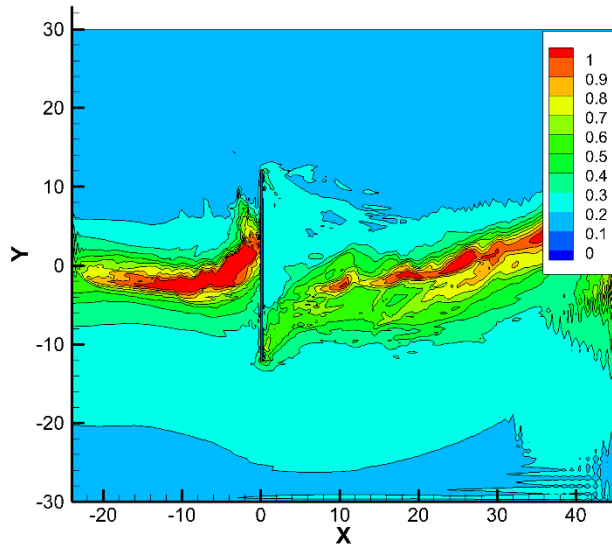
Figure 6.19 Consolidated maximum velocity magnitude xy-contour for Wall 2.
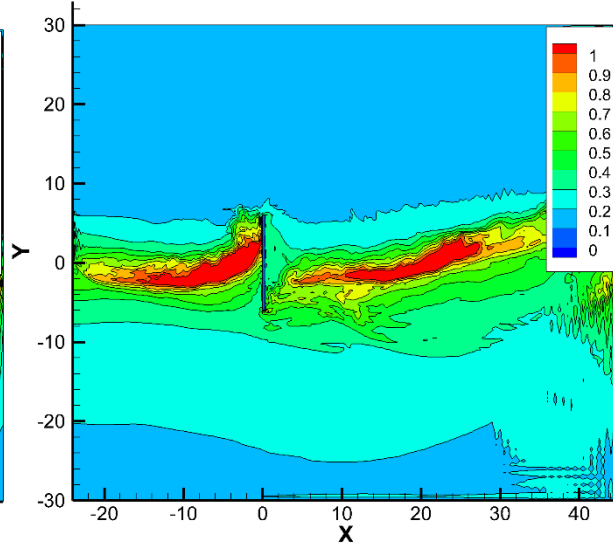
Figure 6.20 Consolidated maximum velocity magnitude xy-contour for Wall 3.

Even the narrowest wall induces both the sheltering effect and the path deviation. For Wall 3 the tornado-like vortex keeps the high velocity magnitudes after the interaction.

Table 6.6 includes the minimum wind speed reduction in the sheltering regions for the tornado-break walls with different width parameter. The dimensions of the sheltering regions are specified in Figure 5.20. Figures 6.21 and 6.22 show the maximum wind speeds in the sheltering region against the simulation time.

Table 6.6 Wind speed reduction in sheltering regions depending on wall width parameter.

Wall #	Wall width parameter, W/r_{max}	Region 1	Region 2	Region 3	Shelter length ($u_{red} > 30\%$)
1	12.0	45.7 %	44.0 %	25.5 %	5.08H (102m)
2	8.0	40.0 %	29.1 %	-2.9 %	2.82H (56m)
3	4.0	2.0 %	0.1 %	-9.2 %	1.42H (28m)

168
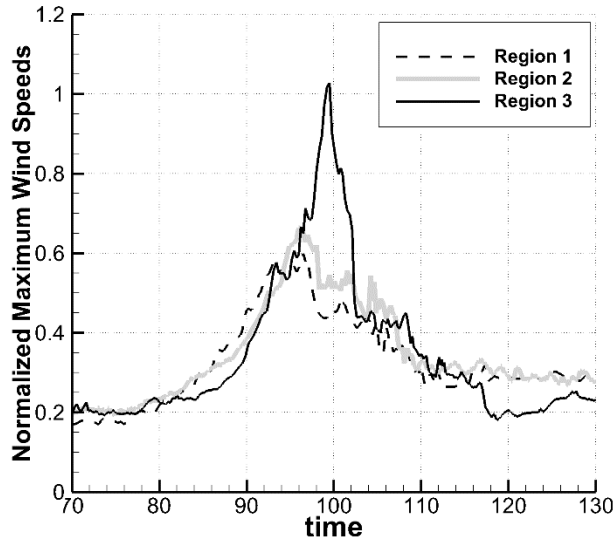
Figure 6.21 Normalized maximum winds speeds in sheltering regions for Wall 2.
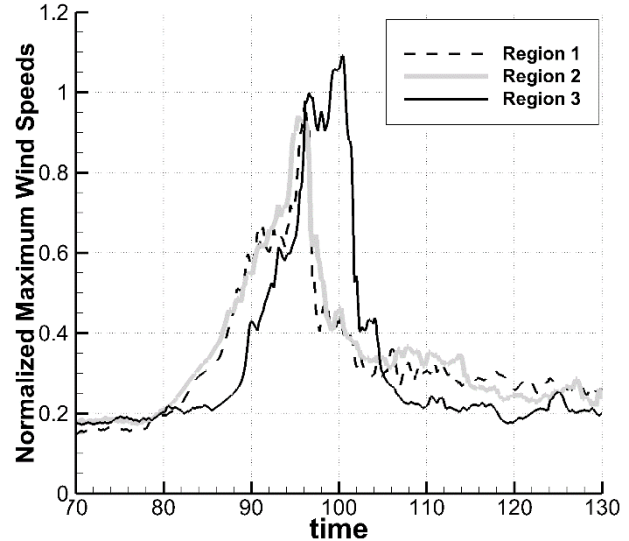
Figure 6.22 Normalized maximum winds speeds in sheltering regions Wall 3.

The sheltering region length is reduced with the decrease in the wall with parameter. This causes substantial wind velocities in the predefined sheltering regions (Table 6.6). To better capture the sheltering effect, the dimensions of the sheltering regions should be related with the wall width and the vortex parameters.

▪ *Forces on Tornado-break Wall*

The overall wind force coefficient induced on the wall for three different wall width parameters is presented in Figure 6.23. The maximum instantaneous force coefficients and pressures on the walls are reported in Table 6.7.

Table 6.7 Maximum instantaneous forces and pressures on walls.

Wall	Wall width parameter, W/r_{max}	$C_{x,max}$	$C_{p,max}$
1	12.0	0.250	0.68
2	8.0	0.330	1.08
3	4.0	0.512	1.21

169
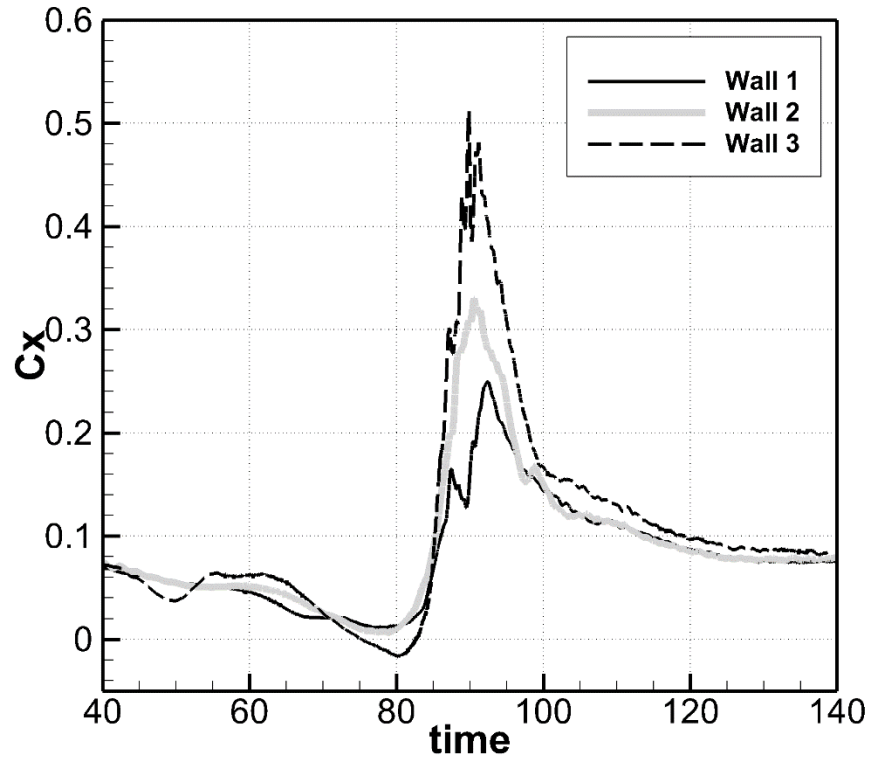
Figure 6.23 Overall force coefficients in x-direction over the simulation time for three walls.

When the vortex is far away from the wall the force coefficients are similar for the three walls. It is noticed that the narrower the wall, the greater the maximum wind force coefficients are. This is related to the tangential wind velocity distribution of a tornado. When the wall is narrow, it is exposed to wind speeds around the vortex core, which are the highest. For wider walls only a certain portion of the structure is subjected to the substantial wind loads.

6.5. Wall Height Parameter

To study the influence of the wall height on the sheltering effect an additional simulations is conducted. The wall height dimension is related to the vortex core radius by the wall height parameter. For all simulations the width of the wall is equal to 360 m and the thickness is 2.5 m. The height dimension of the wall is equal to 10 meters for the additional simulation. The dimensions of the walls are summarized in Table 6.8.

Table 6.8 Dimensions of tornado-break walls for height parameter influence study.

Wall	Wall height		Wall thickness		Wall width		Wall height parameter
	ND	SI	ND	SI	ND	SI	H/r_{max}
1	2.0	20 m	0.25	2.5 m	36.0	360 m	0.667
4	1.0	10 m	0.25	2.5 m	36.0	360 m	0.333

Based on the vortex-prism interaction analysis conducted in *Chapter 5*, it is expected that the wall height parameter lowers the sheltering efficiency of tornado-break walls.

- *Sheltering Effect*

The tornado sheltering efficiency of Wall 4 is measured in the regions defined in Figure 5.20. To calculate the wind speed reduction in the sheltering regions the maximum computed wind speeds are normalized to the maximum tornado-induced wind speed for the no-wall simulation (6.92 units or 69.2 ms^{-1}). Figures 6.24 and 6.25 present the xz- and xy-contours of the maximum normalized wind speeds over the entire simulation time for Wall 4. In Figure 6.26 the maximum velocities are found up to the wall height.
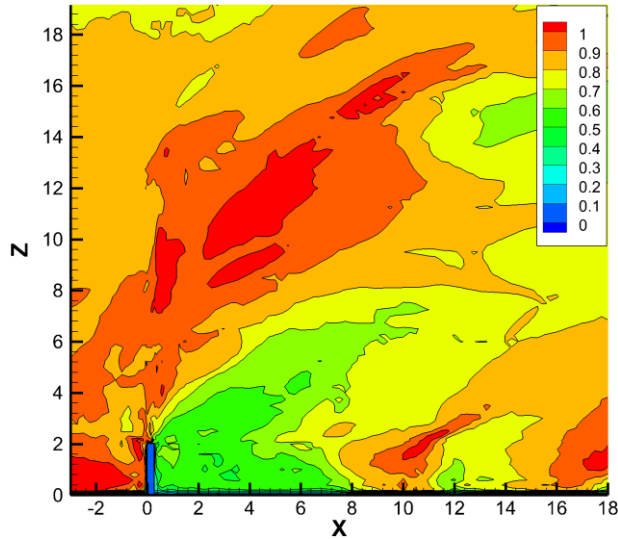
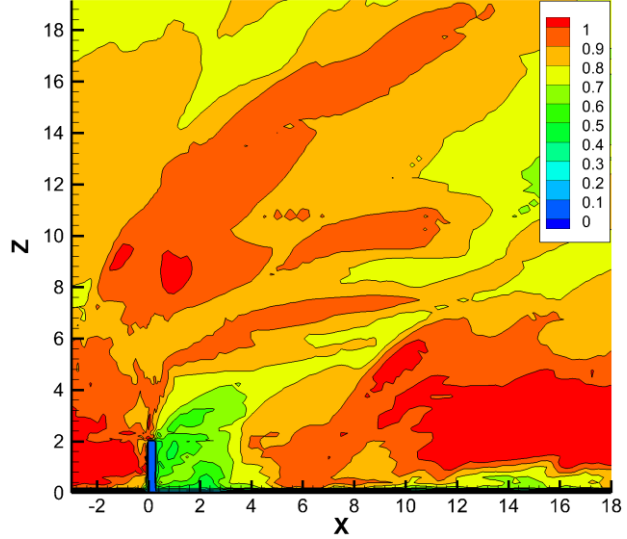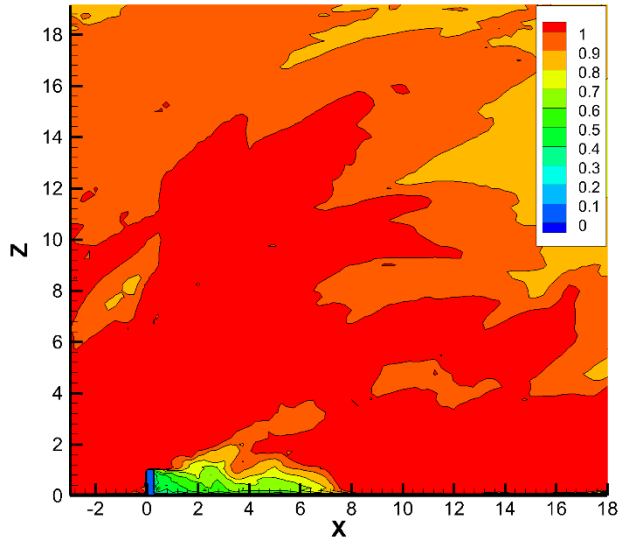**Figure 6.24** Consolidated maximum velocity magnitude xz-contour for Wall 4.
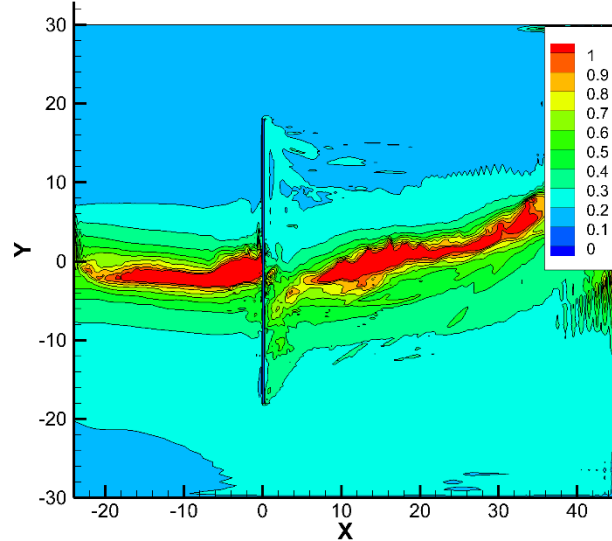
Figure 6.25 Consolidated maximum velocity magnitude xy-contour for Wall 4.

The magnitude of the tornado-break wall sheltering efficiency is clearly lowered when the wall is smaller relatively to the vortex diameter. When the ratio of the wall height to the vortex core diameter is 1/6, the 10 m high wall provides about 60 meters of sheltering region (Figure 6.24). Outside the sheltering region the wind speeds are exceeding 69.2 ms^{-1}, which is the maximum wind speed for the no-wall simulation. In Figure 6.25 it is noticed that the tornado-like vortex induced very high wind speeds right before the interaction. The high wind velocities are preserved behind the wall. Nevertheless, there is a region of low wind velocities on the leeward side of the wall.

Table 6.9 includes the minimum wind speed reduction in the sheltering regions for tornado-break walls with different height parameter. The dimensions of the sheltering regions are specified in Figure 5.20.

Table 6.9 Wind speed reduction in sheltering regions depending on wall height parameter.

Wall #	Wall height parameter, H/r_{max}	Region 1	Region 2	Region 3	Shelter length ($u_{red} > 30\%$)
1	0.667	45.7 %	44.0 %	25.5 %	5.08H (102m)
4	0.333	39.3 %	25.5 %	9.0 %	1.26H (13m)

Figure 6.26 illustrates the maximum normalized wind speeds in the sheltering region against the

simulation time.
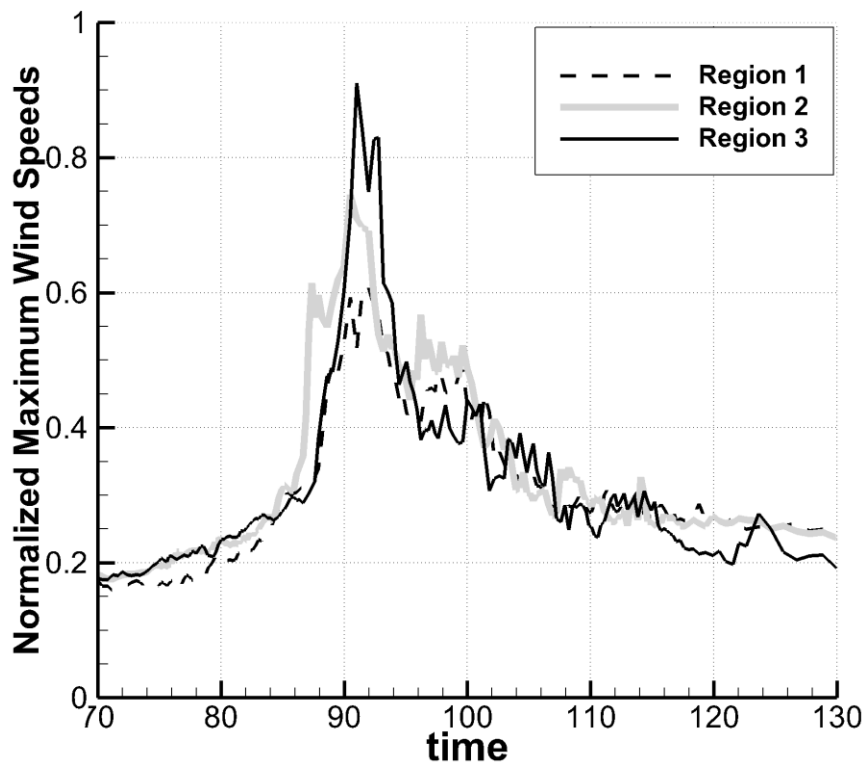
Figure 6.26 Normalized maximum winds speeds in sheltering regions for Wall 4.

The wall of height 10 m provides the most favorable tornado sheltering conditions in Region 1

This region extends for 30 m away from the wall leeward face. Maximum wind speeds in this

region are reduced from 69.2 ms^{-1} into 42.0 ms^{-1}, which is about 40%. Above Region 1, up to the

wall height, the wind speeds are reduced by more than 25.5 %. The lowest wind speed reduction

is observed in Region 3, which ranges from 30 m to 60 m behind the wall. The wind velocities

173

there are less than 63 ms^{-1}. For Wall 4 the tornado wind speed reductions in Region 2 and Region

3 are limited. This may indicate that the assumed size of the sheltering regions needs to be

related with the wall size parameter and the vortex characteristics.

- *Forces on Tornado-break Wall*

The maximum force and pressure coefficients on the two analysed prisms are included in Table

6.10. The overall force coefficient on the walls against the simulation time is plotted in Figure

6.27.

Table 6.10 Maximum instantaneous forces and pressure for different height parameters.

Wall	Wall height parameter, H/r_{max}	$C_{x,max}$	$C_{p,max}$
1	0.667	0.250	0.68
4	0.333	0.262	3.17
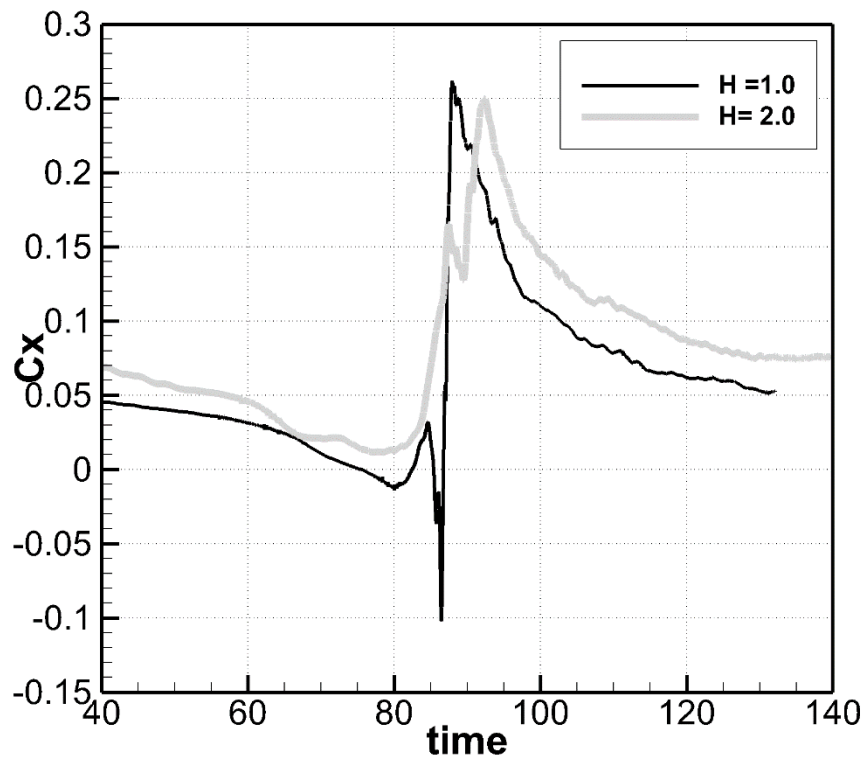
Figure 6.27 Overall force coefficients in x-direction over the simulation time for two wall heights.

174

The translating tornado-like vortex induces about 4.8 % greater force coefficients on the 10 m high wall than on the 20 m wall. Figure 6.27 shows that on the 10 m high wall the vortex creates negative force coefficients of about 0.1 unit, which is not observed for taller walls and prisms. The force coefficient on Wall 4 instantaneously changes its direction. Between t=86.4 s and t=88.0 s the force coefficient increases from -0.1 to 0.262.

6.6. Tornado Impact Angle

To study the influence of the tornado-like vortex angle of attack on the wall sheltering effect, four additional simulations are conducted. The size of the tornado-break wall is similar for the studied simulations. The tornado-break wall is assumed to have the dimensions of the reference wall (Table 6.2). The vortex size, strength and translational velocity are also constant (Table 6.1). The only parameter which varies among the simulations is the vortex impact angle, which is defined in Figure 6.28. The input parameters for the simulations are summarized in Table 6.11. Since the vortex generates asymmetric wind profile, the additional cases of the negative impact angle are analysed. Appendix 2 includes vortex path deviations of the simulated impact angles.

Table 6.11 Input parameters for vortex impact angle influence study.

Vortex	Vortex angle of impact, β	Wall dimensions	
		ND	SI
2	-30°	36.0 x 0.25 x 2.0	360 m x 2.5 m x 20 m
3	-15°	36.0 x 0.25 x 2.0	360 m x 2.5 m x 20 m
1	0°	36.0 x 0.25 x 2.0	360 m x 2.5 m x 20 m
4	15°	36.0 x 0.25 x 2.0	360 m x 2.5 m x 20 m
5	30°	36.0 x 0.25 x 2.0	360 m x 2.5 m x 20 m

175
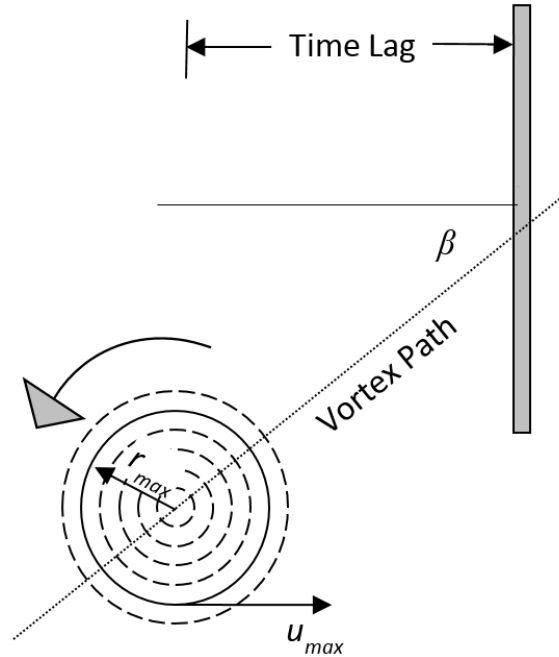
Figure 6.28 Description of vortex impact angle, β.

- *Sheltering Effect*

The sheltering efficiency of the walls is measured in the regions defined in Figure 5.20. To calculate the wind speed reduction in sheltering regions the maximum computed wind speeds are normalized to the maximum tornado-induced wind speed for the no-wall simulation (6.92 units or 69.2 ms^{-1}). Figures 6.29 – 6.32 present the xz-contours of the maximum normalized wind speeds over the entire simulation time for Vortex 2, 3, 4 and 5. It is noticed that the angle of vortex impact influences the maximum wind speeds distribution behind the tornado-break wall. The negative impact angles result in different wall sheltering effect than the positive impact angles.
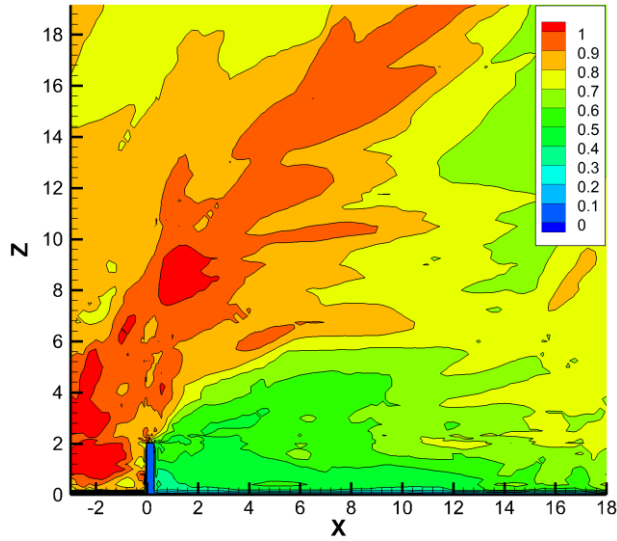
Figure 6.29 Consolidated maximum velocity magnitude xz-contour for -30° impact angle.
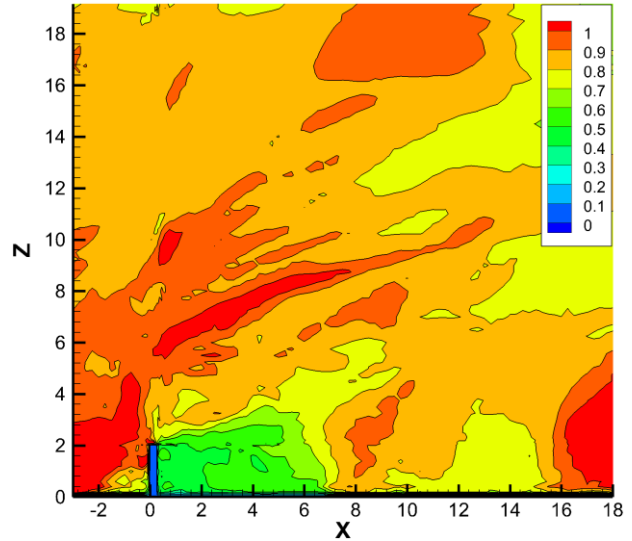
Figure 6.30 Consolidated maximum velocity magnitude xz-contour for 30° impact angle.
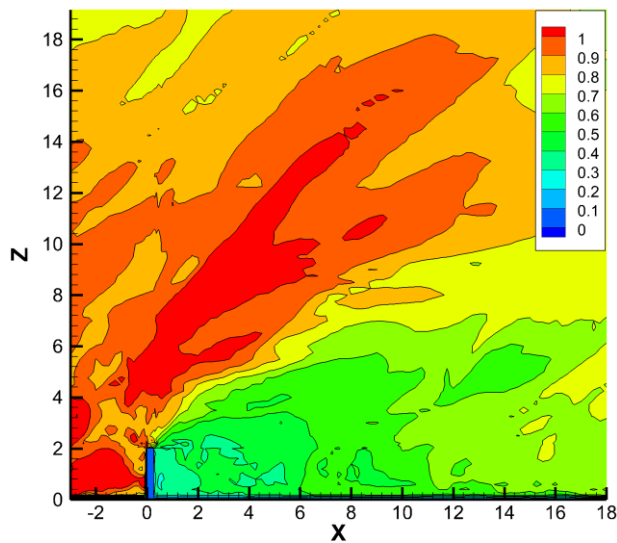
Figure 6.31 Consolidated maximum velocity magnitude xz-contour for -15° impact angle.
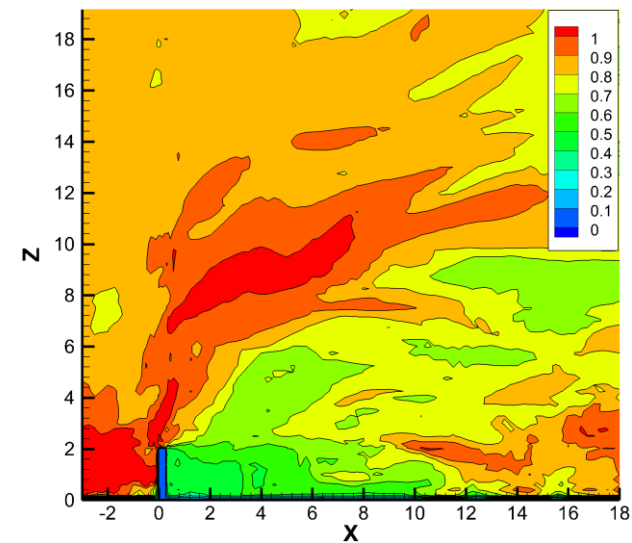
Figure 6.32 Consolidated maximum velocity magnitude xz-contour for 15° impact angle.

When the vortex approaches the wall with the positive angle it causes much higher wind speed behind the wall. This is related with the vortex-structure interaction. The vortex rotates counter clockwise. Thus, when the vortex is very close to the wall it induces velocity components in the positive y-direction. When the tornado-like vortex travels in the same direction the vortex-structure interaction is smooth and sheltering effect is limited.

177

Figures 6.33 – 6.36 illustrate the vortex path and the sheltering effect depending on the tornado impact angle. The maximum wind velocity magnitudes are found over the entire simulation time and in all the horizontal planes up to the wall height.
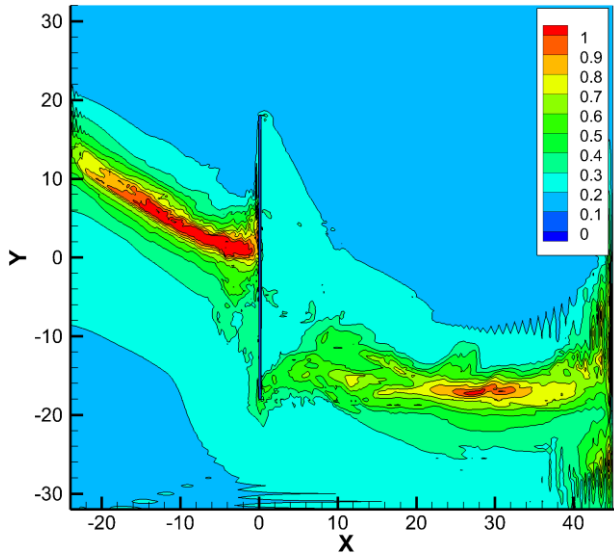
Figure 6.33 Consolidated maximum velocity magnitude xy-contour for -30° impact angle.
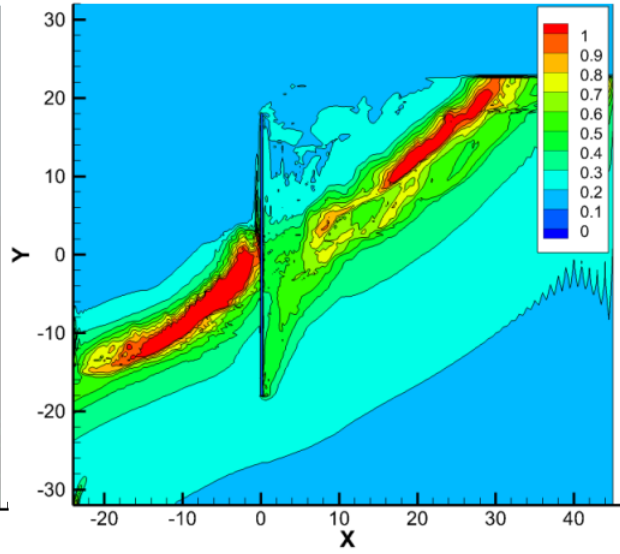
Figure 6.34 Consolidated maximum velocity magnitude xy-contour for 30° impact angle.
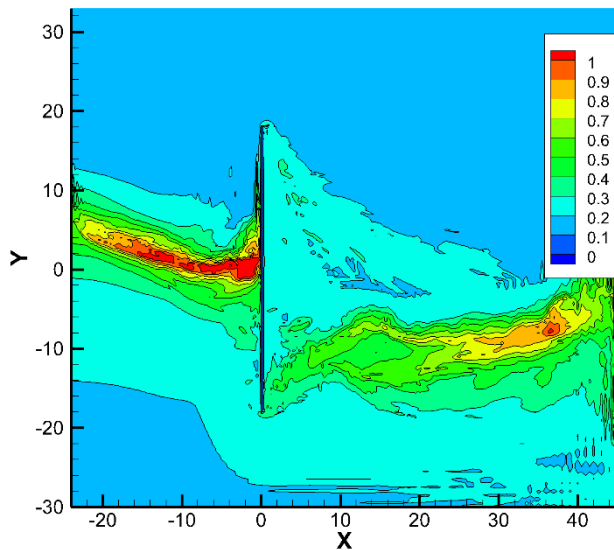
Figure 6.35 Consolidated maximum velocity magnitude xy-contour for -15° impact angle.
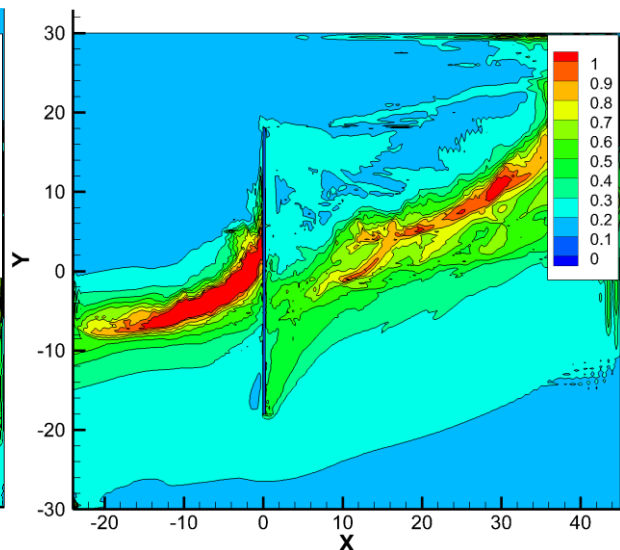
Figure 6.36 Consolidated maximum velocity magnitude xy-contour for 15° impact angle.

For the negative angles the wind speeds begin the wall are lower. The vortex recovers its near-ground circulation further away on the leeward side. The maximum wind speeds in the sheltering regions are summarized in Figures 6.37 – 6.40. The velocities are normalized to 69.2 ms⁻¹.
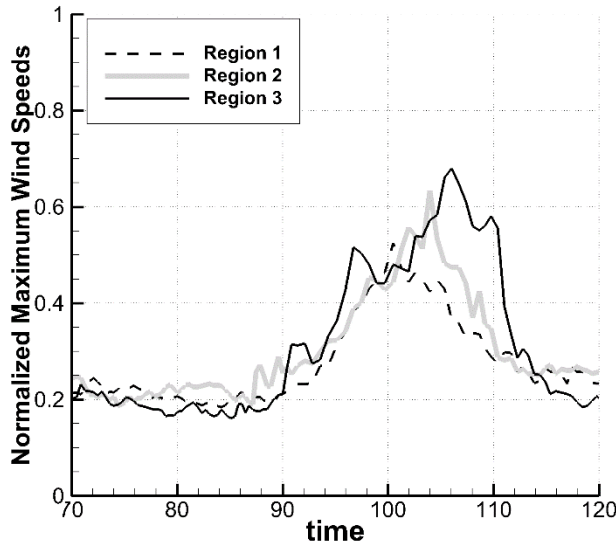
Figure 6.37 Normalized maximum winds speeds in sheltering regions for -30° impact angle.
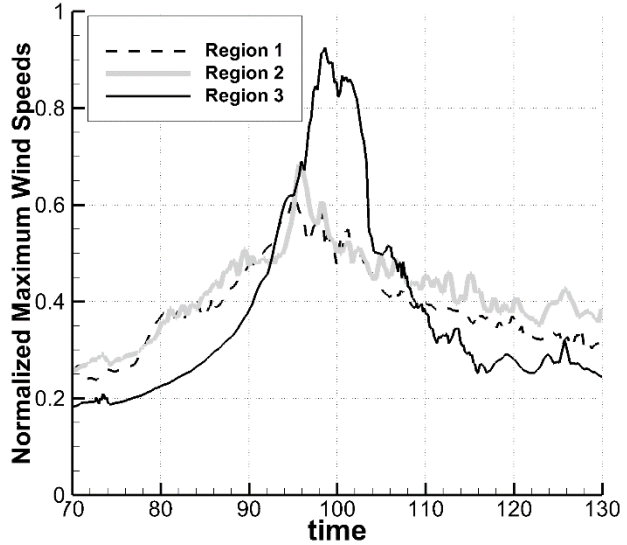
Figure 6.38 Normalized maximum winds speeds in sheltering regions 15° impact angle.
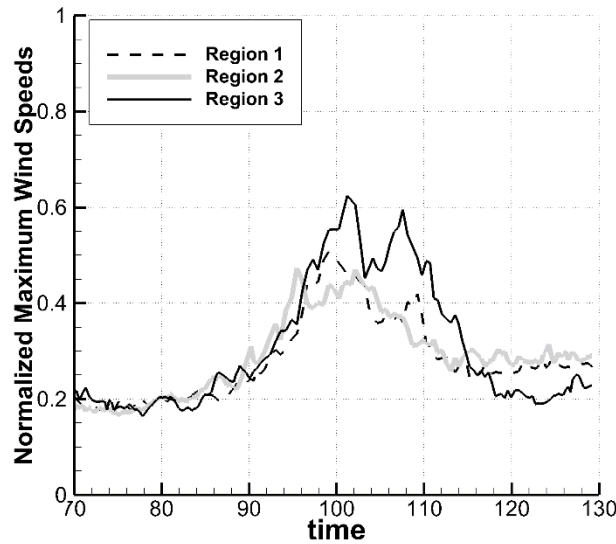
Figure 6.39 Normalized maximum winds speeds in sheltering regions for -15° impact angle.
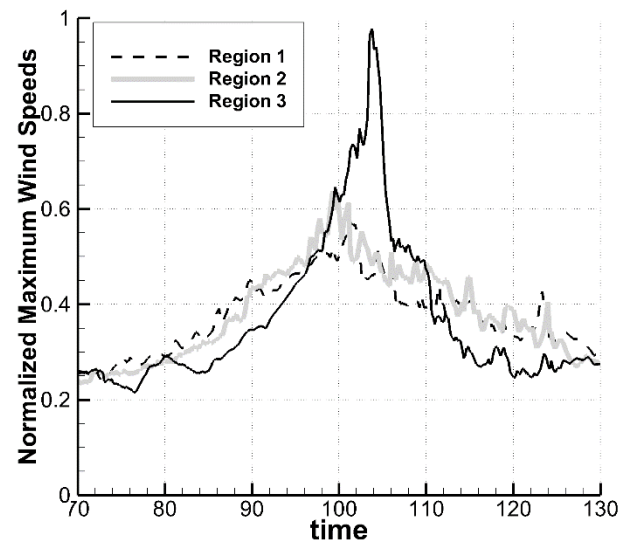
Figure 6.40 Normalized maximum winds speeds in sheltering regions 15° impact angle.

179

The wind speed reductions in the sheltering regions are provided in Table 6.12. The sheltering regions dimensions are specified in Figure 5.20

Table 6.12 Wind speed reduction in sheltering regions depending on vortex impact angle.

Vortex	Vortex angle of impact, β	Region 1	Region 2	Region 3	Shelter length ($u_{red} > 30\%$)
2	-30°	47.5 %	36.6 %	32.0 %	5.96H (119m)
3	-15°	49.2 %	52.6 %	37.5 %	7.52H (150m)
1	0°	45.7 %	44.0 %	25.5 %	5.08H (102m)
4	15°	42.8 %	36.2 %	2.2 %	3.03H (61m)
5	30°	38.2 %	31.5 %	7.4 %	3.01H (60m)

Figure 6.41 illustrates the sheltering efficiency dependence on the vortex impact angle. The tornado-break wall is observed to be the most efficient for the positive angles of vortex attack. The best sheltering effect is for the angle equal to 15°. When the angle is positive the efficiency of the tornado-break wall decreases. Especially in Region 3, the wind speed reduction is significantly lowered for negative angles. For negative angles the tornado-break wall almost does not provide any shelter in Region 3. When the tornado attacks the wall with the positive angle, it structure is less disrupted, therefore the near-ground circulation can be recovered closer to the wall leeward face.
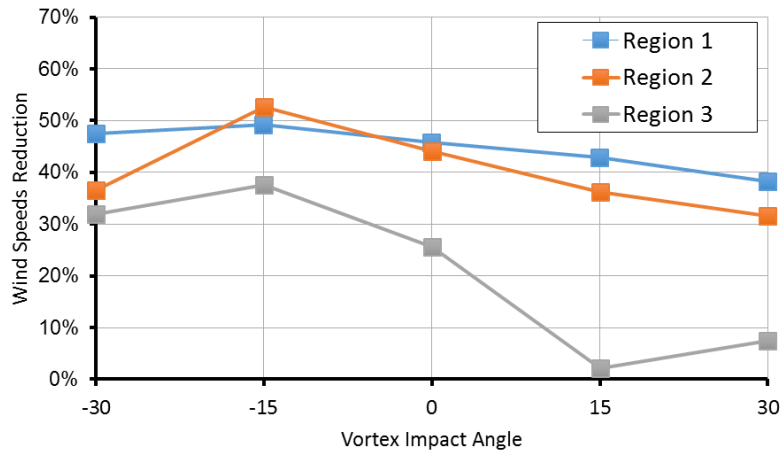
Figure 6.41 Tornado-break wall wind speed reductions in sheltering regions.

Forces on Tornado-break Wall

The overall wind force coefficients induced on the walls for five different vortex impact angles

are presented in Figure 6.42. The maximum instantaneous force coefficients and pressures on the

walls are reported in Table 6.13.

Table 6.13 Maximum instantaneous forces and pressures on walls for different impact angle.

Vortex	Vortex angle of impact, β	$C_{x,max}$	$C_{p,max}$
2	-30°	0.200	1.55
3	-15°	0.201	1.63
1	0°	0.250	0.68
4	15°	0.234	1.28
5	30°	0.266	1.18
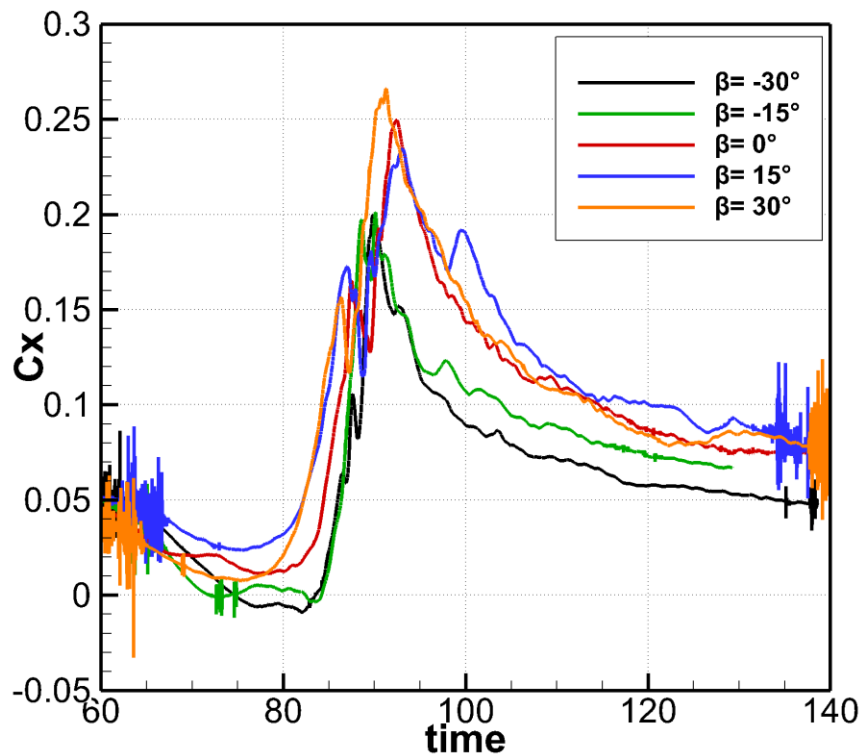
Figure 6.42 Force coefficients in x-direction for different vortex impact angles.

181

The maximum force coefficients are generally higher for the negative angles of the vortex impact. The difference between the positive and the negative 30° vortex angle impact is about 33%. The difference in the maximum force coefficients is related to the vortex-wall interaction.

6.7.   Conclusion

CFD simulations were conducted to study a magnitude of wind speed reductions provided by a tornado-break wall. First, the perpendicular vortex interaction with the reference wall was investigated. The height of the reference wall was 20 m and the width was 360 m. The maximum wind speed of the simulated tornado-like vortex was 69.2 ms^{-1}. It was noticed that the reference wall substantially reduces the maximum wind speeds up to 120 meters, behind the leeward face of the tornado break wall. This sheltering zone was divided into three sheltering regions. In each of the sheltering region the maximum wind speed reductions were reported. Region 1 and Region 2 spread on a distance equal to 60 meters behind the leeward face of the tornado-break wall. The height of both regions is equal to half of the wall height. Region 2 is located above Region 1. In those two regions the wind speed reductions were at least 44%. Such a wind speed reduction would result in three times lower wind pressures on potential structures located in these sheltering regions. Less favorable tornado sheltering efficiency was indicated in Region 3, which is further on the leeward side than Region 1 and Region 2. The length of Region 3 is 60 m, and the height is equal to the wall height. The tornado-break wall provides there at least 25% of the wind speed reduction. This would reduce wind pressures by almost two times.

The sheltering efficiency a tornado-break wall was investigated under different wall and vortex parameters. The following parameters were studied:

182

- *Wall Width Parameter.* It was defined as a ratio of the tornado-break wall width to the tornado vortex core radius. Three simulations were studied with different wall width parameters. It was showed that the width is a key factor in the tornado-wall interaction. When a wall is much wider than a tornado core, the vortex cannot circulate around the wall. This forces the tornado to split the near-ground portion of the vortex and introduce new vertical circulation behind the wall. Due to that the flow speeds behind the wall and near the ground are diminished. The wind velocities are reduced by at least 25% on a distance of six times the wall height, for the wall width parameter equal to twelve. For narrower walls the vortex can flow over the sides of the wall, not only over the top. Thus, the sheltering efficiency is reduced wall width parameters less than twelve. The break wall is able to provide tornado sheltering conditions (more than 33% wind speed reduction) on a distance of three times the wall height, when the wall width parameter is eight. When the wall width parameter is equal to four, the sheltering region length is limited to a distance of the break wall height.

- *Wall Height Parameter.* Defined as a ratio of the wall height to the tornado vortex core radius. Two simulations were analyzed to study the influence of the wall height parameter on the tornado sheltering effect. The height parameter was found be to another crucial factor in the vortex-wall interaction. The greater the wall height is, the better the tornado sheltering efficiency. This is associated with the vortex-wall interaction. When the wall is relatively small, comparing to the vortex core diameter, it creates less effective barrier for the tornado-like vortex. However, even a 10 m high wall provides about 30 m length sheltering region, with wind speeds reduced by more than 25%. For taller walls the tornado sheltering region length and the wind speed reductions are improved.

183

- *Vortex Impact Angle.* Defined as an angular deviation of the tornado vortex path from the perpendicular vortex-wall interaction. Five simulations were analyzed with different vortex impact angles, ranging from -30° to 30°. It was shown that the sign of the vortex impact angle influences the sheltering effect and the vortex-wall interaction. When the vortex approaches the wall with positive angles it causes higher wind speeds behind the wall than the vortex approaching with the negative angles. This is related with the way of the vortex-structure interaction. The sheltering region length is significantly lowered for positive angles. Nevertheless, for five studied vortex angle impacts the tornado-break wall reduces by more than 38 % wind speeds on a length of three times the wall height, on the leeward side.

184

7.   CONCLUSION

A three dimensional CFD model was utilized to numerically simulate different types of interactions between a traveling vortex and large structures. The vortex impact on a rectangular prism, was proposed to be representative of flow aspects in a tornado interaction with large natural or man-made structures. One of the main challenges in vortex-structure simulations, presented in this dissertation, was handling extensive computer simulations. To optimize the CFD simulation process, the pre-processing and the post-processing were automated using *FORTRAN* codes, *Tecplot* macros, batch files and *Tecplot* visualization layouts. This enabled to substantially reduce the entire CFD simulation process time and provide consistent result plots over different simulations. The new visualization techniques developed in this work helped to quickly and efficiently investigate flow features of a particular vortex-structure interaction. Based on visualizations of the interaction between a Rankine vortex and a wide rectangular prism, it was explained why actual tornadoes exhibit less damage on leeward side of hills. This sheltering effect was qualitatively investigated by flow speed reductions on the leeward side of a prism. Following findings from the vortex-prism interaction studies, it was proposed to investigate tornado sheltering performance of a wide tornado-break wall. The results presented in the current work have applications both in wind engineering and vortex-structure interactions problems. The major contributions to the knowledge are:

- Based on visualizations it was showed that when a rectangular-shaped structure is six times wider than the vortex core diameter, the translating vortex cannot circulate around the structure. To pass the structure, the vortex has to go over the prism. To accomplish this, the vortex splits its low-level portion and introduced a new near-ground vortex behind the prism. This causes mitigation of flow velocity magnitudes, close to the

185

ground, on the leeward side of a prism. When the prism height and length were equal to the vortex core radius, the prism created a tornado sheltering region, where resultant velocities were reduced by more than 30%. This sheltering region was defined along the width of the prism, on the leeward side. The length of the region was found to be six times the prism height. The parametric study revealed that the magnitude of flow speed reductions depends on the prism height parameter, the prism length parameter and the vortex impact parameter.

- The vortex-prism interaction studies presented in this dissertation provided the explanation for local path deviations observed when an actual tornado travels in complex terrain, or when a tornado interacts with large structures (Appendix 4). Ahmed and Selvam (2015), showed that the path of a real tornado depends on the ratio of the maximum tangential velocity to the vortex translational velocity. Here, their findings are confirmed and extended further for a vortex-prism interaction. It is showed that the vortex lateral displacement in front of the prism is a result of directing the flow along the leading face of the prism, as the vortex approaches the prism. The vortex follows the ambient flow and it is displaced along the prism leading wall. Behind the prism, the translating vortex recovers near-ground rotation from a horizontal recirculation wake. The magnitude of the vortex displacement depends not only on the vortex impact parameter, as showed by Ahmed and Selvam (2015). It also depends on the ratio of the prism height to the vortex core radius. The higher the prism is, the larger the path deviation of the translating vortex. The vortex lateral displacement was also investigated for different prism lengths. In this case, the vortex path deviations were similar for the simulated prisms.

186

- In the current work it was showed that the tornado sheltering effect exhibited by hills can be reproduced by a wide solid wall. In the wind engineering problems a wall that reduces tornado wind speeds is a novel idea. Until now wind barriers were analyzed only in the case of straight-line winds. It was demonstrated that a 20 m high wall reduced tornado-like wind speeds by more than 25% in a region that extends up to 120 m away from the wall. The sheltering efficiency of a tornado-break wall was found to vary under different tornado impact conditions. The size of the sheltering region, behind the wall, is related to the wall height parameter and the wall width parameter. The higher and the wider the wall is, the larger the tornado-protected region. The size of the tornado-protected area also depends on the tornado-like vortex impact angle. For the negative impact angles the tornado sheltering efficiency is higher than for the positive angles. It is associated with the direction of the vortex rotation, which influences the way of the vortex-wall interaction.

- *Suggestions for future work*

The suggestion for the future work are formulated based on conclusions from the current work:

- Determine tornado wind speed reductions, close to the ground, during an interaction with different kinds of man-made structures (walls, large buildings, towers, etc.) and natural structures (trees, hills and valleys). The objective is to verify whether existing structures are able to provide tornado protected zones.
- Determine wind force reductions on a cubic building located in the sheltering region, behind a tornado-break wall. The wind forces induced on a building would be studied

187

under: different wall sizes (relatively to a cubic building size) and different tornado parameters (maximum wind speed, vortex strength, angle of attack, translational velocity).

- Determine tornado sheltering efficiency of wall-type shelterbelts. A tornado shelterbelt surrounds certain area of wind sensitive structures (e.g. mobile homes). Inside the tornado shelterbelt the wind speed reductions are studied. Different shapes and sizes of shelterbelts are analysed (rectangular, circular and polygon) to improve the sheltering effect.

- Develop a shape of man-made structure to locally change the near-ground vortex path and course a translating tornado-like vortex into a specific direction.

- Couple the computational fluid dynamic (CFD) model with the discrete element model (DEM) to study the efficiency of a tornado-break wall in protecting from tornado-like windborne debris. Compute paths and impact velocities of debris of different shapes and masses.

- Develop a CFD model able to simulate porous tornado-break walls. Porous walls were proven to be more efficient in reducing straight-line wind speeds.

188

REFERENCES

Affes, H., & Conlisk, A. T. (1993). Model for rotor tip vortex-airframe interaction. I - Theory. *AIAA Journal, 31*(12), 2263-2273.

Ahmed, N., & Selvam, R. P. (2015). Topography Effects on Tornado Path Deviation. *Journal of Applied Meteorology and Climatology*.

Aliwan, A., & Selvam, R. P. (2015). *Analysis of tornado path using Google Earth data.* University of Arkansas, Fayetteville, Ar: Class Report.

Allaby, M. (1997). *Tornadoes.* New York: Facts On File.

Alrasheedi, H. N. (2012). Computer Modeling of the Influence of Structure Plan Areas on Tornado Forces. *PhD dissertation, University of Arkansas*. Fayetteville, USA.

Alrasheedi, N. H., & Selvam, R. P. (2011). Computing Tornado Forces on Different Building Sizes. *13th International Conference on Wind Engineering* (pp. 1-6). Amsterdam, Netherlands: ICWE13.

Ashley, W. S. (2007). Spatial and Temporal Analysis of Tornado Fatalities in the United States: 1880–2005. *Weather and Forecasting, 22*, 1214-1228.

Bech, J., Gaya, M., Aran, M., Figuerola, F., Amaro, J., & Arus, J. (2009). Tornado damage analysis of a forest area using site survey observations, radar data and a simple analytical vortex model. *Atmospheric Research, 93*(1-3), 118-30.

Bienkiewicz, B., & Dudhia, P. (1993). Physical modeling of tornado-like flow and tornado effects on building loading. *Seventh US National Conference on Wind Engineering*, (pp. 95–104).

Bosart, L. F., Seimon, A., LaPenta, K. D., & Dickinson, M. J. (2006). Supercell tornadogenesis over complex terrain: The Great Barrington, Massachusetts, tornado on 29 May 1995. *Weather and Forecasting, 21*(6), 897-922.

Brooks, H. E. (2004). On the Relationship of Tornado Path Length and Width to Intensity. *Weather and Forecasting, 19*(2), 310–319.

Castro, I. P. (1971). Wake Characteristics Of Two-dimensional Perforated Plates Normal To An Air-stream. *Journal of Fluid Mechanics, 46*(03), 599- 609.

Cornelis, W., & Gabriels, D. (2005). Optimal Windbreak Design For Wind-erosion Control. *Journal of Arid Environments, 61*(2), 315-332.

Coton, F., Marshall, J. S., Galbraith, R., & Green, R. (2004). Helicopter Tail Rotor Orthogonal Blade Vortex Interaction. *Progress in Aerospace Sciences, 40*(7), 453-486.

Dessens, J. J. (1972). Influence of ground roughness on tornadoes: A laboratory simulation. *Journal of Applied Meteorology, 11*(1), 72-75.

189

Dierickx, W., Cornelis, W. M., & Gabriels, D. (2003). Wind Tunnel Study on Rough and Smooth Surface Turbulent Approach Flow and on Inclined Windscreens. *Biosystems Engineering, 86*(2), 151–166.

Dong, Z., Luo, W., Qian, G., & Wang, H. (2007). A Wind Tunnel Simulation Of The Mean Velocity Fields Behind Upright Porous Fences. *Agricultural and Forest Meteorology, 146*(1-2), 82-93.

Dutta, P. K., Ghosh, A. K., & Agarwal, B. L. (2002). Dynamic response of structures subjected to tornado loads by FEM. *Journal of Wind Engineering and Industrial Aerodynamics, 90*, 55-69.

Elsom, D., & Meaden, G. (1982). Suppression and dissipation of weak tornadoes in metropolitan areas: a case study of Greater London. *Monthly Weather Review, 110*(7), 745-756.

Filippone, A., & Afgan, I. (2008). Orthogonal Blade-Vortex Interaction on a Helicopter Tail Rotor. *AIAA Journal, 46*(6), 1476-1489.

Fujita, T. T. (1971). *Proposed Characterization of Tornadoes and Hurricanes by Area and Intensity* (Vol. 91). University of Chicago: Research Project.

Fujita, T. T. (1989). The Teton-Yellowstone Tornado of 21 July 1987. *Monthly Weather Review, 117*(9), 1913-1940.

Gorecki, P., & Selvam, R. P. (2013). Three-dimensional simulation of tornado over complex terrain. *12th Americas Conference on Wind Engineering 2013, ACWE 2013: Wind Effects on Structures, Communities, and Energy Generation*, *1*, pp. 543-560.

Gorecki, P., & Selvam, R. P. (2014). Visualization of tornado-like vortex interacting with wide tornado-break wall. *Journal of Visualization*, 1-14. doi:10.1007/s12650-014-0245-y

Gorecki, P., & Selvam, R. P. (2015). Rankine Combined Vortex Interaction with a Rectangular Prism. *International Journal of Computational Fluid Dynamics, 29*(1), 120-132.

Grazulis, T. P. (1993). A 110-year perspective of significant tornadoes. In C. Church et al. (Eds.), *The Tornado: its structure, dynamics, prediction, and hazard* (pp. 467–474). Washington D.C.: AGU.

Haan, F. L., Balaramudu, V. K., & Sarkar, P. P. (2010). Tornado-Induced Wind Loads on a Low-Rise Building. *ASCE Journal of Structural Engineering, 136*, 106-116.

Haan, F. L., Sarkar, P. P., & Gallus, W. A. (2008). Design, Construction and Performance of a Large Tornado Simulator for Wind Engineering Applications. *Engineering Structures, 30*, 1146–1159.

Hamada, A., Damatty, A. E., Hangan, H., & Shehata, A. (2010). Finite element modeling of transmission line structures under tornado wind loading. *Wind and Structures, 13*(5), 451-469.

Hangan, H., & Kim, J. (2008). Swirl ratio effects on tornado vortices in relation to the Fujita scale. *Wind and Structures*, 291-302.

Hannesen, R., Dotzek, N., & Handwerker, J. (2000). Radar analysis of a tornado over hilly terrain on 23 July 1996. *Physics and Chemistry of the Earth: Part B, 25*, 1079–1084.

Hannesen, R., Dotzek, N., Gysi, H., & Beheng, K. D. (1998). Case study of a tornado in Upper Rhine valley. *Meteorologische Zeitschrift, 7*, 163-170.

Harrington, J. B., & Newark, M. J. (1986). The interaction of a tornado with rough terrain. *Weather, 41*(10), 310-319.

Holmén, V. (2012). Methods for Vortex Identification. *PhD Dissertation, Lund University, Sweden*.

Holmes, J. D. (2007). *Wind Loading of Structures.* New York, NY: Taylor & Francis.

Homar, V., Gaya, M., Romero, R., Ramis, C., & Alonso, S. (2003). Tornadoes over complex terrain: an analysis of the 28th August 1999 tornadic event in eastern Spain. *Atmospheric Research, 67-68*, 301-317.

Hu, H., Yang, Z., & Sarkar, P. (2011). Characterization of the wind loads and flow fields around a gable-roofed building model in tornado-like winds. *Experiments in Fluids, 51*(3), 835-851.

Huschke, R. E. (1959). *Glossary of Meteorology.* Boston, MA: American Meteororology Society.

Jischke, M. C., & Light, B. D. (1979). Laboratory simulation of tornadic wind loads on a cylindrical structure. *Sixth International Conference on Wind Engineering*, (pp. 1049–1059).

Jischke, M. C., & Light, B. D. (1983). Laboratory simulation of tornadic wind loads on a rectangular model structure. *Journal of Wind Engineering and Industrial Aerodynamics, 13*, 371–382.

Kaiser, H. (1959). Die Stromungan Windschutzstreifen. *Berichte Des Deutschen Wetterdienstes, 53*(7), 1–36.

Karstens, C. D. (2012). Observations and Laboratory Simulations of Tornadoes in Complex Topographical Regions. *PhD Dissertation, Department of Meteorology, Iowa State University*.

Karstens, C. D., Samaras, T. M., Lee, B. D., Gallus, W. A., & Finley, C. A. (2010). Near-Ground Pressure and Wind Measurements in Tornadoes. *Monthly Weather Review, 138*, 2570–2588.

Kosiba, K. A., Robinson, P., Chan, P. W., & Wurman, J. (2014). Wind Field of a Nonmesocyclone Anticyclonic Tornado Crossing the Hong Kong International Airport. *Advances in Meteorology*, 1-7.

Kosiba, K. A., Trapp, R. J., & Wurman, J. (2008). An analysis of the axisymmetric three-dimensional low level wind field in a tornado using mobile radar observations. *Geophysical Research Letters, 35*, 1-6.

Kosiba, K., & Wurman, J. (2010). The Three-Dimensional Axisymmetric Wind Field Structure of the Spencer, South Dakota, 1998 Tornado. *Journal of the Atmospheric Sciences, 67*, 3074-3083.

Kozmar, H., Procino, L., Borsani, A., & Bartoli, G. (2012). Sheltering efficency of wind barriers on bridges. *Journal of Wind Engineering & Industrial Aerodynamics, 107-108*, 274-284.

Krishnamoorthy, S., & Marshall, J. S. (1994). An experimental investigation of ''vortex shocks''. *Physics of Fluids, 6*, 3737.

Krishnamoorthy, S., & Marshall, J. S. (1998). Three-dimensional blade–vortex interaction in the strong vortex regime. *Physics of Fluids, 10*(11), 2828-2845.

Krishnamoorthy, S., Gossler, A. A., & Marshall, J. S. (1999). Normal Vortex Interaction with a Circular Cylinder. *AIAA Journal, 37*(1), 50-57.

Kuai, L., Haan Jr, F. L., Gallus Jr, W. A., & Sarkar, P. P. (2008). CFD Simulations of the flow field of a laboratory-simulated tornado for parameter sensitivity studies and comparison with field measurements. *Wind and Structures, 11*(2), 75-96.

Kumar, N., Dayal, V., & Sarkar, P. P. (2012). Failure of wood-framed low-rise buildings under tornado wind loads. *Engineering Structures, 39*, 79–88.

Kun, Y., & Renxian, L. (2012). Optimization Analysis of Height and Distance for Shelter Wind Wall of High Speed Railway. *Advanced Materials Research, 588-589*, 1794-1800.

Kwon, S. D., Kim, D. H., Lee, S. H., & Song, H. S. (2011). Design criteria of wind barriers for traffic. Part 1: wind barrier performance. *Wind and Structures, 14*(1), 55-70.

Lee, S. J., & Lim, H. C. (2001). A Numerical Study on Flow around a Triangular Prism Located behind a Porous Fence. *Fluid Dynamics Research, 28*, 209–221.

Lee, S., & Kim, H. (1999). Laboratory measurements of velocity and turbulence field behind porous fences. *Journal of Wind Engineering and Industrial Aerodynamics, 80*, 311-326.

Lee, S.-J., & Park, C.-W. (1998). Surface-pressure Variations On A Triangular Prism By Porous Fences In A Simulated Atmospheric Boundary Layer. *Journal of Wind Engineering and Industrial Aerodynamics, 73*(1), 45–58.

Lewellen, D. C. (2012). Effects of topography on tornado dynamics: a simulation study. *26th Conference on Severe Local Storms (5 - 8 November 2012)*, (pp. 1-7). Nashville, TN.

Lewellen, D. C., Gong, B., & Lewellen, W. S. (2008). Effects of Finescale Debris on Near-Surface Tornado Dynamics. *Journal of the Atmospheric Sciences, 65*(10), 3247–3262.

Li, B., Feng, S. H., Yang, Q. S., & Hou, Y. W. (2011). Researches And Application Of Railway Wind-Break Wall. *Advanced Materials Research, 194-196*, 1126-1129.

Li, W., Wang, F., & Bell, S. (2007). Simulating The Sheltering Effects Of Windbreaks In Urban Outdoor Open Space. *Journal of Wind Engineering and Industrial Aerodynamics, 95*(7), 533-549.

Lingling, Z., Xifeng, L., Mingzhi, Y., & Sha, H. (2012). Optimization of bridge windbreak on high-speed railway through strong wind area. *Advanced Materials Research, 452-453*, 1518-1521.

Liu, X., & Marshall, J. S. (2004). Blade penetration into a vortex core with and without axial core flow. *Journal of Fluid Mechanics, 519*, 81-103.

Marshall, J. S. (2002). Models of Secondary Vorticity Evolution during Normal Vortex-Cylinder Interaction. *AIAA Journal, 40*(1), 170-172.

Marshall, J. S., & Beninati, M. L. (2005). External turbulence interaction with a columnar vortex. *Journal of Fluid Mechanics, 540*, 221-245.

Marshall, J. S., & Krishnamoorthy, S. (1997). On the instantaneous cutting of a columnar vortex with non-zero axial flow. *Journal of Fluid Mechanics, 351*, 41-74.

Marshall, J. S., & Yalamanchili, R. (1994). Vortex Cutting by a Blade, Part II: Computations of Vortex Response. *AIAA Journal, 32*(7), 1428-1436.

McDonald, J. R., & Selvam, R. P. (1985). Tornado forces on building using the boundary element method. *Fifth U.S. National Conference on Wind Engineering*, *5B*, pp. 41-48. Texas Tech University, Lubbock, TX, USA.

Mishra, A. R., James, D. L., & Letchford, C. W. (2008). Physical simulation of a single-celled tornado-like vortex, Part B: Wind loading on a cubical model. *Journal of Wind Engineering and Industrial Aerodynamics, 96*, 1258–1273.

Murakami, S., & Mochida, A. (1995). On turbulent vortex-shedding flow past 2D square cylinder predicted by CFD. *Journal of Wind Engineering and Industrial Aerodynamics, 54-55*, 191-211.

Natarajan, D., & Hangan, H. (2012). Large eddy simulations of translation and surface roughness effects on tornado-like vortices. *Journal of Wind Engineering and Industrial Aerodynamics, 104-106*, 577-584.

NOAA. (2012). *National Oceanic and Atmospheric Administration*. Retrieved from www.noaa.gov

Nuss, W. (1986). Observations of a mountain tornado. *Monthly Weather Review, 114* (1), 233-237.

Orlandi, P., & Verzicco, R. (1993). Vortex rings impinging on walls: axisymmetric and three-dimensional simulations. *Jounal of Fluid Mechanics, 256*, 615-646.

Park, C. W., & Lee, S. J. (2003). Experimental study on surface pressure and flow structure around a triangular prism located behind a porous fence. *Journal of Wind Engineering and Industrial Aerodynamics, 91*, 165-184.

Passe-Smith, M. S. (2006). Exploring Local 'Tornado Alleys' for Predictive Environmental Parameters. *26th Annual Esri International User Conference*, (pp. 1-28). San Diego, CA.

Perera, M. (1981). Shelter Behind Two-dimensional Solid And Porous Fences. *Journal of Wind Engineering and Industrial Aerodynamics, 8*(1-2), 93-104.

Raine, J., & Stevenson, D. (1977). Wind Protection By Model Fences In A Simulated Atmospheric Boundary Layer. *Journal of Wind Engineering and Industrial Aerodynamics, 2*(2), 159-180.

Rizzetta, D. P., & Visbal, M. R. (2011). Exploration of plasma-based control for low-Reynolds number airfoil/gust interaction. *International Journal of Computational Fluid Dynamics, 25*(10), 509-533.

Santiago, J. L., Martin, F., Cuerva, A., Bezdenejnykh, N., & Sanz-Andrés, A. (2007). Experimental and numerical study of wind flow behind windbreaks. *Atmospheric Environment, 41*, 6406–6420.

Sarkar, P. P., Haan, F. L., Balaramudu, V., & Sengupta, A. (2006). Laboratory simulation of tornado and microburst to asses wind loads on buildings. *ASCE Structures Congress*, (pp. 1-10). St. Louis, MO.

Savory, E., Parke, G. A., Zeinoddini, M., Toy, N., & Disney, P. (2001). Modelling of tornado and microburst-induced wind loading and failure of a lattice transmission tower. *Engineering Structures, 23*, 365–375.

Selvam, R. P. (1985). Application of the Boundary Element Method for Tornado Forces on Building. *PhD Dissertation*. Texas Tech University, Lubbock, TX, USA.

Selvam, R. P. (1990). Computer Simulation of Wind Load on a House. *Journal of Wind Engineering and Industrial Aerodynamics, 36*, 1029-1036.

Selvam, R. P. (1993). Computer Modeling of Tornado Forces on Buildings. *7th US National Conference on Wind Engineering*, (pp. 605-613). Los Angeles, CA.

Selvam, R. P. (1996a). Comparison of flow around circular cylinder using FE and FD procedures. In S. K. Ghosh, & J. Mohammadi, *Building an International Community of Structural Engineers* (Vol. 2, pp. 1021-1028). New York: ASCE.

Selvam, R. P. (1996b). Computation of flow around Texas Tech building using k-e and Kato-Launder k-e turbulence model. *Engineering Structures, 18*, 856-860.

Selvam, R. P. (1997a). Computation of pressures on Texas Tech University building using large eddy simulation. *Journal of Wind Engineering and Industrial Aerodynamics, 67-68*, 647-657.

Selvam, R. P. (1997b). Finite element modelling of flow around a circular cylinder using LES. *Journal of Wind Engineering and Industrial Aerodynamics, 67-68*, 129-139.

Selvam, R. P. (1998). Computer modelling of Flow around bridges using LES and FEM. *Journal of Wind Engineering and Industrial Aerodynamics, 77-78*, 643-651.

Selvam, R. P. (2008). Developments in computational wind engineering. *Journal of Wind and Engineering, 5*, 47-54.

Selvam, R. P. (2010a). Building and bridge aerodynamics using computational wind engineering. *International workshop on wind engineering research and practice.* Chapel Hill, NC, USA.

Selvam, R. P. (2010b). The Influence of Near-Wall Grid Resolution on the Computation of Peak Pressures. *International workshop on wind engineering research and practice.* Chapel Hill, NC, USA.

Selvam, R. P., & Ahmed, N. S. (2013). The Effect of Terrain Elevation on Tornado Path. *12th Americas Conference on Wind Engineering* (pp. 603-612). Seattle, WA, USA: American Association for Wind Engineering (AAWE).

Selvam, R. P., & Gorecki, P. (2012a). Effect of tornado size on forces on thin 2D cylinder. *3rd American Association for Wind Engineering Workshop*, (pp. 1-8). Hyannis, Massachusetts, USA.

Selvam, R. P., & Gorecki, P. (2012b). CFD for Infrastructure, Thermal Management and Energy. *International Conference on Application of Fluid Dynamic*, (pp. 1-6). Gaborone, Botswana.

Selvam, R. P., & Millet, P. C. (2002). Computer modeling of the tornado structure interaction: investigation of structural loading on cubic building. In K. Kumar (Ed), *Wind Engineering* (pp. 895-902). New Delhi, India: Phoenix Publishing House.

Selvam, R. P., & Millett, P. C. (2003). Computer modeling of tornado forces on buildings. *Wind and Structures, 6*, 209-220.

Selvam, R. P., & Millett, P. C. (2005). Large eddy simulation of the tornado-structure interaction to determine structural loadings. *Wind and Structures, 8*, 49-60.

Selvam, R. P., & Qu, Z. Q. (2002). Adaptive p-finite element method for wind engineering. *Wind and Structures, 5*, 301-316.

Selvam, R. P., & Ragan, Q. S. (2012). Mitigation of tornado effects-a study of the shielding effects of hills. *3rd American Association for Wind Engineering Workshop*, (pp. 1-8). Hyannis, Massachusetts, USA.

Selvam, R. P., Roy, U. K., Jung, Y., & Mehta, K. C. (2002). Investigation of tornado forces on a 2D cylinder using computer modeling. In K. Kumar (Ed), *Wind Engineering* (pp. 342-353). New Delhi, India: Phoenix Publishing House.

Sengupta, A., Haan, F. L., Sarkar, P. P., & Balaramudu, V. (2008). Investigation of tornado Transient loads on buildings in microburst and tornado winds. *Journal of Wind Engineering and Industrial Aerodynamics, 96*, 2173-2187.

Thom, A., & Duraisamy, K. (2010). High-Resolution Simulations of Parallel Blade–Vortex Interactions. *AIAA Journal, 48*(10), 2313-2324.

Wang, Z., & Zheng, X. (2003). A Numerical Simulation Of Fluid Flowing Through A Windbreak. *Key Engineering Materials, 243-244*, 607-612.

Wen, Y. (1975). Dynamic tornadic wind loads on tall buildings. *Journal of the Structural Division, 101*, 169-185.

Whipple, A. B. (1982). *Storm.* New York: Time-Life Books.

Wurman, J. (2002). The multiple-vortex structure of a tornado. *Weather and Forecasting, 17*(3), 473-505.

Wurman, J., & Alexander, C. R. (2005). The 30 May 1998 Spencer, South Dakota, storm. Part II: Comparison of observed damage and radar-derived winds in the tornadoes. *Monthly Weather Review, 1*, 97-119.

Wurman, J., Kosiba, K., & Robinson, P. (2013). In Situ, Doppler Radar, and Video Observations of the Interior Structure of a Tornado and the Wind–Damage Relationship. *Bulletin of the American Meteorological Society, 94*(6), 835–846.

Wurman, J., Robinson, P., Alexander, C., & Richardson, Y. (2007). Low-Level Winds In Tornadoes And Potential Catastrophic Tornado Impacts In Urban Areas. *Bulletin of the American Meteorological Society, 88*(1), 31-46.

Wurman, J., Straka, J. M., & Rasmussen, E. N. (1996). Fine-scale Doppler radar observations of tornadoes. *Science, 272*(21), 1774-1777.

Yang, Z., Sarkar, P. P., & Hu, H. (2011). An experimental study of a high-rise building model in tornado-like winds. *Journal of Fluids and Structures, 27*, 471-486.

Yaragal, S. C., Govinda Ram, H. S., & Murthy, K. K. (1997). An Experimental Investigation Of Flow Fields Downstream Of Solid And Porous Fences. *Journal of Wind Engineering and Industrial Aerodynamics, 66*(2), 127–140.

Yeh, C., Tsai, C., & Yang, R. (2010). An Investigation Into The Sheltering Performance Of Porous Windbreaks Under Various Wind Directions. *Journal of Wind Engineering and Industrial Aerodynamics, 98*(10-11), 520-532.

196

APPENDIX 1: Calculations in post-processing stage

In each time step velocity vectors and pressures, of the flow, are calculated through Navier-Stokes equations. From this data resultant velocities are calculated as:

$$|u| = \sqrt{u_x^2 + u_y^2 + u_z^2} \tag{A1.1}$$

Where: u_x, u_y, u_z – velocity vector component in respectively x-, y- and z-direction.

The streamlines of the flow $\vec{x}_s$ are defined as instantaneously tangential to the velocity vectors.

Thus, a vector cross product of streamline derivative and velocity $\vec{u}$ must be equal to zero:

$$\frac{d\vec{x}_s}{ds} \times \vec{u}(\vec{x}_s) = 0 \tag{A1.2}$$

The force and pressure coefficients are used in a quantitative analysis of wind loading induced on the building surfaces. The force coefficients are dimensionless values that mostly depend on the shape of the body immersed in the flow. They are calculated as:

$$C_x = F_x / \left(0.5 \rho V_{ref}^2 A \right) \tag{A1.3}$$

$$C_y = F_y / \left(0.5 \rho V_{ref}^2 A \right) \tag{A1.4}$$

$$C_z = F_z / \left(0.5 \rho V_{ref}^2 A \right) \tag{A1.5}$$

$$C_p = \Delta p / \left(0.5 \rho V_{ref}^2 \right) \tag{A1.6}$$

Where: C_x, C_y, C_z – force coefficients in respectively x-, y- and z- direction, F_x, F_y, F_z – forces in respectively x-, y- and z- direction, ρ - density of the air (ρ=1.2kg/m^3), V_{ref} – reference velocity of the flow, A – reference area, Δp – pressure obtained from subtraction of the computed pressure and the reference pressure (p_{ref}); p_{ref} is assumed to be 0.

197

APPENDIX 2: Vortex strength during interaction with tornado-break wall
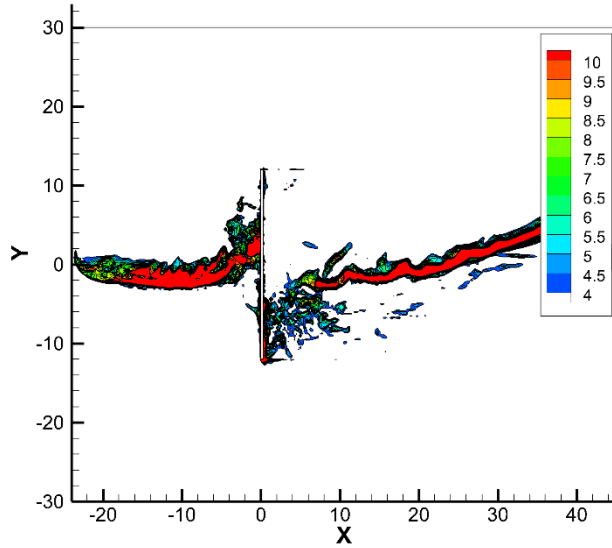
Figure A2.1 Consolidated z-vorticity xy-contour at height 20 m for wall width 240 m (Wall 2).
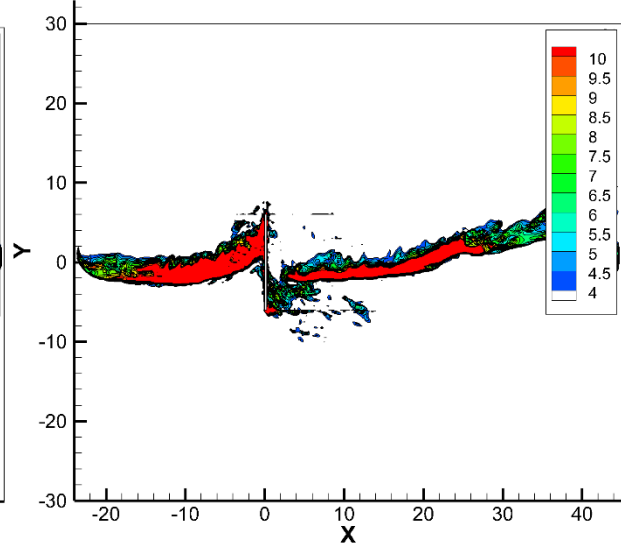
Figure A2.2 Consolidated z-vorticity xy-contour at height 20 m for wall width 120 m (Wall 3).
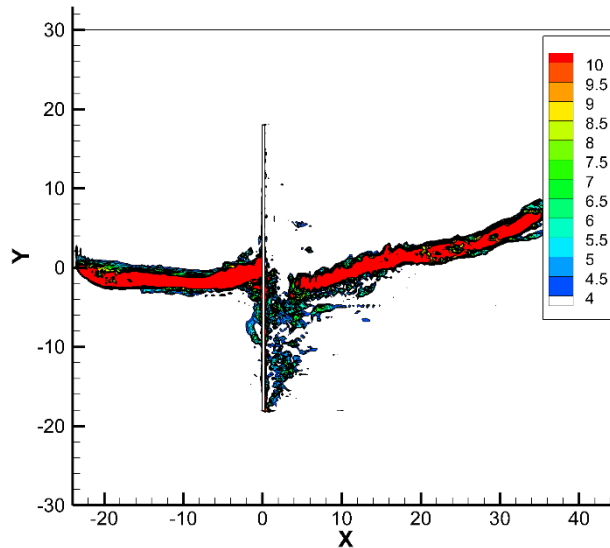
Figure A2.3 Consolidated z-vorticity xy-contour at height 10 m for wall height 10 m (Wall 4).

198
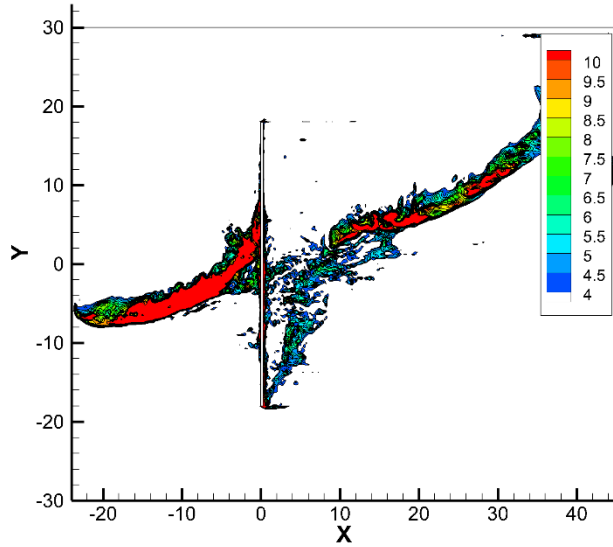
Figure A2.4 Consolidated z-vorticity xy-contour at height 20 m for vortex impact angle 15° (Vortex 4).
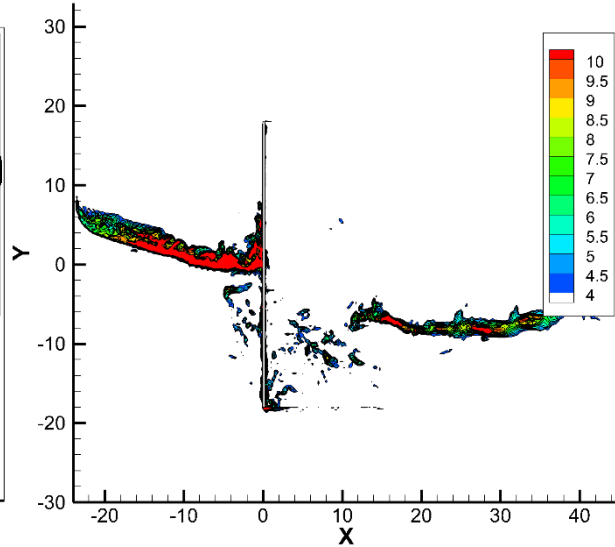
Figure A2.5 Consolidated z-vorticity xy-contour at height 20 m for vortex impact angle -15° (Vortex 3).
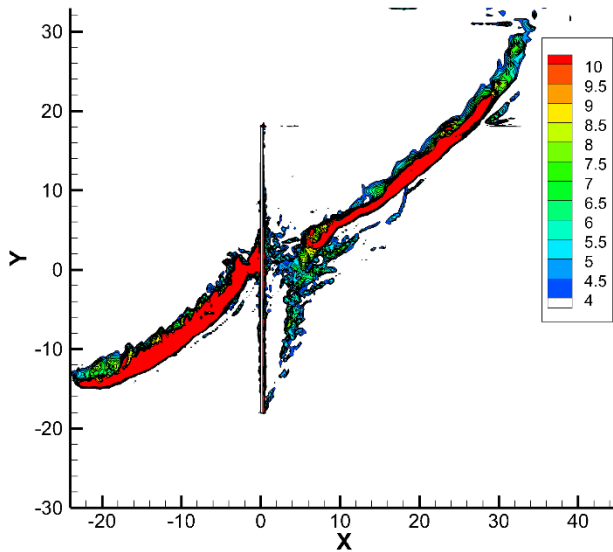
Figure A2.6 Consolidated z-vorticity xy-contour at height 20 m for vortex impact angle 30° (Vortex 5).
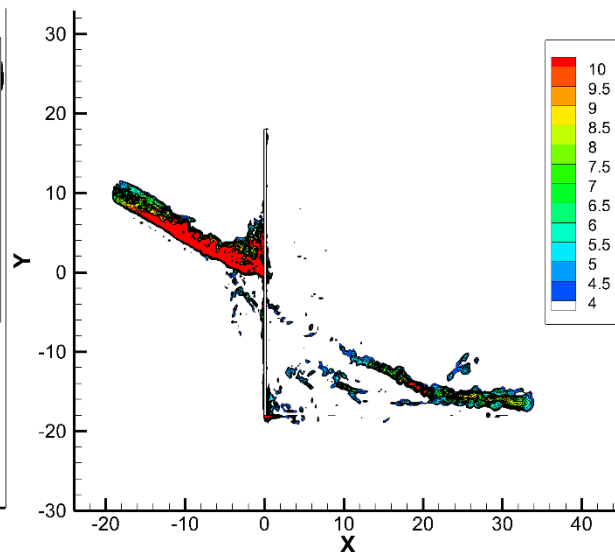
Figure A2.7 Consolidated z-vorticity xy-contour at height 20 m for vortex impact angle -30° (Vortex 2).

199

APPENDIX 3: CFD vortex simulation using U of A Vortex Code

▪ *Pre-processing*

The pre-processing stage of the numerical simulation consists in preparing the input data file. The input data file includes the following information:

- Rankine vortex (RV) parameters

- Building size

- Grid dimensions

The RV parameters are defined by the radius of the forced vortex region (r_{max}), the rotational constant (α) and the translational velocity of a tornado (u_{tran}). The RV parameters have to be scaled in accordance to the reference length and the reference velocity, assumed in non-dimensionalization of the Navier-Stokes equations (see Section 3.1). The translational velocity of a vortex is set in the program's code to be the reference velocity. Thus, for u_{tran} different than 1.0 the output time dimension has to scaled.

The building is inserted, in the computational domain, between appropriate grid lines. Since the code is formulated for an orthogonal grid the building must have a cuboid shape. The size of a building is specified by respectively: starting point of the building in the x-axis (IMK1), ending point of the building in the x-axis (IMK2), starting point of the building in the y-axis (JMK1), ending point of the building in the y-axis (JMK2), total number of the grid points of the building in the z-axis (KH).
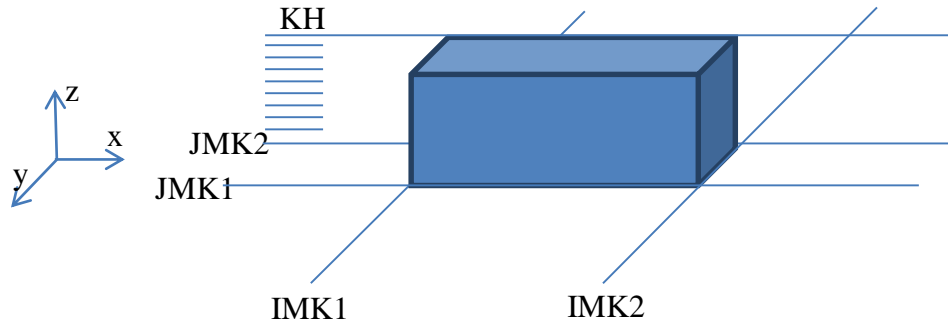
Figure A3.1 Building dimensions by grid lines.

Grid spacing is a crucial factor in the numerical simulation. Converged and reliable results can be obtained only from properly constructed grids. The four key factors that must be accounted in constructing a grid are included in Table A3.1.

Table A3.1 Important grid properties for vortex-structure interaction.

#	Grid Property	Purpose
1	Size of the computation domain	Simulate vortex with stable properties over its travel
2	Refined grid on vortex path	Simulate vortex with stable properties over the travel
3	Fine grid spacing close to building's walls	Capture wall boundary layer
4	Sufficient number of grid points on the building's walls	Accurate pressure distribution on building's walls

Each grid property depends on RV parameters and the structure size. The study on grid parameters and computational domain size is included in Section 4.2

- *Numerical Solver*

The numerical simulation of the Navier-Stokes equations, with boundary conditions provided in the input data, is performed using CFD software developed by Computational Mechanics

201

Laboratory at the University of Arkansas. The executable file is run under Linux cluster. The

cluster is remotely accessed by PC using SSH Security Shell software. Table A3.2 includes the

useful Linux commands.

Table A3.2 Frequently used UNIX commands.

Command	Description
cd *name of folder* cd ..	Change a folder Go one level up in directories
ls ls -l	List files and directories in the current location Detailed list
mkdir *name of new directory*	create a folder
mv *file1 file2*	Rename *file1* to *file2*
rm 'name of file'	Remove file
cp *path of copied file path of new file* cp *path of copied file* .	Copy file Copy file to current location
pwd	Path to current location
ps -ef	Check id for running processes
df	Disc space
vi 'file name' i Esc G :q :wq	View txt file Switch to insert mode Switch back to command line mode Go to the last line of the txt file Quit file without saving Save and quit file
./*file.out* nohup ./*file.out* nohup ./*file.out*>dum kill *process id*	Execute *file.out* program Execute *file.out* program in background Execute *file.out* program in background and write display output in *dum* file Terminate already running program
ssh username@cmln1.uark.edu ssh *n2* scp username1@cmln1.uark.edu:*path/file1* username2@comp.uark.edu:*path*	change to cmln1 server Change node to node 2 Copy *file1* from *cmln1* server to *comp* server
cd /scr cd /tmp cd /home	Go to scratch directory Go to temporary directory Go to home directory
f95 *file.f*	Compile Fortran source code *file.f*

All program runs are performed on scratch drive. The output data is moved to home directory and downloaded on PC.

- ▪ *Post-processing*

The output data consist of field data files and aerodynamic forces file. The filed data in a certain time step (i.e. velocity vectors, pressures) is written as a Tecplot (.plt) file. For extensive numerical simulation, where number of grid points is about 5 million, a single Tecplot file exceeds 1GB. Since there is about several thousand time steps, it is very difficult to store all the data. To reduce data storage, a Tecplot file is written every certain time step (e.g. 1, 101, 201, …,10001). Tecplot files are needed to create a video of a simulation. Vortex-structure simulation is time-dependent and only by analyzing multiple movie files it is possible to properly visualize the simulation.

- • *Converting ASCII to binary*

The visualization of the simulation is carried out in Tecplot software. It is a Computer-aided Engineering (CEA) visualization software. Tecplot package provides *preplot.exe* program, which enables converting ASCII data files into binary data files. Such an operation reduces the size of an ASCII movie file by about 85%. Moreover, Tecplot works faster with binary data, so the post-processing time is reduced. The movie files are converted one by one using preplot.exe program. To speed up the process the following batch file (*preplot.bat*) was written, which creates a loop over all movie files to run preplot.exe.

```
@echo off
FOR /L %%G IN (1,1,20) DO (
start preplot.exe mv%%G.plt m%%G.plt
```

203

```
ping 192.0.2.2 -n 1 -w 25000 > nul
)
```

Where:

(– beginning of the loop,

%%G – incremental integer,

 (1,1,20) – (1,1,20) – starting movie number, increment, final movie number,

start preplot.exe mv%%G.plt m%%G.plt – command to run preplot program and convert *mv*

ASCII file into *m* binary file,

ping 192.0.2.2 -n 1 -w 25000 > nul – time lag equal to 25 sec,

) – end of the loop.

The time lag has to be adjusted to the size of a movie file, so that the processor is not overloaded

with many preplot programs running at the same time.

A binary data file can be again converted to ASCII through Tecplot:

Open binary file in Tecplot > File > Write data file > check field data box and ASCII box.

- *Creating videos*

There are two ways of creating videos from output movie files. The first involves using macro

file. The procedure is described below. The macro is include in a box

Create a layout file using a single movie file > run macro over all movie files


```
#!MC 800
$!VarSet |NumFiles| = 99
$!EXPORTSETUP EXPORTFORMAT = RASTERMETAFILE
$!EXPORTSETUP IMAGEWIDTH = 879
$!EXPORTSETUP ANIMATIONSPEED = 5
$!ExportSetup ExportFName ='C:\Users\pmgoreck\Desktop\pressure\video.rm'
$!Loop |NumFiles|
$!OpenLayout 'C:\Users\pmgoreck\Desktop\pressure\2.lay'
  AltPlotFNames = 'C:\Users\pmgoreck\Desktop\pressure\mv|LOOP|..plt'
```

```
$! IF |LOOP|==1
  $!EXPORT
    APPEND =NO
$!ENDIF
$! IF |LOOP| !=1
  $!EXPORT
    APPEND =yes
$!ENDIF
$!Endloop
$!quit
```

The above Tecplot macro has to be saved with *mcr* extension. It creates video.rm file over 99

movie files. In the video each frame is a one movie file. The video is desired to be opened in

Framer.exe program that is provided by Tecplot package.

The second way of creating videos consist in …..

APPENDIX 4: Tornado path deviation due to large structure
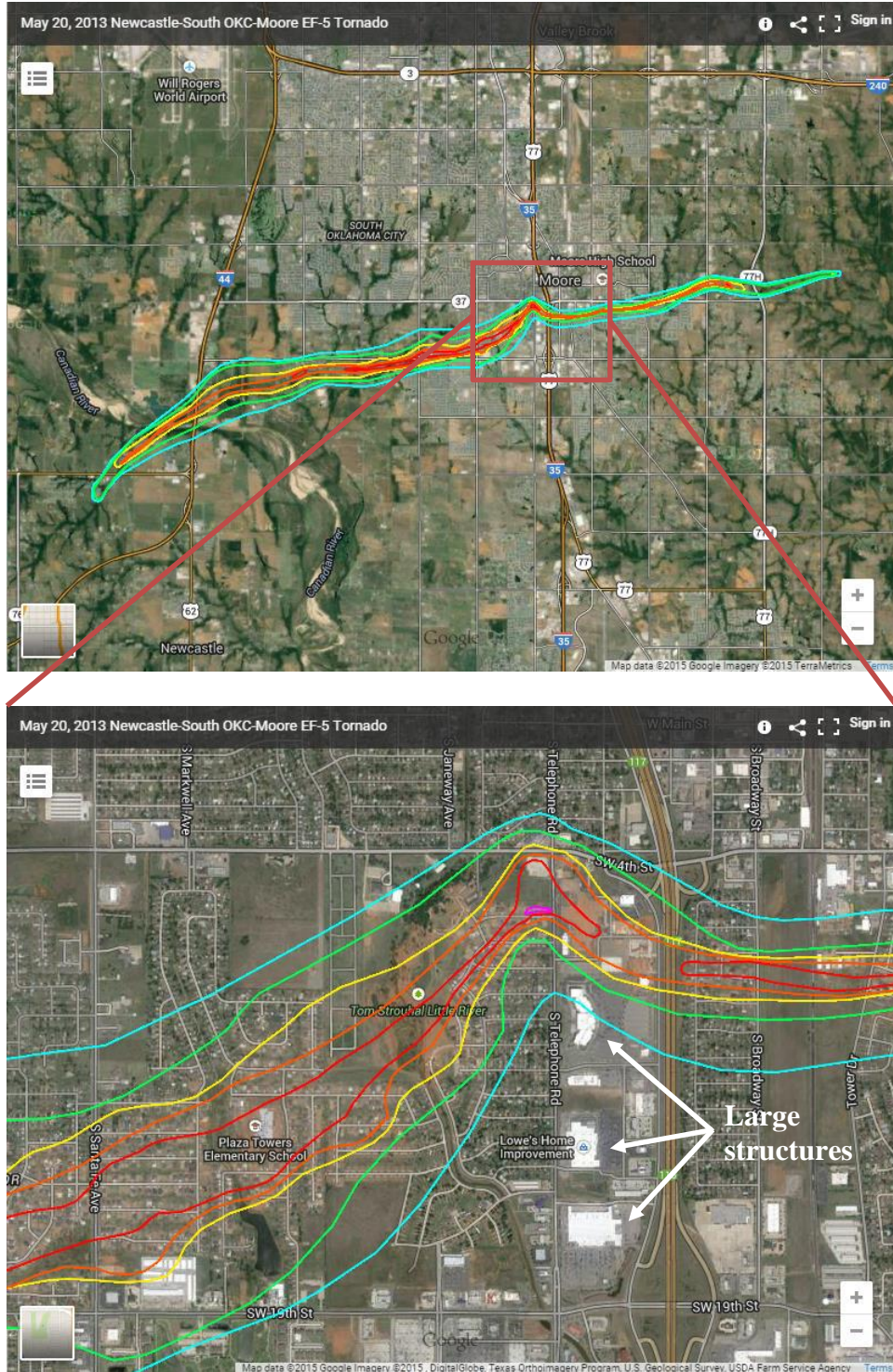
Figure A4.1 Oklahoma City-Moore EF-5 tornado path analyzed by Aliwan and Selvam (2015).

APPENDIX 5: Post-processing FORTRAN code

```fortran
      PARAMETER(NX=250,NY=250,NZ=150)

      IMPLICIT REAL*8 (A-H,O-Z)
      DIMENSION V(NX,NY,NZ,4),X(NX),Y(NY),Z(NZ),v2(nx,ny,nz,4),
     &vh2d(nx,ny),vent(nx,ny),Q(nx,ny,nz),Q2d(nx,ny),Qenv(nx,ny),
     &Psurf(nx,ny),vorz2d(nx,ny),Vzenv(nx,ny),vxyt(nx,ny),vxyenv(nx,ny),
     &Ptemp(nx,ny)

      character*50 finp,fout
c.....detail of v2
c   1  2  3  4
c   wx wy wz rv
C    Building dimensions read from thill.txt
C
C    Sheltering zones diensions
C    Zone 1: +3H x W x 0-0.5H
C    Zone 2: +3H x W x 0.5H-H
C    Zone 3: 3H-6H x W x H

      print *,'read number of starting file'
      read(*,*)istrt
      print *,'read number of ending file'
      read(*,*)iend

      OPEN(5,FILE='thill.txt')
      OPEN(3,FILE='char.txt')
      OPEN(4,FILE='char2.txt')
      OPEN(9,FILE='zones.txt')
      OPEN(7,FILE='xy-plane.plt')

      read(5,*) im,jm,km,IMK1,IMK2,JMK1,JMK2,KH

      do j=1,jm
      do i=1,im
      vent(i,j)=0.0D+00
      Qenv(i,j)=0.0D+00
      Psurf(i,j)=0.0D+00
      Vzenv(i,j)=0.0D+00
      vxyenv(i,j)=0.0D+00
      enddo
      enddo

      do k=1,km
      do j=1,jm
      do i=1,im
      Q(i,j,k)=0.0D+00
      end do
      end do
      end do

 200  format(a)
      close(5)
```

```fortran
      do n=1,500
      read(3,200) finp
      read(4,200) fout

      if ((n.ge.istrt).and.(n.le.iend)) then
      OPEN(1,FILE=finp)
      OPEN(2,FILE=fout,status='new')

      do j=1,jm
      do i=1,im
      vh2d(i,j)=0.0D+00
      Q2d(i,j)=0.0D+00
      vorz2d(i,j)=0.0D+00
      vxyt(i,j)=0.0D+00
      Ptemp(i,j)=0.0D+00
      end do
      end do

c.....read tecplot file
c     skip two line
      read(1,*)
      read(1,*)
      do k=1,km
      do j=1,jm
      do i=1,im
      read(1,*)x(i),y(j),z(k),(v(i,j,k,i1),i1=1,4)
      end do
      end do
      end do
      print *,'check1',n
c.....process further for otehr info
c.....calculate resultant velocities in 4
c.....the vortices around the building is not correct

C     for sheltering zones
      inode1=0
      inode2=0
      inode3=0
      vmax1=0
      vavg1=0
      vmax2=0
      vavg2=0
      vmax3=0
      vavg3=0

      do k=1,km
      do j=1,jm
      do i=1,im

C     resultant velocity calculation
      v2(i,j,k,4)=sqrt(v(i,j,k,1)*v(i,j,k,1)+v(i,j,k,2)*v(i,j,k,2)
     &+v(i,j,k,3)*v(i,j,k,3)+1.e-10)


      if (i.gt.1.and.i.lt.im.and.j.gt.1.and.j.lt.jm.and.k.gt.1.
     &and.k.lt.km)then
```

208

```fortran
      dx2=x(i+1)-x(i-1)
      dy2=y(j+1)-y(j-1)
      dz2=z(k+1)-z(k-1)

      ux=(v(i+1,j,k,1)-v(i-1,j,k,1))/dx2
      vy=(v(i,j+1,k,2)-v(i,j-1,k,2))/dy2
      wz=(v(i,j,k+1,3)-v(i,j,k-1,3))/dz2

      vx=(v(i+1,j,k,2)-v(i-1,j,k,2))/dx2
      wx=(v(i+1,j,k,3)-v(i-1,j,k,3))/dx2
      uy=(v(i,j+1,k,1)-v(i,j-1,k,1))/dy2
      wy=(v(i,j+1,k,3)-v(i,j-1,k,3))/dy2
      uz=(v(i,j,k+1,1)-v(i,j,k-1,1))/dz2
      vz=(v(i,j,k+1,2)-v(i,j,k-1,2))/dz2

C   vorticity calculation
      v2(i,j,k,1)=wy-vz
      v2(i,j,k,2)=uz-wx
      v2(i,j,k,3)=vx-uy

C   Q-criterion calculation
      s11 = ux
      s12 = 0.5*(uy+vx)
      s13 = 0.5*(uz+wx)
      s22 = vy
      s23 = 0.5*(vz+wy)
      s33 = wz

      Omga12 = 0.5*(uy-vx)
      Omga13 = 0.5*(uz-wx)
      Omga23 = 0.5*(vz-wy)

      Q(i,j,k)=2*Omga12**2+2*Omga13**2+2*Omga23**2-s11**2-s22**2-s33**2-
     &2*s12**2-2*s13**2-2*s23**2

      end if

C   values @ prism level velocity mag, q-criterion and vorticity
      vh2d(i,j)=v2(i,j,KH,4)
      Q2d(i,j)=Q(i,j,KH)
      vorz2d(i,j)=v2(i,j,KH,3)

C   resultant velocity envelope
      if (k.lt.KH) then
        if (v2(i,j,k,4).gt.vxyt(i,j)) then
          vxyt(i,j)=v2(i,j,k,4)
        end if
      end if

C   Sheltering Region Velocities
      H3=3.0*z(KH)
      H05=0.5*z(KH)
      Z1ZE=x(IMK2)+H3
      Z3ZE=Z1ZE+H3

C   Zone 1
```

```
      if (((x(i).gt.x(IMK2)).and.(x(i).lt.Z1ZE)).and.((y(j).gt.y(JMK1)).
   &and.(y(j).lt.y(JMK2))).and.(z(k).lt.H05)) then

        if (v2(i,j,k,4).gt.vmax1) then
          vmax1=v2(i,j,k,4)
        end if
        inode1=inode1+1
        vavg1=vavg1+v2(i,j,k,4)
      end if

C    Zone 2
      if (((x(i).gt.x(IMK2)).and.(x(i).lt.Z1ZE)).and.((y(j).gt.y(JMK1)).
   &and.(y(j).lt.y(JMK2))).and.((z(k).gt.H05)).and.(z(k).lt.z(KH)))
   & then

        if (v2(i,j,k,4).gt.vmax2) then
          vmax2=v2(i,j,k,4)
        end if
        inode2=inode2+1
        vavg2=vavg2+v2(i,j,k,4)
      end if

C    Zone 3
      if (((x(i).gt.Z1ZE).and.(x(i).lt.Z3ZE)).and.((y(j).gt.y(JMK1)).
   &and.(y(j).lt.y(JMK2))).and.(z(k).lt.z(KH))) then

        if (v2(i,j,k,4).gt.vmax3) then
          vmax3=v2(i,j,k,4)
        end if
        inode3=inode3+1
        vavg3=vavg3+v2(i,j,k,4)
      end if

C     Pressure at surface
      if ((i.ge.IMK1).and.(i.le.IMK2)) then
      Ptemp(i,j)=v(i,j,KH,4)
      else
      Ptemp(i,j)=v(i,j,1,4)
      end if

      end do
      end do
      end do

      vavg1=vavg1/inode1
      vavg2=vavg2/inode2
      vavg3=vavg3/inode3

 110 format(6(F10.5))
      write(9,110) vavg1,vmax1,vavg2,vmax2,vavg3,vmax3

C     Envelopes over time xyplane
      do j=1,jm
      do i=1,im
C     velocity mag on prism level
      if (vh2d(i,j).gt.vent(i,j)) then
```

```fortran
      vent(i,j)=vh2d(i,j)
      end if
C    q-criterion on prism level
      if (Q2d(i,j).gt.Qenv(i,j)) then
      Qenv(i,j)=Q2d(i,j)
      end if
C    pressure on the surface & on prism level
      if (Ptemp(i,j).lt.Psurf(i,j)) then
      Psurf(i,j)=Ptemp(i,j)
      end if
C    vorticity on prism level
      if (vorz2d(i,j).gt.Vzenv(i,j)) then
      Vzenv(i,j)=vorz2d(i,j)
      end if
C    velocity magnitude envelope up to the prism level
      if (vxyt(i,j).gt.vxyenv(i,j)) then
      vxyenv(i,j)=vxyt(i,j)
      end if

      end do
      end do

      print *,'check2'
c.....write tecplot file correct

      write(2,*)'VARIABLES = "X","Y","U-velocity","V-velocity","W-veloci
     &ty","P","Q-criterion"'
      write(2,*)'ZONE I=',IM, ',J=',JM, ',F=POINT'

      do j=1,jm
      do i=1,im
      write(2,*)x(i),y(j),(v(i,j,KH,i1),i1=1,4),Q2d(i,j)
      end do
      end do

      close(1)
      close(2)

      end if
      end do

      write(7,*)'VARIABLES = "X","Y","Velocity Magnitude","Q-criterion",
     &"P_@_surf","Z-vorticity","Velocity Envelope"'
      write(7,*)'ZONE I=',IM, ',J=',JM, ',F=POINT'
      do j=1,jm
      do i=1,im
      write(7,*)x(i),y(j),vent(i,j),Qenv(i,j),Psurf(i,j),Vzenv(i,j),
     &vxyenv(i,j)
      end do
      end do

      close(7)

      STOP
      END
```